Control and prevention of tropical diseases by advanced tools and the One Health approach

Edited by
Jun-Hu Chen, Yang Hong, Kokouvi Kassegne,
Moses Okpeku and Bin Zheng

About Frontiers

Frontiers is more than just an open access publisher of scholarly articles: it is a pioneering approach to the world of academia, radically improving the way scholarly research is managed. The grand vision of Frontiers is a world where all people have an equal opportunity to seek, share and generate knowledge. Frontiers provides immediate and permanent online open access to all its publications, but this alone is not enough to realize our grand goals.

Frontiers journal series

The Frontiers journal series is a multi-tier and interdisciplinary set of open-access, online journals, promising a paradigm shift from the current review, selection and dissemination processes in academic publishing. All Frontiers journals are driven by researchers for researchers; therefore, they constitute a service to the scholarly community. At the same time, the *Frontiers journal series* operates on a revolutionary invention, the tiered publishing system, initially addressing specific communities of scholars, and gradually climbing up to broader public understanding, thus serving the interests of the lay society, too.

Dedication to quality

Each Frontiers article is a landmark of the highest quality, thanks to genuinely collaborative interactions between authors and review editors, who include some of the world's best academicians. Research must be certified by peers before entering a stream of knowledge that may eventually reach the public - and shape society; therefore, Frontiers only applies the most rigorous and unbiased reviews. Frontiers revolutionizes research publishing by freely delivering the most outstanding research, evaluated with no bias from both the academic and social point of view. By applying the most advanced information technologies, Frontiers is catapulting scholarly publishing into a new generation.

What are Frontiers Research Topics?

Frontiers Research Topics are very popular trademarks of the *Frontiers journals series*: they are collections of at least ten articles, all centered on a particular subject. With their unique mix of varied contributions from Original Research to Review Articles, Frontiers Research Topics unify the most influential researchers, the latest key findings and historical advances in a hot research area.

Find out more on how to host your own Frontiers Research Topic or contribute to one as an author by contacting the Frontiers editorial office: frontiersin.org/about/contact

Control and prevention of tropical diseases by advanced tools and the One Health approach

Topic editors

Jun-Hu Chen — National Institute of Parasitic Diseases, China
Yang Hong — National Institute of Parasitic Diseases, China
Kokouvi Kassegne — Shanghai Jiao Tong University, China
Moses Okpeku — University of KwaZulu-Natal, South Africa
Bin Zheng — Zhejiang Academy of Medical Sciences, China

Table of contents

frontiers | Frontiers in Microbiology

Editorial: Control and prevention of tropical diseases by advanced tools and the One Health approach

Yang Hong[1,2], Kokouvi Kassegne[3], Moses Okpeku[4], Bin Zheng[5] and Jun-Hu Chen[1,2]*

[1]National Health Commission of the People's Republic of China (NHC) Key Laboratory of Parasite and Vector Biology, National Institute of Parasitic Diseases, Chinese Center for Diseases Control and Prevention (Chinese Center for Tropical Diseases Research), World Health Organization (WHO) Collaborating Center for Tropical Diseases, National Center for International Research on Tropical Diseases, Shanghai, China, [2]Hainan Tropical Diseases Research Center (Hainan Sub-Center, Chinese Center for Tropical Diseases Research), Haikou, China, [3]School of Global Health, Chinese Centre for Tropical Diseases Research, Shanghai Jiao Tong University School of Medicine, Shanghai, China, [4]Discipline of Genetics, School of Life Sciences, University of KwaZulu-Natal, Durban, South Africa, [5]School of Basic Medicine and Forensics, Hangzhou Medical College, Hangzhou, China

Editorial on the Research Topic
Control and prevention of tropical diseases by advanced tools and the One Health approach

One Health is described as the collaborative efforts of multiple disciplines working locally, nationally, and globally to attain optimal health for humans, animals and the environment. It recognizes the health of humans, domestic and wild animals, plants, and the wider environment (including ecosystems) which are closely linked and interdependent. The final aim of One Health is to sustainably balance and optimize the health of humans, animals and ecosystems. It is a collaborative global approach to understanding and managing risks for planetary health and encouraging a more sustainable ecosystem balance.

In recent years, many factors have changed interactions between humans, animals, plants, and the environment. These changes have led to the spread of existing or known (endemic) and new or emerging zoonotic diseases that can spread between animals and humans. Every year, millions of humans and animals are affected by zoonotic diseases worldwide. Emerging and re-emerging zoonotic diseases represent a public health challenge of global concern. They include a large group of tropical diseases (TDs), many of which are zoonotic in nature. TDs are especially common in tropical areas, including several countries in Africa, Asia, and Latin America, where humans do not have full access to clean water or safe ways to dispose of human waste. TDs include several parasitic, viral, and bacterial diseases that are transmitted directly from person to person or through vectors (e.g., insects and mollusks) and cause more than one million human deaths globally. Affecting the world's poorest humans, TDs impair physical and cognitive development, contribute to mother, child illness, and death, affect humans' ability to work, and limit productivity at work. As a result, TDs trap the poor in a cycle of poverty and disease.

There are five parasite species that regularly cause malaria in humans, and two of these species – *Plasmodium falciparum* and *P. vivax* – account for large morbidity and mortality,

particularly in sub-Saharan Africa, where the greatest burden of the disease is borne. In 2020, nearly half of the world's population was at risk of malaria. Developing malaria vaccines is a good choice to prevent the occurrence and spread of this disease. Sun et al. used the reverse genetics system to construct recombinant vesicular stomatitis virus (rVSVs), which is a single-stranded negative-strand RNA virus widely used as a vector for virus or cancer vaccines, expressing apical membrane protein 1 (AMA1), rhoptry neck protein 2 (RON2), and reticulocyte-binding protein homolog 5 (RH5). These proteins are required for *P. falciparum* invasion. The authors found that a VSV-based viral vaccine approach for malaria exhibited efficacy in inducing specific humoral and cellular immune responses as well as inhibiting *P. falciparum* invasion. *Plasmodium*-specific IgG levels and lymphocyte proliferation could be significantly increased after vaccination. Prime-boost regimens with VSV-PyAMA1 and VSV-PyRON2sp could significantly improve the levels of IL-2 and IFN-γ produced by CD_4^+ and CD_8^+ T cells and suppress invasion *in vitro*. Meanwhile, the rVSV prime-protein boost regimen significantly increased *Plasmodium* antigen-specific IgG levels in the serum of mice. In the immunoprotection experiment, the mice immunized by rVSV prime protein boost displayed a better protective efficacy against *P. yoelii* 17XL compared to traditional antigen immunization.

Liu et al. examined genomic epidemiology during the pre-elimination stage by retrospectively reporting whole-genome sequence variation of 10 *P. vivax* isolates from inland China in the 2010s, which were highly structured compared to the surrounding area, with a single potential ancestor. Some genes, such as ugt, krs1, and crt, could be used as selection signatures in drug resistance. The proportion of susceptible isolates (wild-type dhps and dhfr-ts) fluctuated in response to the prohibition of sulfadoxine-pyrimethamine. The findings of the study also implied that superinfection or cotransmission events are rare in low-endemic circumstances.

The filarial nematodes that cause these debilitating diseases are transmitted by blood-feeding insects and produce chronic and long-term infection through suppression of host immunity. Lymphatic filariasis and onchocerciasis are parasitic helminth diseases that constitute a serious public health issue in tropical regions, and the two diseases are mainly treated via mass drug administration (MDA), such as ivermectin, albendazole and diethylcarbamazine.

OXF and flubendazole (FBZ) are two benzimidazoles that selectively target the β-tubulin subunits of nematodes, and they have shown macrofilaricidal activities against different filarial species. Risch et al. demonstrated the significant contributions of the immune system during anti-filarial treatment with OXF and FBZ using the *Litomosoides sigmodontis* rodent model. OXF and FBZ induced marked differences in both spleen and thoracic cavity cell compositions with distinct differential patterns in various immunodeficient mouse strains.

IL-5, but not IL-4 or IL-33, combined with OXF could improve the macrofilaricidal efficacy, and a shortened 3-day treatment could be boosted for worm burden reduction. The number of microfilaria-positive animals decreased, and no lung pathological changes were observed in treated mice. Thus, some components

of the host immune system could support the filaricidal effect of benzimidazoles *in vivo* and present an opportunity to boost treatment efficacy. These findings may yield more treatment options for human filarial patients.

Dirofilaria immitis, known as heartworm or dog heartworm, is a small thread-like parasitic roundworm. It is a type of filarial worm that causes dirofilariasis, which is a major emergent veterinary parasitic infection and a human zoonosis. Marriott et al. demonstrated that multiple lymphopenic immunodeficient mouse strains with ablation of the interleukin-2/7 common gamma chain (γc) are susceptible to the initial tissue larval development phase of *D. immitis*. This model provides universal access to accurate and facile PK-PD assessments of preventative *D. immitis* drug candidate responses against the prophylactic L3–L4 larval target. Meanwhile, it could avoid the risk of welfare issues and allow for rapid assessments. In the future, it might reduce the requirements for long-term cat and dog experimentation in heartworm studies.

Toxoplasma gondii (*T. gondii*) is an obligate intracellular parasite that can infect virtually all warm-blooded animals, including humans, cats, and birds. It threatens one-third of the world's population because of its broad host range, high infection rate, and benign coexistence with the host. Although various vaccination strategies have been used to develop an effective toxoplasmosis vaccine, there is still no safe and effective vaccine for *T. gondii*. To date, only Toxovax$^{\circledR}$ has been approved in a few regions for reducing the losses in sheep farming caused by congenital toxoplasmosis. Li et al. used TGGT1_316290 (TG290) as a potential vaccine target to construct TG290 mRNA-LNPs by the lipid nanoparticle (LNP) technology. After vaccination, TG290 mRNA-LNPs elicit humoral and cellular immune responses, enhanced cytokine production, and evoked DCs and T lymphocytes. TG290-specific total IgG and subtype IgG1 and IgG2a antibodies and cytokines (IFN-γ, IL-12, IL-4, and IL-10) were significantly elevated. Cytokine-related transcription factors, such as T-Box 21 (T-bet), nuclear factor kappa B (NF-kB) p65, and interferon regulatory factor 8 (IRF8) subunit, were also overexpressed. Meanwhile, TG290 mRNA-LNP vaccination prolonged the survival time of *T. gondii*-infected BALB/c mice. TG290 might be a potential candidate for an anti-*T. gondii* vaccine.

Babesiosis is globally distributed, and numerous wild and domestic animals may serve as infection reservoir hosts. The disease is mainly caused by *Babesia microti*, which is a tick-transmitted protozoan hemoparasite, and it usually induces a serious public health concern. Song et al. found that nearly 40% of erythrocytes could change their structure and shrink in *B. microti*-infected BALB/c mice. The infection could also cause significant splenomegaly, severe anemia, a massive loss of late erythroblasts and induce eryptosis. However, the population of early erythroblasts was identified to increase in both the bone marrow and spleen, which played a critical protective role in controlling *B. microti* infection and preventing anemia.

Schistosomiasis caused by three main species of schistosomes (trematode blood flukes) infecting humans, *Schistosoma mansoni*, *S. haematobium*, and *S. japonicum*, affects more than 230 million people worldwide. Diagnosis and treatment are the two effective methods to control the disease.

Mu et al. set up a urine-based enzyme-linked immunosorbent assay (ELISA) using SjSAP4 + Sj23-LHD as detection antigens. The diagnostic performance of the urine ELISA was evaluated in a human cohort recruited from areas in the Philippines that are moderately endemic for schistosomiasis japonica. Compared with other diagnostic tests, the urine ELISA showed a 47.2–56.9% sensitivity and a 50.7–55.2% specificity in the detection of *S. japonicum* infection. Although urine-based methods are convenient and highly acceptable non-invasive methods for clinical sample collection, they show insufficient sensitivity compared with corresponding serum-based methods. This disadvantage will limit its use in subjects with low worm burdens in rural schistosome-endemic areas post mass drug administration in the Philippines.

To date, the most effective drug for the treatment of schistosomiasis is still praziquantel (PZQ) in the clinic without any backup drugs. The neurotransmitter glutamate is involved in many physiological functions. Glutamate neuronal signaling can interact with various cell surface receptors for signal transduction, including ionotropic gated channels and metabotropic glutamate receptors (mGluRs, also known as GRMs). Thus, they might be promising drug targets for schistosomiasis.

Wang et al. identified two putative glutamate-specific mGluRs (GRM7 and GRM) in *S. japonicum*. SjGRM is mainly located in the gonads of both males and females, and SjGRM7 is principally found in the nerves and gonads of males and gonads of females. The expression of SjGRM was relatively stable during schistosome development in the definitive host. SjGRM7 was first downregulated before 26 dpi and then upregulated after 26 dpi. After dsRNA interference of SjGRM7 *in vivo*, the development of worms and egg production were affected, and host liver granulomas and fibrosis were alleviated. RNA sequencing data implied that SjGRM7 propagates its signals through the G protein-coupled receptor signaling pathway to promote nervous system development. This study prompted further drug development research to treat *S. japonicum*, and SjGRM7 might be a potential anti-schistosomiasis target.

Skin-associated lymphoid tissue is crucial for parasite control because the skin of mammals accomplishes complex physiological and immunological functions. Epiddermal Langerhans cells (LCs), favor the generation of *Leishmania*-specific T cells *in vivo*, and LCs are involved in adaptive immunity against *Leishmania* parasites, which are spread by the bite of phlebotomine sand flies.

Nerb et al. thought that the immunological attributes of LCs under "microbiome-free" and "microbiome-containing" sand fly or syringe conditions were not systematically compared. The role of LCs in adaptive immunity and the generation of long-lasting immunological memory need to be deciphered in detail. Natural transmission of *Leishmania* parasites is also not sterile. Using novel vector-associated "natural" microbial adjuvants might be an improvement of alternative rationally designed vaccination strategies for *Leishmania* parasites in the future.

Many species of mosquitoes can ingest pathogens while biting and transmit them to future hosts. Mosquitoes are important vectors for the transmission of vector-borne diseases, such as malaria, dengue or Zika.

Musah et al. identified that many open-source data sources from Brazil could be harnessed as risk factors for the spatial prediction of mosquito occupancy or infestation. They could be brought together and reproducibly implemented using the MAXENT algorithm within a Brazilian context. To address the problems of data paucity and avoid potential biases that are typically found in studies using open source datasets, the use of novel bespoke technologies, such as smartphone applications, might be considered a better method for collecting primary entomological data. This will improve a study's internal and external validity. The thread and reproducible method are applicable to different mosquito species and other areas in the Global South with similar environmental and socioeconomic conditions.

In summary, this themed Research Topic advances our knowledge of controlling, preventing, or eliminating TDs under the One Health concept. Many great efforts in epidemiology, vector control, and the use of drugs have been very helpful in bringing reduced incidence alongside great advancements toward TD eradication. Moreover, environmental factors greatly influence the prevalence of TDs. More effective and environmentally friendly strategies are needed to support TDs control. These studies provide useful information to better control TDs and to achieve the final aim of One Health.

Author contributions

YH: Conceptualization, Writing—original draft. KK: Writing—review and editing. MO: Writing—review and editing. BZ: Writing—review and editing. J-HC: Conceptualization, Funding acquisition, Writing—review and editing.

Funding

Conflict of interest

The authors declare that the research was conducted in the absence of any commercial or financial relationships that could be construed as a potential conflict of interest.

The author(s) declared that they were an editorial board member of Frontiers, at the time of submission. This had no impact on the peer review process and the final decision.

Publisher's note

All claims expressed in this article are solely those of the authors and do not necessarily represent those of their affiliated organizations, or those of the publisher, the editors and the reviewers. Any product that may be evaluated in this article, or claim that may be made by its manufacturer, is not guaranteed or endorsed by the publisher.

Have We Ignored Vector-Associated Microbiota While Characterizing the Function of Langerhans Cells in Experimental Cutaneous Leishmaniasis?

Benedikt Nerb [1,2], Diana Dudziak [3,4], André Gessner [5], Markus Feuerer [1,2] and Uwe Ritter [1,2]*

[1] Department for Immunology, Leibniz Institute for Immunotherapy (LIT), Regensburg, Germany, [2] Chair for Immunology, University of Regensburg, Regensburg, Germany, [3] Department of Dermatology, Laboratory of Dendritic Cell Biology, Friedrich-Alexander Universität Erlangen-Nürnberg (FAU), University Hospital Erlangen, Erlangen, Germany, [4] Deutsches Zentrum Immuntherapie (DZI), Erlangen, Germany, [5] Institute of Clinical Microbiology and Hygiene, University Hospital Regensburg, Regensburg, Germany

Keywords: Langerhans cells, dendritic cells, microbiome, skin, experimental cutaneous leishmaniasis, T cell-mediated immunity, lymph node

THE SKIN-ASSOCIATED LYMPHOID TISSUE IS CRUCIAL FOR PARASITE CONTROL

The skin represents one of the largest organs in mammalians and accomplishes complex physiological and immunological functions (1). The most outer epidermal layer of this cutaneous shield is pivotal to protect the body from invading microorganisms. However, this barrier is futile, once pathogens are incorporated into deeper dermal compartments by bloodsucking arthropods. In this case, arthropod-associated pathogens such as fungi, protozoans, viruses, and bacteria are transmitted into the dermis of mammalians (2). After such a barrier-breakdown, a promptly reacting innate immune response is crucial to eliminate most of the arthropod-associated pathogens at the site of infection (3).

Pathogens have learned to evade some mechanisms of innate immunity (4–6). Thus, a precise pathogen-specific adaptive immunity has to be generated, to avoid an uncontrolled spreading of pathogens and tissue damage. This highly evolved immune response combines a network of cellular and humoral components capable of recognizing foreign antigens to eliminate pathogens and pathogen-harbouring cells (7, 8). In the case of bloodsucking arthropods, most of these host-pathogen interactions take place within the skin-associated lymphoid tissue (SALT) that combines three major components: First, the cutaneous microenvironment equipped with immune cells capable of accepting, processing, and presenting antigens at the site of adaptive effector cell function. Second, the efferent lymphatics connecting the dermal compartment with skin-draining lymph nodes (SDLN). Third, the paracortex within the SDLN where T cell-mediated immunity against skin-derived antigens is generated (9).

A coordinated interaction of immune cells is a precondition for efficient adaptive immunity within the SALT. In this context, the experimental cutaneous leishmaniasis (ECL) of mice has to be emphasized. In the model, promastigote *Leishmania* (L.) *major* parasites are mostly incorporated by a syringe into the dermal compartment to mimic the natural transmission by bloodsucking sand flies (10). Ground-breaking aspects of T cell-mediated immunity, such as T helper (T$_h$) 1 and T$_h$2 polarization arose from studies in ECL (11, 12). It has been shown, that healing of ECL correlates with the presence of a profound T$_h$1 cell expansion and the production of IFN-γ that activates macrophages to eliminate intracellular parasites (13). IL-12 has been identified as the T$_h$1-polarizing cytokine important for T$_h$1 cell differentiation (14, 15). By contrast, IL-4 promotes T$_h$2 cell development and susceptibility for ECL (16).

LANGERHANS CELLS ARE INVOLVED IN ADAPTIVE IMMUNITY AGAINST *LEISHMANIA* PARASITES

A subset of specialized myeloid cells, the epidermal Langerhans cells (LCs), has been favoured to generate *Leishmania*-specific T cells *in vivo*. In 1992, studies revealed that epidermal cells, including LCs, can activate the *Leishmania*-specific T cell clone L1/1 and antigen-primed T cells derived from susceptible BALB/c mice (17). Furthermore, DEC-205/CD205/NLDC-145$^+$ LCs can transport *L. major* antigens (L-Ag) to the SDLNs of susceptible BALB/c mice (18). Flohé *et al.* demonstrated that a single i.v. treatment with epidermal-derived LCs, that had been pulsed with L-Ags, induces adaptive immunity and resistance against a *L. major* (MHOM/IL/81/FE/BNI) infection (2×10^5 stationary-phase promastigote parasites/i.d.) in normally susceptible BALB/c mice (19). The release of T$_h$1-polarizing cytokines by LCs has also been proven by other groups using *L. major* clone V1 (MHOM/IL/80/Friedlin) and low-dose models of ECL (20, 21). Thus, LCs have been in the spotlight as decisive cells to induce a protective adaptive immunity in ECL for a long time.

CHANGING VIEWS ON LC FUNCTIONS IN ECL

Inspired by novel markers, useful for the dissection of LCs and dendritic cell (DC) subsets, it has been shown by different *in vivo* configurations, varying in *L. major* strains and dose of application, that LCs are not the only "antigen-presenting cells" that are involved in orchestrating T cell-mediated immunity (22–26). L-Ag-specific T cell proliferation is predominantly driven by Langerin/CD207$^-$ DC subsets (epidermal LCs are Langerin/CD207$^+$), suggesting that Langerin/CD207$^-$ dermal-derived DCs (dDCs) are crucial for protective immunity in ECL using different *L. major* strains [MHOM/IL81/FE/BNI or clone VI (MHOM/IL/80/Friedlin)] and applications (low- or high-dose) for needle infections (27–30). Indeed, LCs can present L-Ags to T cells under certain conditions (17–21). However, the question remains, which pathways of T cell development and immunity are induced by LCs in ECL? To address this aspect, *in vivo* models of inducible ablation of LCs and other DC subsets have been used (31). It has been proven that C57BL/6-LangDTR mice remain resistant against *L. major* (MHOM/IL/81/FE/BNI) high-dose infection even after depleting LCs (29). Protective T$_h$1 cells are also induced in SDLNs in the absence of LCs (29). Other groups using low-dose models and the *L. major* strain clone VI (MHOM/IL/80/Friedlin), were able to confirm that finding - mice depleted for LCs can still control the disease (28). Consequently, the presence of lymph node resident or dDCs is sufficient to generate a protective immunity in *in vivo* ECL (28, 29).

One should not get the impression that epidermal LCs represent a kind of rudimental or redundant myeloid subset, without specific immunological functions. Speculations in this field assumed that LCs are involved in dampening the immune response against *Leishmania* parasites (32, 33). This hypothesis has been confirmed some years later, by demonstrating that LCs participate in expanding regulatory CD4$^+$ T cells (T$_{reg}$) [low-dose model; *L. major* strain clone VI (MHOM/IL/80/Friedlin) (28)] and other IL-10 and IFN-γ expressing CD4$^+$ T cells [high-dose model; *L. major* MHOM/IL/81/FE/BNI (29)] with regulatory capacity (34). Consequently, LCs are involved in balancing immune responses within the SALT. This aspect has also been supported by other experimental systems, showing that LCs are involved in the maintenance of tolerance to peripheral skin-associated antigens (35–37).

Apart from this tolerance promoting functions, LCs are also crucial in ECL for priming and differentiation of follicular helper T cells (T$_{fh}$) and the subsequent formation of early germinal centres (GC) within SDLNs [high-dose; *L. major* MHOM/IL/81/FE/BNI (38)]. A number of other immunization-based and disease models, such as atopic dermatitis, have also confirmed that LCs promote T$_{fh}$ differentiation and GC formation (39–42). This general "LC attribute" of T$_{fh}$ polarization, needs to be examined in more detail. In ECL, B cell-deficient μMT mice develop severe lesions, compared to WT mice. However, the absence of B cell-mediated immunity does not affect the final

outcome of ECL (43). These facts might explain why LC-depleted C57BL/6-LangDTR mice can control ECL, even in the absence of early GC formation and restricted T_{fh} development (38).

NATURAL TRANSMISSION OF *LEISHMANIA* PARASITES IS NOT STERILE

In ECL, LCs contribute to the differentiation of distinct CD4$^+$ T cell subsets such as Foxp3$^+$ T_{reg} cells, IL-10 and IFN-γ producing CD4$^+$ T cells, and T_{fh} cells. However, the absence of LCs does not affect the generation of protective immunity in ECL. Are LCs really "sufficient but not necessary" for protective immunity? Most of the studies involved in the decoding of LCs function in ECL have been performed under standardized conditions such as defined parasite numbers, sterile needle injection and animal housing under specific pathogen free (SPF) conditions (21, 27–29). This standardization is crucial to compare data between studies and in terms of reproducibility, but have we underestimated some vector-associated important factors while decrypting the function of LCs in ECL?

This question is more than justified, because all metazoans coexist intimately with a community of commensal microorganisms (44). Sand flies can harbour fungi, bacteria and viruses (44). In addition, there are sand fly-associated components, such as the saliva and others, that can also influence immune cells (45). The elaboration of all these "vector additives" in ECL is very ambitious. We nonetheless are of the opinion that these factors, most prominent the microbiota-associated side effects, should not be ignored while decrypting the function of LCs in ECL. Given the fact that *L. major* parasites are transmitted selectively by *Phlebotomus* (P.) *papatasi* (46), this vector-parasite constellation will be considered in the following paragraphs.

Comparable to the human gut microbiome (47), wild caught *Phlebotomus* species (sp.) host distinct microbiomes (2) (**Figure 1B**). During the blood meal of sand flies, gut microbes are egested into the skin - alongside with *L. major* parasites (89). This "multicomponent infection" triggers early inflammatory responses within the dermal compartment, such as inflammasome activation and neutrophil infiltration (89). The potential impact of microbes on innate and adaptive immunity in ECL has been already demonstrated. In this case, a needle infection of C57BL/6 mice using a combination of *Staphylococcus* (S.) *aureus* plus *L. major* (90) supports the recruitment of neutrophil granulocytes, γδ T cells, and IL-17 releasing T_h17 cells to the dermal compartment (90). These microbiome-associated side effects seem beneficial for parasite replication and spreading, based on three reasons: First, *L. major* parasites have the ability to maintain infectivity in neutrophil granulocytes. Second, the parasites use granulocytes as "Trojan horses" before they enter their definitive host cells, the macrophages (91, 92). Third, IL-17 favours the recruitment of additional "Trojan horses" such as neutrophil granulocytes (93). This suggests that the

inflammatory micro milieu mediated by *S. aureus* is responsible for exacerbating lesion development (90). Arthropod-associated microbiota might therefore represent "natural adjuvants" capable of catalysing parasite spreading. Whether functional capacities of LCs are also affected, needs to be analysed. Additionally, it remains speculative whether such an exacerbation of lesion development is crucial for long-lasting immunity.

Given the fact that most cell types at the infection site including LCs, dermal macrophages and keratinocytes, are equipped with pattern recognition receptors (PRRs), capable of sensing the bacterial PAMPs (**Figure 1A**), it is plausible that microbiota-associated PAMPs strongly influence adaptive immunity in ECL (**Figure 1B**). For instance, application of isolated PRR ligands, in parallel to *Leishmania* parasites or antigens, displayed beneficial effects. In addition, C57BL/6 mice treated intradermally with *L. major* and the TLR9 ligand CpG oligodeoxynucleotides developed little or no dermal lesions (94) and the treatment of BALB/c mice with L-Ag fractions plus the NOD2 ligand muramyl dipeptide induced resistance against cutaneous leishmaniasis (85). Moreover, an administration of the TLR2/TLR6 agonist BPPcysMPEG in combination with fixed *L. major* parasites protected BALB/c mice against *L. major* infection (95). Based on these and other data, it is obvious that arthropod microbiota might represent important additional parameters in orchestrating immunity in ECL (96, 97) (**Figure 1**).

CONCEIVABLE IMPACT OF ARTHROPOD-ASSOCIATED MICROBIOTA ON LC FUNCTIONS IN ECL

LCs and other cells associated to the SALT are equipped with PRRs sensing microbial PAMPs (**Figure 1**). It is obvious that LCs must get in contact with bacterial compounds during the blood meal of vectors, harbouring microbiota and *Leishmania* parasites. In this context, LCs will be "stimulated" by PAMPs based on the expression of the corresponding PRRs (compare **Figure 1B**). Additionally epidermal LCs, while migrating through the dermal compartment, will be exposed to a micromilieu of soluble factors including cytokines, chemokines and other metabolites, that are released by keratinocytes or other dermal immune cells in response to microbial compounds. This natural *Leishmania*-infection, in the presence of additional vector-derived microbes, is might be capable to modify the transcriptome and proteome of LCs. The consequence remains still speculative. Many scenarios are conceivable based on the given expression PRRs and immune receptors sensing the environment. Here just one example: After PRR-ligation, LCs can release cytokines such as IL-17 (98), IL-12 (49) and TNF-alpha (99) - known to support T_h-cell polarization and LC maturation programs (99). Consequently, it is feasible that LCs might lose their "tolerogenic capacity" (23, 32) and support T_h-cell programs, resulting in adaptive immunity against *L. major* parasites (**Figure 1B**).

A

Leishmania promastigotes

A.1
LPGs -TLR2
GIPLs - TLR2/4
GPI anchors - TLR2/4
ssRNA* - TLR7 & 8
dsRNA*-TLR3 & 7
CpGunmet -TLR9

A.2
Selected PRRs:
TLR1
TLR2
TLR3
TLR4
TLR5
TLR6
TLR7
TLR8
TLR9
CD205
CD206
CD207
NOD2
Dectin-1

A.3

A.4

A.5

T$_h$1 cell   T$_{fh}$ cell   T$_{reg}$ cell

B

B.1
Gram$^+$ bacteria
Gram$^-$ bacteria

B.2
LPS - TLR4
Porins -TLR2
WSP - TLR2 & 4

B.3
PGN - TLR2, NOD2
LTA - TLR2
WTA,
β1,4-GlcNAc-CD207

B.4
CpGunmet -TLR9
Flagellin -TLR5
Triacyl LPPs -TLR1/6
Diacyl LPPs -TLR2/6
Beta-glucan - Dectin-1
MDP - NOD2
Mannose - CD206

B.5

B.6

B.7

T$_h$1 cell   T$_{fh}$ cell   T$_{reg}$ cell   T$_h$17 cell

Langerhans cell   Fibroblast   Connective tissue   PRR expression

Macrophage   Bacteria and antigens   *Stratum corneum*   possible interactions
                                                                         with LM-PRRs

Granulocyte   *Leishmania* (pro and   *Leishmania* infected   possible interactions
                      amastigote) parasites   cells   with BAC-PRRs
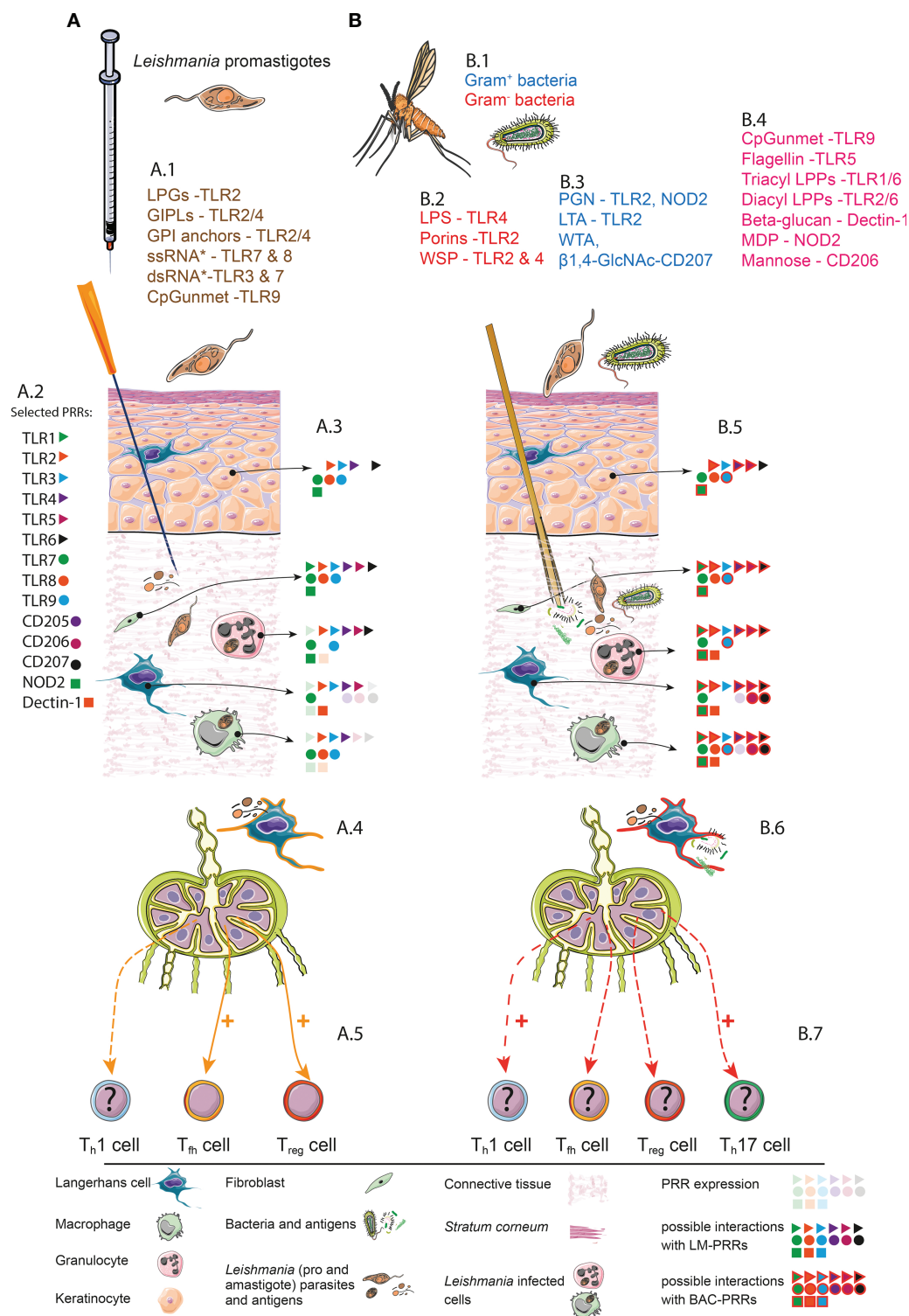Keratinocyte   and antigens

FIGURE 1 | Continued

FIGURE 1 | Simplified synopsis of LC-functions in experimental cutaneous leishmaniasis. Comparison of needle infection **(A)** and transmission by vectors **(B)**. **(A)** Needle infection. A.1. Selected PAMPs of *Leishmania* parasites and their possible interactions with PRRs. *single strand (ss) RNA and *double strand (ds) RNA from *Leishmania*-associated viruses (48). A.2. Representative PRRs and assigned symbols. A.3. PRRs expression and interaction with *Leishmania* (LM)-PAMPs. Pale symbols represent PRRs that are expressed by the indicated cell subset. Solid symbols represent a possible interaction between PRRs and LM-PAMPs. Keratinocytes (49–53), Fibroblasts (54–58), TLR8 (54, 59), Neutrophil granulocytes (60–69), Epidermal Langerhans cells (24, 70–73), Dermal Macrophages (69, 74, 75). A.4. Migratory LC that has been primed in a sterile context (orange contour). This subset can present LM-derived antigens. A.5. LC-driven immune responses in skin-draining lymph nodes. Documented LC functions such as the induction (highlighted by "+") of T_{fh} and T_{reg} cells are highlighted with solid orange arrows. So far unclear (highlighted by "?") involvement of LCs in T_h1 cells differentiation is depicted with a dashed orange arrow. **(B)** Natural transmission. B.1. Gut microbiome of *P. papatasi*. Gram⁻ bacteria: *Wolbachia* sp. (2), *Klebsiella* sp., *Serratia* sp., *Stenotrophomonas gen.*, *Thauera* sp (76), *Pseudomonas* sp (77), *Brevundimonas* sp., *Ochrobactrum gen* (76). Gram⁺ bacteria: *Spiroplasma* sp (2) *Staphylococcus* sp., *Micrococcus* sp., *Corynebacteriaceae* sp. (2) *Bacillus* gen (78), *Microbacteria gen* (77). Gram⁺ or gram⁻ *Paenibacillus gen* (2). B.2. PAMP/PRR-interactions of gram⁻ bacteria (79–81). B.3. PAMP/PRR-interactions of gram⁺ bacteria (82–84). B.4. PAMP/PRR-interactions with bacterial components in general (68, 79, 85–88). B.5. PRRs expression and interaction with LM and bacterial (BAC) PAMPs. Pale symbols represent PRRs that are expressed by the indicated cell subset. Solid symbols represent a possible interaction between PRRs and LM-PAMPs. Solid symbols highlighted with red lines represent possible interactions with BAC-PAMPs. B.6. Migratory LC that has been primed in a nonsterile context (red contour). A presentation of BAC- as well as LM-derived antigens is possible. B.7. Putative (highlighted by "?") LC-driven immune responses in SDLNs. The LC-driven T_h1 and/or T_h17 immune responses might be enhanced (+) by LCs that has been primed in a nonsterile context (solid red arrow). Whether LCs still prime *Leishmania*-specific T_{reg} or T_{fh} cell subsets under nonsterile conditions remains speculative (dashed red arrow). It is possible that LCs fulfill novel functions if conditioned within a nonsterile microenvironment such as the induction of T_h17 and T_h1 cells. All components and symbols are explained by the legend below the figure. LPG, Lipophosphoglycan; GIPLs, glycoinositolphospholipids; TLRs, Toll-like receptors; CpG, cytosine-phosphate-guanine; unmet, unmethylated; LPS, lipopolysaccharide; WSP, *Wolbachia* surface protein; PGN, peptidoglycan; LTA, lipoteichoic acid; WTA, wall teichoic acid; β1,4-GlcNAc, β 1,4-N-acetyl glucosamine; LPP, lipoprotein; NOD, nucleotide-binding oligomerization domain; MDP, muramyl dipeptide; LM, *Leishmania*; BAC, *Bacteria*; PRR, pattern recognition receptors.

CONCLUSION

It is very likely that LCs can support so far unknown immunological programs in the presence of distinct sand fly-associated factors. Up to now, no systematic studies have been performed comparing the immunological attributes of LCs under "microbiome-free" and "microbiome-containing" sand fly or syringe conditions. In our opinion, these aspects need to be deciphered to understand the role of LCs in adaptive immunity and the generation of long-lasting immunological memory in detail. This understanding is pivotal for the improvement of alternative rationally designed vaccination strategies, using novel vector-associated "natural" microbial adjuvants. This new studies are more than overdue based on two aspects: First, L-Ag plus classical adjuvants such as CpG does not protect mice from ECL after challenge with infected sand flies (100). Second, people living in endemic areas seem to be "vaccinated" by multiple sand fly bites in the absence of clinical symptoms of ECL (101). Let's get started to decrypt the impact of LCs in ECL under more physiological conditions.

AUTHOR CONTRIBUTIONS

Conceptualization and investigation, UR. Writing – Original Draft, UR. Writing – Review & Editing, BN, MF, AG, DD. Visualization, UR and BN. Funding Acquisition, UR, MF, AG,

and DD. All authors contributed to the article and approved the submitted version.

REFERENCES

1. Nguyen AV, Soulika AM. The Dynamics of the Skin's Immune System. *Int J Mol Sci* (2019) 20(8). doi: 10.3390/ijms20081811
2. Papadopoulos C, Karas PA, Vasileiadis S, Ligda P, Saratsis A, Sotiraki S, et al. Host Species Determines the Composition of the Prokaryotic Microbiota in Phlebotomus Sandflies. *Pathogens* (2020) 9(6):1–15. doi: 10.3390/pathogens9060428
3. Ritter U. Presentation of Skin-Derived Leishmania Antigen by Dendritic Cell Subtypes. In: E Jirillo, editor. *Immune Response to Parasitic Infections. 1*

Saif Zone Sharjah: Bentham e-Books (2010). p. 123–36 (14). doi: 10.2174/978160805148911001010123
4. Bogdan C, Rollinghoff M. The Immune Response to Leishmania: Mechanisms of Parasite Control and Evasion. *Int J Parasitol* (1998) 28 (1):121–34. doi: 10.1016/s0020-7519(97)00169-0
5. Rosbjerg A, Genster N, Pilely K, Garred P. Evasion Mechanisms Used by Pathogens to Escape the Lectin Complement Pathway. *Front Microbiol* (2017) 8:868. doi: 10.3389/fmicb.2017.00868
6. Sacks D, Sher A. Evasion of Innate Immunity by Parasitic Protozoa. *Nat Immunol* (2002) 3(11):1041–7. doi: 10.1038/ni1102-1041

7. Kautz-Neu K, Schwonberg K, Fischer MR, Schermann AI, von Stebut E. Dendritic Cells in Leishmania Major Infections: Mechanisms of Parasite Uptake, Cell Activation and Evidence for Physiological Relevance. *Med Microbiol Immunol* (2012) 201(4):581–92. doi: 10.1007/s00430-012-0261-2

8. Kaye P, Scott P. Leishmaniasis: Complexity at the Host-Pathogen Interface. *Nat Rev Microbiol* (2011) 9(8):604–15. doi: 10.1038/nrmicro2608

9. Streilein JW. Skin-Associated Lymphoid Tissues (Salt): Origins and Functions. *J Invest Dermatol* (1983) 80 Suppl:12s–6s. doi: 10.1111/1523-1747.ep12536743

10. Scott P, Novais FO. Cutaneous Leishmaniasis: Immune Responses in Protection and Pathogenesis. *Nat Rev Immunol* (2016) 16(9):581–92. doi: 10.1038/nri.2016.72

11. Heinzel FP, Sadick MD, Holaday BJ, Coffman RL, Locksley RM. Reciprocal Expression of Interferon Gamma or Interleukin 4 During the Resolution or Progression of Murine Leishmaniasis. Evidence for Expansion of Distinct Helper T Cell Subsets. *J Exp Med* (1989) 169(1):59–72. doi: 10.1084/jem.169.1.59

12. Scott P, Natovitz P, Coffman RL, Pearce E, Sher A. Immunoregulation of Cutaneous Leishmaniasis. T Cell Lines That Transfer Protective Immunity or Exacerbation Belong to Different T Helper Subsets and Respond to Distinct Parasite Antigens. *J Exp Med* (1988) 168(5):1675–84. doi: 10.1084/jem.168.5.1675

13. Goncalves R, Zhang X, Cohen H, Debrabant A, Mosser DM. Platelet Activation Attracts a Subpopulation of Effector Monocytes to Sites of Leishmania Major Infection. *J Exp Med* (2011) 208(6):1253–65. doi: 10.1084/jem.20101751

14. Heinzel FP, Schoenhaut DS, Rerko RM, Rosser LE, Gately MK. Recombinant Interleukin 12 Cures Mice Infected With Leishmania Major. *J Exp Med* (1993) 177(5):1505–9. doi: 10.1084/jem.177.5.1505

15. Sypek JP, Chung CL, Mayor SE, Subramanyam JM, Goldman SJ, Sieburth DS, et al. Resolution of Cutaneous Leishmaniasis: Interleukin 12 Initiates a Protective T Helper Type 1 Immune Response. *J Exp Med* (1993) 177(6):1797–802. doi: 10.1084/jem.177.6.1797

16. Chatelain R, Varkila K, Coffman RL. Il-4 Induces a Th2 Response in Leishmania Major-Infected Mice. *J Immunol* (1992) 148(4):1182–7.

17. Will A, Blank C, Rollinghoff M, Moll H. Murine Epidermal Langerhans Cells Are Potent Stimulators of an Antigen-Specific T Cell Response to Leishmania Major, The Cause of Cutaneous Leishmaniasis. *Eur J Immunol* (1992) 22(6):1341–7. doi: 10.1002/eji.1830220603

18. Moll H, Fuchs H, Blank C, Rollinghoff M. Langerhans Cells Transport Leishmania Major From the Infected Skin to the Draining Lymph Node for Presentation to Antigen-Specific T Cells. *Eur J Immunol* (1993) 23(7):1595–601. doi: 10.1002/eji.1830230730

19. Flohe SB, Bauer C, Flohe S, Moll H. Antigen-Pulsed Epidermal Langerhans Cells Protect Susceptible Mice From Infection With the Intracellular Parasite Leishmania Major. *Eur J Immunol* (1998) 28(11):3800–11. doi: 10.1002/(SICI)1521-4141(199811)28:11<3800::AID-IMMU3800>3.0.CO;2-0

20. von Stebut E, Belkaid Y, Jakob T, Sacks DL, Udey MC. Uptake of Leishmania Major Amastigotes Results in Activation and Interleukin 12 Release From Murine Skin-Derived Dendritic Cells: Implications for the Initiation of Anti-Leishmania Immunity. *J Exp Med* (1998) 188(8):1547–52. doi: 10.1084/jem.188.8.1547

21. von Stebut E, Belkaid Y, Nguyen BV, Cushing M, Sacks DL, Udey MC. Leishmania Major-Infected Murine Langerhans Cell-Like Dendritic Cells From Susceptible Mice Release Il-12 After Infection and Vaccinate Against Experimental Cutaneous Leishmaniasis. *Eur J Immunol* (2000) 30(12):3498–506. doi: 10.1002/1521-4141(2000012)30:12<3498::AID-IMMU3498>3.0.CO;2-6

22. Romani N, Brunner PM, Stingl G. Changing Views of the Role of Langerhans Cells. *J Invest Dermatol* (2012) 132(3 Pt 2):872–81. doi: 10.1038/jid.2011.437

23. Moreno J. Changing Views on Langerhans Cell Functions in Leishmaniasis. *Trends Parasitol* (2007) 23(3):86–8. doi: 10.1016/j.pt.2007.01.002

24. Kaplan DH. *In Vivo* Function of Langerhans Cells and Dermal Dendritic Cells. *Trends Immunol* (2010) 31(12):446–51. doi: 10.1016/j.it.2010.08.006

25. Doebel T, Voisin B, Nagao K. Langerhans Cells - the Macrophage in Dendritic Cell Clothing. *Trends Immunol* (2017) 38(11):817–28. doi: 10.1016/j.it.2017.06.008

26. Soares H, Waechter H, Glaichenhaus N, Mougneau E, Yagita H, Mizenina O, et al. A Subset of Dendritic Cells Induces Cd4+ T Cells to Produce Ifn-Gamma by an Il-12-Independent But Cd70-Dependent Mechanism in Vivo. *J Exp Med* (2007) 204(5):1095–106. doi: 10.1084/jem.20070176

27. Ritter U, Meissner A, Scheidig C, Korner H. Cd8 Alpha- and Langerin-Negative Dendritic Cells, But Not Langerhans Cells, Act as Principal Antigen-Presenting Cells in Leishmaniasis. *Eur J Immunol* (2004) 34(6):1542–50. doi: 10.1002/eji.200324586

28. Kautz-Neu K, Noordegraaf M, Dinges S, Bennett CL, John D, Clausen BE, et al. Langerhans Cells Are Negative Regulators of the Anti-Leishmania Response. *J Exp Med* (2011) 208(5):885–91. doi: 10.1084/jem.20102318

29. Brewig N, Kissenpfennig A, Malissen B, Veit A, Bickert T, Fleischer B, et al. Priming of Cd8+ and Cd4+ T Cells in Experimental Leishmaniasis Is Initiated by Different Dendritic Cell Subtypes. *J Immunol* (2009) 182(2):774–83. doi: 10.4049/jimmunol.182.2.774

30. Merad M, Ginhoux F, Collin M. Origin, Homeostasis and Function of Langerhans Cells and Other Langerin-Expressing Dendritic Cells. *Nat Rev Immunol* (2008) 8(12):935–47. doi: 10.1038/nri2455

31. Bennett CL, Clausen BE. Dc Ablation in Mice: Promises, Pitfalls, and Challenges. *Trends Immunol* (2007) 28(12):525–31. doi: 10.1016/j.it.2007.08.011

32. Ritter U, Osterloh A. A New View on Cutaneous Dendritic Cell Subsets in Experimental Leishmaniasis. *Med Microbiol Immunol* (2007) 196(1):51–9. doi: 10.1007/s00430-006-0023-0

33. Weiss R, Scheiblhofer S, Thalhamer J, Bickert T, Richardt U, Fleischer B, et al. Epidermal Inoculation of Leishmania-Antigen by Gold Bombardment Results in a Chronic Form of Leishmaniasis. *Vaccine* (2007) 25(1):25–33. doi: 10.1016/j.vaccine.2006.07.044

34. Jankovic D, Kullberg MC, Feng CG, Goldszmid RS, Collazo CM, Wilson M, et al. Conventional T-Bet(+)Foxp3(-) Th1 Cells Are the Major Source of Host-Protective Regulatory Il-10 During Intracellular Protozoan Infection. *J Exp Med* (2007) 204(2):273–83. doi: 10.1084/jem.20062175

35. Shibaki A, Sato A, Vogel JC, Miyagawa F, Katz SI. Induction of Gvhd-Like Skin Disease by Passively Transferred Cd8(+) T-Cell Receptor Transgenic T Cells Into Keratin 14-Ovalbumin Transgenic Mice. *J Invest Dermatol* (2004) 123(1):109–15. doi: 10.1111/j.0022-202X.2004.22701.x

36. Luo Y, Wang S, Liu X, Wen H, Li W, Yao X. Langerhans Cells Mediate the Skin-Induced Tolerance to Ovalbumin *Via* Langerin in a Murine Model. *Allergy* (2019) 74(9):1738–47. doi: 10.1111/all.13813

37. Clayton K, Vallejo AF, Davies J, Sirvent S, Polak ME. Langerhans Cells-Programmed by the Epidermis. *Front Immunol* (2017) 8:1676. doi: 10.3389/fimmu.2017.01676

38. Zimara N, Florian C, Schmid M, Malissen B, Kissenpfennig A, Mannel DN, et al. Langerhans Cells Promote Early Germinal Center Formation in Response to Leishmania-Derived Cutaneous Antigens. *Eur J Immunol* (2014) 44(10):2955–67. doi: 10.1002/eji.201344263

39. Kervevan J, Bouteau A, Lanza JS, Hammoudi A, Zurawski S, Surenaud M, et al. Targeting Human Langerin Promotes Hiv-1 Specific Humoral Immune Responses. *PLoS Pathog* (2021) 17(7):e1009749. doi: 10.1371/journal.ppat.1009749

40. Levin C, Bonduelle O, Nuttens C, Primard C, Verrier B, Boissonnas A, et al. Critical Role for Skin-Derived Migratory Dcs and Langerhans Cells in Tfh and Gc Responses After Intradermal Immunization. *J Invest Dermatol* (2017) 137(9):1905–13. doi: 10.1016/j.jid.2017.04.016

41. Vardam T, Anandasabapathy N. Langerhans Cells Orchestrate Tfh-Dependent Humoral Immunity. *J Invest Dermatol* (2017) 137(9):1826–8. doi: 10.1016/j.jid.2017.06.014

42. Marschall P, Wei R, Segaud J, Yao W, Hener P, German BF, et al. Dual Function of Langerhans Cells in Skin Tslp-Promoted Tfh Differentiation in Mouse Atopic Dermatitis. *J Allergy Clin Immunol* (2021) 147(5):1778–94. doi: 10.1016/j.jaci.2020.10.006

43. Woelbing F, Kostka SL, Moelle K, Belkaid Y, Sunderkoetter C, Verbeek S, et al. Uptake of Leishmania Major by Dendritic Cells Is Mediated by Fcgamma Receptors and Facilitates Acquisition of Protective Immunity. *J Exp Med* (2006) 203(1):177–88. doi: 10.1084/jem.20052288

44. Telleria EL, Martins-da-Silva A, Tempone AJ, Traub-Cseko YM. Leishmania, Microbiota and Sand Fly Immunity. *Parasitology* (2018) 145(10):1336–53. doi: 10.1017/S0031182018001014

45. Lima HC, Titus RG. Effects of Sand Fly Vector Saliva on Development of Cutaneous Lesions and the Immune Response to Leishmania Braziliensis in Balb/C Mice. *Infect Immun* (1996) 64(12):5442–5. doi: 10.1128/iai.64.12.5442-5445.1996

46. Dobson DE, Kamhawi S, Lawyer P, Turco SJ, Beverley SM, Sacks DL. Leishmania Major Survival in Selective Phlebotomus Papatasi Sand Fly Vector Requires a Specific Scg-Encoded Lipophosphoglycan Galactosylation Pattern. *PLoS Pathog* (2010) 6(11):e1001185. doi: 10.1371/journal.ppat.1001185

47. Lozupone CA, Stombaugh JI, Gordon JI, Jansson JK, Knight R. Diversity, Stability and Resilience of the Human Gut Microbiota. *Nature* (2012) 489 (7415):220–30. doi: 10.1038/nature11550

48. Chauhan P, Shukla D, Chattopadhyay D, Saha B. Redundant and Regulatory Roles for Toll-Like Receptors in Leishmania Infection. *Clin Exp Immunol* (2017) 190(2):167–86. doi: 10.1111/cei.13014

49. Sun L, Liu W, Zhang LJ. The Role of Toll-Like Receptors in Skin Host Defense, Psoriasis, and Atopic Dermatitis. *J Immunol Res* (2019) 2019:1824624. doi: 10.1155/2019/1824624

50. Stremnitzer C, Manzano-Szalai K, Willensdorfer A, Starkl P, Pieper M, Konig P, et al. Papain Degrades Tight Junction Proteins of Human Keratinocytes in Vitro and Sensitizes C57bl/6 Mice *Via* the Skin Independent of Its Enzymatic Activity or Tlr4 Activation. *J Invest Dermatol* (2015) 135(7):1790–800. doi: 10.1038/jid.2015.58

51. Crain B, Yao S, Keophilaone V, Promessi V, Kang M, Barberis A, et al. Inhibition of Keratinocyte Proliferation by Phospholipid-Conjugates of a Tlr7 Ligand in a Myc-Induced Hyperplastic Actinic Keratosis Model in the Absence of Systemic Side Effects. *Eur J Dermatol* (2013) 23(5):618–28. doi: 10.1684/ejd.2013.2155

52. Sugita K, Kabashima K, Atarashi K, Shimauchi T, Kobayashi M, Tokura Y. Innate Immunity Mediated by Epidermal Keratinocytes Promotes Acquired Immunity Involving Langerhans Cells and T Cells in the Skin. *Clin Exp Immunol* (2007) 147(1):176–83. doi: 10.1111/j.1365-2249.2006.03258.x

53. Muller-Anstett MA, Muller P, Albrecht T, Nega M, Wagener J, Gao Q, et al. Staphylococcal Peptidoglycan Co-Localizes With Nod2 and Tlr2 and Activates Innate Immune Response *Via* Both Receptors in Primary Murine Keratinocytes. *PLoS One* (2010) 5(10):e13153. doi: 10.1371/journal.pone.0013153

54. Rodriguez-Martinez S, Cancino-Diaz ME, Jimenez-Zamudio L, Garcia-Latorre E, Cancino-Diaz JC. Tlrs and Nods Mrna Expression Pattern in Healthy Mouse Eye. *Br J Ophthalmol* (2005) 89(7):904–10. doi: 10.1136/bjo.2004.056218

55. Satta N, Dunoyer-Geindre S, Reber G, Fish RJ, Boehlen F, Kruithof EK, et al. The Role of Tlr2 in the Inflammatory Activation of Mouse Fibroblasts by Human Antiphospholipid Antibodies. *Blood* (2007) 109(4):1507–14. doi: 10.1182/blood-2005-03-024463

56. Yu FY, Xie CQ, Jiang CL, Sun JT, Huang XW. Tnfalpha Increases Inflammatory Factor Expression in Synovial Fibroblasts Through the Tolllike Receptor3mediated Erk/Akt Signaling Pathway in a Mouse Model of Rheumatoid Arthritis. *Mol Med Rep* (2018) 17(6):8475–83. doi: 10.3892/mmr.2018.8897

57. Jung YO, Cho ML, Lee SY, Oh HJ, Park JS, Park MK, et al. Synergism of Toll-Like Receptor 2 (Tlr2), Tlr4, and Tlr6 Ligation on the Production of Tumor Necrosis Factor (Tnf)-Alpha in a Spontaneous Arthritis Animal Model of Interleukin (Il)-1 Receptor Antagonist-Deficient Mice. *Immunol Lett* (2009) 123(2):138–43. doi: 10.1016/j.imlet.2009.03.004

58. Green BB, Kandasamy S, Elsasser TH, Kerr DE. The Use of Dermal Fibroblasts as a Predictive Tool of the Toll-Like Receptor 4 Response Pathway and Its Development in Holstein Heifers. *J Dairy Sci* (2011) 94 (11):5502–14. doi: 10.3168/jds.2011-4441

59. Hergert B, Grambow E, Butschkau A, Vollmar B. Effects of Systemic Pretreatment With Cpg Oligodeoxynucleotides on Skin Wound Healing in Mice. *Wound Repair Regener* (2013) 21(5):723–9. doi: 10.1111/wrr.12084

60. Ding R, Xu G, Feng Y, Zou L, Chao W. Lipopeptide Pam3cys4 Synergizes N-Formyl-Met-Leu-Phe (Fmlp)-Induced Calcium Transients in Mouse Neutrophils. *Shock* (2018) 50(4):493–9. doi: 10.1097/SHK.0000000000001062

61. Deng T, Feng X, Liu P, Yan K, Chen Y, Han D. Toll-Like Receptor 3 Activation Differentially Regulates Phagocytosis of Bacteria and Apoptotic Neutrophils by Mouse Peritoneal Macrophages. *Immunol Cell Biol* (2013) 91 (1):52–9. doi: 10.1038/icb.2012.45

62. Wang Y, Du F, Hawez A, Morgelin M, Thorlacius H. Neutrophil Extracellular Trap-Microparticle Complexes Trigger Neutrophil Recruitment *Via* High-Mobility Group Protein 1 (Hmgb1)-Toll-Like Receptors(Tlr2)/Tlr4 Signalling. *Br J Pharmacol* (2019) 176(17):3350–63. doi: 10.1111/bph.14765

63. Shibata T, Takemura N, Motoi Y, Goto Y, Karuppuchamy T, Izawa K, et al. Prat4a-Dependent Expression of Cell Surface Tlr5 on Neutrophils, Classical Monocytes and Dendritic Cells. *Int Immunol* (2012) 24(10):613–23. doi: 10.1093/intimm/dxs068

64. Bellocchio S, Moretti S, Perruccio K, Fallarino F, Bozza S, Montagnoli C, et al. Tlrs Govern Neutrophil Activity in Aspergillosis. *J Immunol* (2004) 173 (12):7406–15. doi: 10.4049/jimmunol.173.12.7406

65. Regli IB, Passelli K, Martinez-Salazar B, Amore J, Hurrell BP, Muller AJ, et al. Tlr7 Sensing by Neutrophils Is Critical for the Control of Cutaneous Leishmaniasis. *Cell Rep* (2020) 31(10):107746. doi: 10.1016/j.celrep.2020.107746

66. Prince LR, Whyte MK, Sabroe I, Parker LC. The Role of Tlrs in Neutrophil Activation. *Curr Opin Pharmacol* (2011) 11(4):397–403. doi: 10.1016/j.coph.2011.06.007

67. Jeong YJ, Kang MJ, Lee SJ, Kim CH, Kim JC, Kim TH, et al. Nod2 and Rip2 Contribute to Innate Immune Responses in Mouse Neutrophils. *Immunology* (2014) 143(2):269–76. doi: 10.1111/imm.12307

68. Goodridge HS, Wolf AJ, Underhill DM. Beta-Glucan Recognition by the Innate Immune System. *Immunol Rev* (2009) 230(1):38–50. doi: 10.1111/j.1600-065X.2009.00793.x

69. Taylor PR, Brown GD, Reid DM, Willment JA, Martinez-Pomares L, Gordon S, et al. The Beta-Glucan Receptor, Dectin-1, Is Predominantly Expressed on the Surface of Cells of the Monocyte/Macrophage and Neutrophil Lineages. *J Immunol* (2002) 169(7):3876–82. doi: 10.4049/jimmunol.169.7.3876

70. van der Aar AM, Picavet DI, Muller FJ, de Boer L, van Capel TM, Zaat SA, et al. Langerhans Cells Favor Skin Flora Tolerance Through Limited Presentation of Bacterial Antigens and Induction of Regulatory T Cells. *J Invest Dermatol* (2013) 133(5):1240–9. doi: 10.1038/jid.2012.500

71. Becerril-Garcia MA, Yam-Puc JC, Maqueda-Alfaro R, Beristain-Covarrubias N, Heras-Chavarria M, Gallegos-Hernandez IA, et al. Langerhans Cells From Mice at Birth Express Endocytic- and Pattern Recognition-Receptors, Migrate to Draining Lymph Nodes Ferrying Antigen and Activate Neonatal T Cells *In Vivo*. *Front Immunol* (2020) 11:744. doi: 10.3389/fimmu.2020.00744

72. Shrimpton RE, Butler M, Morel AS, Eren E, Hue SS, Ritter MA. Cd205 (Dec-205): A Recognition Receptor for Apoptotic and Necrotic Self. *Mol Immunol* (2009) 46(6):1229–39. doi: 10.1016/j.molimm.2008.11.016

73. Donadei A, Gallorini S, Berti F, O'Hagan DT, Adamo R, Baudner BC. Rational Design of Adjuvant for Skin Delivery: Conjugation of Synthetic Beta-Glucan Dectin-1 Agonist to Protein Antigen. *Mol Pharm* (2015) 12 (5):1662–72. doi: 10.1021/acs.molpharmaceut.5b00072

74. Ley K, Pramod AB, Croft M, Ravichandran KS, Ting JP. How Mouse Macrophages Sense What Is Going on. *Front Immunol* (2016) 7:204. doi: 10.3389/fimmu.2016.00204

75. Corbett Y, Parapini S, D'Alessandro S, Scaccabarozzi D, Rocha BC, Egan TJ, et al. Involvement of Nod2 in the Innate Immune Response Elicited by Malarial Pigment Hemozoin. *Microbes Infect* (2015) 17(3):184–94. doi: 10.1016/j.micinf.2014.11.001

76. Karakus M, Karabey B, Orcun Kalkan S, Ozdemir G, Oguz G, Erisoz Kasap O, et al. Midgut Bacterial Diversity of Wild Populations of Phlebotomus (P.) Papatasi, the Vector of Zoonotic Cutaneous Leishmaniasis (Zcl) in Turkey. *Sci Rep* (2017) 7(1):14812. doi: 10.1038/s41598-017-13948-2

77. Maleki-Ravasan N, Oshaghi MA, Afshar D, Arandian MH, Hajikhani S, Akhavan AA, et al. Aerobic Bacterial Flora of Biotic and Abiotic Compartments of a Hyperendemic Zoonotic Cutaneous Leishmaniasis (Zcl) Focus. *Parasit Vectors* (2015) 8:63. doi: 10.1186/s13071-014-0517-3

78. Mukhopadhyay J, Braig HR, Rowton ED, Ghosh K. Naturally Occurring Culturable Aerobic Gut Flora of Adult Phlebotomus Papatasi, Vector of Leishmania Major in the Old World. *PLoS One* (2012) 7(5):e35748. doi: 10.1371/journal.pone.0035748

79. Mogensen TH. Pathogen Recognition and Inflammatory Signaling in Innate Immune Defenses. *Clin Microbiol Rev* (2009) 22(2):240–73. doi: 10.1128/CMR.00046-08

80. Brattig NW, Buttner DW, Hoerauf A. Neutrophil Accumulation Around Onchocerca Worms and Chemotaxis of Neutrophils Are Dependent on Wolbachia Endobacteria. *Microbes Infect* (2001) 3(6):439–46. doi: 10.1016/s1286-4579(01)01399-5

81. Brattig NW, Bazzocchi C, Kirschning CJ, Reiling N, Buttner DW, Ceciliani F, et al. The Major Surface Protein of Wolbachia Endosymbionts in Filarial

Nematodes Elicits Immune Responses Through Tlr2 and Tlr4. *J Immunol* (2004) 173(1):437–45. doi: 10.4049/jimmunol.173.1.437

82. Wolf AJ, Underhill DM. Peptidoglycan Recognition by the Innate Immune System. *Nat Rev Immunol* (2018) 18(4):243–54. doi: 10.1038/nri.2017.136

83. van Dalen R, de la Cruz Diaz JS, Rumpret M, Fuchsberger FF, van Teijlingen NH, Hanske J, et al. Langerhans Cells Sense Staphylococcus Aureus Wall Teichoic Acid Through Langerin to Induce Inflammatory Responses. *mBio* (2019) 10(3):1–14. doi: 10.1128/mBio.00330-19

84. Jawdat DM, Rowden G, Marshall JS. Mast Cells Have a Pivotal Role in Tnf-Independent Lymph Node Hypertrophy and the Mobilization of Langerhans Cells in Response to Bacterial Peptidoglycan. *J Immunol* (2006) 177 (3):1755–62. doi: 10.4049/jimmunol.177.3.1755

85. Ogunkolade BW, Monjour L, Vouldoukis I, Rhodes-Feuillette A, Frommel D. Inoculation of Balb/C Mice Against Leishmania Major Infection With Leishmania-Derived Antigens Isolated by Gel Filtration. *J Chromatogr* (1988) 440:459–65. doi: 10.1016/s0021-9673(00)94550-3

86. Ryu S, Song PI, Seo CH, Cheong H, Park Y. Colonization and Infection of the Skin by S. Aureus: Immune System Evasion and the Response to Cationic Antimicrobial Peptides. *Int J Mol Sci* (2014) 15(5):8753–72. doi: 10.3390/ijms15058753

87. Grady EN, MacDonald J, Liu L, Richman A, Yuan ZC. Current Knowledge and Perspectives of Paenibacillus: A Review. *Microb Cell Fact* (2016) 15 (1):203. doi: 10.1186/s12934-016-0603-7

88. Watanabe T, Asano N, Murray PJ, Ozato K, Tailor P, Fuss IJ, et al. Muramyl Dipeptide Activation of Nucleotide-Binding Oligomerization Domain 2 Protects Mice From Experimental Colitis. *J Clin Invest* (2008) 118(2):545–59. doi: 10.1172/JCI33145

89. Dey R, Joshi AB, Oliveira F, Pereira L, Guimaraes-Costa AB, Serafim TD, et al. Gut Microbes Egested During Bites of Infected Sand Flies Augment Severity of Leishmaniasis *Via* Inflammasome-Derived Il-1beta. *Cell Host Microbe* (2018) 23(1):134–43 e6. doi: 10.1016/j.chom.2017.12.002

90. Borbon TY, Scorza BM, Clay GM, Lima Nobre de Queiroz F, Sariol AJ, Bowen JL, et al. Coinfection With Leishmania Major and Staphylococcus Aureus Enhances the Pathologic Responses to Both Microbes Through a Pathway Involving Il-17a. *PLoS Negl Trop Dis* (2019) 13(5):e0007247. doi: 10.1371/journal.pntd.0007247

91. Laskay T, van Zandbergen G, Solbach W. Neutrophil Granulocytes–Trojan Horses for Leishmania Major and Other Intracellular Microbes? *Trends Microbiol* (2003) 11(5):210–4. doi: 10.1016/s0966-842x(03)00075-1

92. Ritter U, Frischknecht F, van Zandbergen G. Are Neutrophils Important Host Cells for Leishmania Parasites? *Trends Parasitol* (2009) 25(11):505–10. doi: 10.1016/j.pt.2009.08.003

93. Goncalves-de-Albuquerque SDC, Pessoa ESR, Trajano-Silva LAM, de Goes TC, de Morais RCS, da COCN, et al. The Equivocal Role of Th17 Cells and Neutrophils on Immunopathogenesis of Leishmaniasis. *Front Immunol* (2017) 8:1437. doi: 10.3389/fimmu.2017.01437

94. Wu W, Weigand L, Belkaid Y, Mendez S. Immunomodulatory Effects Associated With a Live Vaccine Against Leishmania Major Containing

Cpg Oligodeoxynucleotides. *Eur J Immunol* (2006) 36(12):3238–47. doi: 10.1002/eji.200636472

95. Pandey SP, Chandel HS, Srivastava S, Selvaraj S, Jha MK, Shukla D, et al. Pegylated Bisacycloxypropylcysteine, a Diacylated Lipopeptide Ligand of Tlr6, Plays a Host-Protective Role Against Experimental Leishmania Major Infection. *J Immunol* (2014) 193(7):3632–43. doi: 10.4049/jimmunol.1400672

96. Oliveira MR, Tafuri WL, Afonso LC, Oliveira MA, Nicoli JR, Vieira EC, et al. Germ-Free Mice Produce High Levels of Interferon-Gamma in Response to Infection With Leishmania Major But Fail to Heal Lesions. *Parasitology* (2005) 131(Pt 4):477–88. doi: 10.1017/S0031182005008073

97. Lopes ME, Dos Santos LM, Sacks D, Vieira LQ, Carneiro MB. Resistance Against Leishmania Major Infection Depends on Microbiota-Guided Macrophage Activation. *Front Immunol* (2021) 12:730437. doi: 10.3389/fimmu.2021.730437

98. Igyarto BZ, Haley K, Ortner D, Bobr A, Gerami-Nejad M, Edelson BT, et al. Skin-Resident Murine Dendritic Cell Subsets Promote Distinct and Opposing Antigen-Specific T Helper Cell Responses. *Immunity* (2011) 35 (2):260–72. doi: 10.1016/j.immuni.2011.06.005

99. Sumpter TL, Balmert SC, Kaplan DH. Cutaneous Immune Responses Mediated by Dendritic Cells and Mast Cells. *JCI Insight* (2019) 4(1):1–13. doi: 10.1172/jci.insight.123947

100. Peters NC, Bertholet S, Lawyer PG, Charmoy M, Romano A, Ribeiro-Gomes FL, et al. Evaluation of Recombinant Leishmania Polyprotein Plus Glucopyranosyl Lipid a Stable Emulsion Vaccines Against Sand Fly-Transmitted Leishmania Major in C57bl/6 Mice. *J Immunol* (2012) 189 (10):4832–41. doi: 10.4049/jimmunol.1201676

101. Kamhawi S, Belkaid Y, Modi G, Rowton E, Sacks D. Protection Against Cutaneous Leishmaniasis Resulting From Bites of Uninfected Sand Flies. *Science* (2000) 290(5495):1351–4. doi: 10.1126/science.290.5495.1351

Conflict of Interest: The authors declare that the research was conducted in the absence of any commercial or financial relationships that could be construed as a potential conflict of interest.

Publisher's Note: All claims expressed in this article are solely those of the authors and do not necessarily represent those of their affiliated organizations, or those of the publisher, the editors and the reviewers. Any product that may be evaluated in this article, or claim that may be made by its manufacturer, is not guaranteed or endorsed by the publisher.

Check for updates

Diagnostic performance of a urine-based ELISA assay for the screening of human schistosomiasis japonica: A comparative study

Yi Mu[1], Kosala G. Weerakoon[1‡], Remigio M. Olveda[2†], Allen G. Ross[3], Donald P. McManus[1†] and Pengfei Cai[1*]

[1]Molecular Parasitology Laboratory, Infection and Inflammation Program, QIMR Berghofer Medical Research Institute, Brisbane, QLD, Australia, [2]Department of Health, Research Institute for Tropical Medicine, Manila, Philippines, [3]Research Institute for Rural Health, Charles Sturt University, Orange, NSW, Australia

The current study developed and evaluated the performance of a urine-based enzyme-linked immunosorbent assay (ELISA) for the screening of *Schistosoma japonicum* infection in a human cohort (*n*=412) recruited from endemic areas, Northern Samar, the Philippines. The diagnostic performance of the urine ELISA assay was further compared with the Kato-Katz (KK) technique, serum-based ELISA assays, point-of-care circulating cathodic antigen (POC-CCA) urine cassette test, and droplet digital (dd) PCR assays performed on feces, serum, urine, and saliva samples, which were designated as F_ddPCR, SR_ddPCR, U_ddPCR, and SL_ddPCR, respectively. When urine samples concentrated 16× were assessed, the SjSAP4+Sj23-LHD-ELISA (U) showed sensitivity/specificity values of 47.2/93.8% for the detection of *S. japonicum* infection in KK-positive individuals (n=108). The prevalence of *S. japonicum* infection in the total cohort determined by the urine ELISA assay was 48.8%, which was lower than that obtained with the F_ddPCR (74.5%, *p* <0.001), SR_ddPCR (67.2%, *p* <0.001), and SjSAP4+Sj23-LHD-ELISA (S) (66.0%, *p* <0.001), but higher than that determined by the Sj23-LHD-ELISA (S) (24.5%, *p* <0.001), POC-CCA assay (12.4%, *p* <0.001), and SL_ddPCR (25.5%, *p* <0.001). Using the other diagnostic tests as a reference, the urine ELISA assay showed a sensitivity between 47.2 and 56.9%, a specificity between 50.7 and 55.2%, and an accuracy between 49.3 and 53.4%. The concentrated urine SjSAP4+Sj23-LHD-ELISA developed in the current study was more sensitive than both the KK test and POC-CCA assay, and showed a comparable level of diagnostic accuracy to that of the U_ddPCR. However, its diagnostic performance was less robust than that of the F_ddPCR, SR_ddPCR, and SjSAP4+Sj23-LHD-ELISA (S) assays. Although they are convenient and involve a highly acceptable non-invasive procedure for clinical sample collection, the insufficient sensitivity of the three urine-based assays (the urine ELISA assay, the U_ddPCR test, and the POC-CCA assay) will limit their value for the routine screening of schistosomiasis japonica in the

post mass drug administration (MDA) era, where low-intensity infections are predominant in many endemic areas.

Introduction

One of the major neglected tropical diseases, schistosomiasis, caused by three main species of schistosomes (trematode blood flukes) infecting humans, *Schistosoma mansoni*, *S. haematobium*, and *S. japonicum*, affects more than 230 million people worldwide (McManus et al., 2018). The control of the disease relies predominantly on mass drug administration (MDA) programs with praziquantel; however, MDA on its own is insufficient to provide long-term sustainable control of the disease (Ross et al., 2015). Due to the COVID-19 pandemic, it has been reported that a total of 28.6 million fewer people were treated for schistosomiasis in 2020 than in 2019 with preventive treatment targeting school-aged children decreased from 66.8% in 2019 to 44.9% in 2020 (World Health Organization, 2021). Schistosomiasis outbreaks during the COVID-19 pandemic were also reported due to MDA program activities being postponed in 2020 across the endemic countries (Olamiju et al., 2022). The impact of the disruptions to schistosomiasis control programs due to COVID-19 thus needs to be closely monitored and evaluated. In this regard, the need for highly accurate, as well as cost-effective and convenient diagnostics has become a major priority.

In Asia, the major endemic foci of intestinal human schistosomiasis, caused by *S. japonicum* infection, are found in China, the Philippines, and small pockets of Indonesia (Ross et al., 2013). The transmission of the disease has decreased substantially in China due to extensive integrated control efforts (Gordon et al., 2021). In the Philippines, the infection remains endemic in 28 provinces across 12 geographical zones, with endemicity mostly located in the Central and Southern parts of the country (Olveda and Gray, 2019). Two and half million Filipinos are directly exposed to schistosomiasis, with approximately 12 million residing in endemic zones (Department of Health, 2018). As of 2019, it was reported that the national prevalence of schistosomiasis in the country was 4.0% (Belizario et al., 2022). However, this figure was derived from focal surveys and only one or two microscopy-based Kato-Katz (KK) slides were read for each individual, which may significantly underestimate the true burden of the disease (Olveda et al., 2016). Indeed, an integrated surveillance system has been recommended to help identify high-priority areas for targeted interventions, entailing the development of affordable and accurate diagnostic tools for rapid mapping and monitoring of schistosomiasis in the endemic zones in the Philippines (Belizario et al., 2022).

Currently, a variety of diagnostic methods are available for the detection of schistosome infection (Cavalcanti et al., 2013; Weerakoon et al., 2015). Parasitological-based diagnostics (e.g., the KK procedure for *S. japonicum* and *S. mansoni* detection, and the miracidium hatching technique) exhibit a considerable level of specificity but compromised sensitivities, particularly when used in endemic areas with reduced schistosome infection intensity (Cavalcanti et al., 2013). Improved coprological tests, such as the saline gradient method (Coelho et al., 2009), formalin-ethyl acetate sedimentation-digestion (FEA-SD) (Xu et al., 2012), and the Helmintex method (a procedure that isolates eggs from fecal samples with the use of paramagnetic particles in a magnetic field) (Lindholz et al., 2018), showed increased diagnostic sensitivity compared with the traditional techniques; on the down side, these procedures are usually labor-intensive, and have a lengthy processing time. Molecular methods based on polymerase chain reaction (PCR) technology, including real-time quantitative (q)PCR (Cnops et al., 2013; Gordon et al., 2015; Magalhaes et al., 2020; Mu et al., 2020; Halili et al., 2021), loop-mediated isothermal amplification (LAMP) (Gandasegui et al., 2015, 2018; Garcia-Bernalt Diego et al., 2021), and droplet digital (dd) PCR-based tests (Weerakoon et al., 2016, 2017a,b), are alternatives for schistosomiasis surveillance due to their exceptional diagnostic performance; however, these tests are expensive (e.g., the high price of DNA extraction, qPCR assay reagents, and equipment), and require experienced human resources, making their implementation in resource-limited areas challenging.

We recently developed serum-based IgG-ELISA assays targeting a pair of recombinant antigens or antigen combinations for diagnosis of *S. japonicum* in cohorts from endemic areas in the Philippines (Cai et al., 2017, 2019). The serum-based SjSAP4 + Sj23-LHD-ELISA assay [SjSAP4 + Sj23-LHD-ELISA (S)] exhibited a high level of diagnostic performance with 87.04% sensitivity and 96.67% specificity in testing 108 KK-positive subjects, the majority harboring low-intensity *S. japonicum* infections (Cai et al., 2017). The schistosomiasis prevalence determined by the SjSAP4 + Sj23-LHD-ELISA (S) was similar to that obtained by ddPCR assays performed on feces and serum samples, and was about 2.7-fold higher than that obtained with the KK procedure (Cai et al., 2019). However, serum-based diagnostic assays involve the invasive, onerous, and potentially hazardous of blood sampling (Archer et al., 2020). In contrast, urine-based diagnostic tests involve convenient and completely non-invasive urine sampling, with

the limited chance of participants being exposed to biological risks. Previously, urine-based ELISA assays have been suggested as a possible alternative tool to diagnose a number of parasitic helminthiases such as echinococcosis, filariasis, opisthorchiasis, and schistosomiasis (Itoh et al., 2001, 2003; Sunita et al., 2007; Sawangsoda et al., 2012; Samad et al., 2013; Chirag et al., 2015; Eamudomkarn et al., 2018; Nagaoka et al., 2021; Chungkanchana et al., 2022). In this study, we aimed to validate a urine-based SjSAP4 + Sj23-LHD-ELISA assay for the diagnosis of *S. japonicum* infection in a human cohort recruited from areas in the Philippines moderately endemic for schistosomiasis japonica. The performance of the urine ELISA assay was further comprehensively compared with other diagnostic tests, including the KK procedure, serum-based ELISA assays (Cai et al., 2017), point-of-care circulating cathodic antigen (POC-CCA) urine cassette test (Cai et al., 2021), and ddPCR assays performed on feces, serum, urine, and saliva samples, which were designated as F_ddPCR, SR_ddPCR, U_ddPCR, and SL_ddPCR, respectively (Weerakoon et al., 2017b).

Materials and methods

Ethics statement

Human research ethical approval for the study was obtained from the Institutional Review Board (IRB) of the Research Institute for Tropical Medicine (RITM), Manila, the Philippines (IRB Number 2015-12), and the Human Research Ethics Committee (HREC), QIMR Berghofer Medical Research Institute (QIMRB), Brisbane, Australia (Ethics Approval: P524). Written consent was obtained from each study participant (for children under the age of 15 years, written consent was obtained from their legal guardians).

Study cohort, sample collection, processing, and storage

The study recruited human subjects from 18 barangays moderately endemic for schistosomiasis japonica in the municipalities of Laoang and Palapag, Northern Samar, the Philippines, in 2015 (Cai et al., 2017, 2019; Weerakoon et al., 2017b). A variety of clinical samples (feces, serum, urine, and saliva) were collected from the participating subjects. For each participant, two fecal samples (10–15 g each) were sought on different days within a week for the Kato-Katz test. After fixing in 80% ethanol, the remainder of the first fecal sample (~10 g) was stored at 4°C. A blood sample (10 ml) was collected from each individual using a 10 ml serum silica vacutainer. The blood sample was allowed to clot at ambient temperature for 30 min. After centrifugation at 1,500× g for 10 min, the serum sample was then aliquoted and stored at 2–8°C. Around 40 ml of spot urine sample was collected in a 50 ml Falcon tube from each participant. Saliva

(~2 ml) was collected into a 5 ml centrifuge tube using the passive drool method. All clinical samples were stored at 4°C and transported on wet ice to the RITM, where the samples were stored at −20°C. All samples were subsequently shipped to QIMRB, Brisbane, Australia, on dry ice for further analysis. Urine samples from healthy individuals from a non-endemic area in Australia were used as negative controls ($n = 16$).

Parasitological detection

Kato-Katz (KK) analysis on the stool samples collected was performed at RITM as previously described (Gordon et al., 2015). Six thick smear slides per participant (three from each stool sample) were prepared and examined under a light microscope by experienced technicians. Infection intensity was recorded as the number of eggs per gram of feces (EPG). To ensure the accuracy of the KK test, 10% of the KK slides were randomly re-examined by an experienced microscopist.

Urine ELISA

Urine samples were concentrated as previously described (Cai et al., 2021). Briefly, after thawing, urine samples were thoroughly mixed and centrifuged at 3,700× g for 10 min to remove urinary sediment. The supernatants were concentrated 20 times using 4 ml single-use 10 kDa Amicon Ultra filter units (Merck Millipore, Bayswater, VIC, Australia). The ELISA procedure was performed as described previously (Cai et al., 2017). MaxiSorp high protein-binding capacity 96-well ELISA plates (Nunc, Roskilde, Denmark) were coated with SjSAP4 and Sj23-LHD (0.5 μg/ml each in coating buffer; 100 μl/well) overnight at 4°C. Wells were blocked with PBST (Phosphate-buffered saline, pH 7.5 with 0.05% Tween-20) containing 1% (w/v) BSA for 1 h at 37°C. Urine samples 100 μl 10× concentrated urine samples (50 μl of concentrated urine samples plus 50 μl PBST containing 2% BSA) or 100 μl 16× concentrated urine samples (80 μl of concentrated urine samples plus 20 μl PBST containing 5% BSA) were added to the wells and the mixtures incubated for 1 h at 37°C. A mouse monoclonal anti-human IgG (Fc specific)-biotin antibody (Sigma-Aldrich Co, MO, USA) was then added as secondary antibody (1:20,000, 100 μl/well) for 1 h at 37°C. The plates were further incubated with Streptavidin-HRP (BD Pharmingen, CA, USA; 1:10,000, 100 μl/well) at 37°C for 0.5 h. Plates were washed with PBST for 5 times after each step. Colorimetric reactions were developed by adding 100 μl TMB substrate to each well and terminated after 5 min by adding 50 μl stop reagent (2 N H_2SO_4 per well). The ELISA plates were read at OD 450 nm with a POLARstar OPTIMA multidetection microplate reader (BMG LABTECH, VIC, Australia). Duplicate ELISA readings were undertaken. The cut-off value for a positive IgG response was set at 2.1 times the mean OD 450 nm value of urine samples from healthy controls.

Comparative analysis using the KK, POC-CCA, ddPCR, and serum ELISA assays as reference

For ddPCR assays, DNA were extracted from the collected clinical samples (feces, serum, urine, and saliva) using the Maxwell 16 Instrument (Promega, Wisconsin; for fecal samples) or a ChemagicTM360 instrument (PerkinElmer Inc., Massachusetts; for serum, urine and saliva samples) (Weerakoon et al., 2017b). The purified DNA samples were analyzed on the QX200 ddPCR System (Bio-Rad) by amplifying an 82-bp fragment of the *S. japonicum* mitochondrial NADH I (nad1) gene (Weerakoon et al., 2017a,b). The ddPCRs performed on feces, serum, urine, and saliva were designated as F_ddPCR, SR_ddPCR, U_ddPCR, and SL_ddPCR, respectively. The ddPCR results are presented as the target gene copy number index (CNI) (Weerakoon et al., 2017b). For the POC-CCA assay, the detection of CCA in concentrated urine samples was performed using a commercially available POC-CCA urine cassette kit (Rapid Medical Diagnostics, Pretoria, South Africa) (Cai et al., 2021). The results of the POC-CCA assays were read after 20 min and transformed to a quantified value by introducing an R value, which was defined as the intensity of the test band divided by that of the control band within the same strip. In addition, three IgG-ELISA assays [Sj23-LHD-ELISA (S), SjSAP4-ELISA (S), and SjSAP4 + Sj23-LHD-ELISA (S)] were performed on the sera collected from the same cohort (Cai et al., 2017). Comparative analysis was undertaken on the results obtained for the urine ELISA assay and the other diagnostic methods (i.e., the KK, ddPCR, POC-CCA, and serum ELISA assays) used.

Statistical analysis

All results were entered in a Microsoft Excel 2016 database. Statistical analysis was performed with GraphPad Prism Version 9 for windows (GraphPad Software, Inc., San Diego, CA, USA). All the data are presented as the mean ± standard error (SE). For the ELISA, the urine IgG responses between the different subsets of the cohort and healthy controls were analyzed by the Mann–Whitney U-test. Diagnostic performance was evaluated by receiver operating characteristic (ROC) curve analysis. The area under the ROC curve (AUC) was calculated to assess the diagnostic performance of the SjSAP4 + Sj23-LHD-ELISA (U) assay in the different subsets of the cohort. Differences in the positive rates and infection prevalences determined by the urine ELISA assay and the other diagnostic approaches (the ddPCR, POC-CCA, and serum ELISA assays) were tested using McNemar's test across the different infection intensity groups. Using the different diagnostics methods (the KK, ddPCR, POC-CCA, and serum ELISA assays) as reference, sensitivity, specificity, positive

predictive value (PPV), negative predictive value (NPV), and accuracy were analyzed for the urine ELISA assay. Agreement between the urine ELISA assay and the other tests was determined using the Kappa statistic.[1] The strength of agreement was measured by the scale according to the κ value, with the scores divided into: <0, no agreement; 0.00–0.20 slight agreement; 0.21–0.40 fair agreement; 0.41–0.60 moderate agreement; 0.61–0.80 substantial agreement; and 0.81–1.00 perfect agreement (Landis and Koch, 1977).

Results

Study population and schistosome fecal egg burdens

A total of 412 participants were recruited from 18 barangays in a schistosomiasis-endemic rural area, Northern Samar, the Philippines. Among them, 108 (26.2%) participants were *S. japonicum* egg-positive determined by six smear slides from two stool samples (three slides each) with a mean EPG of 17.6. Of these KK-positives, the majority ($n = 104$; 96.1%) had a light-intensity infection (EPG < 100) (Cai et al., 2021). Sixteen subjects were recruited from a non-endemic area in Australia as controls.

Optimization of loading volume of concentrated urine samples for ELISA assay

Urine samples were concentrated 20 times using 10 kDa Amicon Ultra filter units. We then optimized the loading volume of concentrated (20×) urine samples in the SjSAP4 + Sj23-LHD-ELISA (U) assay. By employing 48 F_ddPCR-positive subjects and 12 healthy controls, 50 or 80 µl concentrated (20×) urine samples (i.e., the final urine concentration is 10× and 16×, respectively) were tested in the SjSAP4 + Sj23-LHD-ELISA (U) assay. No significant difference in the IgG levels was observed between individuals in the control group and the F_ddPCR-positives at a urine concentration of 10× (Figure 1A), whereas the OD values of the SjSAP4 + Sj23-LHD-ELISA (U) assay were significantly higher in the F_ddPCR-positives than those of the healthy control group ($p = 0.0018$) at a urine concentration of 16× (Figure 1B). The ROC analysis indicated that the SjSAP4 + Sj23-LHD-ELISA (U) was unable to discriminate the F_ddPCR-positives from the healthy controls ($p = 0.0824$) when the urine concentration was at 10× (Figure 1C). The ROC analysis for discriminating F_ddPCR-positives from the healthy controls showed that the AUC level for the urine ELISA assay was 0.7847 ($p = 0.0024$) when 16× concentrated urine samples were tested (Figure 1D).

---

1 https://www.graphpad.com/quickcalcs/kappa1/
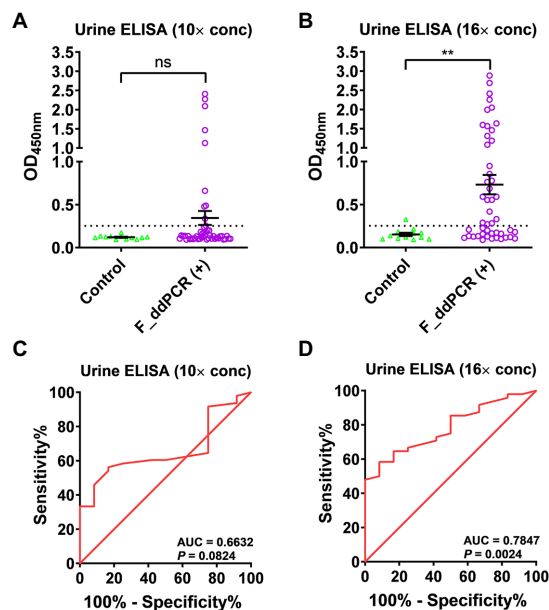
FIGURE 1
Determination of the optimal loading volume of concentrated (20×) urine samples for the SjSAP4+Sj23-LHD-ELISA assay. **(A,B)** Scatter plots showing the IgG responses in 50 **(A)** and 80 µl **(B)** urine sample, respectively, to the *S. japonicum* antigen combination SjSAP4+Sj23-LHD. Healthy controls (*n*=12), F_ddPCR-positives (*n*=48). *p* values were determined using the Mann−Whitney *U*-test. ns, no significant difference; **$p<0.01$. **(C,D)** Receiver operating characteristic curve (ROC) analysis was performed to evaluate the capability of the urine ELISA in discriminating the healthy control group (*n*=12) and F_ddPCR-positives (*n*=48). Fifty µl **(C)** and 80 µl **(D)** concentrated (20×) urine samples were loaded on the plate during the ELISA assay, respectively.

Diagnostic performance of the SjSAP4+Sj23-LHD-ELISA (U) test using different subsets of diagnosed positives with other tests as a reference

We then tested the SjSAP4 + Sj23-LHD-ELISA (U) assay on all 16× concentrated urine samples of the endemic human cohort (*n* = 412) and healthy controls (*n* = 16). IgG levels of the urine ELISA assay were significantly higher in the KK-, F_ddPCR-, U_ddPCR-, and serum SjSAP4 + Sj23-LHD-ELISA-positive groups (*n* = 108, 307, 196, and 272, respectively) than those of the healthy control group (Figures 2A–D). The urine ELISA assay showed a diagnostic sensitivity of 47.2, 50.2, 49.0, and 50.0%, respectively, for the diagnosis of *S. japonicum* infection in the above-mentioned subgroups, with a specificity of 93.8%. The ROC analysis for discriminating the KK, F_ddPCR, U_ddPCR, and serum SjSAP4 + Sj23-LHD-ELISA-positive subjects from the healthy controls showed that the AUC level for the urine ELISA assay was 0.7882, 0.7861, 0.7827 and 0.7800, respectively (*p* = 0.0002, 0.0001, 0.0002 and 0.0002, respectively; Figures 2E–H).

Positivity rate and prevalence analysis

In the KK-moderate infection group (EPG: 100–399), the SjSAP4 + Sj23-LHD-ELISA (U) assay showed a 75% positivity rate, while the other diagnostic tests had a 100% positivity rate. In the subgroup with a low egg burden (EPG: 10–99, *n* = 26), the positivity rate was significantly higher when determined by the F_ddPCR (100%, *p* = 0.0015), SR_ddPCR (100%, *p* = 0.0015), U_ddPCR (88.5%, *p* = 0.0265), the SjSAP4-ELISA (S) (92.3%, *p* = 0.0094), and the SjSAP4 + Sj23-LHD-ELISA (S) (92.3%, *p* = 0.0094) compared with the SjSAP4 + Sj23-LHD-ELISA (U) assay (53.8%). There was no difference when the positivity rate determined by the SL_ddPCR, POC_CCA, and the SjSAP4-ELISA (S) were compared with the urine ELISA assay. In all subjects with an extremely low egg burden (EPG: 1–9, n = 78), the positivity rate determined by the urine ELISA assay (43.6%) was significantly lower than that obtained with the F_ddPCR (97.4%, *p* < 0.0001), the SR_ddPCR (92.3%, *p* < 0.0001), the SjSAP4-ELISA (S) (80.8%, *p* < 0.0001), and the SjSAP4 + Sj23-LHD-ELISA (S) (84.6%, *p* < 0.0001), but higher than those determined by the SL_ddPCR (24.4%, *p* = 0.0180) and the POC-CCA test (16.7%, *p* = 0.0007). In all KK-negatives (EPG: 0, n = 304), the positivity rate determined by the SjSAP4 + Sj23-LHD-ELISA (U) test (49.3%) was significantly lower than that obtained with the F_ddPCR (66.1%, *p* < 0.0001), and the SjSAP4 + Sj23-LHD-ELISA (S) (58.6%, *p* = 0.0265), but higher than that determined by the SL_ddPCR (20.4%, *p* < 0.0001), the POC-CCA test (6.3%, *p* < 0.0001), and the Sj23-LHD-ELISA (S) (18.1%, *p* < 0.0001; Table 1). Among the total cohort participants (n = 412), the prevalence determined by the urine ELISA assay (48.8) was significantly lower than that obtained with the F_ddPCR, SR_ddPCR, SjSAP4-ELISA (S), and the SjSAP4 + Sj23-LHD-ELISA (S) assays (*p* < 0.0001 in all comparisons), but higher than that resulting from the SL_ddPCR, POC-CCA, and Sj23-LHD-ELISA (S) assays (*p* < 0.0001 in all comparisons); no difference was evident in prevalence between the urine ELISA assay and that obtained with the U_ddPCR assay (*p* > 0.05; Table 1).

A comparison of the performance of the SjSAP4+Sj23-LHD-ELISA (U) assay with the other diagnostic tests in detecting *Schistosoma japonicum* infection

We determined the sensitivity, specificity, PPV, NPV, and accuracy of the SjSAP4 + Sj23-LHD-ELISA (U) using the KK, F_ddPCR, SR_ddPCR, U_ddPCR, SL_ddPCR, POC-CCA assay, Sj23-LHD-ELISA (S), SjSAP4-ELISA (S), and SjSAP4 + Sj23-LHD-ELISA (S), respectively, as the reference tests (Table 2). The SjSAP4 + Sj23-LHD-ELISA (U) had the highest sensitivity (56.9%), using the POC-CCA assay as the reference, followed by using the Sj23-LHD-ELISA (S) as the reference, showing a sensitivity of 54.5%. The urine ELISA assay showed an accuracy of about 50% when using other diagnostic methods as references, with the highest accuracy of 53.4%

FIGURE 2

Urinary IgG levels against the antigen combination SjSAP4+Sj23-LHD in different subgroups. **(A–D)** Scatter plots showing the urine IgG responses to SjSAP4 + Sj23-LHD in the KK-positives ($n=108$; **A**), F_ddPCR-positives ($n=307$; **B**), U_ddPCR-positives ($n=196$; **C**) and serum SjSAP4+Sj23-LHD-ELISA-positives ($n=272$; **D**), respectively, for the diagnosis of schistosomiasis japonica. Urine samples from 16 healthy individuals were used as controls. p values were determined using the Mann−Whitney U-test. ***$p<0.001$; ****$p<0.0001$. **(E−H)** ROC analysis was performed to evaluate the capability of the urine ELISA in discriminating the healthy control group and different subsets of the cohorts [KK-positives **(E)**, F_ddPCR-positives **(F)**, U_ddPCR-positives **(G)** and serum SjSAP4+Sj23-LHD-ELISA (S)-positives **(H)**, respectively].

TABLE 1 Comparison of positivity rates in different subgroups and prevalence in the whole cohort determined by the urine ELISA assay with those obtained with other diagnostic tests.

Diagnostic test	KK (+) moderate (EPG: 100–399)	KK (+) light[§] (EPG: 10–99)		(EPG: 1–9)		KK (−) (EPG: 0)		Whole cohort (EPG: 0–399)	
	% positive	% positive	p^*	% positive	p^*	% positive	p^*	% prevalence	p^*
SjSAP4 + Sj23-LHD-ELISA (U)[†]	75 (3/4)	53.8 (14/26)		43.6 (34/78)		49.3 (150/304)		48.8 (201/412)	
F_ddPCR	100 (4/4)	100 (26/26)	0.0015	97.4 (76/78)	<0.0001	66.1 (201/304)	<0.0001	74.5 (307/412)	<0.0001
SR_ddPCR	100 (4/4)	100 (26/26)	0.0015	92.3 (72/78)	<0.0001	57.6 (175/304)	>0.05	67.2 (277/412)	<0.0001
U_ddPCR	100 (4/4)	88.5 (23/26)	0.0265	47.4 (37/78)	>0.05	43.4 (132/304)	>0.05	47.6 (196/412)	>0.05
SL_ddPCR	100 (4/4)	76.9 (20/26)	>0.05	24.4 (19/78)	0.0180	20.4 (62/304)	<0.0001	25.5 (105/412)	<0.0001
POC-CCA[#]	100 (4/4)	57.7 (15/26)	>0.05	16.7 (13/78)	0.0007	6.3 (19/304)	<0.0001	12.4 (51/412)	<0.0001
Sj23-LHD-ELISA (S)[††]	100 (4/4)	53.8 (14/26)	>0.05	35.9 (28/78)	>0.05	18.1 (55/304)	<0.0001	24.5 (101/412)	<0.0001
SjSAP4-ELISA (S)[††]	100 (4/4)	92.3 (24/26)	0.0094	80.8 (63/78)	<0.0001	56.3 (171/304)	>0.05	65.5 (262/412)	<0.0001
SjSAP4 + Sj23-LHD-ELISA (S)[††]	100 (4/4)	92.3 (24/26)	0.0094	84.6 (66/78)	<0.0001	58.6 (178/304)	0.0265	66.0 (272/412)	<0.0001

[§]Individuals with a light infection were categorised into two subgroups with EPGs of 10–99 and 1–9.

*p values were determined by McNemar's test.

[#]R cut-off value: 0.1344 (Cai et al., 2021).

[†]OD 450 cut-off value for the urine ELISA assay: SjSAP4 + Sj23-LHD-ELISA (U), 0.2570.

[††]OD 450 cut-off values for the serum ELISA assays: Sj23-LHD-ELISA (S), 0.2185; SjSAP4-ELISA (S), 0.1832; SjSAP4 + Sj23-LHD-ELISA (S), 0.2003 (Cai et al., 2017).

TABLE 2 Diagnostic performance of the urine ELISA assay using different tests as reference.

SjSAP4+Sj23-LHD-ELISA (U)[†]	Reference test		% sensitivity (95% CI)	% specificity (95% CI)	% PPV (95% CI)	% NPV (95% CI)	% accuracy (95% CI)	Kappa index (95% CI)
	+	−						
KK								
+	51	150	47.2 (38.1–56.6)	50.7 (45.1–56.2)	25.4 (19.9–31.8)	73.0 (66.6–78.5)	49.8 (45.0–54.8)	−0.017 (−0.102–0.069)
−	57	154						
F_ddPCR								
+	154	47	50.2 (44.6–55.7)	55.2 (45.7–64.4)	76.6 (70.3–81.9)	27.5 (21.9–33.9)	51.5 (46.6–56.3)	0.041 (−0.042–0.124)
−	153	58						
SR_ddPCR								
+	135	66	48.7 (42.9–54.6)	51.1 (42.8–59.4)	67.2 (60.4–73.3)	32.7 (26.7–39.3)	49.5 (44.7–54.3)	−0.001 (−0.091–0.089)
−	142	69						
U_ddPCR								
+	96	105	49.0 (42.1–56.0)	51.4 (44.8–58.0)	47.8 (41.0–54.6)	52.6 (45.9–59.2)	50.2 (45.4–55.1)	0.004 (−0.093–0.100)
−	100	111						
SL_ddPCR								
+	52	149	49.5 (40.2–58.9)	51.5 (45.9–57.0)	25.9 (20.3–32.3)	74.9 (68.6–80.3)	51.0 (46.2–55.8)	0.008 (−0.078–0.093)
−	53	158						
POC-CCA[#]								
−	29	172	56.9 (43.3–69.5)	52.4 (47.2–57.5)	14.4 (10.2–20.0)	89.6 (84.7–93.0)	52.9 (48.1–57.7)	0.041 (−0.024–0.106)
+	22	189						
Sj23-LHD-ELISA (S)[††]								
+	55	146	54.5 (44.8–63.8)	53.1 (47.5–58.5)	27.4 (21.7–33.9)	78.2 (72.2–83.2)	53.4 (48.6–58.2)	0.056 (−0.028–0.140)
−	46	165						
SjSAP4-ELISA (S)[††]								
+	127	74	48.5 (42.5–54.5)	50.7 (42.8–58.6)	63.2 (56.3–69.6)	36.0 (29.8–42.7)	49.3 (44.5–54.1)	−0.008 (−0.100–0.084)
−	135	76						
SjSAP4+Sj23-LHD-ELISA (S)[††]								
+	136	65	50.0 (44.1–55.9)	53.6 (45.3–61.6)	67.7 (60.9–73.7)	35.6 (29.4–42.2)	51.2 (46.4–56.0)	0.032 (−0.063–0.118)
−	136	75						

[#]*R* cut-off value: 0.1344 (Cai et al., 2021).

[†]OD450 cut-off value for the urine ELISA assay: SjSAP4+Sj23-LHD-ELISA (U), 0.2570.

[††]OD450 cut-off values for the serum-based ELISA assays: Sj23-LHD-ELISA (S), 0.2185; SjSAP4-ELISA (S), 0.1832; SjSAP4+Sj23-LHD-ELISA (S), 0.2003 (Cai et al., 2017).

using the Sj23-LHD-ELISA (S) as the reference. A similar but moderate specificity (50.7–55.2%) was observed by comparing the SjSAP4+Sj23-LHD-ELISA (U) assay with the other diagnostic tests. The Kappa statistics analysis indicated that the urine ELISA assay showed a slight concordance with the SjSAP4+Sj23-LHD-ELISA (S), Sj23-LHD-ELISA (S), POC-CCA, and F_ddPCR assays ($\kappa < 0.2$), but no agreement with the other tests ($\kappa < 0$).

Schistosomiasis japonica prevalence analysis

The prevalence of *S. japonicum* infection in the total human cohort and different age groups determined by the KK procedure and three urine-based tests, i.e., the U_ddPCR, the SjSAP4+Sj23-LHD-ELISA (U) and the POC-CCA assay, is shown in Figure 3A. In the total cohort, the prevalence of schistosomiasis determined by the urine ELISA assay was similar to that determined by the U_ddPCR,

and was about 1.8 times higher than obtained with the KK method, while the prevalence of schistosomiasis determined by the POC-CCA cassette test was about half of that obtained with the KK method (Figure 3A). The prevalence determined for each age group using the urine ELISA assay and the U_ddPCR test was between 1.0 and 2.4 times of that obtained with the KK method, while the prevalence determined by the immunochromatographic POC-CCA assay was between 0.24 and 1.09 times of that obtained with the KK method (Figure 3B).

Discussion

Due to the relative ease and the non-invasive nature of urine collection, as well as the minimal technical and ethical issues involved in the procedure, urine represents an accessible clinical sample that can be readily collected from patients or healthy volunteers for diagnostic testing (Gao, 2013; Archer et al., 2020).
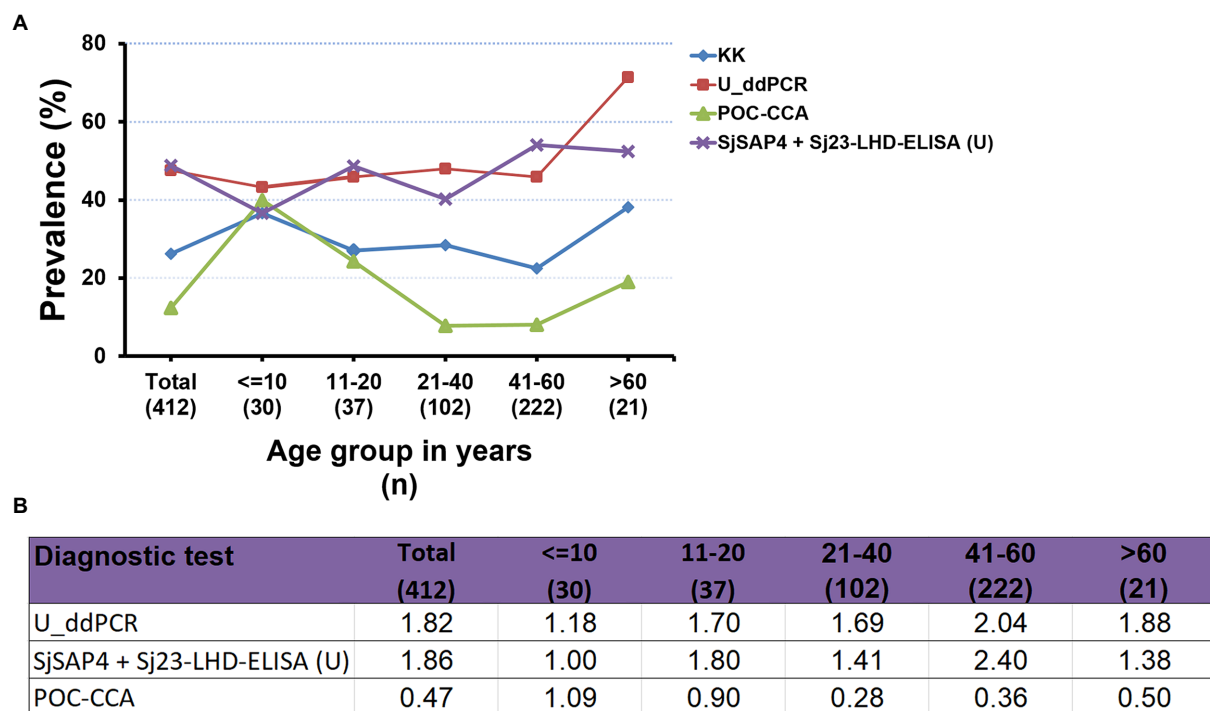
FIGURE 3

Comparison of the prevalence of *S. japonicum* infection determined by the different diagnostic tests. **(A)** The prevalence of schistosomiasis japonica determined by the KK procedure and three urine-based diagnostic tests [the U_ddPCR, SjSAP4+Sj23-LHD-ELISA (U) and the POC-CCA assay] for the total human cohort by different age groups. **(B)** Fold changes in the prevalence of *S. japonicum* infection obtained with the U_ ddPCR, the urine ELISA and the POC-CCA assay vs. the KK examined for the total cohort by each age group.

While urine samples have been used widely for the diagnosis of African schistosomiasis (Tchuem Tchuente et al., 2012; Coulibaly et al., 2013; Casacuberta et al., 2016; de Dood et al., 2018; Mewamba et al., 2021; Mohammed et al., 2022), few studies have reported the utility of urine for the diagnostic testing of schistosomiasis japonica (Itoh et al., 2003; Weerakoon et al., 2017b; Cai et al., 2021). In the field setting, this is convenient where only a single urine sample is required whereas a minimum of two stool samples are required for the KK procedure. In addition, participants can personally collect a urine sample following simple instructions, without the need for personnel trained in venipuncture, and this can reduce the potential risk of individuals contracting and spreading other diseases such as COVID-19. We previously reported that a serum-based IgG-ELISA assay targeting the antigen combination SjSAP4 + Sj23-LHD was a promising diagnostic assay for the surveillance of *S. japonicum* infection (Cai et al., 2017, 2019). Here, we aimed to validate the diagnostic capacity of the SjSAP4 + Sj23-LHD-ELISA assay for the screening of *S. japonicum* infection by testing specific IgG antibodies in urine samples collected from a human cohort living in schistosomiasis-endemic areas of the Philippines.

Using the WHO criteria for KK-based EPG grading, the human cohort utilized in this study was characterized as having a moderate *S. japonicum* prevalence and a low infection intensity (Cai et al., 2019). Hence, there was a high possibility that there could have been even lower intensity infections in the community cohort, which

would have been undetected by the KK procedure due to its inherent limited sensitivity. The present study confirmed this premise by demonstrating a low sensitivity of the KK test compared with the urine ELISA assay, i.e., the KK method exhibited 35% sensitivity (Weerakoon et al., 2017b) compared with 50.2% sensitivity of the urine ELISA procedure (Table 2), with both using the high performance F_ddPCR assay as reference test. We investigated the diagnostic performance of the urine ELISA assay against other molecular and serological methods using clinical samples collected from the well-defined cohort from the Philippines (Cai et al., 2017, 2019, 2021; Weerakoon et al., 2017b). While the F_ddPCR, SR_ ddPCR, SjSAP4 + Sj23-LHD-ELISA (S), and SjSAP4-ELISA (S) recorded higher prevalence than the urine ELISA assay, the latter outperformed the SL_ddPCR, POC-CCA, and Sj23-LHD-ELISA (S) assays in the determination of schistosomiasis prevalence in the target human cohort (Table 1).

Previously, Itoh et al. (2003) developed an ELISA to detect IgG levels against *S. japonicum* soluble egg antigens (SEA) in un-concentrated urine samples collected from participants in a schistosomiasis japonica endemic area adjacent to the Dongting Lake, Hunan Province, China, in 1995 and 1996, showing that within 129 serum ELISA-positive individuals, 112 (86.8%) tested positive with the urine ELISA. When using the SjSAP4 + Sj23-LHD-ELISA (S) as reference, the sensitivity of the urine ELISA we obtained here was 50% (Table 2); the low sensitivity of the

SjSAP4 + Sj23-LHD-ELISA (U) assay reflects the relatively low specific IgG concentration in the urine samples, as most of the cohort KK-positive individuals harbored an EPG less than 10 (Cai et al., 2021). For the SjSAP4 + Sj23-LHD-ELISA (S) assay, the optimized serum dilution was 1:250 (Cai et al., 2017). The concentration of antibodies in urine is only about 1/4,000 to 10,000 of that in serum (Nagaoka et al., 2021). Previously, it had been shown that the sensitivity of a urine-based ELISA was improved in the diagnosis of strongyloidiasis by adding a concentration protocol of urine samples (Chungkanchana et al., 2022). In addition, the diagnostic accuracy of the POC-CCA methodology was significantly increased by introducing a phase of urine concentration in two Brazilian *S. mansoni* endemic areas (Grenfell et al., 2018). In the present study, the SjSAP4 + Sj23-LHD-ELISA (U) assay exhibited an improved performance when 16× concentrated urine samples were tested compared with 10× concentrated samples. Nevertheless, the sensitivity of the SjSAP4 + Sj23-LHD-ELISA (U) assay was still relatively lower than that obtained with the SjSAP4 + Sj23-LHD-ELISA (S) assay [50.2% vs. 76.5% (Cai et al., 2019) using the F_ddPCR as reference test], which is a common phenomenon observed when comparing the sensitivity of serum and urine ELISA assays against the same antigen/s (Pearson et al., 2021).

Overall, the SjSAP4 + Sj23-LHD-ELISA (U) assay developed in the current study exhibited a diagnostic performance commensurate with that of the U_ddPCR. Although the U_ddPCR showed a higher positivity rate than that of the urine ELISA assay (88.5% vs. 53.8%, $p = 0.0265$) in the group of individuals with an EPG 10–99, there was no difference in the positivity rate for the SjSAP4 + Sj23-LHD-ELISA (U) and U_ddPCR in the group of individuals with an EPG of 1–9 (43.6% vs. 47.4%, $p > 0.05$) and in KK-negatives (49.3% vs. 43.4%, $p > 0.05$), respectively (Table 2); this resulted in a similar schistosomiasis prevalence determined by the urine ELISA assay and the U_ddPCR assay (48.8% vs. 47.6%, $p > 0.05$), i.e., about 1.8-fold higher than that obtained with the KK procedure (26.2%). When using the accurate F_ddPCR as reference, the urine ELISA assay and the U_ddPCR test showed a similar sensitivity (50.2% vs. 49%), specificity (55.2% vs. 57%; Table 2; Weerakoon et al., 2017b), accuracy (51.5% vs. 51.2%), and agreement (0.041 vs. 0.047; Table 2; Supplementary Table S1).

The POC-CCA assay has been evaluated extensively for the rapid diagnosis of schistosomiasis, particularly for *S. mansoni* infection. It has been shown in schistosomiasis mansoni-endemic areas with a prevalence less than 50% by KK, the prevalence determined by the POC-CCA assay was between 1.5- and 6-fold higher than that obtained with the KK procedure (Kittur et al., 2016). We previously detected the presence of *Schistosoma* circulating cathodic antigen (CCA) in concentrated urine samples (the same samples as used in the current study) by the commercial available POC-CCA strips, which showed a very limited sensitivity (29.6% and 14.3% using the KK and the F_ddPCR as reference test, respectively) in detecting *S. japonicum* infection (Cai et al., 2021). In contrast, the urine ELISA assay had a sensitivity of 47.2% and 50.2% when using the KK method and the F_ddPCR assay as reference test, respectively. In addition, the SjSAP4 + Sj23-LHD-ELISA (U) assay showed a greater

positivity rate than the POC-CCA technique in the group of individuals with an EPG of 1–9 (43.6% vs. 16.7%, $p = 0.0007$) and in KK-negatives (49.3% vs. 6.3%, $p < 0.0001$), respectively (Table 2). The schistosomiasis prevalence determined by the urine ELISA assay was about 4-fold higher than that obtained with the immunochromatographic POC-CCA assay (48.8% vs. 12.4%, $p < 0.0001$). These observations thus indicate that the urine ELISA assay would be more effective than the POC-CCA assay in monitoring the infection transmission status in *S. japonicum*-endemic communities. Being an antibody (IgG) detection assay, the SjSAP4 + Sj23-LHD-ELISA (U) test has limited capability in discriminating a past from an active infection. However, this is potentially an important method for identifying the presence of schistosome infections in a particular population, and also to provide supporting evidence to confirm a positive case of clinical schistosomiasis.

The SjSAP4 + Sj23-LHD-ELISA (U) assay showed slight concordance with the SjSAP4 + Sj23-LHD-ELISA (S), Sj23-LHD-ELISA (S), POC-CCA, and F_ddPCR, while no significant agreement was evident with the other tests. The relatively low agreement we report is most likely due to the specific sample types used for each assay; e.g., the SjSAP4 + Sj23-LHD-ELISA (U) detects host urinary IgG, while ddPCR assays capture the parasite DNA in multiple clinical sample types, and the POC-CCA detects parasite-derived CCA in urine. Moreover, these differences can be potentiated by the fact that antibodies are detectable even in the absence of active infection and no eggs passed in the host stools. Nonetheless, the low agreement with other diagnostic tests has also been observed with other urine-based assays, including the POC-CCA (Cai et al., 2021) and U_ddPCR assay (Supplementary Table S1). In addition, it has been suggested that the enhanced leakage of anti-parasite antibodies from plasma into urine is associated with the presence of immune complexes in the kidneys as well as vascular inflammation due to glomerulonephritis (Eamudomkarn et al., 2018). In this context, the pathogenesis of glomerular disease associated with schistosomiasis is complicated, with multiple potential mechanisms such as polyclonal B-cell activation, autoimmunity, portal-systemic shunting, hepatic macrophage function, and genetic and environmental factors (chronic salmonellosis) being involved in the development of schistosomal glomerulopathy (van Velthuysen and Florquin, 2000). Therefore, in light of the above-mentioned findings, clinical urine samples are far too intricate and may contain variables that may interfere with antibody detection due to individual variability in schistosomal glomerulopathy. In addition, highly diluted urine due to water intake is among the most commonly observed factors affecting the validity of urinalysis (Franz et al., 2019). In the future, it may be necessary to collect water ingestion controlled urine samples in order to help decrease the daily fluctuation of concentrations of schistosome-derived substances (such as cell-free DNA and antigens) and specific anti-schistosome antibodies in urine samples, thus potentially increasing agreement with other diagnostic tests for urine-based assays. Another issue needs to be considered is that the influence of the storage condition of urine samples on the performance of urine-based diagnostic tests. For example, it has been

reported that compared with fresh urine samples, using frozen urine (−20°C) after 1 year in the POC-CCA test resulted in a significant decrease in both the positive rate (Mewamba et al., 2021) and specificity (Graeff-Teixeira et al., 2021). Also, a previous study showed that the IgG level in urine sample without preservatives can drop rapidly upon storage at −20°C (Tencer et al., 1994). The urine samples used in this study were stored at −80°C for a long period without additives, whether such storage condition has affected the sensitivity of the SjSAP4 + Sj23-LHD-ELISA (U) assay needs to be further investigated. In addition, as high prevalence of helminth parasites other than *S. japonicum* was observed in the Palapag and Laoang endemic areas, i.e., 70.3% of study participants harbored at least two and up to five different helminth parasite species (Gordon et al., 2020), further studies on the potential antigenic cross-reactivity, especially for Sj23-LHD, are required.

Conclusion

The SjSAP4 + Sj23-LHD-ELISA (U) assay showed a sensitivity of 47.2% and a specificity of 93.8% in the detection of low-intensity *S. japonicum* infection in KK-positive individuals from moderately endemic area. A comprehensive comparison of the performance further revealed that the urine ELISA assay was more sensitive than the SL_ddPCR test and the POC-CCA assay and had a comparable diagnostic capability with that of the U_ddPCR. The schistosomiasis prevalence determined by the urine ELISA assay was similar with that determined by the U_ddPCR, and was about 1.8-fold higher than that obtained with the KK procedure (6 slides from two stool samples). However, the urine ELISA assay provided a reduced level of sensitivity compared with more accurate assays, such as the F_ddPCR, SR_ddPCR, and serum SjSAP4 + Sj23-LHD-ELISA assay in the detection of *S. japonicum* infection in subjects with low worm burdens in rural schistosome-endemic areas in the Philippines. This study reinforces the challenge of applying urine-based tests for the diagnosis of schistosomiasis japonica in this post-MDA era, where light-intensity infections are predominant in many endemic areas.

Data availability statement

The original contributions presented in the study are included in the article/Supplementary material, further inquiries can be directed to the corresponding author.

Ethics statement

The studies involving human participants were reviewed and approved by The Institutional Review Board (IRB) of the Research Institute for Tropical Medicine (RITM), Manila, the Philippines; The Human Research Ethics Committee (HREC), QIMR Berghofer Medical Research Institute (QIMRB), Brisbane, Australia. Written informed consent to participate in this study was provided by the participants' legal guardian/next of kin.

Author contributions

YM, PC, and DM participated in conceptualization. YM, KW, RO, and PC participated in performing experiments, formal analysis, and data visualization. RO, AR, DM, and PC provided the resources. YM, KW, and PC participated in original draft preparation. AR, DM, and PC edited and revised the manuscript. DM and PC supervised the project. All authors contributed to the article and approved the submitted version.

Funding

Acknowledgments

Conflict of interest

The authors declare that the research was conducted in the absence of any commercial or financial relationships that could be construed as a potential conflict of interest.

Publisher's note

All claims expressed in this article are solely those of the authors and do not necessarily represent those of their affiliated organizations, or those of the publisher, the editors and the reviewers. Any product that may be evaluated in this article, or claim that may be made by its manufacturer, is not guaranteed or endorsed by the publisher.

Supplementary material

The Supplementary material for this article can be found online at: https://www.frontiersin.org/articles/10.3389/fmicb.2022.1051575/full#supplementary-material

References

Archer, J., LaCourse, J. E., Webster, B. L., and Stothard, J. R. (2020). An update on non-invasive urine diagnostics for human-infecting parasitic helminths: what more could be done and how? *Parasitology* 147, 873–888. doi: 10.1017/s0031182019001732

Belizario, V. Y., de Cadiz, A. E., Navarro, R. C., Flores, M. J. C., Molina, V. B., Dalisay, S. N. M., et al. (2022). The status of schistosomiasis japonica control in the Philippines: the need for an integrated approach to address a multidimensional problem. *Int. J. One Health* 8, 8–19. doi: 10.14202/IJOH.2022.8-19

Cai, P., Mu, Y., Weerakoon, K. G., Olveda, R. M., Ross, A. G., and McManus, D. P. (2021). Performance of the point-of-care circulating cathodic antigen test in the diagnosis of schistosomiasis japonica in a human cohort from Northern Samar, the Philippines. *Infect. Dis. Poverty* 10:121. doi: 10.1186/s40249-021-00905-5

Cai, P., Weerakoon, K. G., Mu, Y., Olveda, D. U., Piao, X., Liu, S., et al. (2017). A parallel comparison of antigen candidates for development of an optimized serological diagnosis of schistosomiasis japonica in the Philippines. *EBioMedicine* 24, 237–246. doi: 10.1016/j.ebiom.2017.09.011

Cai, P., Weerakoon, K. G., Mu, Y., Olveda, R. M., Ross, A. G., Olveda, D. U., et al. (2019). Comparison of Kato Katz, antibody-based ELISA and droplet digital PCR diagnosis of schistosomiasis japonica: lessons learnt from a setting of low infection intensity. *PLoS Negl. Trop. Dis.* 13:e0007228. doi: 10.1371/journal.pntd.0007228

Casacuberta, M., Kinunghi, S., Vennervald, B. J., and Olsen, A. (2016). Evaluation and optimization of the circulating Cathodic antigen (POC-CCA) cassette test for detecting *Schistosoma mansoni* infection by using image analysis in school children in Mwanza region, Tanzania. *Parasite Epidemiol. Control* 1, 105–115. doi: 10.1016/j.parepi.2016.04.002

Cavalcanti, M. G., Silva, L. F., Peralta, R. H., Barreto, M. G., and Peralta, J. M. (2013). Schistosomiasis in areas of low endemicity: a new era in diagnosis. *Trends Parasitol.* 29, 75–82. doi: 10.1016/j.pt.2012.11.003

Chirag, S., Fomda, B. A., Khan, A., Malik, A. A., Lone, G. N., Khan, B. A., et al. (2015). Detection of hydatid-specific antibodies in the serum and urine for the diagnosis of cystic echinococcosis in patients from the Kashmir Valley, India. *J. Helminthol.* 89, 232–237. doi: 10.1017/S0022149X13000837

Chungkanchana, N., Sithithaworn, P., Worasith, C., Wongphutorn, P., Ruantip, S., Kopolrat, K. Y., et al. (2022). Concentration of urine samples improves sensitivity in detection of *Strongyloides*-specific IgG antibody in urine for diagnosis of Strongyloidiasis. *J. Clin. Microbiol.* 60:e0145421. doi: 10.1128/JCM.01454-21

Cnops, L., Soentjens, P., Clerinx, J., and Van Esbroeck, M. (2013). A *Schistosoma haematobium*-specific real-time PCR for diagnosis of urogenital schistosomiasis in serum samples of international travelers and migrants. *PLoS Negl. Trop. Dis.* 7:e2413. doi: 10.1371/journal.pntd.0002413

Coelho, P. M., Jurberg, A. D., Oliveira, A. A., and Katz, N. (2009). Use of a saline gradient for the diagnosis of schistosomiasis. *Mem. Inst. Oswaldo Cruz* 104, 720–723. doi: 10.1590/s0074-02762009000500010

Coulibaly, J. T., N'Goran, E. K., Utzinger, J., Doenhoff, M. J., and Dawson, E. M. (2013). A new rapid diagnostic test for detection of anti-*Schistosoma mansoni* and anti-*Schistosoma haematobium* antibodies. *Parasit. Vect.* 6:29. doi: 10.1186/1756-3305-6-29

de Dood, C. J., Hoekstra, P. T., Mngara, J., Kalluvya, S. E., van Dam, G. J., Downs, J. A., et al. (2018). Refining diagnosis of *Schistosoma haematobium* infections: antigen and antibody detection in urine. *Front. Immunol.* 9:2635. doi: 10.3389/fimmu.2018.02635

Department of Health. (2018) Schistosomiasis control and elimination program. Available at: https://doh.gov.ph/node/211 (Accessed on September 13, 2022).

Eamudomkarn, C., Sithithaworn, P., Kamamia, C., Yakovleva, A., Sithithaworn, J., Kaewkes, S., et al. (2018). Diagnostic performance of urinary IgG antibody detection: a novel approach for population screening of strongyloidiasis. *PLoS One* 13:e0192598. doi: 10.1371/journal.pone.0192598

Franz, S., Skopp, G., Boettcher, M., and Musshoff, F. (2019). Creatinine excretion in consecutive urine samples after controlled ingestion of water. *Drug Test. Anal.* 11, 435–440. doi: 10.1002/dta.2514

Gandasegui, J., Fernandez-Soto, P., Carranza-Rodriguez, C., Perez-Arellano, J. L., Vicente, B., Lopez-Aban, J., et al. (2015). The rapid-heat LAMPellet method: a potential diagnostic method for human urogenital schistosomiasis. *PLoS Negl. Trop. Dis.* 9:e0003963. doi: 10.1371/journal.pntd.0003963

Gandasegui, J., Fernandez-Soto, P., Muro, A., Simoes Barbosa, C., Lopes de Melo, F., Loyo, R., et al. (2018). A field survey using LAMP assay for detection of *Schistosoma mansoni* in a low-transmission area of schistosomiasis in Umbuzeiro, Brazil: assessment in human and snail samples. *PLoS Negl. Trop. Dis.* 12:e0006314. doi: 10.1371/journal.pntd.0006314

Gao, Y. (2013). Urine-an untapped goldmine for biomarker discovery? *Sci. China Life Sci.* 56, 1145–1146. doi: 10.1007/s11427-013-4574-1

Garcia-Bernalt Diego, J., Fernandez-Soto, P., Febrer-Sendra, B., Crego-Vicente, B., and Muro, A. (2021). Loop-mediated isothermal amplification in schistosomiasis. *J. Clin. Med.* 10:511. doi: 10.3390/jcm10030511

Gordon, C. A., Acosta, L. P., Gobert, G. N., Olveda, R. M., Ross, A. G., Williams, G. M., et al. (2015). Real-time PCR demonstrates high prevalence of *Schistosoma japonicum* in the Philippines: implications for surveillance and control. *PLoS Negl. Trop. Dis.* 9:e0003483. doi: 10.1371/journal.pntd.0003483

Gordon, C. A., Krause, L., McManus, D. P., Morrison, M., Weerakoon, K. G., Connor, M. C., et al. (2020). Helminths, polyparasitism, and the gut microbiome in the Philippines. *Int. J. Parasitol.* 50, 217–225. doi: 10.1016/j.ijpara.2019.12.008

Gordon, C. A., Williams, G. M., Gray, D. J., Clements, A. C. A., Zhou, X.-N., Li, Y., et al. (2021). Schistosomiasis in the People's Republic of China – down but not out. *Parasitology* 149, 218–233. doi: 10.1017/S0031182021001724

Graeff-Teixeira, C., Favero, V., Pascoal, V. F., de Souza, R. P., Rigo, F. V., Agnese, L. H. D., et al. (2021). Low specificity of point-of-care circulating cathodic antigen (POCCCA) diagnostic test in a non-endemic area for schistosomiasis mansoni in Brazil. *Acta Trop.* 217:105863. doi: 10.1016/j.actatropica.2021.105863

Grenfell, R. F. Q., Taboada, D., Coutinho, L. A., Pedrosa, M. L. C., Assis, J. V., Oliveira, M. S. P., et al. (2018). Innovative methodology for point-of-care circulating cathodic antigen with rapid urine concentration for use in the field for detecting low *Schistosoma mansoni* infection and for control of cure with high accuracy. *Trans. R. Soc. Trop. Med. Hyg.* 112, 1–7. doi: 10.1093/trstmh/try014

Halili, S., Grant, J. R., Pilotte, N., Gordon, C. A., and Williams, S. A. (2021). Development of a novel real-time polymerase chain reaction assay for the sensitive detection of *Schistosoma japonicum* in human stool. *PLoS Negl. Trop. Dis.* 15:e0009877. doi: 10.1371/journal.pntd.0009877

Itoh, M., Ohta, N., Kanazawa, T., Nakajima, Y., Sho, M., Minai, M., et al. (2003). Sensitive enzyme-linked immunosorbent assay with urine samples: a tool for surveillance of schistosomiasis japonica. *Southeast Asian J. Trop. Med. Public Health* 34, 469–472. PMID: 15115114

Itoh, M., Weerasooriya, M. V., Qiu, G., Gunawardena, N. K., Anantaphruti, M. T., Tesana, S., et al. (2001). Sensitive and specific enzyme-linked immunosorbent assay for the diagnosis of *Wuchereria bancrofti* infection in urine samples. *Am. J. Trop. Med. Hyg.* 65, 362–365. doi: 10.4269/ajtmh.2001.65.362

Kittur, N., Castleman, J. D., Campbell, C. H., King, C. H., and Colley, D. G. (2016). Comparison of *Schistosoma mansoni* prevalence and intensity of infection, as determined by the circulating Cathodic antigen urine assay or by the Kato-Katz fecal assay: a systematic review. *Am. J. Trop. Med. Hyg.* 94, 605–610. doi: 10.4269/ajtmh.15-0725

Landis, J. R., and Koch, G. G. (1977). The measurement of observer agreement for categorical data. *Biometrics* 33, 159–174. PMID: 843571

Lindholz, C. G., Favero, V., Verissimo, C. M., Candido, R. R. F., de Souza, R. P., Dos Santos, R. R., et al. (2018). Study of diagnostic accuracy of Helmintex, Kato-Katz, and POC-CCA methods for diagnosing intestinal schistosomiasis in Candeal, a low intensity transmission area in northeastern Brazil. *PLoS Negl. Trop. Dis.* 12:e0006274. doi: 10.1371/journal.pntd.0006274

Magalhaes, F. D. C., Resende, S. D., Senra, C., Graeff-Teixeira, C., Enk, M. J., Coelho, P. M. Z., et al. (2020). Accuracy of real-time polymerase chain reaction to detect *Schistosoma mansoni* - infected individuals from an endemic area with low parasite loads. *Parasitology* 147, 1140–1148. doi: 10.1017/S003118202000089X

McManus, D. P., Dunne, D. W., Sacko, M., Utzinger, J., Vennervald, B. J., and Zhou, X. N. (2018). Schistosomiasis. *Nat. Rev. Dis. Primers* 4:13. doi: 10.1038/s41572-018-0013-8

Mewamba, E. M., Tiofack, A. A. Z., Kamdem, C. N., Ngassam, R. I. K., Mbagnia, M. C. T., Nyangiri, O., et al. (2021). Field assessment in Cameroon of a reader of POC-CCA lateral flow strips for the quantification of *Schistosoma mansoni* circulating cathodic antigen in urine. *PLoS Negl. Trop. Dis.* 15:e0009569. doi: 10.1371/journal.pntd.0009569

Mohammed, H., Landeryou, T., Chernet, M., Liyew, E. F., Wulataw, Y., Getachew, B., et al. (2022). Comparing the accuracy of two diagnostic methods for detection of light *Schistosoma haematobium* infection in an elimination setting in Wolaita zone, South Western Ethiopia. *PLoS One* 17:e0267378. doi: 10.1371/journal.pone.0267378

Mu, Y., Cai, P., Olveda, R. M., Ross, A. G., Olveda, D. U., and McManus, D. P. (2020). Parasite-derived circulating microRNAs as biomarkers for the detection of human *Schistosoma japonicum* infection. *Parasitology* 147, 889–896. doi: 10.1017/S0031182019001690

Nagaoka, F., Yamazaki, T., Akashi-Takamura, S., and Itoh, M. (2021). Detection of urinary antibodies and its application in epidemiological studies for parasitic diseases. *Vaccines* 9:778. doi: 10.3390/vaccines9070778

Olamiju, F., Nebe, O. J., Mogaji, H., Marcus, A., Amodu-Agbi, P., Urude, R. O., et al. (2022). Schistosomiasis outbreak during COVID-19 pandemic in Takum, Northeast Nigeria: analysis of infection status and associated risk factors. *PLoS One* 17:e0262524. doi: 10.1371/journal.pone.0262524

Olveda, R. M., and Gray, D. J. (2019). Schistosomiasis in the Philippines: innovative control approach is needed if elimination is the goal. *Trop. Med. Infect. Dis.* 4:66. doi: 10.3390/tropicalmed4020066

Olveda, R. M., Tallo, V., Olveda, D. U., Inobaya, M. T., Chau, T. N., and Ross, A. G. (2016). National survey data for zoonotic schistosomiasis in the Philippines grossly underestimates the true burden of disease within endemic zones: implications for future control. *Int. J. Infect. Dis.* 45, 13–17. doi: 10.1016/j.ijid.2016.01.011

Pearson, M. S., Tedla, B. A., Mekonnen, G. G., Proietti, C., Becker, L., Nakajima, R., et al. (2021). Immunomics-guided discovery of serum and urine antibodies for diagnosing urogenital schistosomiasis: a biomarker identification study. *Lancet Microbe* 2, e617–e626. doi: 10.1016/S2666-5247(21)00150-6

Ross, A. G. P., Olveda, R. M., Acosta, L., Harn, D. A., Chy, D., Li, Y., et al. (2013). Road to the elimination of schistosomiasis from Asia: the journey is far from over. *Microbes Infect.* 15, 858–865. doi: 10.1016/j.micinf.2013.07.010

Ross, A. G., Olveda, R. M., Chy, D., Olveda, D. U., Li, Y., Harn, D. A., et al. (2015). Can mass drug administration lead to the sustainable control of schistosomiasis? *J. Infect. Dis.* 211, 283–289. doi: 10.1093/infdis/jiu416

Samad, M. S., Itoh, M., Moji, K., Hossain, M., Mondal, D., Alam, M. S., et al. (2013). Enzyme-linked immunosorbent assay for the diagnosis of *Wuchereria bancrofti* infection using urine samples and its application in Bangladesh. *Parasitol. Int.* 62, 564–567. doi: 10.1016/j.parint.2013.08.007

Sawangsoda, P., Sithithaworn, J., Tesana, S., Pinlaor, S., Boonmars, T., Mairiang, E., et al. (2012). Diagnostic values of parasite-specific antibody detections in saliva and urine in comparison with serum in opisthorchiasis. *Parasitol. Int.* 61, 196–202. doi: 10.1016/j.parint.2011.06.009

Sunita, T., Dubey, M. L., Khurana, S., and Malla, N. (2007). Specific antibody detection in serum, urine and saliva samples for the diagnosis of cystic echinococcosis. *Acta Trop.* 101, 187–191. doi: 10.1016/j.actatropica.2006.07.014

Tchuem Tchuente, L. A., Kuete Fouodo, C. J., Kamwa Ngassam, R. I., Sumo, L., Dongmo Noumedem, C., Kenfack, C. M., et al. (2012). Evaluation of circulating cathodic antigen (CCA) urine-tests for diagnosis of *Schistosoma mansoni* infection in Cameroon. *PLoS Negl. Trop. Dis.* 6:e1758. doi: 10.1371/journal.pntd.0001758

Tencer, J., Thysell, H., Andersson, K., and Grubb, A. (1994). Stability of albumin, protein HC, immunoglobulin G, K- AND γ-chain immunoreactivity, orosomucoid and a 1-antitrypsin in urine stored at various conditions. *Scand. J. Clin. Lab. Invest.* 54, 199–206. doi: 10.1080/00365519409088425

van Velthuysen, M. L., and Florquin, S. (2000). Glomerulopathy associated with parasitic infections. *Clin. Microbiol. Rev.* 13, 55–66. doi: 10.1128/CMR.13.1.55

Weerakoon, K. G., Gobert, G. N., Cai, P., and McManus, D. P. (2015). Advances in the diagnosis of human schistosomiasis. *Clin. Microbiol. Rev.* 28, 939–967. doi: 10.1128/CMR.00137-14

Weerakoon, K. G., Gordon, C. A., Cai, P., Gobert, G. N., Duke, M., Williams, G. M., et al. (2017a). A novel duplex ddPCR assay for the diagnosis of schistosomiasis japonica: proof of concept in an experimental mouse model. *Parasitology* 144, 1005–1015. doi: 10.1017/S003118201700021X

Weerakoon, K. G., Gordon, C. A., Gobert, G. N., Cai, P., and McManus, D. P. (2016). Optimisation of a droplet digital PCR assay for the diagnosis of *Schistosoma japonicum* infection: a duplex approach with DNA binding dye chemistry. *J. Microbiol. Methods* 125, 19–27. doi: 10.1016/j.mimet.2016.03.012

Weerakoon, K. G., Gordon, C. A., Williams, G. M., Cai, P., Gobert, G. N., Olveda, R. M., et al. (2017b). Droplet digital PCR diagnosis of human schistosomiasis: parasite cell-free DNA detection in diverse clinical samples. *J. Infect. Dis.* 216, 1611–1622. doi: 10.1093/infdis/jix521

World Health Organization (2021). *Schistosomiasis and Soiltransmitted Helminthiasess: Progress Report, 2020.* WHO; Geneva, Switzerland. Available at: https://apps.who.int/iris/bitstream/handle/10665/350005/WER9648-eng-fre.pdf?sequence=1&isAllowed=y (Accessed Aug 22, 2022).

Xu, B., Gordon, C. A., Hu, W., McManus, D. P., Chen, H. G., Gray, D. J., et al. (2012). A novel procedure for precise quantification of *Schistosoma japonicum* eggs in bovine feces. *PLoS Negl. Trop. Dis.* 6:e1885. doi: 10.1371/journal.pntd.0001885

Check for updates

*CORRESPONDENCE
Chunsheng Dong
chunshengdong@suda.edu.cn
Yang Cheng
woerseng@126.com

†These authors have contributed equally to
this work

Vesicular stomatitis virus-based vaccine targeting plasmodium blood-stage antigens elicits immune response and protects against malaria with protein booster strategy

Yifan Sun[1,2†], Xiaodan Shi[2†], Feng Lu[3], Haitian Fu[2,4], Yi Yin[3],
Jiahui Xu[3], Cheng Jin[5], Eun-taek Han[6], Xuan Huang[1],
Yongquan Chen[7], Chunsheng Dong[8]* and Yang Cheng[2]*

[1]Department of Laboratory Medicine, Affiliated Hospital of Jiangnan University, Wuxi, Jiangsu,
China, [2]Laboratory of Pathogen Infection and Immunity, Department of Public Health and
Preventive Medicine, Wuxi School of Medicine, Jiangnan University, Wuxi, Jiangsu, China, [3]Institute
of Translational Medicine, Medical College, Yangzhou University, Yangzhou, China, [4]Department of
Nuclear Medicine, Affiliated Hospital of Jiangnan University, Wuxi, Jiangsu, China, [5]Department of
Hepatobiliary Surgery, Affiliated Hospital of Jiangnan University, Wuxi, Jiangsu, China, [6]Department
of Medical Environmental Biology and Tropical Medicine, School of Medicine, Kangwon National
University, Chuncheon, Gangwon-do, South Korea, [7]Wuxi School of Medicine, Jiangnan University,
Wuxi, Jiangsu, China, [8]Jiangsu Key Laboratory of Infection and Immunity, Institutes of Biology and
Medical Sciences, Soochow University, Suzhou, Jiangsu, China

Merozoite invasion of the erythrocytes in humans is a key step in the pathogenesis of malaria. The proteins involved in the merozoite invasion could be potential targets for the development of malaria vaccines. Novel viral-vector-based malaria vaccine regimens developed are currently under clinical trials. Vesicular stomatitis virus (VSV) is a single-stranded negative-strand RNA virus widely used as a vector for virus or cancer vaccines. Whether the VSV-based malarial vaccine is more effective than conventional vaccines based on proteins involved in parasitic invasion is still unclear. In this study, we have used the reverse genetics system to construct recombinant VSVs (rVSVs) expressing apical membrane protein 1 (AMA1), rhoptry neck protein 2 (RON2), and reticulocyte-binding protein homolog 5 (RH5), which are required for *Plasmodium falciparum* invasion. Our results showed that VSV-based viral vaccines significantly increased *Plasmodium*-specific IgG levels and lymphocyte proliferation. Also, VSV-PyAMA1 and VSV-PyRON2sp prime-boost regimens could significantly increase the levels of IL-2 and IFN-γ-producing by CD4$^+$ and CD8$^+$ T cells and suppress invasion *in vitro*. The rVSV prime-protein boost regimen significantly increase *Plasmodium* antigen-specific IgG levels in the serum of mice compared to the homologous rVSV prime-boost. Furthermore, the protective efficacy of rVSV prime protein boost immunization in the mice challenged with *P. yoelii* 17XL was better compared to traditional antigen immunization. Together, our results show that VSV vector is a novel strategy for malarial vaccine development and preventing the parasitic diseases.

Introduction

In 2020, approximately 241 million new cases of malaria and 627,000 malaria-related deaths were reported worldwide (WHO, 2021). *Plasmodium falciparum* (*P. falciparum*) is a highly prevalent malarial parasite in sub-Saharan Africa and is a major cause of malaria-related death (WHO, 2021). In the past few decades, continuous efforts have been made to substantially reduce the incidences and deaths associated with malaria by using artemisinin-based combination therapy and long-lasting insecticide-treated nets (WHO, 2021). However, the primary cause for the failure to completely eradicate malaria is the *Plasmodium* parasite's resistance to frontline drugs and tolerance of mosquitoes to insecticides (Haldar et al., 2018; Minetti et al., 2020). Hence, there is a need to develop vaccines to prevent the occurrence and spread of malaria (Laurens, 2018; Stanisic and McCall, 2021). RTS,S/AS01 vaccine targets the circumsporozoite antigen of *P. falciparum* and is currently in pilot implementation in countries endemic to malaria since 2019. However, additional studies are required to evaluate the overall efficacy and safety profile of this vaccine (Laurens, 2020; Chatterjee and Cockburn, 2021). Further, the development and optimization of malaria vaccine strategies are required.

The micronemes, rhoptries, and dense granules are apical organelles of the *Plasmodium* parasite, which play key roles in the erythrocyte invasion. The apical organelle proteins are considered potential candidates for anti-malarial vaccines (Salinas et al., 2019). *P. falciparum* reticulocyte binding-like protein RH5 (PfRH5) is an apical organelle protein and a member of the erythrocyte ligands superfamily, which is essential for erythrocyte invasion (Bustamante et al., 2013; Douglas et al., 2014; Patarroyo et al., 2020). In cultured parasite lines, PfRH5 is typically processed by removing long disordered regions to generate a ∼ 45 kDa fragment called PfRH5ΔNL. The fragment PfRH5ΔNL encompasses 140–526 aa residues but lacks 248–296 aa residues, which bind to basigin and play an inhibitory role in parasite invasion (Wright et al., 2014; Payne et al., 2017; Ragotte et al., 2020; Moore et al., 2021). Therefore, PfRH5 could be a potential target for developing a vaccine against blood-stage *Plasmodium* infection (Ragotte et al., 2020). Furthermore, immunization with adenovirus/poxvirus vector-based protein-in-adjuvant RH5 has been observed to induce immune responses against *P. falciparum* (Douglas et al., 2015).

AMA1 is a micronemal protein of apicomplexan parasites. As a structurally conserved type I integral membrane protein, PfAMA1 is necessary for the invasion of erythrocytes (Tyler et al., 2011). The anti-PfAMA1 antibodies, which primarily recognize domain I (DI) and domain II (DII), have been observed to induces high levels of growth-inhibitory antibodies (Lalitha et al., 2004). In addition, *Plasmodium* rhoptry neck protein 2 (RON2) is a receptor for AMA1, and the AMA1-RON2 complex serves as a strong anchoring point to inhibit host erythrocyte invasion (Srinivasan et al., 2011; Patarroyo et al., 2020). *In vivo* studies have shown that mice immunized with an AMA1-RON2 peptide complex could provide complete protection against the lethal challenge of *Plasmodium yoelii* (*P. yoelii*) compared to immunization with AMA1 alone (Srinivasan et al., 2014). Further, antibodies generated in monkeys immunized with the AMA1-RON2L complex demonstrated enhanced neutralizing potency (Srinivasan et al., 2017). A previous study has shown that antibodies against the AMA1-RON2L/RH5 combination could consistently generate an additive growth-inhibitory effect against *P. falciparum,* as demonstrated using a growth inhibition assay (GIA) (Azasi et al., 2020). Therefore, *Plasmodium* RH5 and AMA1-RON2 combinations serve as potential antigen targets for the development of novel malarial vaccines.

The vesicular stomatitis virus (VSV) belongs to the *Rhabdoviridae* family and is an enveloped, nonsegmented, single-negative-strand RNA virus. In this study, we have used a reverse genetics system to construct recombinant VSVs (rVSVs) expressing a VSV nucleocapsid protein and two polymerase subunits to maintain the replicative ability of the virus (Lawson et al., 1995). In addition, the rVSVs expressing foreign antigens without altering its growth characteristics, which could benefit for vaccine development (Lawson et al., 1995). VSV have been developed as a vaccine vector for multiple pathogens, including bacteria, DNA, and RNA viruses. This could aid in inducing robust cellular and humoral immune responses and confer protection against challenges in animal models (Humphreys and Sebastian, 2018; Fathi et al., 2019). The Food and Drug Administration has approved the rVSVΔG-ZEBOV-GP vaccine for the prevention of Ebola virus disease (Choi et al., 2021). This indicates that VSV could serve as a robust vector backbone for vaccines and can be used against infectious diseases (Fathi et al., 2019). Recently, various studies have used different VSV-based strategies to develop vaccines against SARS-CoV-2 and the protection effect mainly due to affecting the cell entry and inducing neutralizing antibodies (Case et al., 2020; Yahalom-Ronen et al., 2020). The VSV vector has a simple structure as well as genetic makeup and can induce high virus titer. It is mildly pathogenic, has a short immunization period, and has a good safety profile, thus making rVSV a desirable vector for vaccine development (Li et al., 2007; Fathi et al., 2019). However, VSV as a vector for malaria vaccine development has not been explored.

In the current study, we first constructed a novel malaria vaccine using blood-stage antigens as immunogens and VSV as

the vector. Our results showed that the VSV-PfRH5ΔNL or VSV-PfAMA1$_{345}$ + VSV-PfRON2sp immunization strategy in mice induced specific antibodies and polyfunctional T cell responses in mice. These candidate vaccines effectively suppressed the invasion of *P. falciparum in vitro*. Furthermore, our data showed that rVSVs (VSV-PyAMA1$_{343}$ + VSV-PyRON2sp) prime and protein boost strategy stimulated T cells to secrete high levels of IFN-γ and IL-2 compared to protein-only vaccination. However, no significant differences in parasitemia and survival rate of mice were observed between the two vaccination strategies. Interestingly, both vaccines could protect against *P. yoelii* challenge in mice. Our results showed that rVSVs expressing *Plasmodium* blood-stage antigens as candidates for malaria vaccines and extended the potential application of VSV vector vaccine.

Materials and methods

Cell culture

Vero cells are kidney epithelial cells derived from *Cercopithecus aethiops*, and BSR-T7 cells are kidney cells stably expressing T7 polymerase derived from baby hamsters (Buchholz et al., 1999). Vero cells and BSR-T7 cells were cultured in Dulbecco's Modified Eagle's medium (DMEM) (Hyclone, UT, USA) containing 10% fetal bovine serum (Gibco, NY, USA) and supplemented with 1% penicillin–streptomycin solution (Gibco). All cells were maintained at 5% CO_2 in a humidified incubator at 37°C.

Generation of rVSVs

Figure 1A shows the rVSVs containing AMA1$_{345}$ (PF3D7_1133400, Domain I, and Domain II, residues 98–442 aa), RH5ΔNL (PF3D7_0424100, residues 140–526 aa, but lacking residues 248–296 aa), and RON2sp (PF3D7_1452000, C-terminal region residues 2020–2059 aa) from *P. falciparum* 3D7. The second construct was rVSVs containing AMA1$_{343}$ (PYYM_0916000, Domain I, and Domain II, residues 43–385 aa) and RON2sp (PYYM_1316500, residues 1839–1877 aa) from *P. yoelii* 17XL (Py17XL). The codon-optimized antigen-encoding sequences, encompassed the bases expressing Flag-tag, were synthesized with the base by Talen Biotech (Shanghai, China). The restriction enzymes *Xho* I and *Nhe* I were used to insert the sequences between the G and L genes of the VSV expression vector pXN2. The recombinant VSVs were recovered using a reverse genetic system (Publicover et al., 2004). Briefly, 3×10^6 Vero cells were seeded in 10 cm dishes and allowed to adhere overnight. Vero cells were infected with the vaccinia virus expressing the T7 RNA polymerase (Fuerst et al., 1986) at a multiplicity of infection (MOI) of 2.5 in serum-free DMEM medium and incubated for 2 h. The cells were transfected using the Lipofectamine™ LTX Reagent (Invitrogen, CA, USA) with 10 μg of recombinant pXN2 and 4 μg of other plasmids encoding VSV nucleocapsid (N), 5 μg

phosphoprotein (P), and 2 μg large polymerase subunit (L) according to manufacturer's instruction. BSR-T7 cells supernatant was collected after two days of transfection and filtered using a 0.22 μm filter (Millipore, MA, USA) to remove the vaccinia virus. This supernatant was used to infect new BSR-T7 cells. BSR-T7 cytopathy was observed after two days of infection. The rVSVs released into the supernatant were collected and stored at −80°C. The rVSVs were replicated in Vero cells, and the virus titer was determined by 50% tissue culture infective dose(TCID50). The rVSVs titers obtained were within the range of $10^7 \sim 10^9$ PFU. The recombinant VSV-green fluorescent protein (VSV-GFP) was used as a control and cloned as described above. The packaging plasmids pXN2-GFP, pP, pL, and pN were gifted by Prof. John Rose (Yale University).

Expression, purification of proteins, and immunization

The gene fragments AMA1$_{345}$, RON2sp, and RHΔNL from *P. falciparum* 3D7 and AMA1$_{343}$ and RON2sp from Py17XL (same as VSV constructs) were synthesized by Talen Biotech (Shanghai, China). These gene fragments were cloned into the pET28a (+) vector after codon optimization. The cloned vector was sequenced to determine if the sequence assembly was accurate by DNA sequencing. The plasmids were transformed into *Escherichia coli* BL-21 cells to produce recombinant proteins with the His-Tag. The proteins were induced using 0.1 mM IPTG at 37°C and purified using Ni-sepharose beads (YouLong Biotech, Shanghai, China). The endotoxin from the recombinant proteins was removed prior to subsequent use. The purity of the proteins was >80% which was determined by YouLong Biotech. The PfRON2sp polypeptide was synthesized by YouLong Biotech (Shanghai, China), and the purity of the peptide was analyzed by high-performance liquid chromatography (HPLC). All antisera were raised in mice using standard protocol by YouLong Biotech (Shanghai, China).

SDS-PAGE and Western blotting

The purified recombinant proteins were separated and visualized using 10% sodium dodecyl sulfate-polyacrylamide gel electrophoresis (SDS-PAGE) stained with Coomassie brilliant blue. The proteins were separated on 10% SDS-PAGE and transferred to polyvinylidene difluoride (PVDF) membranes (Amersham Biosciences, NJ, USA). The PVDF membranes were blocked with 5% skim milk for 1 h at room temperature, followed by incubation with primary anti-His antibodies (Abcam, Cambridge, UK), or antisera at 4°C overnight. The membranes were washed with tris-buffered saline containing 0.1% Tween 20 (TBST) and incubated with 1:5000 dilution horseradish peroxidase-conjugated secondary antibody (Southern Biotech, UAB, USA). The signal was detected with a chemiluminescence reagent (Thermo, MA, USA) using the ImageQuant LAS4000 system (GE Healthcare, Piscataway, NJ,
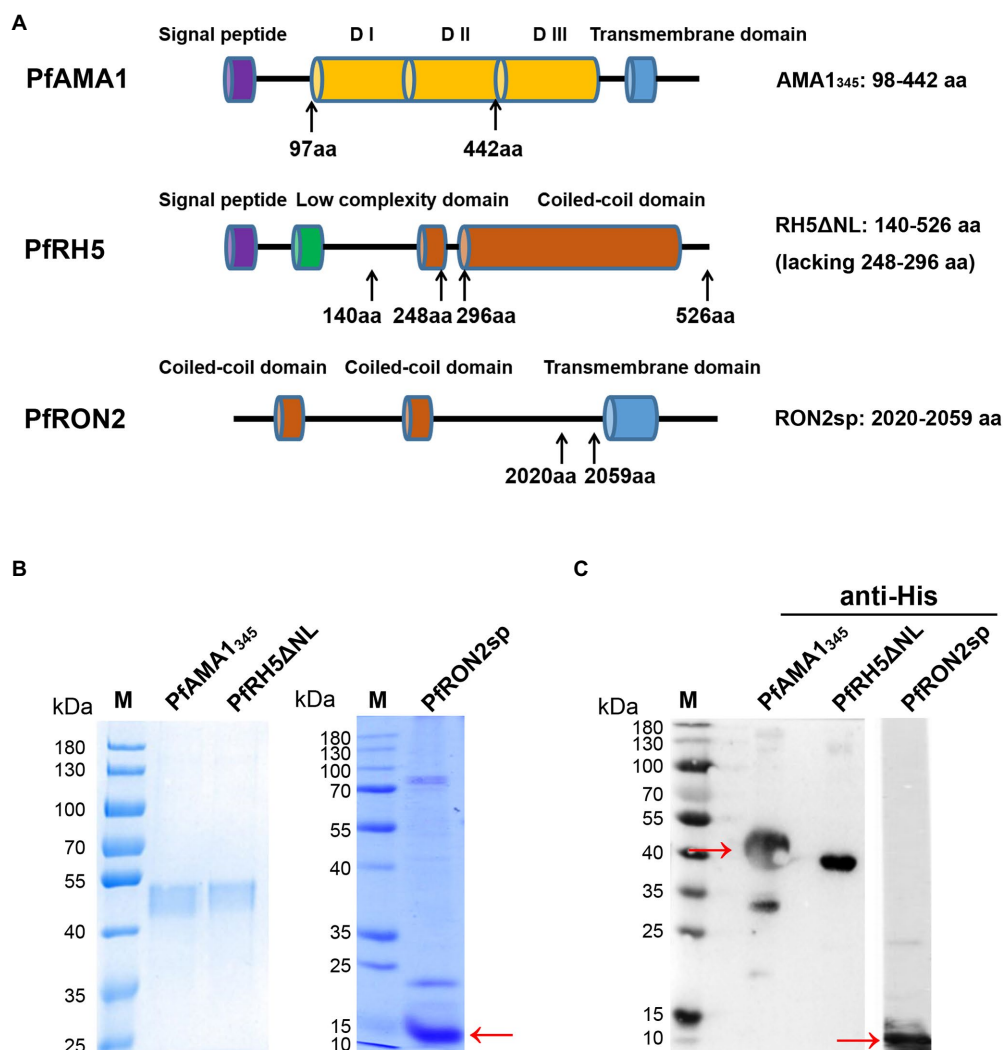
FIGURE 1
Construction, expression, and purification of recombinant PfAMA1$_{345}$ and PfRH5ΔNL proteins, as well as synthesis and identification of PfRON2sp.
(A) Schematic representation of PfAMA1, PfRH5, and PfRON2. The signal peptide is shown in purple, domain I/ domain II/ domain III (D I/D II/D III) in orange, the transmembrane domain in blue, the low complexity domain in green, and the coiled-coil domain in red. The genes encoding PfAMA1$_{345}$ (98-442aa) and PfRH5ΔNL (140-526aa, lacking 248-296aa) were cloned for expression and purification. PfRON2sp (2020-2059aa) peptide was synthesized. The amino acid residue of PfAMA1$_{345}$, PfRH5ΔNL, and PfRON2sp were shown in the right panel. **(B)** Expression and purification of PfAMA1$_{345}$ and PfRH5ΔNL proteins. Codon-optimized PfAMA1$_{345}$ and PfRH5ΔNL genes were cloned in the pET28a (+) vector, transformed in *E. coli*, and purified using Ni-sepharose beads. The purified PfAMA1$_{345}$, PfRH5ΔNL, and PfRON2sp peptides were separated by SDS-PAGE and stained using Coomassie brilliant blue **(B)** and immunoblotting with anti-His antibody for PfAMA1$_{345}$, PfRH5ΔNL, and anti-RON2 for PfRON2sp **(C)**.

USA). BSR-T7 cells were transfected with recombinant VSVs (MOI = 10) for 12 h. The cells were lysed using RIPA buffer containing 1 mM PMSF (Sigma, MO, USA) for 30 min at 4°C. The lysate was boiled for 5 min, and the proteins were separated on 10% SDS-PAGE. Western blotting was performed using primary anti-flag antibodies (Abcam, Cambridge, UK) or anti-PfRON2sp antiserum.

Indirect immunofluorescence assay

BSR-T7 cells were infected with rVSVs at MOI = 10. After 12 h of infection, the cells were collected, and 1×10^5 cells were seeded in a micro-well plate. The cells were fixed with ice-cold acetone for 5 min and blocked using 5% skim milk in phosphate buffer saline (PBS) at 4°C overnight. The cells were incubated with antisera from recombinant protein (anti-PfRH5 and anti-PfAMA1) or peptide (anti-PfRON2)-immunized mouse or rabbit at 1:200 dilution in PBS for 1 h at 37°C. The cells were incubated with Alexa Fluor 546-conjugated goat anti-mouse IgG or Alexa Fluor 488-conjugated goat anti-rabbit IgG secondary antibodies (Invitrogen) for 1 h at 37°C. The nuclei were stained with 4′, 6-diamidino-2-phenylindole (DAPI; Invitrogen) at 37°C for 30 min and mounted using a ProLong Gold antifade reagent (Invitrogen). The cells were visualized under oil immersion using

a confocal laser scanning FV200 microscope (Olympus, Tokyo, Japan) equipped with ×20 dry and ×60 oil objectives. The images were captured with FV10-ASW 3.0 viewer software and prepared for publication with Adobe Photoshop CS5 (Adobe Systems, CA, USA). For immunofluorescence on *Pf* parasite lysate, the *Pf* 3D7 strain was purified using 63% Percoll. The cells were blocked with PBS containing 5% nonfat milk. The cells were incubated with rabbit anti-sera of AMA1, RH5, and RON2, which were used as primary antibodies, followed by incubation with Alexa Flour 546-conjugated goat anti-rabbit IgG (Invitrogen). The cells were counterstained with DAPI and mounted using ProLong Gold antifade reagent. The parasites were visualized under oil immersion using a confocal laser scanning FV200 microscope (Olympus).

Animal vaccination

6–8 weeks old male BALB/c mice were obtained from Shanghai SLAC Laboratory Animal Co. Ltd. (Shanghai, China). The mice were maintained under "specific pathogen-free" conditions per the guidelines established by Jiangnan University Institutional Animal Care and Use Committee (Wuxi, China). To determine the immune response induced by rVSVs expressing *P. falciparum* antigens, BALB/c mice were vaccinated *via* intranasal routes with 10^6 plaque-forming units (PFU) VSV-PfRH5ΔNL or 5×10^5 PFU VSV-PfAMA1$_{345}$ and VSV-PfRON2sp in 1:1 ratio ($n = 5$ mice/group). 25 μl of the vector was used to immunize the mice on day 0, and a booster dose was administered on day 14. The mice vaccinated with VSV-GFP and PBS were used as controls. For immunization with purified proteins, 50 μg PfRH5ΔNL proteins/mice or 25 μg PfAMA1$_{345}$/mice +25 μg PfRON2sp proteins or peptides dissolved in 100 μl PBS with an equal volume of complete Freund's adjuvant were injected intraperitoneally in mice. Freund's incomplete adjuvant was administered on days 14 and 28 to boost immunity. The injections were administered thrice at an interval of 2 weeks.

To investigate the protective efficacy of the vaccines against *P. yoelii* infection, 6–8 weeks old BALB/c mice were divided into five groups and vaccinated with rVSVs through the intranasal route. The proteins were injected intraperitoneally. Group 1 and 2 mice were vaccinated with VSV-GFP and PBS, respectively, and served as controls. Group 3 mice (rVSVs boosting with rVSVs, rVSVs-rVSVs) were primarily immunized with 25 μl of 10^6 PFU VSV-PyAMA1$_{343}$ + VSV-PyRON2sp in 1:1 ratio (5×10^5 PFU each, $n = 5$ mice/group) and booster dose was administered day 14. Group 4 mice (rVSVs boosting with double protein immunizations, rVSVs-P–P) were first immunized with 25 μl of 10^6 PFU VSV-PyAMA1$_{343}$ + VSV-PyRON2sp on day 0. The booster dose consisted of 50 μg PyAMA1$_{343}$ + PyRON2sp proteins (25 μg each) dissolved in 100 μl PBS with an equal volume of incomplete Freund's adjuvant administered on days 14 and 28. Group 5 mice (Triple protein immunization, P-P-P) were immunized with a total of 50 μg PyAMA1$_{343}$ + PyRON2sp proteins (25 μg each) dissolved

in 100 μl PBS with an equal volume of complete Freund's adjuvant on day 0. The booster dose comprised the same proteins with incomplete Freund's adjuvant and was administered on days 14 and 28. Group 4 and 5 mice were vaccinated with VSV-GFP and PBS, respectively, and served as controls. All animal experiments were approved by the Animal Ethics Committee of Jiangnan University [JN. No. 20180615t0900930 (100)].

Enzyme-linked immunosorbent assay

To measure antigen-specific IgG responses, the serum was collected from the immunized mice from a tail vein on days 0, 7, 21, and 35 after first immunization with *P. falciparum* antigens combinations and day 35 after first immunization with *P. yoelii* antigens combinations. First, we coated with PfAMA1 and PfRON2 protein (peptides) for VSV-PfAMA1$_{345}$ + VSV-PfRON2sp and PfAMA1$_{345}$ + PfRON2sp immunization and coated with PfRH5ΔNL protein for VSV-PfRH5ΔNL and PfRH5ΔNL immunization. Similarly, we coated with PyAMA1$_{343}$ and PyRON2sp protein (peptides) for VSV-PyAMA1$_{343}$ + VSV-PyRON2sp and PyAMA1$_{343}$ + PyRON2sp immunization. 96-well polystyrene microplates (Corning, NY, USA) were coated with the corresponding antigens from *P. falciparum* 3D7 [5 μg/ml of PfRH5ΔNL, PfAMA1$_{345}$ + PfRON2sp proteins (peptides)], and *P. yoelii* [5 μg/ml of PyAMA1$_{343}$ + PyRON2sp proteins (peptides)] with 100 μl/well coating buffer (Na$_2$CO$_3$, 50 mM, pH9.6) overnight at 4°C. The antigenic sites were blocked with 5% bovine serum albumin in PBS for 2 h at 37°C. 1:40 diluted serum was added to the antigen-coated plates and incubated for 2 h at 37°C, followed by incubation with HRP-conjugated goat anti-mouse IgG secondary antibody (diluted at 1:3000) for 1.5 h at 37°C. The signals were detected using a tetramethylbenzidine kit (Sigma, MO, USA) at room temperature, and the reactions were terminated using 2 M H$_2$SO$_4$. The optical density of the solution was measured at 450 nm using a Multiskan FC microplate reader (Thermo Fisher Scientific, MA, USA). One-way analysis of variance (AVONA) was used to test the differences.

MTT assay

BALB/c mice from all groups were euthanized on day 35 post-first immunization, and the splenic lymphocytes were harvested. 100 μl of 5×10^5 cells/well splenic lymphocytes were seeded in 96-well plates. The cells were then stimulated with 5 μg/ml PfRH5ΔNL or PfAMA1$_{345}$ + PfRON2sp proteins for 72 h. Next, 50 μg thiazolyl blue tetrazolium bromide (MTT, Beyotime, Shanghai, China) was added to each well and incubated for 4 h. To terminate the reaction100 μl, dimethyl sulfoxide was added to each well and incubated for 10 min. The absorbance was measured at 570 nm using a Multiskan FC microplate reader (Thermo Fisher Scientific). One-way AVONA was used to test the differences.

Flow cytometry

BALB/c mice from all groups were sacrificed on day 35 post-first immunization. The splenocytes were isolated, and the red blood cells were harvested using ACK lysis for 3 min at room temperature. The cells were washed with PBS and centrifuged at 1500 rpm for 5 min. Next, the cell pellet was resuspended in RPMI 1640 complete medium, and 5×10^5 cells/100 μL/well were seeded in 96-well plates. The cells were stimulated with 5 μg/ml PfRH5ΔNL and PfAMA1$_{345}$ + PfRON2sp proteins (peptides) for 24 h, followed by treatment with 50 ng/ml phorbol 12-myristate 13-acetate (PMA; Sigma), 1 μg/ml ionomycin (Sigma), and 1 μg/ml bafilomycin A (Sigma) for 6 h. Next, the cells were incubated with allophycocyanin-conjugated-anti-mouse CD4 and fluorescein isothiocyanate-conjugated-anti-mouse CD8 (Biolegend, CA, USA) for surface staining. The cells were fixed, permeabilized (BD Biosciences, NJ, USA), and stained with phycoerythrin (PE)-conjugated anti-IFN-γ and PE/Cy7-conjugated anti-IL-2 antibodies (Biolegend) to detect interferon (IFN)-γ and interleukin (IL)-2. The cells were sorted using a FASCanto II flow cytometer (BD Biosciences). The splenocytes of mice immunized with antigens derived from *P.yoelii* were isolated on day 10 post-immunization and stimulated with 5 μg/ml PyAMA1$_{343}$ + PyRON2sp proteins. The rest of the protocol is the same as those described above for flow cytometry. One-way AVONA was used to test the differences in cytokine levels in mice immunized with antigens derived from *Pf*. The student's t-test was used to assess the differences in cytokine levels in mice immunized with antigens derived from *Py*.

Growth inhibition assay

Plasmodium falciparum 3D7 parasites were cultured in human O⁺ erythrocytes at 5% hematocrit. Next, the synchronized parasites were collected on day 35 after the first immunization for 24 h at 37°C and incubated with antisera at 1:100, 1:1000, or 1:2000 dilutions. The inhibition assays were carried out in 96-well plates for all strains and antibody concentrations, and the experiment was carried out in triplicates. The cultures were fixed, and parasitized erythrocytes in at least 30 high-power fields were counted using a microscope. A 5% sorbitol solution was used to synchronize the parasites into the ring stage and incubated in the presence of antiserum at the same concentrations indicated above for 24 h at 37°C. The cells were fixed with 0.05% glutaraldehyde and stained using SYBR Green I nucleic acid gel stain (Invitrogen). 1×10^6 cells were used to perform inhibition assays using flow cytometry. The invasion inhibition efficiency was calculated as described previously (Lu et al., 2022). One-way AVONA was used to test the differences.

Plasmodium yoelii 17XL challenge

The mice were infected with Py17XL by administering 5×10^5 parasitized erythrocytes (perythrocytes) on day 35 after the initial immunization. Blood smear microscopy was used to determine parasitemia every day post-infection. Briefly, a drop of blood was smeared on a glass slide, dried, and stained using a Wright's-Giemsa staining kit (JianCheng, Nanjing, China). The slides were observed under an oil microscope. Once all the PBS-treated mice had died, the surviving mice from the other groups were sacrificed on day 10 post-infection. The splenocytes from mice were harvested to analyze the cytokine secretion levels. The mice were observed for 10 days to determine the survival rates. According to the Animal ethics guidelines, humane endpoints were considered in all the *in vivo* experiments. Two-way AVONA was used to test the differences in parasitemia. Log-ranks (Mantel-Cox) tests were used to study the survival rates in mice.

Statistical analysis

GraphPad Prism software (version 5.0) was used to analyze data and create graphs. One-way or two-way ANOVA was used to perform statistical analysis. Log-ranks (Mantel-Cox) tests were used to study the survival rates in mice. $p < 0.05$ was considered statistically significant.

Results

Expression and purification of recombinant proteins using the *Escherichia coli*

A schematic diagram of PfAMA1$_{345}$ (98–442 aa), PfRH5ΔNL (140–526 aa, lacking 248–296aa), and PfRON2sp (2020–2059 aa) is shown in Figure 1A. PfAMA1$_{345}$ and PfRH5ΔNL proteins were expressed using the *E. coli* and purified. PfAMA1$_{345}$ and PfRH5ΔNL proteins were separated using SDS-PAGE and stained with Coomassie brilliant blue (Figure 1B). The protein expression was determined using western blotting (Figure 1C). In addition, PfRON2sp was synthesized and identified by SDS-PAGE, western blotting (Figures 1B,C), and HPLC (Supplementary Figure S1).

Generation of recombinant VSV-PfAMA1$_{345}$, VSV-PfRH5ΔNL, and VSV-PfRON2sp

The codon-optimized antigen-encoding sequences were cloned into the pXN2 vector at the G–L junction in the VSV genome using *Xho* I and *Nhe* I restriction enzymes (Figure 2A). The rVSVs were packaged using the reverse genetic system in BSR-T7 cells. The cytopathic effect caused by rVSVs indicated that rVSVs were successfully packaged in BSR-T7 cells. VSV-GFP served as a control (Supplementary Figure S2A). The expression of PfAMA1$_{345}$ and PfRH5ΔNL proteins with Flag-tag was confirmed using western blot (Figure 2B). In addition, the
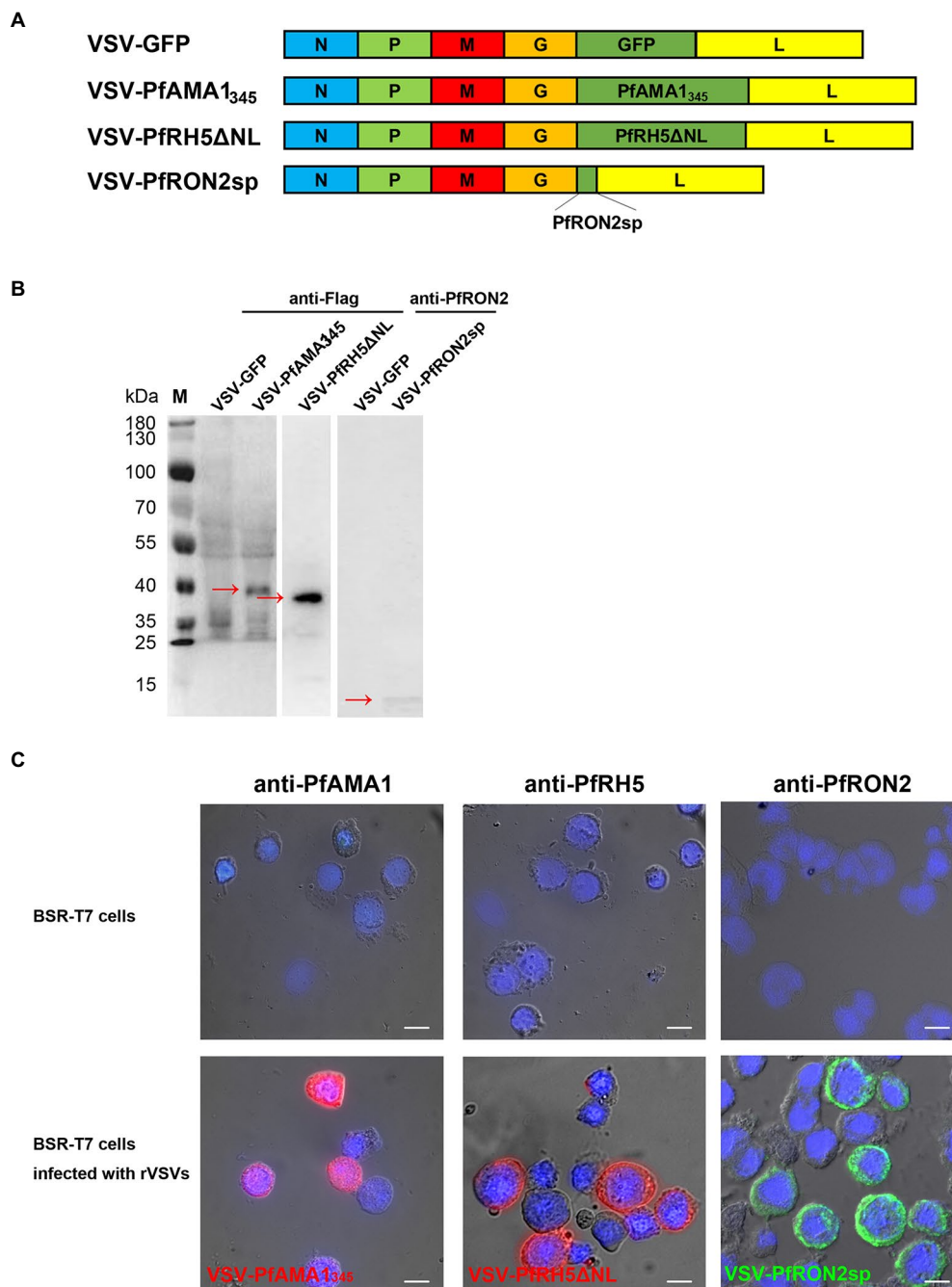
FIGURE 2
Construction and characterization of recombinant VSV-PfAMA1₃₄₅, VSV-PfRH5ΔNL, and VSV-PfRON2sp. **(A)** Construction of VSV-PfAMA1₃₄₅, VSV-PfRH5ΔNL, VSV-PfRON2sp, and VSV-GFP. Gene encoding *Plasmodium falciparum* antigen PfAMA1₃₄₅, PfRH5ΔNL, and PfRON2sp were cloned into VSV vector pXN2 between the G and L genes. The recombinant VSV pseudotype was cloned into pXN2-GFP, recombinant pXN2, and other plasmids encoding VSV nucleocapsid (N), phosphoprotein (P), and large polymerase subunit (L) to reconstruct the VSV genome. **(B)** BSR-T7 cells infected with rVSVs were harvested and analyzed 12h post-infection by western blotting using anti-Flag antibody for VSV-PfAMA1₃₄₅ and VSV-PfRH5ΔNL and anti-PfRON2 antisera for VSV-PfRON2sp. BSR-T7 cells infected with VSV-GFP were used as the control. **(C)** Indirect immunofluorescence was performed to study PfAMA1₃₄₅, PfRON2sp, and PfRH5ΔNL expression in BSR-T7 cells infected with recombinant VSVs 12h post-infection using anti-PfAMA1, PfRH5, or PfRON2sp antisera obtained from antigen-immunized mice. Non-transfected BSR-T7 cells were used as the control. The bar represents 10mm.

expression of PfRON2sp was determined using anti-PfRON2sp antiserum obtained from PfRON2sp peptide-immunized mice (Figure 2B). Immunofluorescence results demonstrated cytoplasmic localization of PfAMA1$_{345}$, PfRH5ΔNL, and PfRON2sp proteins in rVSV-infected BSR-T7 cells (Figure 2C). Together, these results demonstrate that recombinant viruses like VSV-PfAMA1$_{345}$, VSV-PfRH5ΔNL, and VSV-PfRON2sp were successfully cloned and packaged.

rVSVs containing PfAMA1$_{345}$, PfRON2sp, and PfRH5ΔNL induce specific humoral and cellular immune responses

For assessing the humoral and cellular immune responses induced by rVSVs, the mice were immunized *via* the intranasal route with 10^6 PFU rVSVs or boosted with the same dose. The mice were injected with homologous fragments of the three proteins simultaneously *via* the intraperitoneal route, as indicated in the vaccination strategy (Figure 3A). The Pf-specific antibodies were detected in the serum of the mice. The results revealed a significant increase in serum IgG level in mice immunized with a single and booster dose of VSV-PfAMA1$_{345}$ + VSV-PfRON2sp and VSV-PfRH5ΔNL regimens compared to mice immunized with VSV-GFP (Figure 3B). In the mice immunized with the combination of VSV-PfAMA1$_{345}$ and VSV-PfRON2sp, the booster immunization could significantly induce the IgG responses compared to a single dose of vaccination (Figure 3B). Nevertheless, the traditional protein vaccine immunization could still produce a high level of antibody titers (Figure 3B). Furthermore, an increase in antibody levels induced by rVSVs peaked at 3 weeks post-immunization; however, a decrease in antibody levels was observed in the next weeks after a single dose of immunization. Interestingly, an increase in antibody levels was observed 5 weeks after booster immunization (Figure 3C). To determine the specificity of antibodies generated and detect antigens in parasite lysates of *Pf*, immunofluorescence was performed on the serum collected from VSV-*Pf*-immunized mice. The results confirmed that the antisera could recognize the corresponding antigens. PfAMA1 was localized in the microneme, RH5 was localized in rhoptry, and RON2 was localized in the rhoptry neck organelles of the parasite (Figure 3D). These results indicate that strengthening immunization could effectively enhance the production of serum IgG levels and extend the duration of antibody maintenance.

The proliferation of specific lymphocytes was assessed using the MTT assay to investigate antigen-specific T-cell immune responses induced by rVSV immunization in the spleen. In mice immunized with rVSV single and prime-boost vaccination, a significant increase in the proliferation of specific T cells was observed compared to mice immunized with VSV-GFP (Figure 4A). Additionally, a significant increase in IFN-γ and

IL-2-secreting CD4$^+$ T and CD8$^+$ T cells were observed in mice immunized with VSV-PfAMA1$_{345}$ + VSV-PfRON2sp using prime-boost regimen compared with the VSV-GFP group (Figures 4B,C). An increase in IFN-γ and IL-2 secretion by CD4$^+$ T cells was observed in mice immunized with a rVSV boosting regimen, compared to mice immunized with PfAMA1$_{345}$ + PfRON2sp and PfRH5NLΔNL protein only vaccination. Together, these results demonstrate that VSV-based vaccines targeting *P. falciparum* invasion-related antigens could induce antigen-specific T-cell immune responses.

rVSV immunized mice antisera inhibits *Plasmodium falciparum* invasion *in vitro*

The GIA and invasion inhibition assay are widely used functional assays in blood-stage vaccine screening. Therefore, we evaluated the inhibitory effects of antisera from mice immunized with different vaccination strategies on the invasion by the *P. falciparum* 3D7 strain *in vitro*. The microscopic examination and flow cytometry results showed that antisera derived from VSV-PfRH5ΔNL prime-boost immunization regimen could significantly inhibit the parasitic invasion compared to antiserum derived from mice immunized with VSV-GFP (Figures 5A–C). Furthermore, microscopic analysis revealed that VSV-PfRH5NLΔNL single vaccination and VSV-PfAMA1$_{345}$ + VSV-PfRON2sp prime-boost immunization showed a significant inhibitory effect compared to VSV-GFP groups (Figure 5C). In addition, no significant difference in inhibition of invasion by *P. falciparum* 3D7 was observed on treatment with antisera derived from recombinant VSV immunization and homologous protein immunization (Figure 5C). These results indicated that single and prime-boost regimen of VSV-PfRH5ΔNL produced antibodies could inhibit parasite invasion.

VSV-PyAMA1$_{343}$ and VSV-PyRON2sp vaccination protects against *Plasmodium yoelii* challenge

Primates are the only host of *P. falciparum*, and conducting *in vivo* experiments in primates could be challenging (Beignon et al., 2014). Therefore, *P. yoelii,* which can infect rodents and cause malaria, was used as an alternative model to evaluate the efficacy of VSV-based vaccines (Figure 6A). RH5 has no homologous protein in *P. yoelii*; therefore, we could not construct recombinant VSV for *in vivo* experiments. To investigate the protective effect of VSV-based malaria vaccines, a recombinant VSV vaccine was constructed expressing AMA1$_{343}$ and RON2sp of *P. yoelii*, which are homologous fragments of PfAMA1$_{345}$ and PfRON2sp. The cytopathic effect on BSR-T7 cells was observed under a microscope, indicating that VSV-PyAMA1$_{343}$ and VSV-PyRON
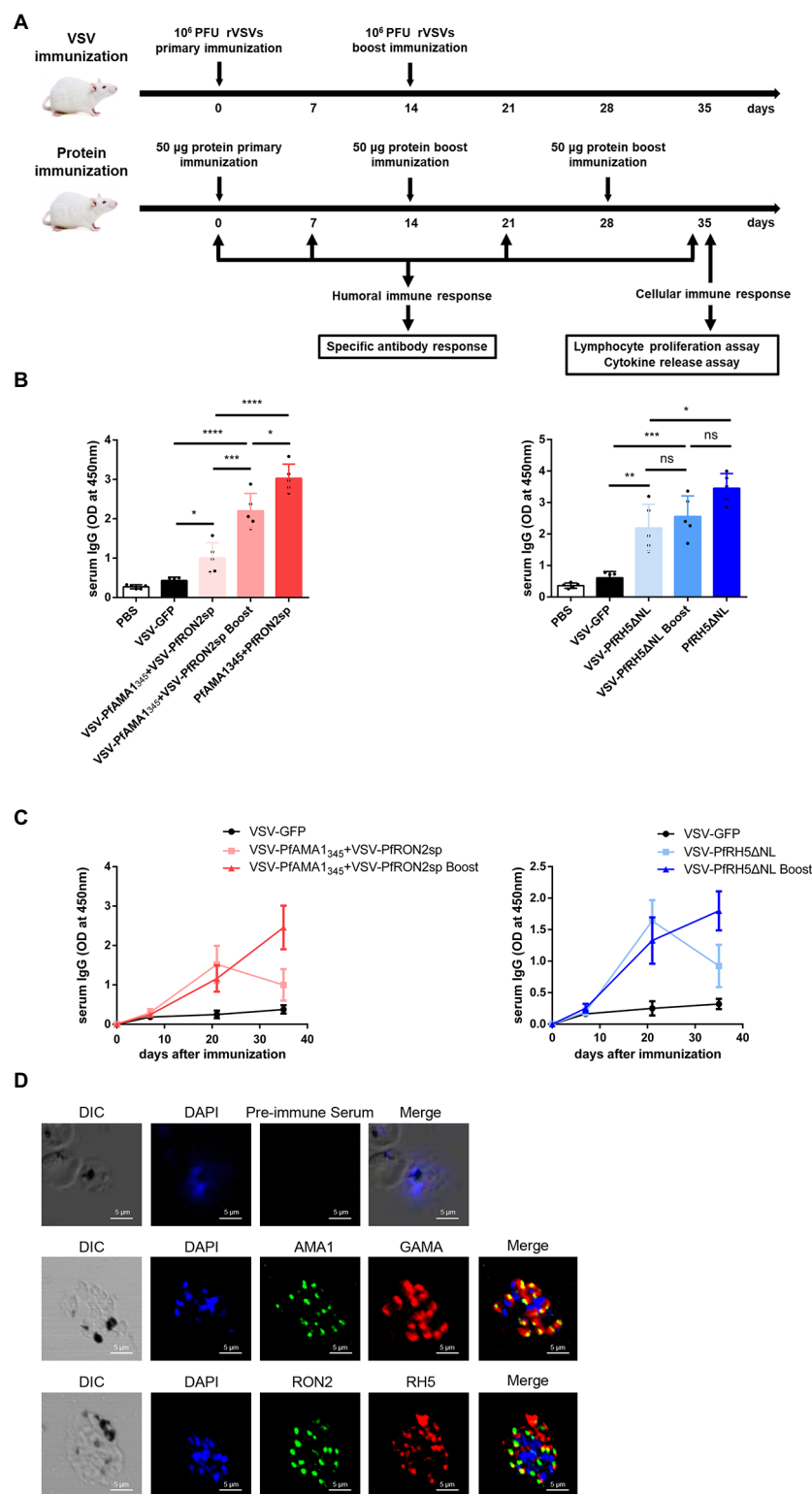
FIGURE 3

Antigen-specific humoral immune responses induced by rVSVs. **(A)** Schematic representation of animal vaccination and detection strategies. BALB/c mice (n=5 per group) were intranasally immunized with 25μl of 10^6 PFU VSV-PfAMA1$_{345}$+VSV-PfRON2sp (VSV-PfAMA1$_{345}$ and VSV-PfRON2sp mixture) or VSV-PfRH5ΔNL as single or prime-boost vaccination. The mice were intraperitoneally injected with 50μg PfAMA1$_{345}$+PfRON2sp and PfRH5ΔNL antigens three times at the indicated time points. The immune responses were detected at the indicated time points. **(B)** Specific IgG titers were analyzed on day 35 after primary immunization with rVSVs single and prime-boost or proteins by ELISA coated with 5μg/ml PfAMA1$_{345}$+PfRON2spor PfRH5ΔNL proteins (peptides). **(C)** The trend of specific IgG antibodies in mice immunized with

(*Continued*)

Figure 3 (Continued)

VSV-PfAMA1$_{345}$+VSV-PfRON2sp or mice inoculated with VSV-PfRH5ΔNL on days 0, 7, 21, and 35 after primary immunization. **(D)** Subcellular localization of PfAMA1, PfRH5, and PfRON2 proteins. The parasite was labeled with antisera against PfAMA1$_{345}$, PfRH5ΔNL, and PfRON2sp in the microneme, rhoptry, and rhoptry neck. PfGAMA was used as the marker of PfAMA1. The pre-immune serum was used as the negative control. Nuclei were stained with DAPI and appeared as blue in merged images. The bar represents 5mm. DIC represents Differential Interference Contrast. One-way AVONA was used to perform statistical analysis. Error bars indicate standard deviation (SD). Ns, no significant, *p<0.05, **p<0.01, ***p<0.001 and **** p<0.0001.

2sp were successfully packaged (Supplementary Figure S2B). Furthermore, PyAMA1$_{343}$ and PyRON2sp were expressed in recombinant VSVs and verified by western blotting (Figure 6B). These results confirm that recombinants VSV-PyAMA1$_{343}$ and VSV-PyRON2sp were successfully generated.

Specific IgGs in serum and cytokine secretion by T cells derived from the spleen were investigated to evaluate the efficacy of VSV-PyAMA1$_{343}$ and VSV-PyRON2sp hybrid immunization strategies. The results showed that immunization with rVSVs-P-P and P-P-P induce higher IgG levels in mice after 5 weeks of vaccination compared to mice immunized with rVSVs-rVSVs (Figure 6C). However, no significant difference between the IgG induced by in sera of mice immunized with rVSVs-P-P and P-P-P (Figure 6C). Furthermore, we evaluated if rVSVs-P-P and P-P-P could induce specific cellular immune responses on *P. yoelii* challenge. The results showed that immunization with rVSV-P-P could induce CD4$^+$ and CD8$^+$ T cells to secrete high levels of IFN-γ and IL-2 in mice compared to immunization with P-P-P (Figure 6D).

BALB/c mice from all the groups were infected with Py17XL by administering 5×10^5 perythrocytes intraperitoneally after 35 days of initial immunization. This will allow us to evaluate whether immunization with rVSVs expressing PyAMA1$_{343}$ and PyRON2sp could protect the mice against *P. yoelii* infection. The microscopic examination revealed that the percentage of perythrocytes was significantly lower in mice immunized with rVSVs-P-P and P-P-P compared to mice immunized with VSV-GFP and PBS, respectively (Figure 6E). On day 6 after the Py17XL challenge, the parasitemia was less than 30% in mice immunized with rVSVs-P-P and P-P-P regimens (Figure 6E). Moreover, all mock-immunized mice died within 8 days of *P. yoelii* challenge. The survival rate of rVSVs-P-P and P-P-P-immunized mice was significantly higher compared to mice immunized with VSV-GFP and PBS, respectively (Figure 6F). Nevertheless, no significant differences in survival rate were observed between mice immunized with rVSVs-P-P and P-P-P (Figure 6F). These results indicate that the rVSVs-P-P and P-P-P immunization strategies protected mice against *P. yoelii* infection and the rVSV prime-protein boost immunization induced stronger polyfunctional T cell responses.

Discussion

An effective vaccine that successfully eliminates malaria could aid in improving public health. RTS,S/AS01 is the only licensed malaria vaccine undergoing phase III clinical trial. However, the vaccine has moderate efficacy and may not be able to eradicate malaria (Neafsey et al., 2015; Olotu et al., 2016; Tinto et al., 2019; Arora et al., 2021). Despite challenges associated with vaccine development, such as the genetic variation and antigenic diversity of parasites (Neafsey et al., 2021), some strategies, including novel viral vectors as an antigenic delivery platform, have been used to enhance the protective efficacy of the malarial vaccines (Frimpong et al., 2018; Humphreys and Sebastian, 2018). Further, vaccines with viral vector backbone are currently being used against Ebola virus disease in clinical settings (Choi et al., 2021). However, VSV has not been used for malaria vaccine development until now. In this study, we have constructed three recombinant VSV-based vaccines expressing *P. falciparum* gene fragments like AMA1$_{345}$, RON2sp, and RH5ΔNL. Our results show that these vaccines could induce high IgG levels and a strong antigen-specific T-cell immune response in immunized mice. Although single immunization with rVSVs could not induce a strong T cell response, the prime-booster rVSVs regimens inhibited invasion of *P. falciparum in vitro*. Interestingly, the protective efficacy of rVSVs prime-protein boost vaccination was comparable to protein immunization in mice against *P. yoelii* infection. Our results provide novel insights into the development of VSV-based vaccines for malaria.

Various studies have used viral vectors for malaria vaccine development (Ewer et al., 2015), including Modified Vaccinia Virus Ankara (MVA), chimpanzee adenovirus 63 (ChAd63) (Kim et al., 2020), Human Adenovirus Serotype 5 (AdHu5), adeno-associated virus serotype 1 (AAV1) (Yusuf et al., 2019), and AAV8 (Shahnaij et al., 2021). Furthermore, the ChAd63-MVA vaccine encoding multiple epitope string thrombospondin-related adhesion proteins (ChAd63-MVA ME-TRAP) is currently undergoing clinical trials (Kimani et al., 2014; Hodgson et al., 2015; Tiono et al., 2018). However, the protective efficacy of the vaccine is still unsatisfactory in infants in the high malaria-endemic region (Tiono et al., 2018). ChAd63 and MVA viral vector vaccines encoding Pfs25-IMX313 induce T-cell and B-cell responses in humans; nevertheless, the efficacy of antibodies in serum to reduce transmission is weak (de Graaf et al., 2021). To the best of our knowledge, our study is the first to use the rVSV vector to develop a malaria vaccine. Further, our results show that booster immunization with VSV-PfRH5ΔNL and VSV-PfAMA1$_{345}$ + VSV-PfRON2sp could trigger high IgG levels in serum and promote the proliferation of specific lymphocytes (Figures 3B, 4A). Moreover, the vaccine can significantly inhibit
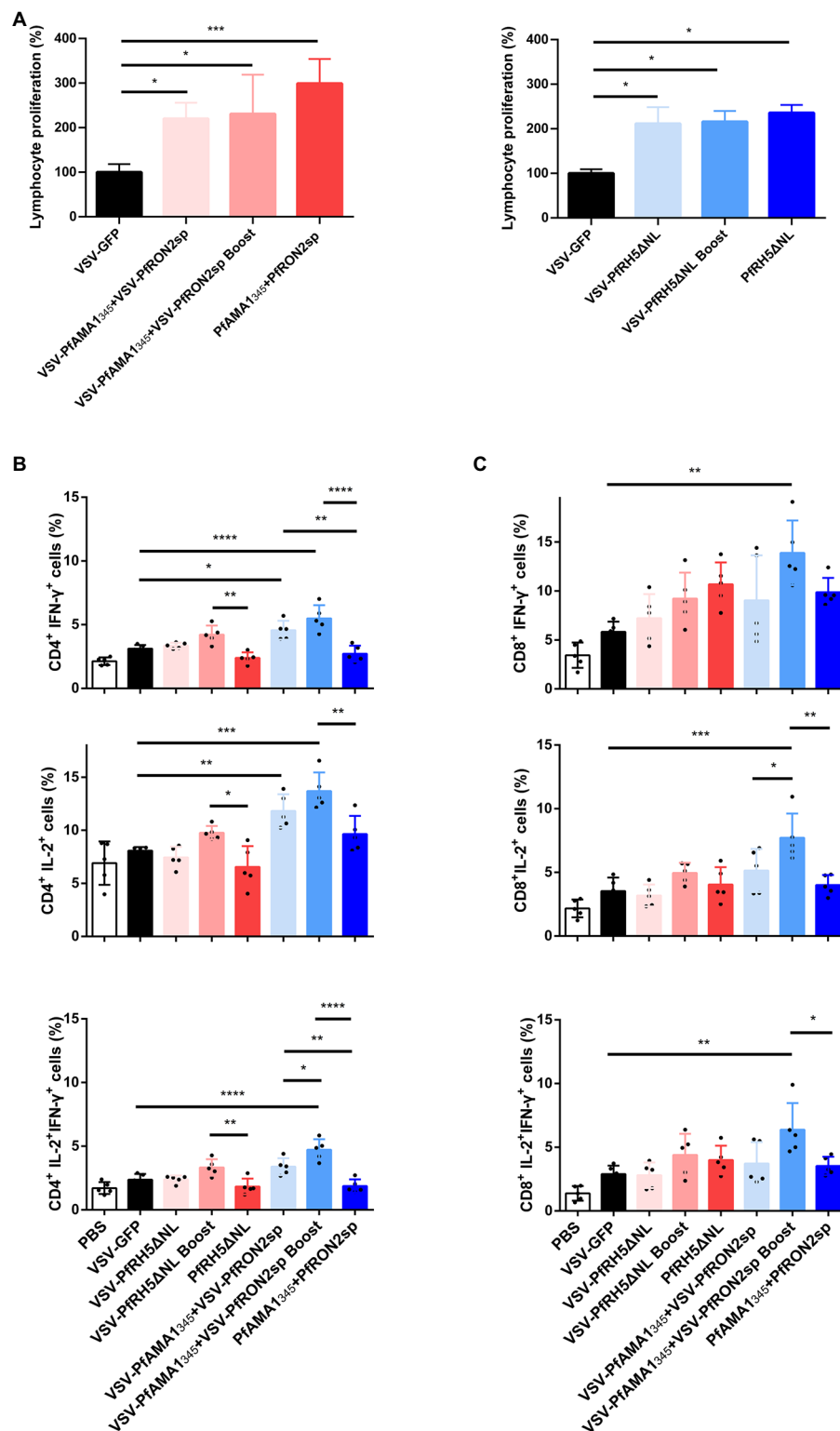
FIGURE 4

Antigen-specific cellular immune responses induced by immunization with VSV-based vaccines. Spleen cells were collected from immunized mice after 5weeks of immunization **(A)** Splenic lymphocyte proliferation was assessed using MTT assay after stimulation with 5μg/ml PfAMA1$_{345}$+PfRON2sp or PfRH5ΔNL proteins (peptides). VSV-GFP was used as the control. **(B,C)** The frequency of CD4$^+$ and CD8$^+$ T cells secreting IFN-γ or IL-2 alone was determined by flow cytometry after stimulation with 5μg/ml PfAMA1$_{345}$+PfRON2sp mixture or PfRH5ΔNL proteins (peptides) *in vitro* for 24h. Treatment with PMA (50ng/ml), ionomycin (1μg/ml), and bafilomycin A (1μg/ml) for 6h. The frequency of CD4$^+$ and CD8$^+$ T cells secreting IFN-γ and IL-2 were determined by flow cytometry after the same stimulation with proteins (peptides) and treatment with PMA, ionomycin, and bafilomycin A. Error bars indicate SD. One-way AVONA was used to perform statistical analysis.*$p<0.05$, **$p<0.01$, ***$p<0.001$ and ****$p<0.0001$.
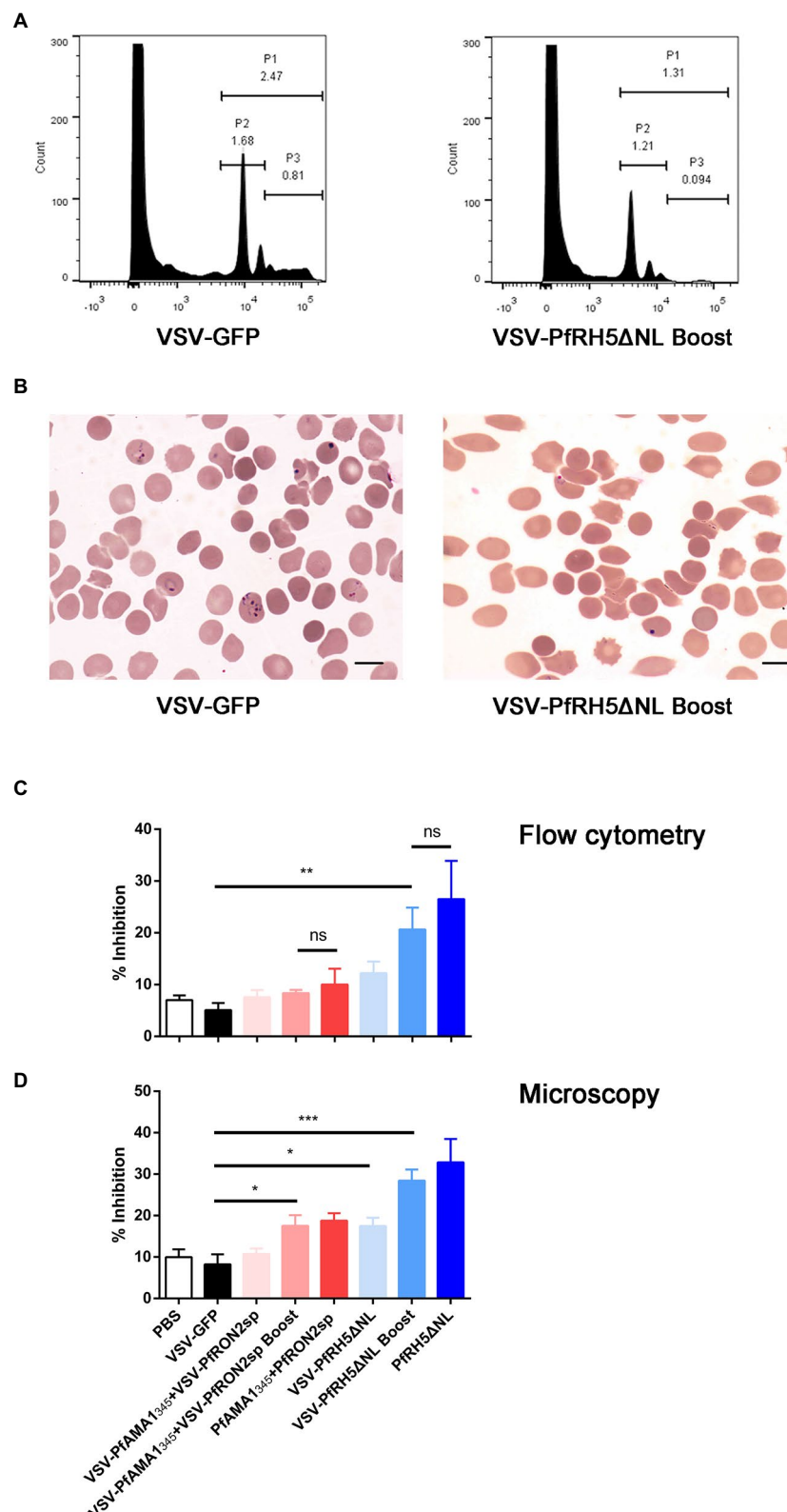
FIGURE 5

Inhibition efficiency of anti-PfAMA1$_{345}$+PfRON2sp and anti-PfRH5ΔNL antisera. **(A)** Parasitemia analysis were determined by flow cytometry using SYBR Green staining. P1 represents *Plasmodium falciparum*-infected erythrocytes, P2 represents ring forms after infecting erythrocytes with *P. falciparum*, P3 represents schizonts after infecting erythrocytes with *P. falciparum*. **(B)** Parasitemia analysis using microscopy. The bar represents 10mm. **(C)** Inhibition of parasite invasion was determined using flow cytometry **(C)** and microscopy **(D)**. Error bars indicate SD. One-way AVONA was used to perform statistical analysis. Ns, no significant, *p<0.05, **p<0.01, and *** p<0.001.
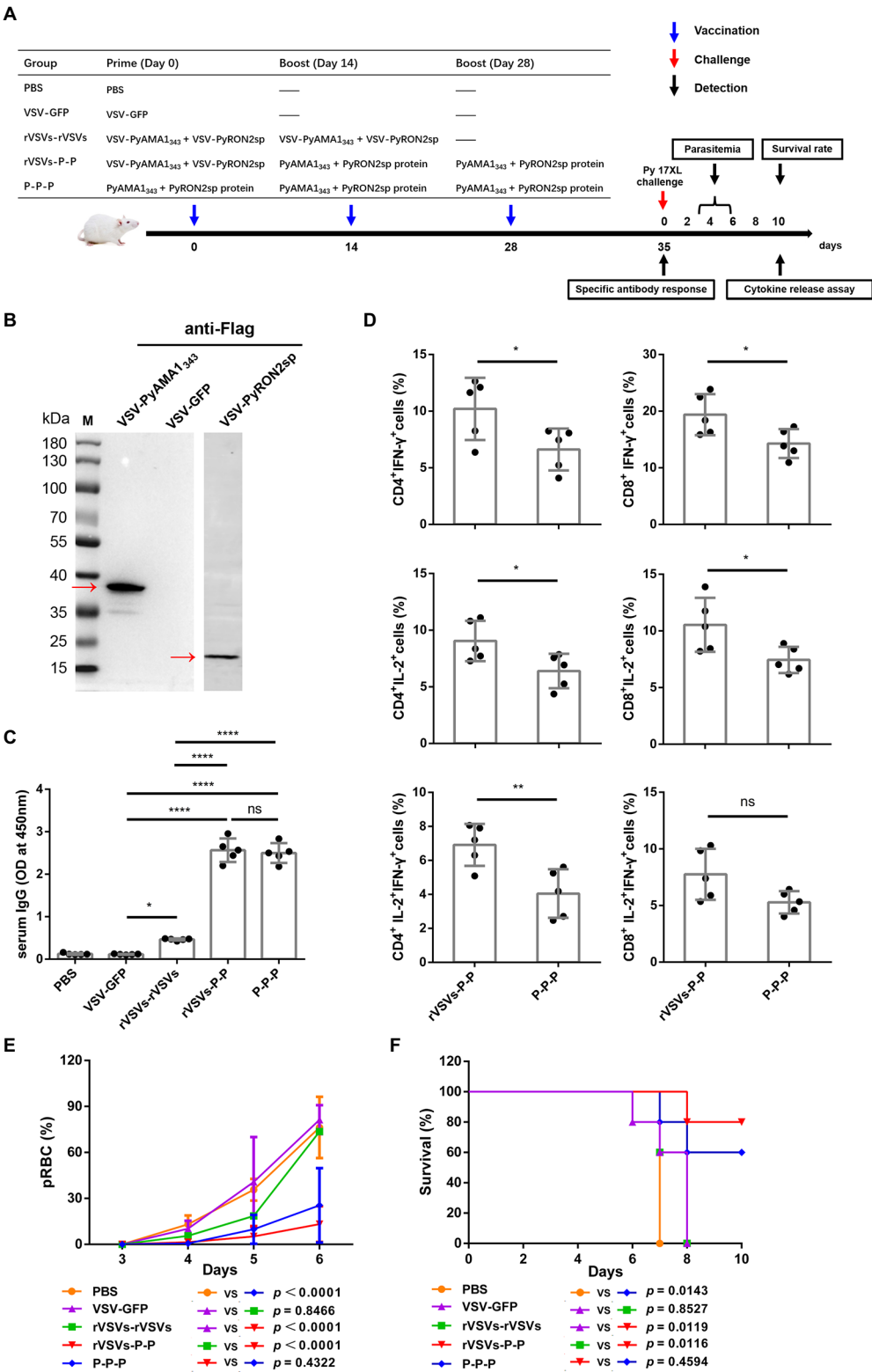
FIGURE 6

Antigen-specific immune response and immune protection induced by rVSVs. **(A)** The workflow of vaccination, challenge, and detection procedure. BALB/c mice (*n*=5 per group) were intranasally immunized with 25μl of 10^6 PFU VSV-PyAMA1$_{343}$+VSV-PyRON2sp (VSV-PyAMA1$_{343}$ and VSV-PyRON2sp mixture) through prime-boost vaccination. The mice were intraperitoneally injected with 50μg PyAMA1$_{345}$+PyRON2sp antigens three times at the indicated time points. Mice were infected with Py17XL with 5×10^5 perythrocytes 35days after first immunization. Immune responses were detected at the indicated time points. **(B)** Western blot analysis of expression of PyAMA1$_{343}$ and PyRON2sp in BSR-T7 cells that

(*Continued*)

Figure 6 (Continued)

infected with recombinant VSV (MOI=10 for 12h) using anti-Flag antibodies. **(C)** Specific IgG titers were analyzed on day 35 after primary immunization with rVSVs single and prime-boost or proteins by ELISA coated with 5μg/ml PyAMA1$_{343}$+PfRON2sp proteins. One-way AVONA was used **(D)** The frequency of CD4$^+$ and CD8$^+$ T cells secreting IFN-γ or IL-2 alone was determined by flow cytometry after stimulation with 5μg/ml PyAMA1$_{343}$+PyRON2sp mixture proteins *in vitro* for 24h. Treatment with PMA (50ng/ml), ionomycin (1μg/ml), and bafilomycin A (1μg/ml) for 6h. The frequency of CD4$^+$ and CD8$^+$ T cells secreting IFN-γ and IL-2 were determined by flow cytometry after the same stimulation with proteins and treatment with PMA, ionomycin, and bafilomycin A. One-way AVONA was used to test the differences. **(E)** Analysis of the infection rate of RBC *via* blood smears on days 3, 4, 5, and 6 post-challenge with Py17XL. Two-way AVONA was used to test the differences. **(F)** Survival rates of different immunization strategies in inoculated mice post-challenge. Log-rank (Mantel-Cox) tests were used to analyze mouse survival curves. Error bars indicate SD. Ns, no significant, *$p<0.05$, **$p<0.01$, ***$p<0.001$, and ****$p<0.0001$.

erythrocyte invasion (Figure 5C), thereby indicating that the rVSV vaccines targeting *Plasmodium* blood-stage antigens could induce functional immune responses.

The humoral immune response plays an important role in conferring protection and developing immunity against parasitic natural infections and vaccine inoculation (Boyle et al., 2017; Gonzales et al., 2020). Our results are consistent with the previous studies, which used VSV as a vector for vaccine development, such as vaccines against COVID-19 (Case et al., 2020) and the Marburg virus (Marzi et al., 2018). These studies have demonstrated that immunizing mice with rVSVs expressing microbial antigens could induce high antibody titers. A consistent increase in IgG levels was observed in sera of mice immunized with prime-boost regimens such as VSV-PfRH5ΔNL or VSV-PfAMA1$_{345}$ + VSV-PfRON2sp (Figure 3B). However, the antibody titers began to decline after 3 weeks of a single dose of immunization (Figure 3C). To address the concerns regarding the loss of potency to generate rVSV-induced functional antibodies after a single immunization, we have developed a new rVSV-P–P strategy. This strategy could induce higher antibody levels compared to the rVSVs-rVSVs regimen; in fact, this strategy can induce antibody levels comparable to those produced by the protein vaccine (Figure 6C).

T cells are indispensable for attenuating the replication of the *Plasmodium* parasite and reducing the severity of malaria (Kurup et al., 2019). Furthermore, IFN-γ plays a critical role in the immune response against *Plasmodium* by inducing phagocytosis and activating macrophages to promote the killing of parasites and other phagocytic cells (Gbedande et al., 2020). Moreover, IFN-γ produced by CD4$^+$T cells in response to *Plasmodium* antigen is IL-2 dependent (Kimura et al., 2010). A subunit malaria vaccine confers protection against sporozoite challenge by increasing the production of IL-2-secreting CD4$^+$T cells (Chawla et al., 2019). Our results showed that single and booster immunization with VSV-PfAMA1$_{345}$ + VSV-PfRON2sp significantly increases the levels of IFN-γ-and IL-2-secreting CD4$^+$T cells compared to VSV-GFP immunization (Figure 4B). IFN-γ activates phagocytosis and killing of parasites, whereas parasitic invasion is primarily dependent on ligand-receptor interactions between parasites and erythrocytes (Patarroyo et al., 2020). Although rVSV immunization could increase the secretion of cytokines, no significant differences in inhibiting parasitic invasion were observed between rVSV regimens and homologous protein immunization (Figure 5C). Studies have shown that MHC-I aids in recognition of *P. vivax* and *P. yoelii*-infected reticulocytes by

cytotoxic CD8$^+$T cells. Further, cytotoxic T-lymphocytes aid in parasite clearance during the blood stage of malaria (Junqueira et al., 2018; Hojo-Souza et al., 2020). Our results show a significant increase in levels of IFN-γ and IL-2-secreting CD8$^+$ T cells in the spleen of mice immunized with VSV-PfAMA1$_{345}$ + VSV-PfRON2sp prime-boost regimen (Figure 4C). This indicates that the VSV based vaccines could effectively induce CD8$^+$ T cell-mediated immune response. A clinical study reported the involvement of cytotoxic CD8$^+$ T cells in the pathogenesis of malarial complications in humans (Kaminski et al., 2019); however, the role and underlying mechanisms of CD8$^+$ T cell responses in *Pf* blood-stage vaccine are unclear and should be explored further.

Although antigen and viral vector-based vaccines can induce CD4$^+$ and CD8$^+$T cell responses, T-cell responses induced by vaccines are influenced by multiple factors, including the type of viral vectors and antigens of specific pathogens (Sasso et al., 2020). For example, non-human primate adenoviruses (NHPAd) are vaccine vectors that can induce a high level of CD4$^+$ and CD8$^+$T cell responses (Sasso et al., 2020). Whereas the proportion of IFN-γ and IL-2 double-positive CD8$^+$T cells induced by the viral antigen coxsackievirus B3(CVB3)-VP1-VSV was less compared to CD4$^+$ T cells (Wu et al., 2014). Our results showed that rVSV vaccines containing malaria antigens could induce both CD4$^+$ and CD8$^+$ T cells secreting IFN-γ and IL-2 (Figures 4B,C). Malaria vaccines with virus-like particles (Lee et al., 2020) and AAV8 (Shahnaij et al., 2021) as vectors can induce the production of high levels of memory T cells, which is an important defense mechanism against malaria. Whether rVSV vaccines could also induce the production of memory T cells should be investigated further (Krzych et al., 2014; Moncunill et al., 2017). Regarding immunization routes, the intranasal route is commonly used for administering VSV-based vaccines, such as STAR-CoV2 (Case et al., 2020). Intranasal inoculation of VSV vaccines could induce mucosal immunity in addition to humoral and cellular immunity (Wu et al., 2014). A recent study has shown that sporozoites inoculated in the skin induce circulating IgA production, and IgA monoclonal antibody reduces the parasitemia in the liver of mice (Tan et al., 2021). Whether the rVSV malaria vaccine induces mucosal immunity should be further investigated.

The microbial infection model could be used to evaluate the effectiveness of vaccines and investigate the underlying mechanisms of protective immunity *in vivo*. Rodent parasites, including *P. yoelii*, have been widely used to study parasite biology and mammalian immune responses to malaria (De Niz and

Heussler, 2018). To verify the effects of recombinant VSV vaccines *in vivo*, we explored the protective efficacy of different vaccine immunization strategies using Py17XL as a model. After the Py17XL challenge, a significant decrease in the parasitemia of mice immunized with rVSVs-P-P and P-P-P groups was observed (Figure 6E). A significant increase in the survival rate of the mice immunized with rVSVs-P-P and P-P-P groups was observed (Figure 6F). Further, a significant increase in IFN-γ and IL-2 secretion by T cells was observed in mice immunized with rVSVs-P-P regimen compared to the mice immunized with P-P-P (Figure 6D). Together, these results indicate that VSV-prime and protein-boost regimen primarily induced high immunogenicity.

Notably, the rVSVs-rVSVs immunization strategy conferred weak protection, likely due to the complex immune mechanisms developed by protozoans. Further, the factors contributing to the reduced efficacy of homologous rVSV regimens include the presence of potential anti-vector antibodies. The pre-existing antibodies against VSV could probably reduce the efficacy of the homologous rVSV regimens. This could inhibit the replication of VSV vectors (Poetsch et al., 2019) and may impair the protective immunity against malaria. In addition, a previous study has suggested that the protective efficacy of the VSV-Ebola vaccine was dependent on antigen dose and immunization route (Jones et al., 2007). Thus, investigating more candidate antigens and different routes of immunization for using VSV vaccines is necessary.

In conclusion, we established a novel VSV-based vaccine approach for malaria and evaluated the vaccine efficacy. Our results demonstrated that rVSVs expressing AMA1$_{345}$, RON2sp, and RH5ΔNL gene fragments of *P. falciparum* could effectively induce specific humoral and cellular immune responses as well as inhibit *P. falciparum* invasion. Furthermore, the rVSVs-P-P immunization strategy was more efficacy in protection against Py17XL infection. Our study demonstrated the use of VSV as a vaccine vector and provided new insights into effective malaria prevention.

Data availability statement

The raw data supporting the conclusions of this article will be made available by the authors, without undue reservation.

Ethics statement

The animal study was reviewed and approved by Animal Ethics Committee of Jiangnan University [JN. No. 20180615t0900930 (100)].

Author contributions

YC and CD conceived this study. YS and XS designed the research protocol, wrote the manuscript, and performed the data acquisition and analysis. XS, YS, YY, and HF performed laboratory work. YS, XS, YC, CJ, FL, and ETH conceived the data handling and analysis process and reviewed the manuscript. JX, ETH, XH, and YC interpreted the results and assisted in writing the manuscript. All authors read and approved the final version of the manuscript.

Conflict of interest

The authors declare that the research was conducted in the absence of any commercial or financial relationships that could be construed as a potential conflict of interest.

Publisher's note

All claims expressed in this article are solely those of the authors and do not necessarily represent those of their affiliated organizations, or those of the publisher, the editors and the reviewers. Any product that may be evaluated in this article, or claim that may be made by its manufacturer, is not guaranteed or endorsed by the publisher.

Supplementary material

The Supplementary material for this article can be found online at: https://www.frontiersin.org/articles/10.3389/fmicb.2022.1042414/full#supplementary-material

SUPPLEMENTARY FIGURE S1
(A) PfRON2sp peptide was purified by chromatography and identified by mass spectrometry. The lower panel showed the peak time, area under the peak and protein concentration of the peak during PfRON2sp peptides were harvest.

SUPPLEMENTARY FIGURE S2
(A) Microscopic images of BSR-T7 cells infected with VSV-PfAMA1$_{345}$, VSV-PfRH5ΔNL and VSV-PfRON2sp 24 h post-infection. Non-infected cells were used as mock control, and VSV-GFP-infected cells were used as positive control. The bar represents 20 mm. **(B)** Images of the microscope for cytopathic effect of BSR-T7 cells infected with VSV-PyAMA1$_{343}$ and VSV-PyRON2sp 24 h post-infection. Non-infected cells as mock control, and VSV-GFP-infected cells as positive control. The bar represents 20 mm.

References

Arora, N., L, C. A., and Pannu, A. K. (2021). Towards eradication of malaria: is the WHO's RTS,S/AS01 vaccination effective enough? *Risk Manag. Healthc Pol.* 14, 1033–1039. doi: 10.2147/RMHP.S219294

Azasi, Y., Gallagher, S. K., Diouf, A., Dabbs, R. A., Jin, J., Mian, S. Y., et al. (2020). Bliss' and Loewe's additive and synergistic effects in *Plasmodium falciparum* growth inhibition by AMA1-RON2L, RH5, RIPR and CyRPA antibody combinations. *Sci. Rep.* 10:11802. doi: 10.1038/s41598-020-67877-8

Beignon, A. S., Le Grand, R., and Chapon, C. (2014). In vivo imaging in NHP models of malaria: challenges, progress and outlooks. *Parasit. Int.* 63, 206–215. doi: 10.1016/j.parint.2013.09.001

Boyle, M. J., Reiling, L., Osier, F. H., and Fowkes, F. J. (2017). Recent insights into humoral immunity targeting *Plasmodium falciparum* and *Plasmodium vivax* malaria. *Int. J. Parasitol.* 47, 99–104. doi: 10.1016/j.ijpara.2016.06.002

Buchholz, U. J., Finke, S., and Conzelmann, K. K. (1999). Generation of bovine respiratory syncytial virus (BRSV) from cDNA: BRSV NS2 is not essential for virus replication in tissue culture, and the human RSV leader region acts as a functional BRSV genome promoter. *J. Virol.* 73, 251–259. doi: 10.1128/JVI.73.1.251-259.1999

Bustamante, L. Y., Bartholdson, S. J., Crosnier, C., Campos, M. G., Wanaguru, M., Nguon, C., et al. (2013). A full-length recombinant *plasmodium falciparum* PfRH5 protein induces inhibitory antibodies that are effective across common PfRH5 genetic variants. *Vaccine* 31, 373–379. doi: 10.1016/j.vaccine.2012.10.106

Case, J. B., Rothlauf, P. W., Chen, R. E., Kafai, N. M., Fox, J. M., Smith, B. K., et al. (2020). Replication-competent vesicular stomatitis virus vaccine vector protects against SARS-CoV-2-mediated pathogenesis in mice. *Cell Host Microbe* 28, 465–474.e4. doi: 10.1016/j.chom.2020.07.018

Chatterjee, D., and Cockburn, I. A. (2021). The challenges of a circumsporozoite protein-based malaria vaccine. *Expert Rev. Vaccines* 20, 113–125. doi: 10.1080/14760584.2021.1874924

Chawla, B., Mahajan, B., Oakley, M., Majam, V. F., Belmonte, A., Sedegah, M., et al. (2019). Antibody-dependent, gamma interferon-independent sterilizing immunity induced by a subunit malaria vaccine. *Infect. Immun.* 87:e00236-19. doi: 10.1128/IAI.00236-19

Choi, M. J., Cossaboom, C. M., Whitesell, A. N., Dyal, J. W., Joyce, A., Morgan, R. L., et al. (2021). Use of Ebola vaccine: recommendations of the advisory committee on immunization practices, United States, 2020. *MMWR Recomm. Rep.* 70, 1–12. doi: 10.15585/mmwr.rr7001a1

de Graaf, H., Payne, R. O., Taylor, I., Miura, K., Long, C. A., Elias, S. C., et al. (2021). Safety and immunogenicity of ChAd63/MVA Pfs25-IMX313 in a phase I first-in-human trial. *Front. Immunol.* 12:694759. doi: 10.3389/fimmu.2021.694759

De Niz, M., and Heussler, V. T. (2018). Rodent malaria models: insights into human disease and parasite biology. *Curr. Opin. Microbiol.* 46, 93–101. doi: 10.1016/j.mib.2018.09.003

Douglas, A. D., Baldeviano, G. C., Lucas, C. M., Lugo-Roman, L. A., Crosnier, C., Bartholdson, S. J., et al. (2015). A PfRH5-based vaccine is efficacious against heterologous strain blood-stage *Plasmodium falciparum* infection in aotus monkeys. *Cell Host Microbe* 17, 130–139. doi: 10.1016/j.chom.2014.11.017

Douglas, A. D., Williams, A. R., Knuepfer, E., Illingworth, J. J., Furze, J. M., Crosnier, C., et al. (2014). Neutralization of *Plasmodium falciparum* merozoites by antibodies against PfRH5. *J. Immunol.* 192, 245–258. doi: 10.4049/jimmunol.1302045

Ewer, K. J., Sierra-Davidson, K., Salman, A. M., Illingworth, J. J., Draper, S. J., Biswas, S., et al. (2015). Progress with viral vectored malaria vaccines: a multi-stage approach involving "unnatural immunity". *Vaccine* 33, 7444–7451. doi: 10.1016/j.vaccine.2015.09.094

Fathi, A., Dahlke, C., and Addo, M. M. (2019). Recombinant vesicular stomatitis virus vector vaccines for WHO blueprint priority pathogens. *Hum. Vaccin. Immunother.* 15, 2269–2285. doi: 10.1080/21645515.2019.1649532

Frimpong, A., Kusi, K. A., Ofori, M. F., and Ndifon, W. (2018). Novel strategies for malaria vaccine design. *Front. Immunol.* 9:2769. doi: 10.3389/fimmu.2018.02769

Fuerst, T. R., Niles, E. G., Studier, F. W., and Moss, B. (1986). Eukaryotic transient-expression system based on recombinant vaccinia virus that synthesizes bacteriophage T7 RNA polymerase. *Proc. Natl. Acad. Sci. U. S. A.* 83, 8122–8126. doi: 10.1073/pnas.83.21.8122

Gbedande, K., Carpio, V. H., and Stephens, R. (2020). Using two phases of the CD4 T cell response to blood-stage murine malaria to understand regulation of systemic immunity and placental pathology in *Plasmodium falciparum* infection. *Immunol. Rev.* 293, 88–114. doi: 10.1111/imr.12835

Gonzales, S. J., Reyes, R. A., Braddom, A. E., Batugedara, G., Bol, S., and Bunnik, E. M. (2020). Naturally acquired humoral immunity against *Plasmodium falciparum* malaria. *Front. Immunol.* 11:594653. doi: 10.3389/fimmu.2020.594653

Haldar, K., Bhattacharjee, S., and Safeukui, I. (2018). Drug resistance in *Plasmodium*. *Nat. Rev. Microbiol.* 16, 156–170. doi: 10.1038/nrmicro.2017.161

Hodgson, S. H., Ewer, K. J., Bliss, C. M., Edwards, N. J., Rampling, T., Anagnostou, N. A., et al. (2015). Evaluation of the efficacy of ChAd63-MVA vectored vaccines expressing circumsporozoite protein and ME-TRAP against controlled human malaria infection in malaria-naive individuals. *J. Infect. Dis.* 211, 1076–1086. doi: 10.1093/infdis/jiu579

Hojo-Souza, N. S., de Azevedo, P. O., de Castro, J. T., Teixeira-Carvalho, A., Lieberman, J., Junqueira, C., et al. (2020). Contributions of IFN-gamma and granulysin to the clearance of *Plasmodium yoelii* blood stage. *PLoS Pathog.* 16:e1008840. doi: 10.1371/journal.ppat.1008840

Humphreys, I. R., and Sebastian, S. (2018). Novel viral vectors in infectious diseases. *Immunology* 153, 1–9. doi: 10.1111/imm.12829

Jones, S. M., Stroher, U., Fernando, L., Qiu, X., Alimonti, J., Melito, P., et al. (2007). Assessment of a vesicular stomatitis virus-based vaccine by use of the mouse model of Ebola virus hemorrhagic fever. *J. Infect. Dis.* 196, S404–S412. doi: 10.1086/520591

Junqueira, C., Barbosa, C. R. R., Costa, P. A. C., Teixeira-Carvalho, A., Castro, G., Sen Santara, S., et al. (2018). Cytotoxic CD8(+) T cells recognize and kill *Plasmodium* vivax-infected reticulocytes. *Nat. Med.* 24, 1330–1336. doi: 10.1038/s41591-018-0117-4

Kaminski, L. C., Riehn, M., Abel, A., Steeg, C., Yar, D. D., Addai-Mensah, O., et al. (2019). Cytotoxic T cell-derived Granzyme B is increased in severe *plasmodium falciparum* malaria. *Front. Immunol.* 10:2917. doi: 10.3389/fimmu.2019.02917

Kim, Y. C., Dema, B., Rodriguez-Garcia, R., Lopez-Camacho, C., Leoratti, F. M. S., Lall, A., et al. (2020). Evaluation of chimpanzee adenovirus and MVA expressing TRAP and CSP from plasmodium cynomolgi to prevent malaria relapse in nonhuman primates. *Vaccines* 8:363. doi: 10.3390/vaccines8030363

Kimani, D., Jagne, Y. J., Cox, M., Kimani, E., Bliss, C. M., Gitau, E., et al. (2014). Translating the immunogenicity of prime-boost immunization with ChAd63 and MVA ME-TRAP from malaria naive to malaria-endemic populations. *Mol. Ther.* 22, 1992–2003. doi: 10.1038/mt.2014.109

Kimura, D., Miyakoda, M., Honma, K., Shibata, Y., Yuda, M., Chinzei, Y., et al. (2010). Production of IFN-gamma by CD4(+) T cells in response to malaria antigens is IL-2 dependent. *Int. Immunol.* 22, 941–952. doi: 10.1093/intimm/dxq448

Krzych, U., Zarling, S., and Pichugin, A. (2014). Memory T cells maintain protracted protection against malaria. *Immunol. Lett.* 161, 189–195. doi: 10.1016/j.imlet.2014.03.011

Kurup, S. P., Butler, N. S., and Harty, J. T. (2019). T cell-mediated immunity to malaria. *Nat. Rev. Immunol.* 19, 457–471. doi: 10.1038/s41577-019-0158-z

Lalitha, P. V., Ware, L. A., Barbosa, A., Dutta, S., Moch, J. K., Haynes, J. D., et al. (2004). Production of the subdomains of the *Plasmodium falciparum* apical membrane antigen 1 ectodomain and analysis of the immune response. *Infect. Immun.* 72, 4464–4470. doi: 10.1128/IAI.72.8.4464-4470.2004

Laurens, M. B. (2018). The promise of a malaria vaccine-are we closer? *Annu. Rev. Microbiol.* 72, 273–292. doi: 10.1146/annurev-micro-090817-062427

Laurens, M. B. (2020). RTS,S/AS01 vaccine (Mosquirix): an overview. *Hum. Vaccin. Immunother.* 16, 480–489. doi: 10.1080/21645515.2019.1669415

Lawson, N. D., Stillman, E. A., Whitt, M. A., and Rose, J. K. (1995). Recombinant vesicular stomatitis viruses from DNA. *Proc. Natl. Acad. Sci. U. S. A.* 92, 4477–4481. doi: 10.1073/pnas.92.10.4477

Lee, S. H., Chu, K. B., Kang, H. J., Basak, S., Kim, M. J., Park, H., et al. (2020). Virus-like particles expressing *Plasmodium berghei* MSP-8 induce protection against *P. berghei* infection. *Parasite Immunol.* 42:e12781. doi: 10.1111/pim.12781

Li, S., Locke, E., Bruder, J., Clarke, D., Doolan, D. L., Havenga, M. J., et al. (2007). Viral vectors for malaria vaccine development. *Vaccine* 25, 2567–2574. doi: 10.1016/j.vaccine.2006.07.035

Lu, J., Chu, R., Yin, Y., Yu, H., Xu, Q., Yang, B., et al. (2022). Glycosylphosphatidylinositol-anchored micronemal antigen (GAMA) interacts with the band 3 receptor to promote erythrocyte invasion by malaria parasites. *J. Biol. Chem.* 298:101765. doi: 10.1016/j.jbc.2022.101765

Marzi, A., Menicucci, A. R., Engelmann, F., Callison, J., Horne, E. J., Feldmann, F., et al. (2018). Protection against Marburg virus using a recombinant VSV-vaccine depends on T and B cell activation. *Front. Immunol.* 9:3071. doi: 10.3389/fimmu.2018.03071

Minetti, C., Ingham, V. A., and Ranson, H. (2020). Effects of insecticide resistance and exposure on *Plasmodium* development in *Anopheles* mosquitoes. *Curr. Opin. Insect Sci.* 39, 42–49. doi: 10.1016/j.cois.2019.12.001

Moncunill, G., De Rosa, S. C., Ayestaran, A., Nhabomba, A. J., Mpina, M., Cohen, K. W., et al. (2017). RTS,S/AS01E malaria vaccine induces memory and polyfunctional T cell responses in a pediatric African phase III trial. *Front. Immunol.* 8:1008. doi: 10.3389/fimmu.2017.01008

Moore, A. J., Mangou, K., Diallo, F., Sene, S. D., Pouye, M. N., Sadio, B. D., et al. (2021). Assessing the functional impact of PfRh5 genetic diversity on ex vivo erythrocyte invasion inhibition. *Sci. Rep.* 11:2225. doi: 10.1038/s41598-021-81711-9

Neafsey, D. E., Juraska, M., Bedford, T., Benkeser, D., Valim, C., Griggs, A., et al. (2015). Genetic diversity and protective efficacy of the RTS,S/AS01 malaria vaccine. *N. Engl. J. Med.* 373, 2025–2037. doi: 10.1056/NEJMoa1505819

Neafsey, D. E., Taylor, A. R., and MacInnis, B. L. (2021). Advances and opportunities in malaria population genomics. *Nat. Rev. Genet.* 22, 502–517. doi: 10.1038/s41576-021-00349-5

Olotu, A., Fegan, G., Wambua, J., Nyangweso, G., Leach, A., Lievens, M., et al. (2016). Seven-year efficacy of RTS,S/AS01 malaria vaccine among young African children. *N. Engl. J. Med.* 374, 2519–2529. doi: 10.1056/NEJMoa1515257

Patarroyo, M. A., Molina-Franky, J., Gomez, M., Arevalo-Pinzon, G., and Patarroyo, M. E. (2020). Hotspots in *Plasmodium* and RBC receptor-ligand interactions: key pieces for inhibiting malarial parasite invasion. *Int. J. Mol. Sci.* 21:4729. doi: 10.3390/ijms21134729

Payne, R. O., Silk, S. E., Elias, S. C., Miura, K., Diouf, A., Galaway, F., et al. (2017). Human vaccination against RH5 induces neutralizing antimalarial antibodies that inhibit RH5 invasion complex interactions. *JCI Insight* 2:e96381. doi: 10.1172/jci.insight.96381

Poetsch, J. H., Dahlke, C., Zinser, M. E., Kasonta, R., Lunemann, S., Rechtien, A., et al. (2019). Detectable vesicular stomatitis virus (VSV)-specific humoral and cellular immune responses following VSV-Ebola virus vaccination in humans. *J. Infect. Dis.* 219, 556–561. doi: 10.1093/infdis/jiy565

Publicover, J., Ramsburg, E., and Rose, J. K. (2004). Characterization of nonpathogenic, live, viral vaccine vectors inducing potent cellular immune responses. *J. Virol.* 78, 9317–9324. doi: 10.1128/JVI.78.17.9317-9324.2004

Ragotte, R. J., Higgins, M. K., and Draper, S. J. (2020). The RH5-CyRPA-Ripr complex as a malaria vaccine target. *Trends Parasitol.* 36, 545–559. doi: 10.1016/j.pt.2020.04.003

Salinas, N. D., Tang, W. K., and Tolia, N. H. (2019). Blood-stage malaria parasite antigens: structure, function, and vaccine potential. *J. Mol. Biol.* 431, 4259–4280. doi: 10.1016/j.jmb.2019.05.018

Sasso, E., D'Alise, A. M., Zambrano, N., Scarselli, E., Folgori, A., and Nicosia, A. (2020). New viral vectors for infectious diseases and cancer. *Semin. Immunol.* 50:101430. doi: 10.1016/j.smim.2020.101430

Shahnaij, M., Iyori, M., Mizukami, H., Kajino, M., Yamagoshi, I., Syafira, I., et al. (2021). Liver-directed AAV8 booster vaccine expressing *Plasmodium falciparum* antigen following adenovirus vaccine priming elicits sterile protection in a murine model. *Front. Immunol.* 12:612910. doi: 10.3389/fimmu.2021.612910

Srinivasan, P., Baldeviano, G. C., Miura, K., Diouf, A., Ventocilla, J. A., Leiva, K. P., et al. (2017). A malaria vaccine protects Aotus monkeys against virulent *Plasmodium falciparum* infection. *NPJ Vacc.* 2:14. doi: 10.1038/s41541-017-0015-7

Srinivasan, P., Beatty, W. L., Diouf, A., Herrera, R., Ambroggio, X., Moch, J. K., et al. (2011). Binding of *Plasmodium* merozoite proteins RON2 and AMA1 triggers commitment to invasion. *Proc. Natl. Acad. Sci. U. S. A.* 108, 13275–13280. doi: 10.1073/pnas.1110303108

Srinivasan, P., Ekanem, E., Diouf, A., Tonkin, M. L., Miura, K., Boulanger, M. J., et al. (2014). Immunization with a functional protein complex required for erythrocyte invasion protects against lethal malaria. *Proc. Natl. Acad. Sci. U. S. A.* 111, 10311–10316. doi: 10.1073/pnas.1409928111

Stanisic, D. I., and McCall, M. B. B. (2021). Correlates of malaria vaccine efficacy. *Expert Rev. Vaccines* 20, 143–161. doi: 10.1080/14760584.2021.1882309

Tan, J., Cho, H., Pholcharee, T., Pereira, L. S., Doumbo, S., Doumtabe, D., et al. (2021). Functional human IgA targets a conserved site on malaria sporozoites. *Sci. Transl. Med.* 13:eabg2344. doi: 10.1126/scitranslmed.abg2344

Tinto, H., Otieno, W., Gesase, S., Sorgho, H., Otieno, L., Liheluka, E., et al. (2019). Long-term incidence of severe malaria following RTS,S/AS01 vaccination in children and infants in Africa: an open-label 3-year extension study of a phase 3 randomised controlled trial. *Lancet Infect. Dis.* 19, 821–832. doi: 10.1016/S1473-3099(19)30300-7

Tiono, A. B., Nebie, I., Anagnostou, N., Coulibaly, A. S., Bowyer, G., Lam, E., et al. (2018). First field efficacy trial of the ChAd63 MVA ME-TRAP vectored malaria vaccine candidate in 5-17 months old infants and children. *PLoS One* 13:e0208328. doi: 10.1371/journal.pone.0208328

Tyler, J. S., Treeck, M., and Boothroyd, J. C. (2011). Focus on the ringleader: the role of AMA1 in apicomplexan invasion and replication. *Trends Parasitol.* 27, 410–420. doi: 10.1016/j.pt.2011.04.002

WHO (2021). *World Malaria Report*. World Health Organization. Available at: https://www.who.int/teams/global-malaria-programme/reports/world-malaria-report-2021 (Accessed November 13, 2022).

Wright, K. E., Hjerrild, K. A., Bartlett, J., Douglas, A. D., Jin, J., Brown, R. E., et al. (2014). Structure of malaria invasion protein RH5 with erythrocyte basigin and blocking antibodies. *Nature* 515, 427–430. doi: 10.1038/nature13715

Wu, F., Fan, X., Yue, Y., Xiong, S., and Dong, C. (2014). A vesicular stomatitis virus-based mucosal vaccine promotes dendritic cell maturation and elicits preferable immune response against coxsackievirus B3 induced viral myocarditis. *Vaccine* 32, 3917–3926. doi: 10.1016/j.vaccine.2014.05.052

Yahalom-Ronen, Y., Tamir, H., Melamed, S., Politi, B., Shifman, O., Achdout, H., et al. (2020). A single dose of recombinant VSV-G-spike vaccine provides protection against SARS-CoV-2 challenge. *Nat. Commun.* 11:6402. doi: 10.1038/s41467-020-20228-7

Yusuf, Y., Yoshii, T., Iyori, M., Mizukami, H., Fukumoto, S., Yamamoto, D. S., et al. (2019). A viral-vectored multi-stage malaria vaccine regimen with protective and transmission-blocking efficacies. *Front. Immunol.* 10:2412. doi: 10.3389/fimmu.2019.02412

frontiers | Frontiers in Microbiology

A metabotropic glutamate receptor affects the growth and development of *Schistosoma japonicum*

Xiaoling Wang[1†], Shaoyun Cheng[2†], Xiangyu Chen[2],
Wei Zhang[2], Yuxiang Xie[2], Wanling Liu[3], Yanmin You[2],
Cun Yi[2], Bingkuan Zhu[2], Mengjie Gu[2], Bin Xu[1], Yan Lu[2],
Jipeng Wang[2] and Wei Hu[1,2,3,4]*

[1]National Institute of Parasitic Diseases, Chinese Center for Disease Control and Prevention
(Chinese Center for Tropical Diseases Research), NHC Key Laboratory of Parasite and Vector
Biology, WHO Collaborating Center for Tropical Diseases, National Center for International
Research on Tropical Diseases, Shanghai, China, [2]State Key Laboratory of Genetic Engineering,
Ministry of Education Key Laboratory of Contemporary Anthropology, Department of Microbiology
and Microbial Engineering, School of Life Sciences, Fudan University, Shanghai, China, [3]Department
of Infectious Diseases, Huashan Hospital, Fudan University, Shanghai, China, [4]College of Life
Sciences, Inner Mongolia University, Hohhot, China

Schistosomiasis is a zoonotic parasitic disease caused by schistosome
infection that severely threatens human health. Therapy relies mainly on
single drug treatment with praziquantel. Therefore, there is an urgent need to
develop alternative medicines. The glutamate neurotransmitter in helminths
is involved in many physiological functions by interacting with various cell-
surface receptors. However, the roles and detailed regulatory mechanisms of
the metabotropic glutamate receptor (mGluR) in the growth and development
of *Schistosoma japonicum* remain poorly understood. In this study, we
identified two putative mGluRs in *S. japonicum* and named them *Sj*GRM7
(Sjc_001309, similar to GRM7) and *Sj*GRM (Sjc_001163, similar to mGluR).
Further validation using a calcium mobilization assay showed that *Sj*GRM7
and *Sj*GRM are glutamate-specific. The results of *in situ* hybridization showed
that *Sj*GRM is mainly located in the nerves of both males and gonads
of females, and *Sj*GRM7 is principally found in the nerves and gonads of
males and females. In a RNA interference experiment, the results showed
that *Sj*GRM7 knockdown by double-stranded RNA (dsRNA) in *S. japonicum*
caused edema, chassis detachment, and separation of paired worms *in vitro*.
Furthermore, dsRNA interference of *Sj*GRM7 could significantly affect the
development and egg production of male and female worms *in vivo* and
alleviate the host liver granulomas and fibrosis. Finally, we examined the
molecular mechanisms underlying the regulatory function of mGluR using
RNA sequencing. The data suggest that *Sj*GRM7 propagates its signals through
the G protein-coupled receptor signaling pathway to promote nervous system
development in *S. japonicum*. In conclusion, *Sj*GRM7 is a potential target for

anti-schistosomiasis. This study enables future research on the mechanisms of action of *Schistosomiasis japonica* drugs.

Introduction

Schistosomiasis is a zoonotic parasitic disease affecting approximately 290 million people worldwide (Afshin et al., 2019). Schistosomiasis mainly affects humans via *Schistosoma mansoni*, *Schistosoma haematobium*, and *Schistosoma japonicum*. *S japonicum* is localized to Asia, primarily the Philippines and China (Colley et al., 2014). These parasites require two hosts to complete their life cycle, including freshwater snails (intermediate host) for asexual reproduction and mammals (final host) for sexual reproduction (Talla et al., 1990).

Currently, praziquantel is the optimal drug to treat schistosomiasis (Zdesenko and Mutapi, 2020). There is an urgent need to develop new therapeutic agents because of the risk of drug resistance due to long-term single-agent use. The nervous system of schistosomes controls neuromuscular signaling related to movement, host attachment and migration, as well as sensory neurons located at the surface that may be involved in host–parasite interactions. If the neuronal connection is interrupted, parasites may be eliminated from the hosts. Therefore, the nervous system of *Schistosoma* is a promising target for therapeutic drug development.

L-Glutamate is a major neurotransmitter in both vertebrates and invertebrates. Glutamate neuronal signaling has been detected in *Caenorhabditis elegans* (Bono and Villu Maricq, 2005), *Fasciola hepatica* (Brownlee and Fairweather, 1996), *Hymenolepis diminuta* (Webb and Eklove, 1989), and *S. mansoni* (Taman and Ribeiro, 2011) and can interact with various cell surface receptors for signal transduction, including ionotropic gated channels and metabotropic glutamate receptors (mGluRs, also known as GRMs). mGluRs are structurally related to γ-aminobutyric acid B receptor (GABABR), calcineurin, and other receptors in the G protein-coupled receptor (GPCR) family (Pin et al., 2003). GPCRs are the largest family of membrane proteins for cellular communication in living organisms. These receptors can detect signal molecules in the extracellular environment, such as ions, hormones, light, neurotransmitters, amino acids, and peptides, and then trigger a series of intracellular signal transduction pathways to generate the corresponding physiological effects (Weis and Kobilka, 2018). Based on sequence homology and similarity, GPCRs are classified into four prominent families: class A (rhodopsin-like), class B (secretin-like), class C (metabotropic glutamate receptor-like), class F (frizzled/smoothened like), and others. Classes A, B, and C are the main receptor families (Bockaert et al., 2002). C-family GPCRs have a unique modular structure consisting of an N-terminal extracellular domain (ECD), a C-terminal intracellular domain, and a 7-Transmembrane (7-TM) fragment. The ECD carries a conserved Venus Flytrap module (VFT) containing a glutamate-binding site and is linked to the 7-TM region by a short cysteine-rich linker (Ferraguti and Shigemoto, 2006; Niswender and Conn, 2010). They are divided into three categories according to their sequence similarity, pharmacological properties, and signal transduction mechanisms (Pin et al., 2003). Gq/11 protein coupling and signaling by the intracellular calcium and inositol phospholipid pathway changes in group I (mGluR1 and mGluR5). The group II (mGluR2 and mGluR3) and group III (mGluR4, mGluR6, mGluR7, and mGluR8) classes bind to Gi/o proteins primarily via inhibition of adenosine acid cyclase, which in turn reduces intracellular cAMP signaling (Pin et al., 2003).

In this study, we first obtained two mGluRs in *S. japonicum* using bioinformatics and then investigated their functions *in vitro* and *in vivo*. The results showed that *Sj*GRM7 is extremely important for the normal physiological activity, growth, development, and egg production of *S. japonicum*. Finally, we used RNA sequencing (RNA-seq) to preliminarily explore the regulatory role of *Sj*GRM7 on downstream signaling pathways, prompting further drug development research to treat *S. japonicum*.

Materials and methods

Sequence analysis

Identification, phylogenetic analysis, and multiple sequence alignment of *Schistosoma japonicum* metabotropic glutamate receptors

Schistosoma japonicum mGluRs were identified by combining a hidden Markov model (HMM) and a protein basic local alignment search tool (blastp). The reviewed mGluRs from UniProt were used to generate HMM models, which were subsequently used for HMM searches of *S. japonicum* protein

sequences. Blastp was also incorporated using *S. mansoni* mGluRs against the *S. japonicum* protein sequences. These two results were combined, followed by a TM domain prediction. Proteins with more than three TM domains were considered mGluRs, including *Sjc_0001163* and *Sjc_0001309*.

A phylogenetic tree of mGluR was constructed using the maximum-likelihood approach. Sequences of *S. mansoni* and non-flatworm species were obtained from Tulio et al. (2014) and Ramos-Vicente et al. (2018). Sequences from *Schmidtea mediterranea* were obtained using Blastp (Grohme et al., 2018). MUSCLE in MEGAX was used for the alignment. Maximum likelihood analysis was conducted using RAxML with the WAG + I + G + F and 1,000 iterations of ultrafast bootstrapping. The tree was illustrated using the iTOL software.

Representative sequences in the phylogenetic tree were chosen for multiple alignments of the mGluR residues involved in ligand binding. The residue numbers at the top of the graph correspond to the human mGluR1. The figure was prepared using JalView v2.10.4b1.

Protein structure and binding pocket prediction

The structures of the two mGluRs in *S. japonicum* were determined using the ColabFold software. The position of the ligand (Protein Data Bank entries: GLU) was predicted using Dock Prep and AutoDock Vina. The *Homo sapiens* mGluR2 (Protein Data Bank identifier: 7MTR) was exhibited with Chimera.

Cell culture, transfection, and calcium mobilization assay

To improve the expression of the two mGluRs in *S. japonicum* within mammalian cells, the Kozak GCC ACC sequence was added before the start codon of the forward primer. PCR amplified the full length of the modified *Sj*GRM and *Sj*GRM7, and the amplified cDNA was cloned into the prK5 expression vector. The restriction endonuclease site of prK5 was located between *Mlu*I and *Sal*I, and the constructed plasmid was verified by DNA sequencing. Human embryonic kidney 293T cells (HEK293T) were transfected with two mGluRs and a heterotrimeric G-protein, Gα16, using Lipofectamine 2000 (Invitrogen), and incubated at 37°C with 5% CO_2 for 24 h. Subsequently, the medium was discarded and 1 mM Fluo-4 AM fluorescent dye (Invitrogen) was added and incubated for 1 h (Caers et al., 2014). Next, different concentrations of L-glutamate, L-aspartate, glycine, GABA, and glutamine (glutamate derivative) (Sangon Bioengineering Co., Ltd., Shanghai, China) were added. A FlexStation instrument was used to excite the dye using a 485 nm laser. The fluorescence was recorded at 525 nm to detect the calcium mobilization

signal in living cells and determine the immediate response after stimulation.

Experimental animals and *Schistosoma japonicum*

Female Kunming mice of specific pathogen-free (SPF) grade, 6 weeks old, and weighing 18 ± 2 g, were purchased from Slack Laboratory Animal Co., Ltd. (Shanghai, China) and raised in the SPF animal room of the Institute of Parasitic Diseases, Chinese Center for Disease Control and Prevention. Cercariae of *S. japonicum* (mainland China strain) were provided by the vector room of the Institute of Parasitic Diseases, Chinese Center for Disease Control and Prevention.

Preparation and collection of *Schistosoma japonicum* at different developmental stages

Eight Kunming mice were randomly divided into two groups, the *Sj*GRM7 double-stranded RNA (dsRNA) group and the GFP control group. Each mouse was infected with 200 ± 10 cercariae via abdominal skin. Kunming mice were euthanized and dissected at 14, 16, 18, 20, 22, 24, 26, 28, and 30 days post infection (dpi). The worms were harvested, and the male and female worms were separated with a soft brush after washing with liquid nitrogen and stored in a −80°C freezer (Wang et al., 2017). *S. japonicum* at 26 to 30 dpi were killed with 0.6 M magnesium chloride, followed by 4% paraformaldehyde (PFA) in phosphate buffered saline with 0.3% Tween20 (PBSTx), incubated for 4 h at room temperature (RT), sequentially dehydrated in 50% methanol in PBSTx, and finally stored at −20°C.

In situ hybridization

Before hybridization, the 10X DIG RNA Labeling Kit (Roche, Germany) was used to synthesize digoxigenin-labeled RNA probes. Primer sequences used are listed in **Supplementary Table 6**. The worms were removed from −20°C and rehydrated in 50% methanol and PBSTx for 5 min, and a bleaching solution was added for 1 h (Cogswell et al., 2011). Worms were rinsed with PBSTx for 5 min, and 5 µg/ml proteinase K (Invitrogen) was added to PBSTx for 45 min and fixed with 4% PFA in PBSTx for 10 min at RT. The worms were then placed in a prehybe solution (50% deionized formamide, 5× SSC, 1 mg/ml torula yeast RNA, 1% Tween20) at 52°C for 2 h. Hybridization was carried out for 16 h at 52°C in the hybe solution [10% dextran sulfate (Sangon) in prehybe solution] and

riboprobe (200 ng/ml; Sigma). The hybe solution was removed and washed in wash hybe, 2xSSC, and 0.2xSSC for 30 min (2 times) at 52°C and washed with 0.1 M Tris pH 7.5, 0.15 M NaCl, 0.1% Tween-20 (TNT) for 10 min at RT. Then, fluorescence *in situ* hybridization (FISH) block solution (5% horse serum, 0.5% Roche Western Blocking Reagent in TNT) was added for 2 h at RT, and anti-DIG-POD (1:1000) was replaced in the FISH block solution, and the solution was incubated overnight at 4°C. The reaction was washed for 5, 10, and 20 min six times with TNT. The cells were incubated in a tyramide solution for 10 min and washed for 5 min with TNT, and incubated with 1 μg/ml 4′,6-diamidino-2-phenylindole (DAPI) 4 h at RT. The cells were observed in 80% glycerol in PBS and imaged using a Nikon A1 upright laser scanning confocal microscope.

Synthesis of double-stranded RNA

Primers were designed, and the primer sequences are listed in **Supplementary Table 6**. Polymerase chain reaction (PCR) was then performed. DNA sequencing confirmed that the product was extracted and recovered from agarose gels and its identity was confirmed by Tsingke Biotechnology Co., Ltd. The recovered product was prepared and purified using a MEGAscript TM T7 High Yield Transcription Kit (Thermo). The size and integrity of the dsRNA were verified using 1% agarose gel electrophoresis. Finally, the correctly synthesized dsRNA was aliquoted and stored at −80°C.

Quantitative polymerase chain reaction

TRIzol reagent (Takara, Japan) was used to extract total RNA from *S. japonicum* and mouse livers, and reverse transcription was performed using a cDNA reverse transcription kit (Takara, Japan). The cDNA was used as a template for quantitative polymerase chain reaction (qPCR) with the SYBR Green Fast qPCR Master Mix (Takara, Japan) and 0.2 μM forward and reverse primers. The amplification conditions were 94°C for 5 min, followed by 38 cycles of 94°C for 30 s, 55°C for 30 s, 72°C for 50 s, and 72°C for 10 min. Primer sequences are listed in **Supplementary Table 6**. *S. japonicum* qPCR data were normalized relative to the endogenous gene 26S proteasome non-ATPase (PSMD), which served as an internal control. Gene expression was calculated using the $1000 \times 2^{-\triangle CT}$ method, as described previously (Li et al., 2018). The relative expression of α-smooth muscle actin (SMA), collagen I, and collagen 3 in the mouse liver was calculated using the $1000 \times 2^{-\triangle \triangle Ct}$ method and glyceraldehyde-3-phosphate dehydrogenase (GAPDH) as an endogenous control to normalize mRNA levels (Hu et al., 2020).

RNA interference of *Schistosoma japonicum in vitro* and sample collection

Adult paired *S. japonicum* (30 dpi) were obtained and cultured in Dulbecco's modified Eagle medium (DMEM; Gibco) containing 10% fetal bovine serum (FBS; Gibco). dsRNA was added on days 1, 3, and 5 of the *in vitro* culture and the phenotype of the worms was observed on day 7. After sample collection, the corresponding gene changes were evaluated from different samples using qPCR, and RNA-seq was performed to explore the downstream signaling pathways. Three independent biological replicates were used in this experiment. Each group consisted of three replicate wells for each biological experiment, with six pairs of adult worms in each replicate well and six worms for qPCR as well as RNA-seq.

RNA interference of *Schistosoma japonicum in vivo* and sample collection

Each mouse was infected with 60 cercariae via abdominal skin penetration and randomly divided into two groups, with four mice per group. *Sj*GRM7 and green fluorescent protein (GFP) dsRNA were injected into the tail vein for interference at 1, 6, 10, 14, 18, 22, and 26 dpi, and the influence of *S. japonicum* on the growth and development of the mice was observed by harvesting worms at 30 dpi (Li et al., 2018). For the egg-laying model, eight mice were randomly divided into two groups, the *Sj*GRM7 dsRNA group and the GFP control group, 40 cercariae were used per mouse. Ten micrograms of dsRNA were injected into the tail vein at 26, 30, 34, and 38 dpi to achieve long-term continuous interference with *Sj*GRM7. Mice were euthanized at 42 days and the liver was collected to detect changes in the number of hepatic eggs and the liver pathology observed (see the section "Histological evaluation"). Finally, five male and five female *S. japonicum* individuals were separated. A small lobe of the liver was washed with diethyl pyrocarbonate (DEPC)/PBS and placed in liquid nitrogen for quick freezing for mRNA quantification. The remaining worms were fixed in 95% alcohol, 3% formaldehyde, and 2% glacial acetic acid (AFA).

RNA sequencing data

Total RNA extraction, library construction, and RNA-seq were conducted by the Novagene Technology Corporation (Beijing, China). RNA was extracted from the worms using a modified phenol-chloroform method and column purification. The integrity and quality of the total RNA were examined using a Nanodrop ND-2000 spectrophotometer (Thermo, United States) and an Agilent 2100 Bioanalyzer (Agilent,

United States). Pooled RNA was used to construct a library using an Illumina TruSeq RNA Sample Prep Kit (Illumina, San Diego, CA, United States) with a Ribo-Zero Magnetic Kit for RNA depletion, according to the TruSeq RNA Sample Preparation Guide. This library was subsequently sequenced on the Illumina Nova 6000 platform to obtain 150 bp paired-end (PE) reads. The sequencing data were deposited in the NCBI Sequence Read Archive (SRA) database under accession numbers (PRJNA880502).

Quality control (QC) of raw sequencing data was performed using the FASTQC program (Andrews, 2013). Low-quality reads and adapter sequences were trimmed using FASTP v.0.20.1. (Parameters: -q 15 -u 40 -n 5 -l 15) (Chen et al., 2018). The clean reads were mapped to the chromosome-level *S. japonicum* reference genome (*Sj*V3) using HISAT2 v2.1.0 (Kim et al., 2019) with default parameters. Gene-level assignments were then performed to estimate transcript abundance using featureCounts 1.6.4 (Liao et al., 2013). Principal component analysis (PCA) was performed using the prcomp function in the stats (v3.6.0) R package. Hierarchical clustering analysis (HCA) was performed using Pheatmap[1]. The R package DEseq2 v1.26.0 (Love et al., 2014) was used to perform differential expression analysis. Gene Ontology (GO) enrichment analysis was performed using the R package clusterProfiler (Yu et al., 2012). The *p*-values were corrected for multiple hypothesis testing using the Benjamini–Hochberg false discovery rate procedure (adjusted *p*-value).

Observation of the effect on the growth and development of *Schistosoma japonicum* after dsRNA interference *in vivo*

The AFA-fixed body was photographed under a microscope and its length was measured using ImageJ[2]. We measured worm length using all schistosomes from each mouse, excluding the six utilized for qPCR. AFA absorption, followed by the addition of deionized water, glacial acetic acid, 35% ethanol, 50% ethanol, and 70% ethanol for decolorization, was carried out for carmine staining and liquid separation. Separation liquid was discarded for 35%, 50%, and 70% ethanol dehydration. Finally, hydrochloric acid and alcohol were added for decolorization. After decolorization, the insects were dehydrated with 85%, 95%, and 100% ethanol, sealed with gum, dried, and placed under a Nikon orthotopic microscope and confocal laser microscope to observe gonadal changes.

---

1 https://cran.r-project.org/web/packages/pheatmap/index.html

2 https://imagej.nih.gov/ij/

Histological evaluation

Fresh liver tissue was fixed overnight in 4% paraformaldehyde. After dehydration, the tissues were paraffin-embedded into 4 mm sections and subjected to hematoxylin, eosin (HE), and Masson staining (Hu et al., 2020). The formerly observed changes in the formation of egg granulomas and the last observed changes in the deposition of collagen fibers were documented, in which collagen fibers were stained blue and the background was stained red. The areas featuring granulomas and fibrosis surrounding single eggs and glance were observed at 200× and 20× magnification.

Statistical analysis

The data analysis performed was in the form of means ± standard deviation (SD). All results were analyzed and statistically plotted using GraphPad Prism 9.0 software. An independent sample Student's *t-test* was used to assess differences between the two groups, and a $p < 0.05$ was considered to indicate statistical significance.

Results

Schistosoma japonicum encodes two metabotropic glutamate receptors, one of which is non-canonical

In this section, we validated the existence of two mGluRs in *S. japonicum* (**Figure 1**, top workflow). We identified two mGluRs, Sjc_0001309 (similar to GRM7, named *Sj*GRM7) and Sjc_0001163 (similar to mGluR, named *Sj*GRM), by combining Blastp and HMM models, and those with fewer than three TM structural domains were filtered out. A phylogenetic study was performed next. The Bayesian and ML trees were in agreement that *Sj*GRM belongs to class II GRM and that *Sj*GRM7 is in a distinct position close to the GABA B family (**Figure 1B**). Except for SMESG000022915001, the homolog of *Sj*GRM7 in *Schmidtea mediterranea*, which is a Class IV GRM, the homologs in *S. mansoni* and *Schmidtea mediterranea* are in the same phylogenetic position.

The glutamate binding of GRM requires the binding of α-carboxy, α-amino, and γ-carboxyl groups. This is achieved using seven conserved amino acid residues, as shown in **Figure 1C**. The function of mGluR is severely damaged if any one of the seven residues mutates. According to the multiple sequence alignment (**Figure 1C**), *Sj*GRM contains all the conserved amino acids involved in ligand binding. However, *Sj*GRM7 contains only a conserved serine (160 in *Sj*GRM7), which is responsible for binding the α-carboxy group of glutamate (**Figures 1C,D**). None of the other conserved
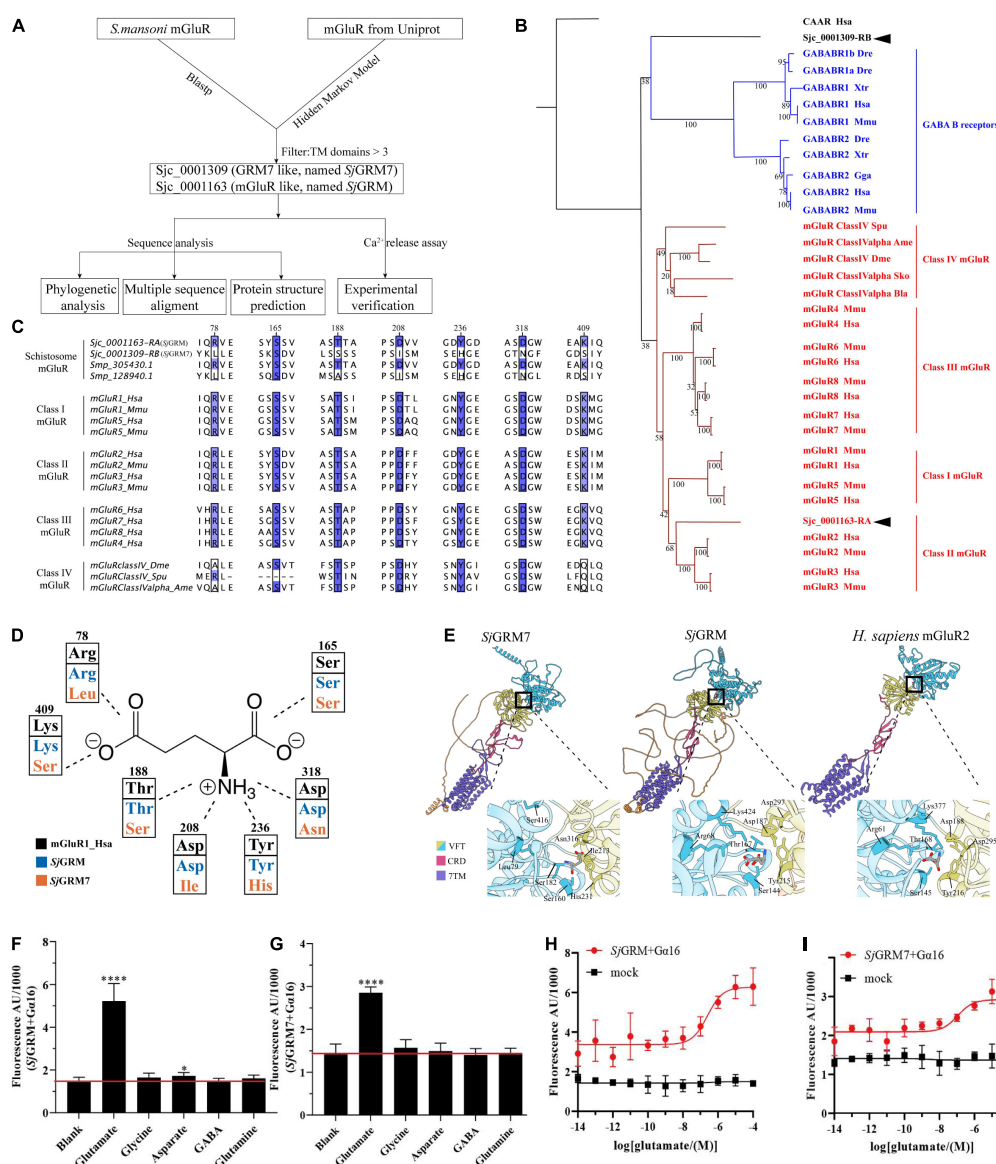
FIGURE 1

Bioinformatic analysis reveals *Sj*GRM7 as a schistosome-specific mGluR. **(A)** A schematic for bioinformatics and functional analysis of *S. japonicum* mGluR. **(B)** mGluR maximum-likelihood tree. mGluRs and GABAB receptors (GABABR) are indicated by the branches and text colors. The text on the right shows further classification. Two *S. japonicum* mGluRs are highlighted in black. The species used in this analysis are implicated using a three-letter species code, except for *S. japonicum* (Sjc), *S. mansoni* (Smp), and *Schmidtea mediterranea* (SMESG). Phylogenetic reconstruction was performed using the maximum-likelihood method with the WAG + I + G + F model and an ultrafast bootstrap of 1,000 iterations. Bootstrap values are shown at the tree nodes, and protein names are shown at the end of each branch. The human calcium-sensing receptor was used as an outgroup. The scale bar denotes the number of amino acid substitutions per site. **(C)** Multiple protein alignments of mGluR ligand-binding residues. Representative sequences were chosen for each class with labels on the left. Key residues are colored according to percentage identity. The residue numbers indicated at the top correspond to those in human mGluR1. **(D)** Schematic depiction of mGluR's key residues involved in ligand binding. Human mGluR key residues and those of *S. japonicum* are shown for comparison. As shown in panel **(C)**, the residue and its number corresponded to multiple protein alignments. Residues are colored based on proteins, as shown in the legend. The dashed line indicates the part of the glutamate the residue that interacts with other residues. **(E)** Protein structure comparisons between the predicted two mGluRs of *S. japonicum* structures and human mGluRII crystal structures. Different classes corresponded to other protein domains, as shown in the legend. Orange structures are intra-cellular regions, but most have low confidence (pLDDT < 50). Dashed lines in human mGluR2 denote disordered fragments. The binding pockets are shown by black boxes and are zoomed at the bottom right of each structure. Key residues involved in ligand binding are depicted in close-up views using the residue number and three-letter code. **(F)** *Sj*GRM-expressing HEK293 cells were treated with various amino acid transmitters (L-glutamate, glutamine, GABA, glycine, and aspartate) at 10^{-4} M or vehicle (blank). **(G)** *Sj*GRM7-expressing HEK293 cells were treated with various amino acid transmitters (L-glutamate, glutamine, GABA, glycine, and aspartate) at 10^{-4} M or vehicle (blank). **(H)** *Sj*GRM-expressing HEK293 cells were treated with different concentrations of L-glutamate, and the vector (blank) was plotted in a dose-dependent manner. **(I)** *Sj*GRM7-expressing HEK293 cells were treated with different concentrations of L-glutamate, and the vector (blank) was plotted in a dose-dependent manner. mGluR and GRM, metabotropic glutamate receptor; HEK293, human embryonic kidney 293T cells, GABA, γ-aminobutyric acid. *P < 0.05, ****P < 0.0001.

amino acids was present in *Sj*GRM7. This is the same for its homolog in *S. mansoni* Smp_128940, where six out of the seven essential amino acids differ from the conserved residues (**Figure 1C**). Additionally, Smp_128940 contains an alanine (183 in Smp_128940) rather than a serine in *Sj*GRM7 (183 in *Sj*GRM7). Despite the differences in conserved residues, Smp_128940 can still be activated by L-glutamate (Taman and Ribeiro, 2011). Protein structures were further predicted by examining the spatial arrangement of critical residues. Both *Sj*GRM and *Sj*GRM7 have typical GRM domains, including a VFT for ligand binding, a cysteine-rich linker domain, and a seven-transmembrane domain (**Figure 1E**). The glutamate docking results showed similar conserved residue positions between *Sj*GRM and human GRM2. However, Leu79 and Ser416 in *Sj*GRM7 are absent from the binding pocket. Furthermore, no other visible residue close to the pocket could replace leucine and serine to bind the γ-carboxyl group.

To confirm that the two mGluRs obtained using a bioinformatics approach can specifically bind glutamate, their ability to bind glutamate was determined using a live intracellular calcium mobilization assay. The cDNAs of these two mGluRs were transiently transfected into HEK293 cells with the heterotrimeric G-protein Gα16 to detect intracellular calcium mobilization. The results showed that *Sj*GRM and *Sj*GRM7 responded only to L-glutamate but not to glutamine (glutamate derivative), γ-aminobutyric acid (GABA), glycine, or aspartate (**Figures 1F,G**), and both showed a dose-dependent relationship with L-glutamate (**Figures 1H,I**). This result further verifies that *Sj*GRM and *Sj*GRM7 are glutamate receptors.

Our results showed that *S. japonicum* encodes two mGluRs, Sjc_0001163 and Sjc_0001309, referred to as *Sj*GRM7 and *Sj*GRM, respectively. *Sj*GRM has all the typical glutamate receptor features, and *Sj*GRM7 can recognize glutamate despite differences in phylogeny, key residues, and binding pockets.

Localization and expression of the metabotropic glutamate receptors in *Schistosoma japonicum*

To further describe these two mGluRs and enable future research on their physiological functions, two of mGluRs' mRNA expression changes during different *S. japonicum* developmental stages were quantified, and their cellular location was observed.

The expression of *Sj*GRM and *Sj*GRM7 at different developmental stages (14, 16, 18, 20, 22, 24, 26, 28, and 30 dpi) was examined by qPCR. Among them, most worms in 14 and 16 dpi are not paired. The results showed that the expression of *Sj*GRM was relatively stable during *S. japonicum* development (**Figure 2B**). *Sj*GRM7 was first downregulated before 26 dpi and then upregulated after 26 dpi at different developmental stages of *S. japonicum* (**Figure 2A**).

The *Sj*GRM has specific signals in the testes of male and female ovaries, notably in mature oocytes (**Figure 2D**, white arrows), whereas its fluorescence intensity is not as strong as *Sj*GRM7. Meanwhile, there are no specific signals in the *Sj*GRM for longitudinal neuraxis and peripheral nerve cells. As a result, *Sj*GRM7 may be crucial for the growth of *S. japonicum*.

*Sj*GRM7 is required for normal physiological activity in *Schistosoma japonicum in vitro*

To observe the function of the two mGluRs in *S. japonicum* and their phenotypes in real time, we performed RNA interference (RNAi) in adult paired worms *in vitro*.

First, the dsRNAs were generated and then added on days 1, 3, and 5 using the immersion method, and microscopic observation was performed on day 7 (see **Figure 3**, top). The results showed no significant change in phenotype in the *Sj*GRM dsRNA group compared with the GFP control group. Conversely, the *Sj*GRM7 dsRNA group failed to attach to the petri dish, and the paired worms showed separation and edema (**Figure 3A**, red arrows). The number of worms that appeared for each phenotype was observed, recorded, and subjected to statistical analysis (**Figure 3B**).

The *Sj*GRM7 dsRNA group showed the highest degree of edema, detachment of the chassis, and separation of paired worms (65.28%, 83.33%, 66.67%, respectively), followed by the *Sj*GRM dsRNA group (12.5%, 15.28%, 15.28%, respectively) and the GFP control group (8.33%, 5.56%, 11.11%, respectively) (**Figure 3B**). RNAi efficiency was measured using qPCR to demonstrate that RNAi caused this phenotype in *Sj*GRM7 and *Sj*GRM. The results confirmed that both male and female *Sj*GRM7 and *Sj*GRM genes were knocked down (**Figure 3C**). These results suggested that *Sj*GRM7 is critical for the maintenance of regular physiological activity in *S. japonicum*.

*Sj*GRM7 affects development and reproduction in *Schistosoma japonicum* and reduces worm burden *in vivo*

Since we showed that *Sj*GRM7 affects the normal physiology of *S. japonicum*, *Sj*GRM7 was further investigated. We examined the *Sj*GRM7 function to investigate whether it also affects the normal physiology of *S. japonicum* in the definitive host. The level of *Sj*GRM7 mRNA was first detected using qPCR after interference. The results showed that the mRNA levels were significantly downregulated in the *Sj*GRM7 dsRNA group compared to the GFP control group, with 86.92% and 72.04% downregulation in females and males, respectively (**Figure 4A**).
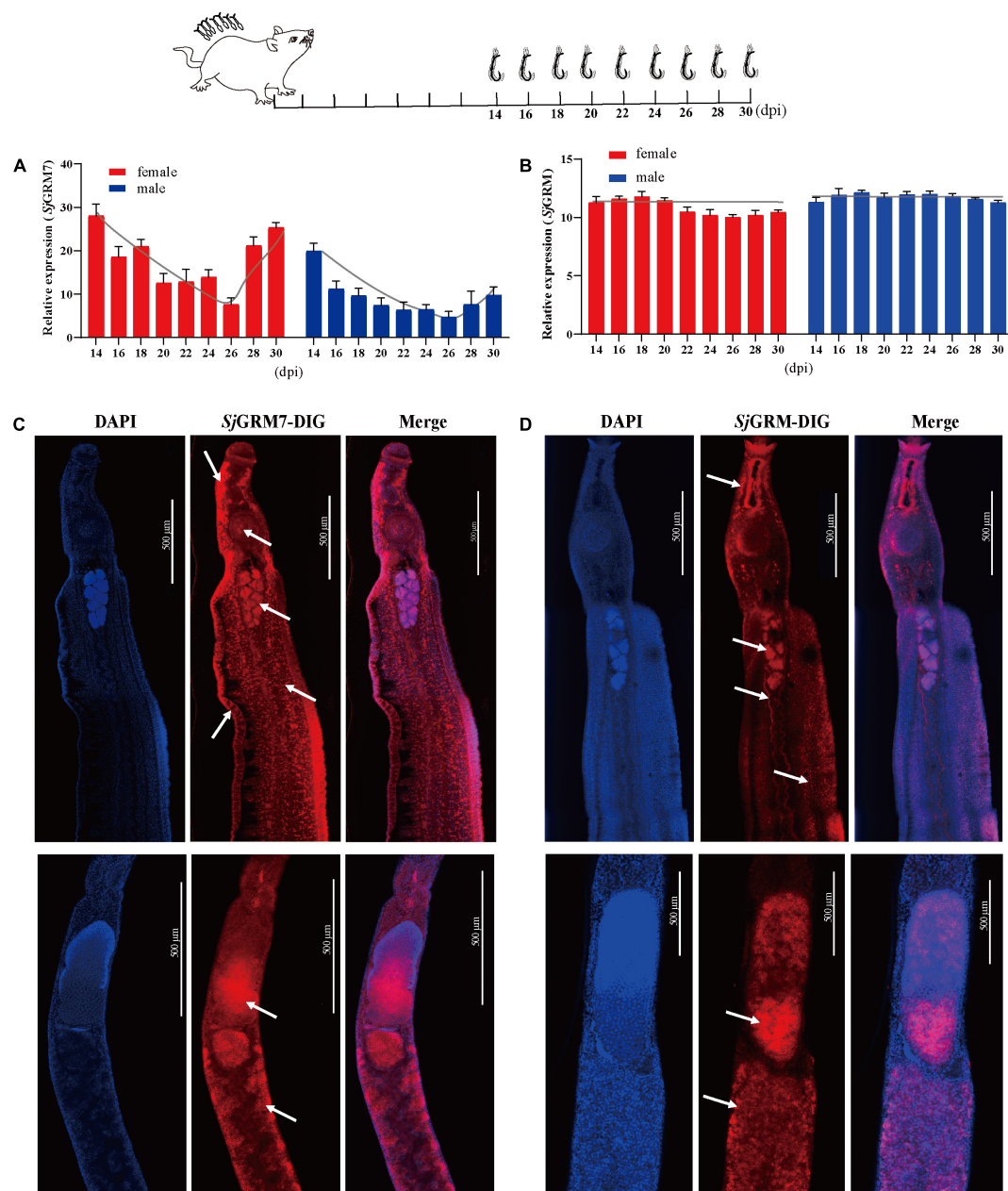
FIGURE 2

Localization and expression of the two mGluRs in *S. japonicum*. The top is a flow chart of the samples collected during the different developmental periods and most worms in 14 and 16 dpi are not paired. **(A)** Expression patterns of *Sj*GRM7 at different time points post-infection. **(B)** Expression patterns of *Sj*GRM at different time points post-infection. **(C)** Sagittal confocal section of FISH showing *Sj*GRM7 mRNA enriched in the testes, brain ganglia, longitudinal neuraxis, ventral suckers, and peripheral nerve cells of a male worm (top) and in the ovaries and vitelline glands of a female worm (bottom) (white arrows). **(D)** Sagittal confocal section of FISH showing *Sj*GRM mRNA enrichment in the testes of male worms (top) and in the ovaries and vitelline glands of female worms (bottom). FISH analysis of the locations of the two *S. japonicum* mGluRs. Nuclei were stained blue (DAPI), and dig-labeled mGluRs were stained red. Fifteen parasites were used in the five experiments. Specific signals are indicated by white arrows. Scale bar: 500 μm **(C,D)**. FISH, fluorescence *in situ* hybridization; mGluR and GRM, metabotropic glutamate receptor; DAPI, 4′,6-diamidino-2-phenylindole.

To study the morphological effects of *Sj*GRM7 on *S. japonicum*, brightfield microscopy was used to image and quantify worm morphology in mice. Compared to the GFP control group, the growth of male (**Figure 4B**, left) and female (**Figure 4B**, right) worms in the *Sj*GRM7 dsRNA group was significantly inhibited (**Figure 4B**). ImageJ was used to measure the length of female and male worms, and the length shortening degrees of females and males were 12.09% and 6.1%, respectively
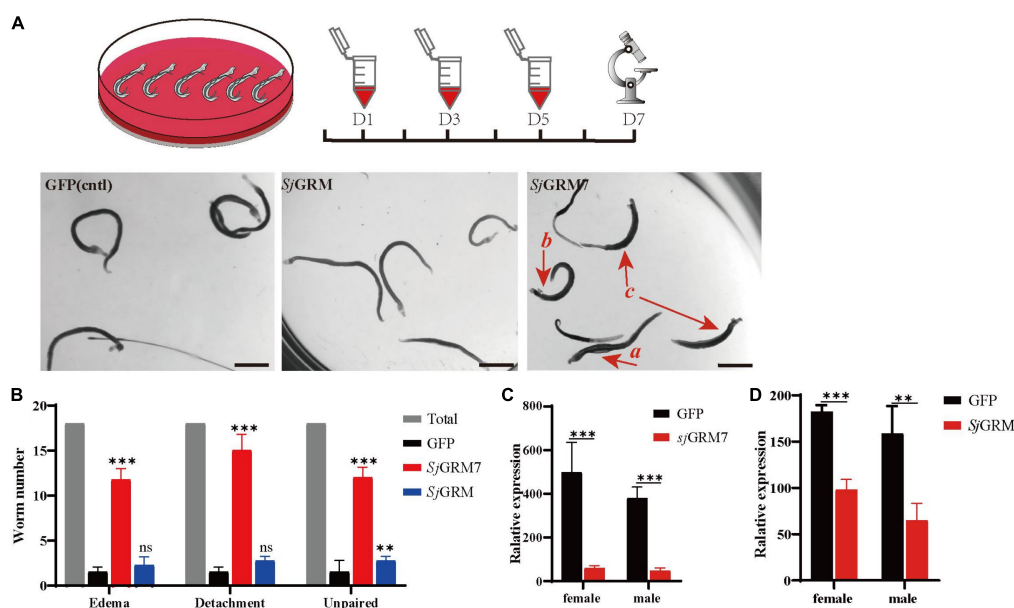
FIGURE 3

*Sj*GRM7 is required for normal physiological activity in *S. japonicum in vitro*. The top is the flow chart of *in vitro* interference. Adults with good pairing activity were added to the petri dish, dsRNA was added for interference on the first, third, and fifth days, and microscopic observation and photography were carried out on the seventh day. Each plate had six pairs of three replicate wells for each biological experiment with four biological replicates. **(A)** Observation under the light microscope on the seventh day after dsRNA treatment of the control (left), *Sj*GRM (middle), and *Sj*GRM7 (right) groups. Scale bar: 200 μm. **(B)** Effect statistics of the control, *Sj*GRM, and *Sj*GRM7 groups after dsRNA treatment, with the statistical indicators of swelling (detachment), no adsorption to the chassis, and unpairing. qPCR was used to detect the mRNA expression of *Sj*GRM7 **(C)** and *Sj*GRM **(D)** after treatment with dsRNA. ***P < 0.001, **P < 0.01. mGluR and GRM, metabotropic glutamate receptor; qPCR, reverse transcription polymerase chain reaction; dsRNA, double-stranded RNA.

(**Figure 4D**). Quantification results showed that the *Sj*GRM7 dsRNA group had significantly reduced worm loads. The degrees of reduction in female and male worms were 22.58% and 29.03%, respectively (**Figure 4C**). These data indicate that the interference of *Sj*GRM7 can affect the development of *S. japonicum* and may even have an insecticidal effect. However, *Sj*GRM knockdown has no influence on *S. japonicum* growth and development (**Supplementary Figure 1**).

To further characterize the gonadal development of *S. japonicum* after *Sj*GRM7 interference, *S. japonicum* was stained with carmine, followed by visualization of changes in the gonads using fluorescence microscopy, and changes at the cellular level using laser confocal microscopy. Morphological observations showed that the GFP control group more mature ovaries, vitelline glands, and testes, which were significantly larger than those of the *Sj*GRM7 dsRNA group (**Figure 4E**). To further observe the development of the reproductive system at the cellular level, we used confocal laser microscopy to observe the gonads of *S. japonicum*. The results showed that the GFP control ovaries were larger and filled with more mature oocytes. In comparison, ovaries of the *Sj*GRM7 dsRNA group were smaller and contained a smaller number of immature oocytes. We also observed that the GFP control group had far more mature vitelline gonad cells than the *Sj*GRM7 dsRNA group (**Figure 4F**, left, middle). The male testicular area and testicular

spermatocytes were significantly reduced in the *Sj*GRM7 dsRNA group (**Figure 4F**, right).

We also measured the ovary area and maximum cross-sectional width of the vitelline gland to quantify the level of female gonad development. The results showed that sexual maturation was significantly inhibited in the ovaries (**Figure 4G**) and vitelline glands (**Figure 4H**) of females in the *Sj*GRM7 dsRNA group, with 35.62% and 19.65% inhibition, respectively. These results suggested that *Sj*GRM7 is essential for the growth, development, and survival of *S. japonicum*.

*Sj*GRM7 affects oviposition in *Schistosoma japonicum* and alleviates host pathology *in vivo*

The results in **Figure 4** indicate that *Sj*GRM7 is necessary for maintaining the normal physiology of *S. japonicum* and plays an essential role in its growth and development. We further investigated the effect of *Sj*GRM7 on egg-laying by *S. japonicum* after sexual maturation (**Figure 5**, top).

Downregulation of *Sj*GRM7 mRNA levels after interference was first detected by qPCR, with 78.99% and 57.32% for females and males, respectively (**Figure 5A**). Growth of female and male *S. japonicum* was inhibited in the *Sj*GRM7 dsRNA group
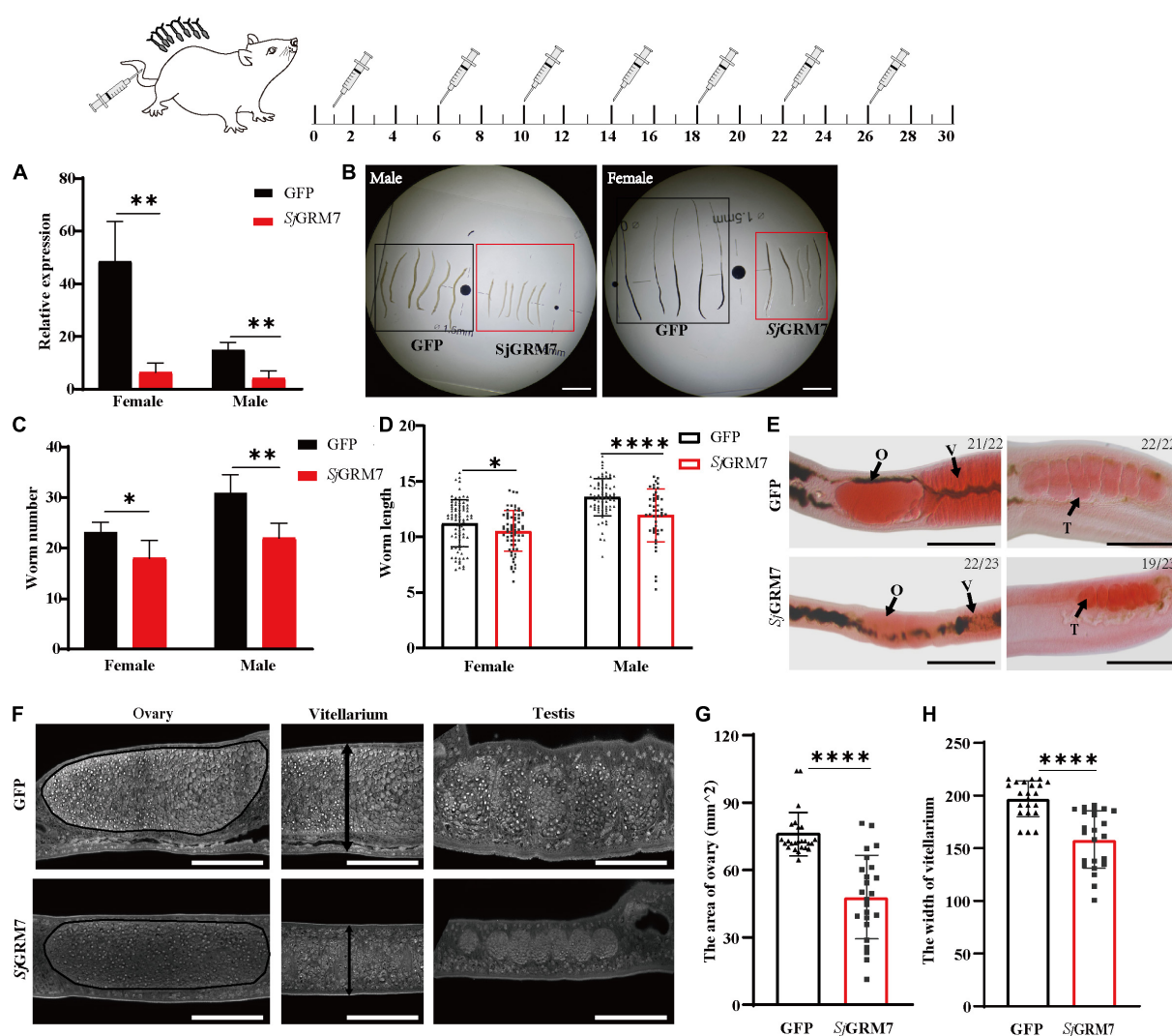
FIGURE 4

Effects of dsRNA-mediated knockdown of *Sj*GRM7 *in vivo*. The top is a flow chart of *in vivo* interference. On the 1st, 6th, 10th, 14th, 18th, 22nd, and 26th days after cercariae infection using the abdominal patch method, dsRNA was injected through the tail vein, and the hepatic portal vein was perfused on the 30th day for observation. Worms were continuously treated with 10 μg *Sj*GRM7 and GFP dsRNA *in vivo*. **(A)** *Sj*GRM7 transcript relative mRNA levels in the *Sj*GRM7 dsRNA group. **(B)** Morphological changes in the worms captured at 30 dpi. **(C)** Comparison of worm numbers between GFP and *Sj*GRM7 dsRNA groups. **(D)** Comparison of worm length between the GFP and *Sj*GRM7 dsRNA groups. **(E)** Morphological changes in the gonads of female and male worms were observed by carmine staining. **(F)** Adult worms from the treatment group were analyzed by confocal laser scanning microscopy. **(G)** The area of the largest cross-section of the ovary of female worms was measured using ImageJ. **(H)** The width of the largest cross-section of the vitellarium of female worms was measured using the ImageJ software. O, oocytes; E, eggs; T, testis; GFP, green fluorescent protein; dpi, days post infection; dsRNA, double-stranded RNA; GRM, metabotropic glutamate receptor. Scale-bars: **(E)** 200 μm; **(F)** 50 μm. ****$P < 0.0001$, **$P < 0.01$, *$P < 0.05$.

(**Figure 5B**), with inhibition lengths of 10.71% and 10.92%, respectively (**Figure 5D**) (ImageJ quantification). The loads were reduced by 17.20% and 20.59% in females and males, respectively (**Figure 5C**).

Observations of the gonads after carmine staining showed that female ovaries of the *Sj*GRM7 dsRNA group were significantly smaller than those of the GFP control group. The morphology of the male testes was significantly smaller than that of the GFP control group (**Figure 5E**). These results indicate that

RNAi affects the development of *Sj*GRM7 and has a repellent effect on *S. japonicum* after maturation up to egg-laying.

We further investigated whether this affected gonadal function in female worms as well as egg-laying and immunopathology of liver damage caused by worm egg antigens. Many studies have shown that liver fibrosis results from an interaction between liver parenchymal cell damage and hepatic stellate activation. The proliferation and activation of stellate cells plays a major role in liver fibrosis. Activated hepatic
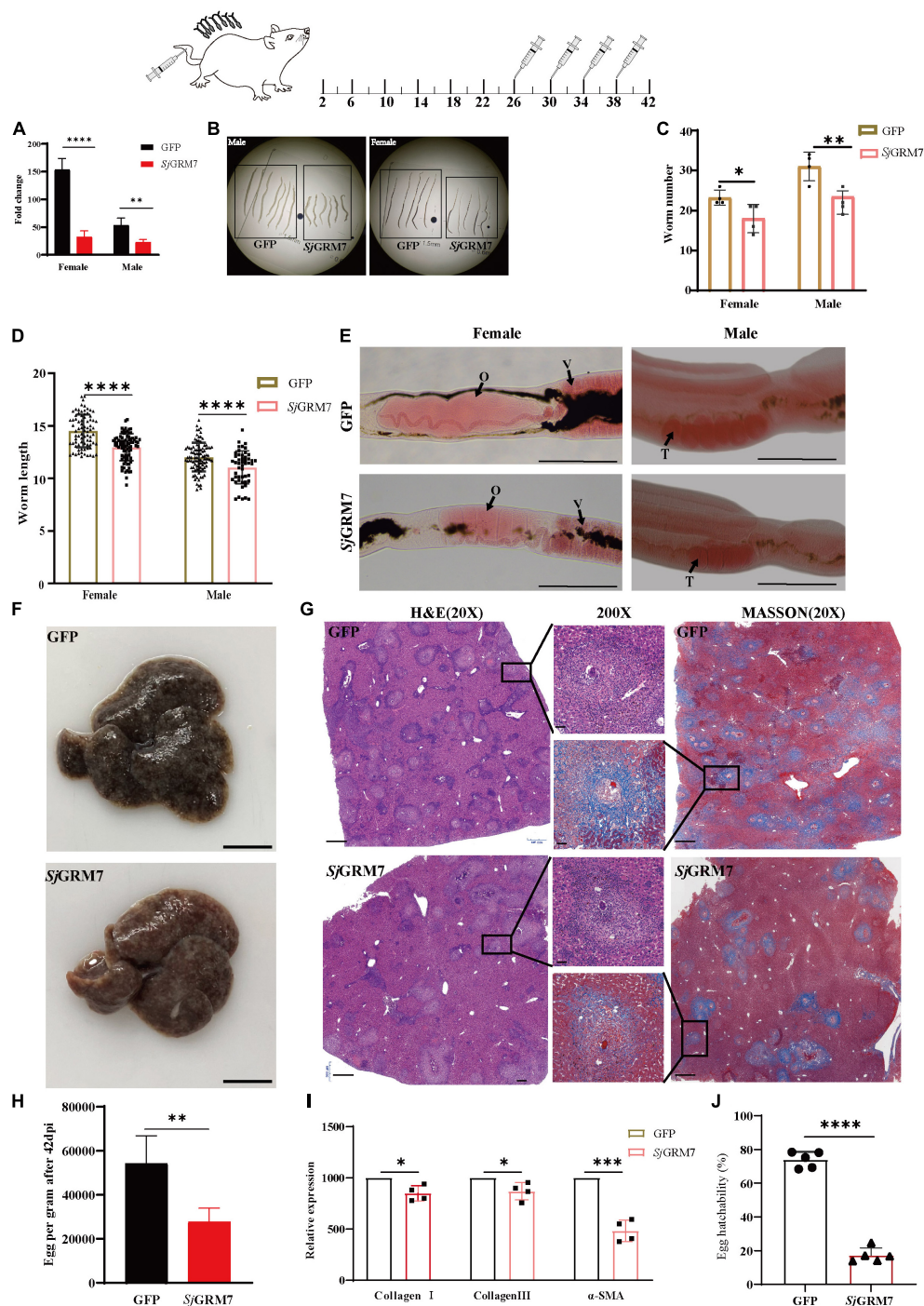
FIGURE 5

*Sj*GRM7 affects oviposition in *S. japonicum* and alleviates host pathology *in vivo*. On the 26th, 30th, 34th, and 38th days after abdominal patch infection, dsRNA was injected through the tail vein, and the hepatic portal vein was perfused on the 42nd day. **(A)** *Sj*GRM7 transcript relative mRNA levels in the *Sj*GRM7 dsRNA group. **(B)** Morphological changes in worms collected at 42 dpi. **(C)** Comparison of worm numbers between GFP and *Sj*GRM7 dsRNA groups. **(D)** Comparison of worm length between the GFP and *Sj*GRM7 dsRNA groups. **(E)** Morphological changes in the gonads of female and male worms were observed by carmine staining. **(F)** Gross observations of the mouse liver in the GFP and *Sj*GRM7 dsRNA groups. **(G)** Liver sections stained with hematoxylin and eosin (H&E) (left) showing egg granulomatous lesions; Masson's trichrome staining (right); liver fibrosis, granuloma formation, and liver fibrosis from individual eggs were also observed (middle). **(H)** Eggs per gram comparison between the GFP control and *Sj*GRM7 dsRNA groups. **(I)** qPCR showed that the mRNA levels of collagen I, collagen III, and α-SMA in the *Sj*GRM7 dsRNA group were significantly lower than those in the GFP control group. **(J)** Comparison of egg hatchability between GFP and *Sj*GRM7 dsRNA groups. O, oocytes; e, eggs; T, testis. E, 200 μm; F, 10 mm.; G, left and right, 500 μm; middle, 50 μm; GFP, green fluorescent protein; dpi, days post infection; dsRNA, double-stranded RNA; GRM, metabotropic glutamate receptor; qPCR, quantitative polymerase chain reaction; α-SMA, α-smooth muscle actin protein ****$P < 0.0001$, ***$P < 0.001$, **$P < 0.01$, *$P < 0.05$.

stellate cells express α-smooth muscle actin protein (α-SMA), and extracellular matrix proteins, mainly collagen I and collagen III, accumulate to form fibrotic scarring that gradually leads to liver fibrosis.

Therefore, we first directly observed the livers after dissecting the mice and found that the livers of the *Sj*GRM7 dsRNA group had only a few nodules formed by worm eggs. In contrast, the livers of the GFP control group exhibited a severe degree of fibrosis (**Figure 5F**). We quantified the number of eggs per gram of liver tissue. We showed that the *Sj*GRM7 dsRNA group had significantly fewer eggs than the GFP control group, with a reduction of 48.98% (**Figure 5H**), while at the same time we also observed the hatching rate of eggs. The results showed that the hatching rate of the *Sj*GRM7 dsRNA group was 76.63% lower than that of the control group (**Figure 5J** and **Supplementary Figure 2**). We hypothesized that the reduction in liver damage in the *Sj*GRM7 dsRNA group may have been caused by reduced egg production and a decrease in egg activity.

To further observe the liver pathology of mice, HE and Masson staining were used to observe the reaction process of liver egg granulomas and liver fibrosis, respectively (**Figure 5G**). HE staining results (**Figure 5G**, left) showed that the number of granulomas formed by eggs in the *Sj*GRM7 dsRNA group was lower than that in the control group, and the area of granulomas formed by individual eggs was also significantly smaller (**Figure 5G**, middle). Masson staining (collagen fibers in blue), which characterizes the pathology of hepatic fibrosis (**Figure 5G**, right), showed that the *Sj*GRM7 dsRNA group had significantly less hepatic fibrosis than the GFP control group, and the area of hepatic fibrosis formed by single eggs was also significantly lower. To quantify the extent of fibrosis, we used qPCR to measure changes in the mRNA levels of α-SMA, collagen I, and collagen III during liver fibrosis. The results showed that the mRNA levels of the three genes were significantly reduced in the *Sj*GRM7 dsRNA group compared to those in the GFP control group, with reductions of 14.92%, 12.98%, and 51.67%, respectively (**Figure 5I**). The pathological section and qPCR results suggest that *Sj*GRM7 interference led to a reduction in liver damage. These results suggested that *Sj*GRM7 interference could reduce pathologically damage to the host by affecting the development, egg production, and egg activity of *S. japonicum*.

RNA-seq analysis shows that knocking down *Sj*GRM7 leads to downregulation of the G protein-coupled receptor signaling pathway in *Schistosoma japonicum*

The results in **Figure 5** show that *Sj*GRM7 plays an essential role in maintaining the normal physiology, growth,

development, and egg production of schistosomes. To further explore the regulatory mechanism of *Sj*GRM7 expression in the development of *S. japonicum*, we performed RNA-seq analysis of both male and female worms after knocking down *Sj*GRM7 *in vitro*.

We set $\log_2$FoldChange > 1 (upregulated), $\log_2$FoldChange < −1 (downregulated), and false discovery rate (FDR) < 0.05, as cutoffs for differential gene expression analysis. We noticed that knockdown of *Sj*GRM7 had strong effects on gene expression, especially the downregulation of gene expression. The overall expression profile of RNAi versus the control revealed 361 downregulated and 56 upregulated genes in females and 634 downregulated and 56 upregulated genes in males (**Figures 6A,B**). After the knockdown of *Sj*GRM7, genes with the most significant expression changes included *ABCA1* (Sjc_0002054), *ATP11a* (Sjc_0009436), *BTBD1* (Sjc_0002226), *SUCO* (Sjc_0002288), *and ELAVL1* (Sjc_0002420) in males, and *GIPC3* (Sjc_0008441), *MFSD12* (Sjc_0005954), *Dys* (Sjc_0003555), and *Sjc_0006942* in females. **Supplementary Figure 3** also shows that validation of genes predicted by RNA-seq to change substantially using qPCR. Thus*, Sj*GRM7 may regulate these genes. GO analysis of the downregulated genes in male worms revealed that *Sj*GRM7 knockdown had powerful effects on cell-cell adhesion (GO:0098609), GPCR signaling pathway (GO:0007186), secretion regulation by cells (GO:1903530), and modulation of chemical synaptic transmission (GO:0050804) (**Figure 6C** and **Supplementary Table 1**). However, we only observed significant enrichment of genes related to axonemal dynein complex assembly (GO:0070286) in females (**Supplementary Table 2**). Considering that the expression of certain genes may only change slightly, and these are not identified as differentially expressed genes after RNAi, we performed gene set enrichment analysis (GSEA) (**Supplementary Tables 3, 4**). By comparing the results obtained in females and males separately, we observed that several genes involved in synaptic signaling (GO:0099536), chemical synaptic transmission (GO:0007268), GPCR signaling pathway (GO:0007186), cyclic-nucleotide-mediated signaling (GO:0019935), axon development (GO:0007409), muscle organ development (GO:0007517), endocrine system development (GO:0035270), and regulation of locomotion (GO:0040012) were downregulated in females and males (**Supplementary Table 5**). This result is highly consistent with functional studies of *Sj*GRM7 in other species (Su et al., 1998; Song et al., 2021). This suggests that *Sj*GRM7 plays an essential role in the neuronal development of *S. japonicum*.

Among these pathways, we noted significant downregulation of the neural-associated endocytic adaptor protein Numb (Sjc_0007478), the first identified cell fate determinant in *Drosophila melanogaster* (Shan et al., 2018).
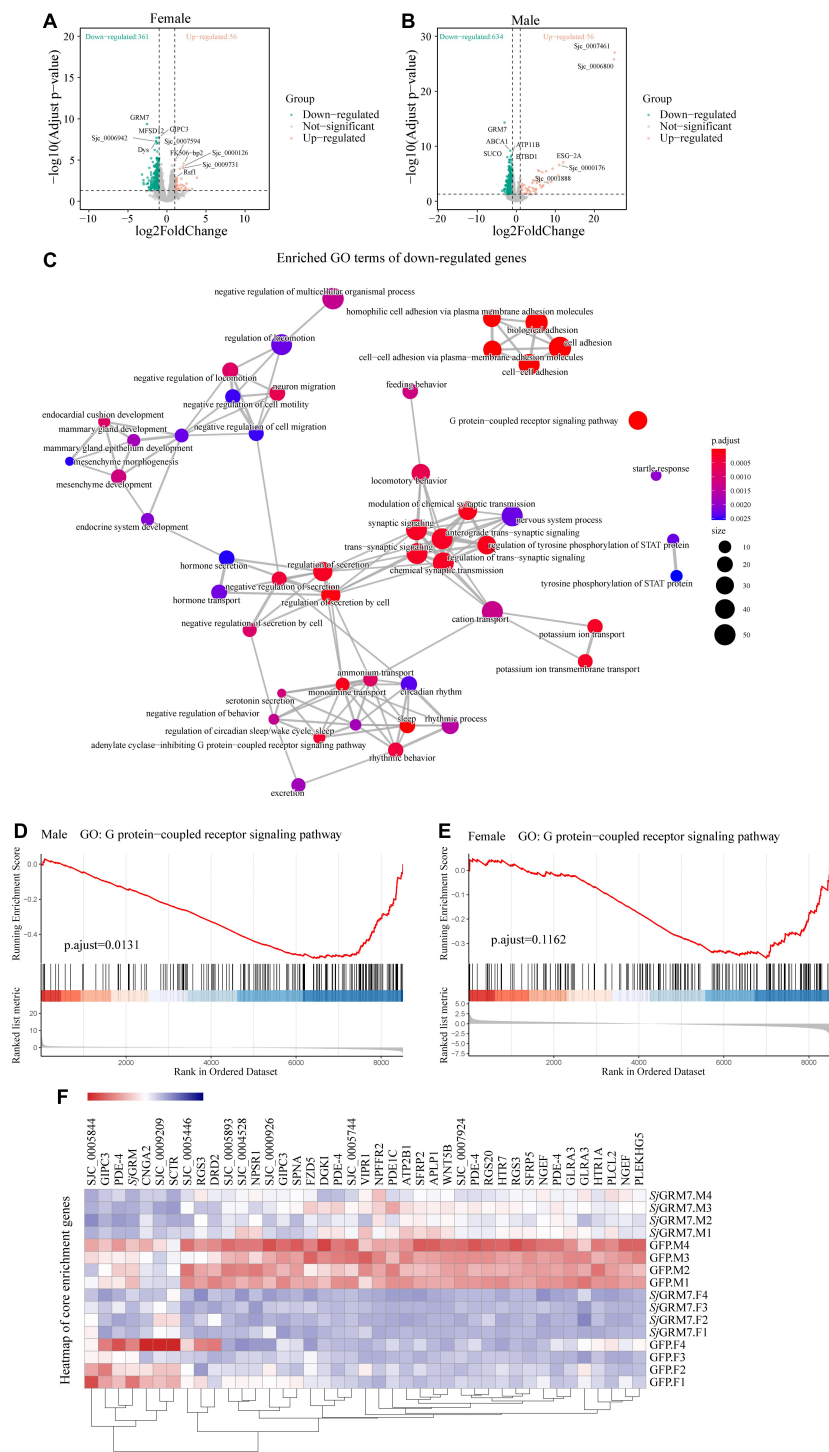
FIGURE 6

Differentially expressed genes (DEGs) of *S. japonicum* after *Sj*GRM7 RNAi *in vitro* and gene ontology (GO) analysis. **(A)** DEG volcano plots in females and males. **(B)** *X*-axis: log$_2$-fold change (ds *Sj*GRM7/GFP). *Y*-axis: log$_{10}$ (adjusted *p*-value). Green points represent significantly downregulated genes, and orange points represent significantly upregulated genes. **(C)** GO term visualization (enrichment calculated using gene-set enrichment analysis, $p < 0.05$, adjusted for FDR, only shown in genes significantly downregulated after *Sj*GRM7 knockdown). **(D)** GSEA showed downregulation of the GPCR signaling pathway in *Sj*GRM7 dsRNA group male worms and female worms **(E)** as compared to GFP controls. **(E)** Heat map of core enrichment genes in both males and females for the GPCR signaling pathway gene set. **(F)** The score at the peak of the plot **(D,E)** is the enrichment score (ES) for this gene set, and genes that appear before or at the peak are defined as core enrichment genes for this gene set. GFP, green fluorescent protein; dsRNA, double-stranded RNA; GRM, metabotropic glutamate receptor; GPCR, G protein-coupled receptor; GSEA, Gene set enrichment analysis; FDR, false discovery rate.

Studies have shown that Numb proteins are present in post-mitotic neurons. *In vitro* studies have shown that Numb is involved in neuronal morphological development, such as synaptic growth and spine development, and that deletion of Numb/Numblike in glutamatergic neurons leads to anxiety-like behavior in mice (Qian et al., 2017). Deficiency of Numb protein impairs prominent mGlu1 expression and motor coordination. This leads to impaired transport of mGlu5 and autistic-like behavior in the neurons (Wang et al., 2019). Additionally, Numb enhances Notch by inhibiting the ubiquitination of the intracellular structural domain of neurogenic locus notch homolog protein 1 (NOTCH1) signaling (Luo et al., 2019).

Furthermore, to understand the effect of *Sj*GRM7 knockdown on the expression of other GPCRs in *S. japonicum*, we examined the gene expression levels in GPCR gene sets that were significantly enriched in both sexes (**Figures 6D,E**). Other GPCR genes that significantly downregulated in male worms included sex peptide receptor (Sjc_0000420), tachykinin-like peptide receptor 99D (Sjc_0003380), Dro/myosuppressin receptor (Sjc_0007429), neuropeptide FF receptor 2 (Sjc_0003026), FMRFamide receptor (Sjc_0006030), PDF receptor (Sjc_0000792), and other neuropeptide GPCR proteins. Interestingly, the gene expression of neuroendocrine protein 7b2 (Sjc_0001267), a canonical molecular marker of developing and definitive neurons, was notably downregulated after the knockdown of *Sj*GRM7. This suggests that knockdown of *Sj*GRM7 may affect the development of neurons, leading to a deregulated phenotype in central nervous system function. In female worms, the most significantly downregulated GPCRs were the 5-hydroxytryptamine receptor (Sjc_0005944), dopamine D2-like receptor (Sjc_0009336), octopamine receptor (Sjc_0000926), 5-hydroxytryptamine receptor 7 (Sjc_0001525), secretin receptor (Sjc_0000311) and other biogenic amine receptors.

As shown in **Figure 6F**, most GPCRs were expressed at higher levels in males than in females. We speculate that the sex differences in their expression levels led to our observation that these genes were significantly downregulated in males after *Sj*GRM7 knockdown but only slightly downregulated in females.

Discussion

Functional genomics has paved the way for drug discovery to combat schistosomiasis. Extensive efforts have been made to characterize the genes essential for development and maintenance (Wang et al., 2020), especially in the neural and reproductive systems. These are potential targets of the only effective drug, praziquantel (Love et al., 2014; Park et al., 2021), and the root of schistosome pathology. Glutamate is

an essential neurotransmitter in worms that interacts with various cell surface receptors to transmit excitatory signals. GRMs are one of the most important classes of glutamate receptors.

Interestingly, *Sj*GRM7 changed six out of seven conserved binding residues but retained its function and selectivity. This receptor can only be activated by L-glutamate but not by GABA, glycine, aspartate, or the glutamate derivative glutamine (**Figure 1E**). This is unexpected because previous work with mutagenesis showed that, except for K409 (in human GRM1), mutations in any of these key residues severely hinder the receptor's ability to bind glutamate (Hara et al., 1993; Sato, 2003). Glutamate and the orthosteric agonist quisqualic acid potency are reduced 1,000- and 100-fold, respectively, in an R78L rat GRM1 mutant (Jensen et al., 2000). Nevertheless, a R78L mutation was present in *Sj*GRM7 and Smp_128940. This inconsistency challenges the current understanding of the mGluR-binding pocket. Only one conserved residue (serine183 in *Sj*GRM7) is unlikely to be involved in glutamate binding. Therefore, unreported residues in the binding pocket may be involved in binding. Three-dimensional (3D) structure determination of the binding pocket and mutagenesis of the associated residues are required to further explain the unique binding mechanism of *Sj*GRM7. In addition, this unique binding pocket is an optimal target for drug discovery, as this difference in *Sj*GRM7 will allow more accessible screening of selective orthosteric chemistries due to the highly conserved glutamate-binding mechanism while minimizing potential side effects.

We think *Sj*GRM7 may have acquired new functions other than typical mGluR's functions, and this new function may play a more important role in the growth and development of schistosomes than *Sj*GRM. Having most of the conserved residues mutated and being evolutionarily distinct from the mGluR group may be signs of it gaining new functions. The previous report shows that the canonical mGluR knockdown only causes a neurodevelopmental disorder phenotype without impairing its growth, development and survival (Fisher et al., 2018). Thus, it can be implied that the knockdown of mGluRs in schistosomes will produce similar phenotypes. In the present study, the *Sj*GRM knockdown worms only show unpairing *in vitro*. No effect on growth, development and survival was detected *in vivo*, consistent with the results of typical mGluR after knockdown. In contrast, the uncanonical *Sj*GRM7 knockdown worms showed edema, non-absorption of chassis, and separation of paired worms *in vitro*. It also shows an effect on maturation, development, survival, egg production, and activity of *S. japonicum in vivo*, which in turn significantly attenuated the pathological damage to the host. We reason this discrepancy may be caused by *Sj*GRM7 acquiring new functions in the time of evolution

beyond merely modulating neurotransmission. It also further suggests that uncanonical *Sj*GRM7 is important and more likely to be a target for a novel anti-schistosomal drug.

Another striking result from our RNA-seq data is the significant downregulation of glioma-Associated oncogene homolog 1 (*GLI1*) and non-ribosomal peptide synthetase (*NRPS*) expression in both females and males, which is essential for the male-derived non-ribosomal peptide pheromone control of female schistosome development (Chen et al., 2022). Combined with this phenotype, we observed *Sj*GRM7 knockdown *in vivo* and *in vitro*. *In vivo*, *Sj*GRM7 knockdown caused abnormal growth in both male and female mice. However, we only observed an abnormal male phenotype after knocking down *Sj*GRM7 *in vitro*. These results suggest that *Sj*GRM7 may play a critical regulatory role, mainly in nervous system development and synaptic transmission in males.

In situ hybridization results showed that *Sj*GRM7 was expressed in neurons and testes in males and only in gonads in females (**Figures 2C,D**), which matched the abnormal male phenotype observed only after *in vitro* knockdown of *Sj*GRM7. Studies have shown that in *Macaca fascicularis*, GRM2 is located in primordial follicles and oocytes (Gill et al., 2008). BLAST was used to identify genes with approximately 83% similarity to *Sj*GRM7 and *Sj*GRM in *S. mansoni*, Smp_128940, and Smp_305430, respectively. The locations of these two genes were predicted using the *S. mansoni* single-cell sequencing website (Wendt et al., 2021). The results showed that both were expressed throughout the body, with Smp_305430 mainly expressed in neurons in both sexes and in the muscle of females. Smp_128940 was mainly expressed in neurons and germ cells (**Supplementary Figure 4**). Smp_128940, is expressed in Germline Stem Cell (GSC) zygotes and late germinating cells, suggesting a conserved role in GSC regulation (Taman and Ribeiro, 2011; Wendt et al., 2020). We speculate that the combined effect of *Sj*GRM7 knockout in females and decreased levels of transmitted non-ribosomal peptide pheromones are due to the downregulation of *GLI1* and *NRPS* genes in males which causes abnormal development in females. In humans, mGluRs mainly affects the central nervous system and are associated with neurodegenerative diseases (Fabiola et al., 2017; Ribeiro et al., 2017). Nevertheless, GPCR signaling plays an important role in germ cell regulation. In *Drosophila melanogaster* neuropeptide Y receptor 1 (NPYR1) in neuroendocrine cells receives signals from NPY8, which in turn regulates germ cell maturation (Amir et al., 2016).

In conclusion, we identified two *S. japonicum* mGluRs: *Sj*GRM and *Sj*GRM7. *Sj*GRM7 diverged from typical mGluRs at an early time point and may have a novel binding pocket. This receptor is expressed in neural and reproductive systems. Knockdown of *Sj*GRM7 affects worm development, viability, and reproduction while dramatically reducing pathology. Further, RNA-seq results demonstrated downregulation of the GPCR pathway, neural function, and cell adhesion. This study presents a promising drug target for schistosomiasis, and further research on *Sj*GRM7 may improve our understanding of sexual gonad maturation and maintenance.

Data availability statement

The sequencing data were deposited in the NCBI Sequence Read Archive (SRA) database under accession numbers (PRJNA880502).

Ethics statement

Animal studies were reviewed and approved by the Laboratory Animal Welfare Review Committee of the Institute for the Prevention and Control of Parasitic Diseases (National Center for Tropical Diseases Research) of the Chinese Center for Disease Control and Prevention (approval number: IPD-2020-10), and did not involve informed consent was not obtained.

Author contributions

XW, WZ, YX, WL, YY, CY, BZ, and MG conducted experiments. XW, BX, JW, YL, and WH designed the experiments and analyzed the data. SC and XC analyzed the bioinformatic data. WZ, XC, MG, and WL provided intellectual input and aided in experimental design. XW wrote the manuscript. WH revised the manuscript accordingly. All authors have contributed to the manuscript and approved the submitted version.

Funding

Acknowledgments

We acknowledge Liu Jianfeng of Huazhong University of Science and Technology for his helpful comments on the fluorescence-based assay of calcium mobilization. We thank Qunfeng Wu from our research group for his enlightening lectures, which have been really beneficial to us in this research.

Conflict of interest

The authors declare that the research was conducted in the absence of any commercial or financial relationships that could be construed as a potential conflict of interest.

Publisher's note

All claims expressed in this article are solely those of the authors and do not necessarily represent those of their affiliated organizations, or those of the publisher, the editors and the reviewers. Any product that may be evaluated in this article, or claim that may be made by its manufacturer, is not guaranteed or endorsed by the publisher.

Supplementary material

The Supplementary Material for this article can be found online at: https://www.frontiersin.org/articles/10.3389/fmicb.2022.1045490/full#supplementary-material

SUPPLEMENTARY TABLE 1
ds*Sj*GRM7_M_VS_dsGFP_M_GOterms_enrichment.

SUPPLEMENTARY TABLE 2
ds*Sj*GRM7_VS_dsGFP_F_GOterms_enrichment.

SUPPLEMENTARY TABLE 3
ds*Sj*GRM7_VS_dsGFP_M_GSEA_enrichment.

SUPPLEMENTARY TABLE 4
ds*Sj*GRM7_VS_dsGFP_F_GSEA_enrichment.

SUPPLEMENTARY TABLE 5
GSEA_shareGOBPs.

SUPPLEMENTARY TABLE 6
All primers.

References

Afshin, A., Sur, P. J., Fay, K. A., Cornaby, L., and Murray, C. (2019). Health effects of dietary risks in 195 countries, 1990–2017: A systematic analysis for the global burden of disease study 2017. *Lancet* 393, 1958–1972. doi: 10.1016/S0140-6736(19)30041-8

Amir, S., Ayana, J., Isabel, B., Liliane, S., Newmark, P. A., and Federica, W. M. (2016). GPCRS direct germline development and somatic gonad function in planarians. *PLoS Biol.* 14:e1002457. doi: 10.1371/journal.pbio.1002457

Andrews, S. (2013). *FastQC: A quality control tool for high throughput sequence data.* Available online at: https://www.bioinformatics.babraham.ac.uk/projects/fastqc/ (accessed November 20, 2020).

Bockaert, J., Claeysen, S., Becamel, C., Pinloche, S., and Dumuis, A. (2002). G protein-coupled receptors: Dominant players in cell-cell communication. *Int. Rev. Cytol.* 212, 63–132. doi: 10.1016/S0074-7696(01)12004-8

Bono, M. D., and Villu Maricq, A. (2005). Neuronal substrates of complex behaviors in *C. elegans. Annu. Rev. Neurosci.* 28:451. doi: 10.1146/annurev.neuro.27.070203.144259

Brownlee, D. J. A., and Fairweather, I. (1996). Immunocytochemical localization of glutamate-like immunoreactivity within the nervous system of the cestode Mesocestoides corti and the trematode *Fasciola hepatica. Parasitol. Res.* 82, 423–427. doi: 10.1007/s004360050139

Caers, J., Peymen, K., Suetens, N., Temmerman, L., Janssen, T., Schoofs, L., et al. (2014). Characterization of G protein-coupled receptors by a fluorescence-based calcium mobilization assay. *J. Vis. Exp.* 89:e51516. doi: 10.3791/51516

Chen, R., Wang, J., Gradinaru, I., Vu, H. S., Geboers, S., Naidoo, J., et al. (2022). A male-derived nonribosomal peptide pheromone controls female schistosome development. *Cell* 185, 1506–1520.e17. doi: 10.1016/j.cell.2022.03.017

Chen, S., Zhou, Y., Chen, Y., and Gu, J. (2018). fastp: An ultra-fast all-in-one FASTQ preprocessor. *Cold Spring Harbor Lab.* 17, i884–i890. doi: 10.1093/bioinformatics/bty560

Cogswell, A. A., Collins, J. R., Newmark, P. A., and Williams, D. L. (2011). Whole mount in situ hybridization methodology for *Schistosoma mansoni. Mol. Biochem. Parasitol.* 178, 46–50. doi: 10.1016/j.molbiopara.2011.03.001

Colley, D. G., Bustinduy, A. L., Secor, W. E., and King, C. H. (2014). Human schistosomiasis. *Lancet* 368, 2253–2264. doi: 10.1016/S0140-6736(13)61949-2

Fabiola, M. R., Vieira, L. B., Pires, R. G., Olmo, R. P., and Ferguson, S. S. (2017). Metabotropic glutamate receptors and neurodegenerative diseases. *Pharmacol. Res.* 115, 179–191. doi: 10.1016/j.phrs.2016.11.013

Ferraguti, F., and Shigemoto, R. (2006). Metabotropic glutamate receptors. *Cell Tissue Res.* 326, 483–504. doi: 10.1007/s00441-006-0266-5

Fisher, N. M., Seto, M., Lindsley, C. W., and Niswender, C. M. (2018). Metabotropic glutamate receptor 7: A new therapeutic target in neurodevelopmental disorders. *Front. Mol. Neurosci.* 11:387. doi: 10.3389/fnmol.2018.00387

Gill, S., Barker, M., and Pulido, O. (2008). Neuroexcitatory targets in the female reproductive system of the nonhuman primate (*Macaca fascicularis*). *Toxicol. Pathol.* 36, 478–484. doi: 10.1177/0192623308315663

Grohme, M. A., Schloissnig, S., Rozanski, A., Pippel, M., Young, G. R., Winkler, S., et al. (2018). The genome of *Schmidtea mediterranea* and the evolution of core cellular mechanisms. *Nature* 554, 6–61. doi: 10.1038/nature25473

Hara, P. J., Sheppard, P. O., Thógersen, H., Venezia, D., Haldeman, B. A., Mcgrane, V., et al. (1993). The ligand-binding domain in metabotropic glutamate receptors is related to bacterial periplasmic binding proteins. *Neuron* 11, 41–52. doi: 10.1016/0896-6273(93)90269-W

Hu, Y., Wang, X., Wei, Y., Liu, H., and Cao, J. (2020). Functional inhibition of natural killer cells in a Balb/c mouse model of liver fibrosis induced by *Schistosoma japonicum* infection. *Front. Cell. Infect. Microbiol.* 10:598987. doi: 10.3389/fcimb.2020.598987

Jensen, A. A., Sheppard, P. O., O'Hara, P. J., Krogsgaard-Larsen, P., and Brauner-Osborne, H. (2000). The role of Arg (78) in the metabotropic glutamate receptor mGlu(1) for agonist binding and selectivity. *Eur. J. Pharmacol.* 397, 247–253.

Kim, D., Paggi, J. M., Park, C., Bennett, C., and Salzberg, S. L. (2019). Graph-based genome alignment and genotyping with HISAT2 and hisat-genotype. *Nat. Biotechnol.* 37:1. doi: 10.1038/s41587-019-0201-4

Li, J., Xiang, M., Zhang, R., Xu, B., and Hu, W. (2018). RNA interference in vivo in *Schistosoma japonicum*: Establishing and optimization of RNAi mediated

suppression of gene expression by long dsRNA in the intra-mammalian life stages of worms. *Biochem. Biophys. Res. Commun.* 503, 1004–1010. doi: 10.1016/j.bbrc.2018.06.109

Liao, Y., Smyth, G. K., and Shi, W. (2013). featureCounts: An efficient general-purpose program for assigning sequence reads to genomic features. *Bioinformatics* 30, 923–930. doi: 10.1093/bioinformatics/btt656

Love, M. I., Huber, W., and Anders, S. (2014). Moderated estimation of fold change and dispersion for RNA-seq data with DESeq2. *Genome Biol.* 15:550. doi: 10.1186/s13059-014-0550-8

Luo, Z., Mu, L., Zheng, Y., Shen, W., Li, J., Xu, L., et al. (2019). NUMB enhances Notch signaling by repressing ubiquitination of NOTCH1 intracellular domain. *J. Mol. Cell Biol.* 12:5. doi: 10.1093/jmcb/mjz088

Niswender, C. M., and Conn, P. J. (2010). Metabotropic glutamate receptors: Physiology. *Pharmacol. Dis. Annu. Rev. Pharmacol.* 50, 295–322. doi: 10.1146/annurev.pharmtox.011008.145533

Park, S. K., Friedrich, L., Yahya, N. A., Rohr, C., and Marchant, J. S. (2021). Mechanism of praziquantel action at a parasitic flatworm ion channel. *Biophys. J.* 120:336a. doi: 10.1016/j.bpj.2020.11.2107

Pin, J. P., Galvez, T., and Prezeau, L. (2003). Evolution, structure, and activation mechanism of family 3/C G-protein-coupled receptors. *Pharmacol. Ther.* 98, 325–354. doi: 10.1016/S0163-7258(03)00038-X

Qian, W., Hong, Y., Zhu, M., Zhou, L., Li, H., and Li, H. (2017). Deletion of Numb/Numblike in glutamatergic neurons leads to anxiety-like behavior in mice. *Brain Res.* 166, 536–549. doi: 10.1016/j.brainres.2017.02.025

Ramos-Vicente, D., Ji, J., Gratacòs-Batlle, E., Gou, G., and Bayés, À (2018). Metazoan evolution of glutamate receptors reveals unreported phylogenetic groups and divergent lineage-specific events. *eLife* 7:e35774. doi: 10.7554/eLife.35774

Ribeiro, F. M., Vieira, L. B., Pires, R. G., Olmo, R. P., and Ferguson, S. S. (2017). Metabotropic glutamate receptors and neurodegenerative diseases. *Pharmacol. Res.* 115, 179–191.

Sato, T. (2003). Amino acid mutagenesis of the ligand binding site and the dimer interface of the metabotropic glutamate receptor 1. Identification of crucial residues for setting the activated state. *J. Biol. Chem.* 278, 4314–4321. doi: 10.1074/jbc.M210278200

Shan, Z., Tu, Y., Yang, Y., Liu, Z., Zeng, M., Xu, H., et al. (2018). Basal condensation of Numb and Pon complex via phase transition during Drosophila neuroblast asymmetric division. *Nat. Commun.* 9:737. doi: 10.1038/s41467-018-03077-3

Song, J. M., Kang, M., Park, D. H., Park, S., and Suh, Y. H. (2021). Pathogenic Grm7 mutations associated with neurodevelopmental disorders impair axon outgrowth and presynaptic terminal development. *J. Neurosci.* 41, 2344–2359. doi: 10.1523/JNEUROSCI.2108-20.2021

Su, W., Wright, R. A., Rockey, P. K., Burgett, S. G., Arnold, J. S., Rosteck, P. R., et al. (1998). Group Iii human metabotropic glutamate receptors 4, 7 and

8: Molecular cloning, functional expression, and comparison of pharmacological properties in RGT cells. *Mol. Brain Res.* 53, 88–97. doi: 10.1016/S0169-328X(97)00277-5

Talla, I., Kongs, A., Verlé, P., Belot, J., Sarr, S., and Coll, A. M. (1990). Outbreak of intestinal schistosomiasis in the Senegal River Basin. *Ann. Soc. Belg. Med. Trop.* 70, 173–180.

Taman, A., and Ribeiro, P. (2011). Characterization of a truncated metabotropic glutamate receptor in a primitive Metazoan, the parasitic flatworm *Schistosoma mansoni. PLos One* 6:e27119. doi: 10.1371/journal.pone.0027119

Tulio, D., Young, N. D., Korhonen, P. K., Hall, R. S., Mangiola, S., Lonie, A., et al. (2014). Identification of G protein-coupled receptors in *Schistosoma haematobium* and *S. mansoni* by comparative genomics. *Parasit. Vectors* 7:242. doi: 10.1186/1756-3305-7-242

Wang, J., Paz, C., Padalino, G., Coghlan, A., Lu, Z., Gradinaru, I., et al. (2020). Large-scale RNAI screening uncovers therapeutic targets in the parasite *Schistosoma mansoni. Science* 369, 1649–1653. doi: 10.1126/science.abb7699

Wang, J., Yu, Y., Shen, H., Qing, T., Zheng, Y., Li, Q., et al. (2017). Dynamic transcriptomes identify biogenic amines and insect-like hormonal regulation for mediating reproduction in *Schistosoma japonicum. Nat. Commun.* 8:14693. doi: 10.1038/ncomms14693

Wang, N., Wang, D. D., and Shen, Y. (2019). Numb deficiency causes impaired trafficking of mGlu5 in neurons and autistic-like behaviors. *Neurosci. Lett.* 707:134291. doi: 10.1016/j.neulet.2019.134291

Webb, R. A., and Eklove, H. (1989). Demonstration of intense glutamate-like immunoreactivity in the longitudinal nerve cords of the cestode *Hymenolepis diminuta. Parasitol. Res.* 75, 545–548. doi: 10.1007/BF00931163

Weis, W. I., and Kobilka, B. K. (2018). The molecular basis of G protein-coupled receptor activation. *Annu. Rev. Biochem.* 87, 897–919. doi: 10.1146/annurev-biochem-060614-033910

Wendt, G., Reese, M., and Collins, J. (2021). SchistoCyte atlas: A single-cell transcriptome resource for adult Schistosomes. *Trends Parasitol.* 37, 585–587. doi: 10.1016/j.pt.2021.04.010

Wendt, G., Zhao, L., Chen, R., Liu, C., O'donoghue, A. J., Caffrey, C. R., et al. (2020). A single-cell RNA-seq atlas of *Schistosoma mansoni* identifies a key regulator of blood feeding. *Science* 369, 1644–1649. doi: 10.1126/science.abb7709

Yu, G., Wang, L. G., Han, Y., and He, Q. Y. (2012). clusterProfiler: An R package for comparing biological themes among gene clusters. *OMICS* 16, 284–287. doi: 10.1089/omi.2011.0118

Zdesenko, G., and Mutapi, F. (2020). Drug metabolism and pharmacokinetics of praziquantel: A review of variable drug exposure during schistosomiasis treatment in human hosts and experimental models. *PLoS Negl. Trop. Dis.* 9:e0008649. doi: 10.1371/journal.pntd.0008649

Enhanced phosphatidylserine exposure and erythropoiesis in *Babesia microti*-infected mice

Peng Song[1,2,3,4], Yu-Chun Cai[1,2,3], Mu-Xin Chen[1,2,3,4],
Shao-Hong Chen[1,2,3] and Jia-Xu Chen[1,2,3,4]*

[1]National Institute of Parasitic Diseases, Chinese Center for Disease Control and Prevention,
Shanghai, China, [2]NHC Key Laboratory of Parasite and Vector Biology, Ministry of Public Health,
Shanghai, China, [3]WHO Collaborating Centre for Tropical Diseases, National Center for
International Research on Tropical Diseases, Ministry of Science and Technology, Shanghai, China,
[4]Hainan Tropical Diseases Research Center (Chinese Center for Tropical Diseases Research,
Hainan), Haikou, Hainan, China

Introduction: *Babesia microti (B. microti)* is the dominant species responsible for human babesiosis, which is associated with severe hemolytic anemia and splenomegaly because it infects mammalian erythrocytes. The actual prevalence of *B. microti* is thought to have been substantially underestimated.

Methods: In this study, Bagg's albino/c (BALB/c) mice were intraperitoneally injected with *B. microti*-infected erythrocytes, and parasitemia was subsequently measured by calculating the proportion of infected erythrocytes. The ultrastructure of infected erythrocytes was observed using scanning and transmission electron microscopes. Quantifying phosphatidylserine (PS) exposure, oxidative stress, intracellular Ca^{2+}, and erythropoiesis of erythrocytes were done using flow cytometry. The physiological indicators were analyzed using a Mindray BC-5000 Vet automatic hematology analyzer.

Results: Of note, $40.7 \pm 5.9\%$ of erythrocytes changed their structure and shrunk in the *B. microti*-infected group. The percentage of annexin V-positive erythrocytes and the levels of reactive oxygen species (ROS) in the erythrocytes were higher in the *B. microti*-infected group than in the control group at 10dpi. Significant splenomegaly and severe anemia were also observed following *B. microti* infection. The parasitemia level in the *B. microti*-infected splenectomized group was higher than that of the *B. microti*-infected sham group. The population of early erythroblasts increased, and the late erythroblasts decreased in both the bone marrow and spleen tissues of the *B. microti*-infected group at 10dpi.

Discussion: PS exposure and elevated ROS activities were hallmarks of eryptosis in the *B. microti*-infected group. This study revealed for the first time that *B. microti* could also induce eryptosis. At the higher parasitemia phase, the occurrence of severe anemia and significant changes in the abundance of erythroblasts in *B. microti*-infected mice group were established. The spleen plays a critical protective role in controlling *B. microti* infection and preventing anemia. *B. microti* infection could cause a massive loss of late erythroblasts and induce erythropoiesis.

1. Introduction

Babesia microti is a tick-transmitted protozoan hemoparasite and a primary etiological agent of human babesiosis globally, thus making it a serious public health concern (Westblade et al., 2017). It has a global distribution and numerous wild and domestic animals may serve as infection reservoirs (Laha et al., 2015). It is endemic in some USA states but rare and more life-threatening in Europe (Meliani et al., 2006). The actual prevalence of *B. microti* is thought to be substantially underestimated given the typically asymptomatic nature of the infection (Xia et al., 2019). *B. microti* causes malaria-like symptoms and splenomegaly in both infected mice and humans (Djokic et al., 2018; Matsushita et al., 2021). In most cases, mild to moderate babesiosis does not require clinical admission. However, severe disease, which is associated with high risks of organ dysfunctions such as acute respiratory distress syndrome, congestive heart failure, renal failure and liver failure requires immediate attention, particularly in immunocompromised patients (Smith et al., 2020; Krause et al., 2021). Confirmed case definitions have been highly characterized by fever and anemia (Stein et al., 2017). In humans, the overall mortality rate for babesiosis is ~6%–9%, but this rises to 20% in immunodeficient patients (Onyiche et al., 2021).

B. microti infects mammalian erythrocytes. Although erythrocytes lack nuclei and chromosomes, they are significant health indicators during systemic or chronic inflammation because the hematological system is always exposed to peripheral inflammatory mediators and erythrocytes interact with several inflammatory molecules and compounds (Onyiche et al., 2021). Erythrocytes are biconcave discoid cup-shaped stomatocytes or spiculated echinocyte shaped under certain circumstances (Mesarec et al., 2019). The morphology of erythrocytes can be a useful tool to assess the body's physiological state and for definitive diagnosis (Ford, 2013). Primarily, *B. microti* invades mature erythrocytes in mice. During invasion, *Babesia* secrete numerous proteins to support their development and to modify erythrocytes (Hakimi et al., 2022). Adhesive properties and permeability of infected erythrocytes are altered while cell volumes are increased (Park et al., 2015).

Erythrocytes have unique asymmetric cell membranes, and different phospholipid-based molecules are located both inside and outside of the cell (De Rosa et al., 2007). Neutral phospholipids, including phosphatidylcholine and sphingomyelin, are always located in the outer leaflet of the bilayer, whereas phosphatidylserine (PS) and anionic phosphatidylethanolamine are normally distributed in the inner monolayer. During inflammation and other conditions, PS is externalized and erythrocytes can undergo programmed death under stress *via* a process called "eryptosis" (Pretorius et al., 2016). Certain diseases, such as malaria, acute cardiac failure, lung cancer, and hemolytic anemia, have been associated with eryptosis (Lang and Qadri, 2012). Similar to the apoptosis of nucleated cells, eryptosis typically leads to cell shrinkage, cell membrane blebbing, and cell membrane scrambling with PS

translocation to the erythrocyte surface (Maguire et al., 1991; Brand et al., 2003). Expression of PS on the outer membrane induces phagocytosis of damaged erythrocytes and the adhesion of erythrocytes to the endothelium (Pankova-Kholmyansky et al., 2003). Eryptosis is a form of suicidal erythrocyte death because it prevents erythrocytes from undergoing haemolysis, causing erythrocyte cell death (Qadri et al., 2017).

The spleen performs numerous immune functions and participates in hematopoiesis, blood-borne pathogen clearance, and erythrocyte homeostasis (Xue et al., 2021). Macrophages in the spleen serve mostly to filter blood and phagocytose aging red blood cells (RBC). When PS is externalized on the membrane surface, it can serve as an "eat-me" signal and be recognized by macrophages (Lemke, 2019). In recent years, more work has been done to clarify the relationship between eryptosis and *Plasmodium*. Notably, manipulating eryptosis of erythrocytes is considered to be a potential approach for malaria control (Lang et al., 2015; Boulet et al., 2018). However, whether *B. microti* can induce eryptosis, and the function of the spleen in this process, remains unknown. Herein, we used scanning electron microscope (SEM) and transmission electron microscope (TEM) technologies to observe the morphological changes of erythrocytes and flow cytometry to determine the effect of *B. microti* on erythrocytes.

2. Materials and methods

2.1. Parasites

Babesia microti strain ATCC®PRA-99TM used in this study was obtained from the Institute of Laboratory Animal Sciences, Chinese Academy of Medical Sciences (CAMS). This strain was maintained through serial passage in i.p. infected Bagg's albino/c (BALB/c) mice. Infection was confirmed by observing for the presence of parasites in thin blood smears using an optical microscope at 3 or 5 dpi.

2.2. Murine infection model and parasitemia

Female specific-pathogen-free laboratory-bred house mice (BALB/c), aged 6–8 weeks, were purchased from the Shanghai Laboratory Animal Center (China). The housing and maintenance of the rodents complied with national regulations. Orbital blood samples were collected from the infected mice and diluted with sterile saline to 5×10^7 *B. microti*-infected erythrocytes per milliliter. The mice in infected groups were intraperitoneally injected with 10^7 infected erythrocytes in a volume of 0.2 ml. To ensure all mice received equal numbers of viable parasites, they were infected with equal parasite inoculum at the same time. Blood for smears was collected daily from the tail snip for 30 days post-infection (dpi) to evaluate the parasitemia level. The proportion of infected erythrocytes was calculated as previously described (Skariah et al., 2017), based on the number of infected

erythrocytes per 1,000 erythrocytes. The counting was performed using a light microscope (Olympus CX41, Tokyo, Japan). The animal protocols were approved by the Laboratory Animal Welfare & Ethics Committee (LAWEC), National Institute of Parasitic Diseases of China CDC (IDP-2019-16).

2.3. Preparation of blood pellets for SEM and TEM

Orbital sinus blood samples were collected in ethylenediaminetetraacetic acid at 10 dpi. The blood was immediately fixed for 2 h by electron microscopy fixative at room temperature. The preservation and transportation temperature was 4°C. Each sample was washed three times for 15 min with 0.1 M phosphate buffer (PB) (pH 7.4) and stained for 1–2 h at room temperature using 1% osmium tetroxide in 0.1 M PB (pH 7.4). The cells were dehydrated for 15 min in serial ethanol concentrations of 50%, 70%, 80%, 90%, and 95% ethanol, twice in 100% ethanol, and finally in isoamyl acetate. The cells were dried using a critical point dryer (K850, Quorum, United Kingdom) and attached to metallic stubs using carbon stickers and sputter-coated with gold for 30 s. The cells were observed using an SEM (SU8100, HITACHI, Japan) and a TEM (HT7800, HITACHI, Japan).

2.4. Quantification of phosphatidylserine exposure

Mouse blood cells were washed twice using Ringer's solution supplemented with 5 mM calcium chloride. To detect FITC annexin V-positive cells, the erythrocytes were suspended in an annexin-binding buffer (BD Pharmingen, San Diego, United States) with FITC annexin V (1:200 dilution, BD Pharmingen, San Diego, United States) and incubated for 15 min at room temperature. Well mixing was performed by pipetting. Finally, erythrocytes were diluted five times in the annexin-binding buffer before analysis in the FACSVerse flow cytometer (Beckman Coulter, CytoFlex S, United States) at an excitation wavelength of 488 nm (blue laser) and emission wavelength of 530 nm.

2.5. Quantification of oxidative stress

The oxidative stress level was determined using 2′, 7′-dichlorodihydrofluorescein diacetate (DCFDA; Sigma, Schnelldorf, Germany). Briefly, the erythrocytes (4 μl) were mixed in 1 ml Ringer's solution, from which 150 μl of the cell suspension was centrifuged at 1,600 rpm for 3 min at room temperature. The collected cells were stained with DCFDA (10 μM) in Ringer's solution at 37°C for 30 min and washed three times with 150 μl of Ringer's solution. The DCFDA-loaded erythrocytes were then resuspended in 200 μl Ringer's solution (125 mM sodium chloride, 5 mM potassium chloride, 1 mM magnesium sulfate, 32 mM

hydroxyethyl piperazine ethane sulfonic acid, 5 mM glucose, and 1 mM calcium chloride; pH 7.4). The reactive oxygen species (ROS)-dependent fluorescence intensity was measured at an excitation wavelength of 488 nm and an emission wavelength of 530 nm.

2.6. Quantification of intracellular Ca^{2+}

Calcium ion influx was evaluated using Fluo-3 Am (Invitrogen, Carlsbad, United States) staining. Erythrocytes were suspended in 200 μl Ringer's solution supplemented with Fluo-3 Am (1 μM) and incubated at 37°C for 30 min. Thereafter, the RBCs were stained with Fluo-3 Am, rinsed, and resuspended in Ringer's solution, and analyzed using a 488 nm blue laser and a 530 nm bandpass filter.

2.7. Murine splenectomy and routine blood testing

Mice were anesthetized using ether and a small incision was made under the left costal margin before ligating the splenic vessels. For mice in the sham group, the spleens were exposed but not removed. Blood was collected from the orbital sinus into a microhematocrit tube every 5 days until 20 dpi. The blood was analyzed using a Vet automatic hematology analyzer (BC-5000, Mindray, China) for animals. The physiological indicators measured included the RBC count, hemoglobin concentration (HGB), red cell distribution width standard deviation (RDW-SD), and red cell distribution width coefficient of variation (RDW-CV).

2.8. Erythropoiesis analysis

Erythropoiesis was analyzed as previously described (Wang et al., 2010). The mouse bone marrow cells were prepared as described previously (Yáñez and Goodridge, 2018). Briefly, the femurs of the mice were dissected from the legs, and the marrow cavity was opened. Bone marrow was harvested with cold, sterile saline until the bones appeared white. The mouse spleens were mechanically dissociated into single-cell suspensions and incubated with FITC Rat Anti-Mouse CD71 antibody (1:200, CD71-FITC, BD Biosciences, San Diego, United States) and APC Rat Anti-Mouse TER-119 antibody (1:200, TER119-APC, BD Biosciences, San Diego, United States) for 45 min. Then, cells were washed by adding 3 ml of staining buffer to each sample tube. Samples were analyzed in the Fortessa X20 flow cytometer (BD Biosciences, San Jose, CA) at an excitation wavelength of 488 nm or 640 nm and an emission wavelength of 520 nm or 680 nm.

2.9. Statistical analysis

Data were analyzed using Microsoft Excel® software (version 2019) and GraphPad Prism (version 8.3.0). Continuous data were

expressed as the mean ± SD. The difference between groups was analyzed using the student's t-test, whereas analysis of variance (ANOVA) was used for multiple groups. Statistical significance was set at $p < 0.05$.

3. Results

3.1. *Babesia microti* infection induced morphological changes in erythrocytes

SEM and TEM analysis revealed that the control group had bowl-shaped erythrocytes (Figures 1A,C). In contrast, the *B. microti*-infected group had a significant increase in spurred erythrocytes that were irregularly distributed, variably sized, and with pointy projections off their surfaces (Figure 1B). *Babesia microti* were visible near the membrane of polymorphic erythrocytes under TEM (Figure 1D). Notably, 40.7 ± 5.9% of erythrocytes in the *B. microti*-infected group lost their biconcave structures, shrunk, and exhibited membrane blebbing. This proportion was significantly higher than that in the control group ($t = 12.9$, $p < 0.01$; Figure 1E).

3.2. *Babesia microti* infection enhanced eryptosis

We analyzed the PS surface expression, ROS level, and calcium ion activity of erythrocytes to evaluate the extent of accelerated eryptosis. PS surface expression was quantified using FACS analysis after staining the cells with fluorescein isothiocyanate (FITC)-labeled Annexin V. Of note, the percentage of annexin V-positive erythrocytes was significantly higher in the *B. microti*-infected group than in the control group at 5, 10, and 15 dpi, indicating increased cell surface expression of PS ($t = 4.7$, 5.2, 5.9, $p < 0.01$; Figure 2A). The levels of ROS in the erythrocytes were also higher in the *B. microti*-infected group than in the control group at 10 dpi ($t = 7.4$, $p < 0.01$; Figure 2B). The calcium ion activity of the erythrocytes from each group was quantified using Fluo-3 fluorescence. The calcium ion activity increased slightly in *B. microti*-infected mice than in mice in the control group at 10 dpi, but not significantly (Figure 2C).

3.3. *Babesia microti* infection caused splenomegaly and severe anemia

The weights and lengths of the spleens were measured at 0, 5, 10, 15, and 20 dpi. The average spleen weights of mice in the *B. microti*-infected group were 2.34 ± 0.09, 3.36 ± 0.13, 3.08 ± 0.08, and 2.74 ± 0.25 g while those of the control group were 1.77 ± 0.16, 1.72 ± 0.08, 1.70 ± 0.14, and 1.78 ± 0.08 g at 5, 10, 15, and 20 dpi ($t = 6.81$, 23.19, 18.78, and 8.11, respectively; $p < 0.01$) (Supplementary Figure S1A). Notably, the spleen enlarged from 1.73 ± 0.05 cm at 0 dpi to 3.36 ± 0.13 cm at 10 dpi, and then recovered to 2.74 ± 0.25 cm at 20 dpi upon *B. microti*
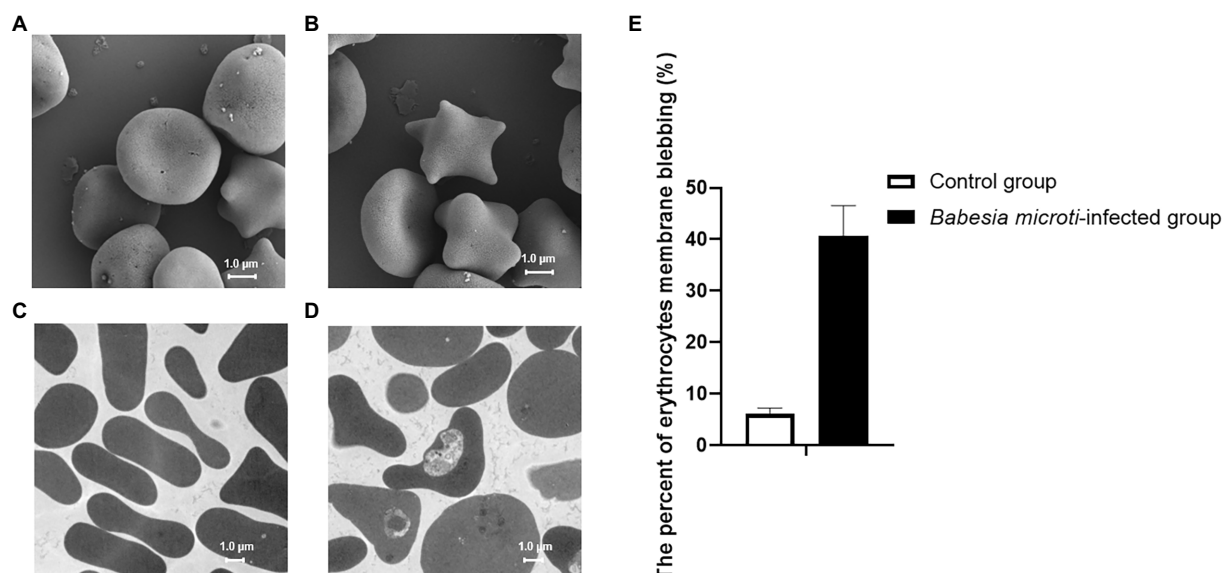
FIGURE 1
Erythrocyte morphology as seen under a scanning electron microscope (SEM) and transmission electron microscope (TEM). **(A)** SEM image showing biconcave-shaped erythrocytes of mice in the control group. **(B)** SEM image showing membrane blebbed erythrocytes of mice in the *Babesia microti(B. microti)*-infected group. **(C)** TEM image showing regularly shaped erythrocytes of mice in the control group. **(D)** TEM image showing the changed shape of erythrocytes of mice in the *B. microti*-infected group. The scale bar is 1.0 μm. **(E)** Bar graph showing the arithmetic means±SD (n =5) of the proportion of erythrocytes with a blebbing membrane without (white bar) and with (black bars) *B. microti* infection.
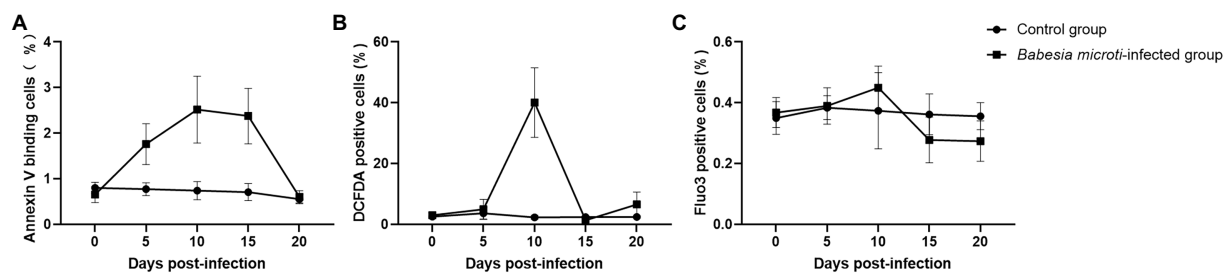
FIGURE 2
Eryptosis assays after *B. microti* infection. Line graphs showing that **(A)** *B. microti* induced more PS exposure to the cell surface of erythrocytes, **(B)** ROS levels in the erythrocytes were higher in the *B. microti* –infected group at 10dpi, and **(C)** Calcium ion activity of erythrocytes increased slightly in *B. microti*-infected group at 10dpi, but not significantly. The results are expressed as the mean percentage of positive cells $\pm$ the standard deviation (SD) from five mice.

infection (Supplementary Figures S1B,C). We harvested the spleen of mice and measured the parasitemia levels in peripheral blood samples from the *B. microti*-infected sham and splenectomized groups (sham mice had the spleen while splenectomized mice had their spleens harvested) to assess the role of the spleen during *B. microti* infection. Parasitemia in both groups increased rapidly at 6 dpi and peaked at 10 or 11 dpi. Of note, $40.56 \pm 4.14\%$ of the erythrocytes from the *B. microti*-infected sham mice and $56.88 \pm 3.97\%$ of the erythrocytes from the *B. microti*-infected splenectomized mice were infected at 10 and 11 dpi, respectively. The peak parasitemia level of the *B. microti*-infected splenectomized group was higher than that of the *B. microti*-infected sham group and persisted for ~6 days. The difference in parasitemia level between the *B. microti*-infected sham and splenectomized groups at 11–20 dpi was statistically significant ($p < 0.01$). In the *B. microti*-infected sham and splenectomized groups, the parasites could not be detected in erythrocytes by 23 and 27 dpi, respectively. These results indicate that the spleen plays a defensive role in *B. microti* infection (Figure 3A).

The hematological parameters of mice in the experimental groups revealed significantly low RBC and HGB in the *B. microti*-infected sham and splenectomized mice compared to mice in the uninfected sham and splenectomized groups at 10 and 15 dpi. However, the RBCs and HGB of mice in the *B. microti*-infected splenectomized group were lower than those in the *B. microti*-infected sham group at 15 and 20 dpi (Figures 3B,C). Conversely, the RDW-CV and RDW-SD of mice in the *B. microti*-infected sham and the splenectomized group were higher than those of mice in the uninfected sham and splenectomized group at 10 and 15 dpi. However, the RDW-CV and RDW-SD of the mice in the *B. microti*-infected splenectomized group were higher than those of mice in the *B. microti*-infected sham group at 15 and 20 dpi (Figures 3D,E). Images for the morphologies of *B. microti*-infected erythrocytes are shown in Supplementary Figure S2. Multiple variabilities, including *anisochromia, acanthocytes*, and Howell–Jolly bodies, were observed in *B. microti*-infected cells.

3.4. *Babesia microti* infection increased erythropoiesis

Erythroid differentiation can be monitored by targeting the erythroid-specific TER119 and nonerythroid-specific CD71 antigens using flow cytometry (Koulnis et al., 2011; An and Chen, 2018). By combining Ter119 and CD71 expression, erythroid cells could be distinguished into four subpopulations: Ter119^{med}CD71^{high}, Ter119^{high}CD71^{high} Ter119^{high}CD71^{med}, and Ter119^{high}CD71^{low}, representing the proerythroblasts-equivalent cells, basophilic erythroblasts-equivalent cells, late basophilic and polychromatophilic erythroblasts-equivalent cells, and orthochromatic erythroblasts-equivalent cells, respectively. Flow cytometry revealed a dramatic increase in the early erythroblast population (basophilic erythroblasts-equivalent cells) and a decrease in the late erythroblast population (orthochromatic erythroblasts-equivalent cells) in both the bone marrow and spleen tissues of the *B. microti*-infected group at 10 dpi (Figures 4A,B). Simultaneously, the percentages of proerythroblasts and late basophilic and polychromatophilic erythroblasts-equivalent cells were elevated in the spleen at 10 dpi (Figure 4B). The analysis of the bone marrow and spleen cells by the Wright-Giemsa staining method was not performed. These results suggest that the maturation of the late erythroblast population was significantly suppressed by *B. microti* infection and the early erythroblast population was recruited to compensate for the loss of abnormally fragile erythrocytes.

4. Discussion

Manipulation of human erythrocyte eryptosis is a potential approach for malaria control, however, it has not been established whether *B. microti* can induce eryptosis. In this study, we used several advanced tools, including scanning electron microscopy, transmission electron microscopy, flow cytometry, and murine splenectomy to reveal, for the first time, that *B. microti* can induce
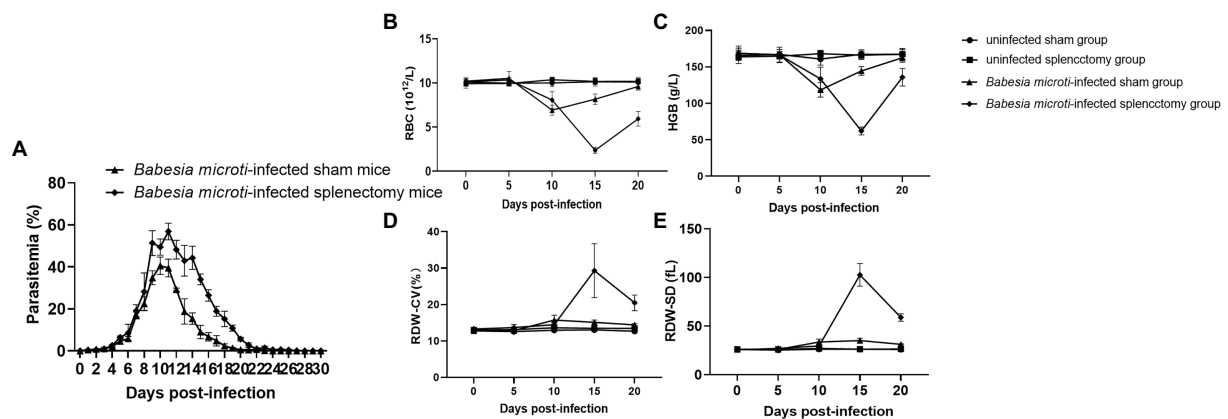
FIGURE 3
Changes in blood parasitemia and parameters after *B. microti* infection. Line graphs showing **(A)** the peak parasitemia level of the *B. microti*-infected splenectomized group was higher than that of the *B. microti*-infected sham group and persisted for ~6days, **(B)** the red blood cell (RBC) count, **(C)** Hemoglobin concentration (HGB), **(D)** Red cell distribution width coefficient of variation (RDW-CV), and **(E)** Red cell distribution width standard deviation (RDW-SD). The results are expressed as the mean±standard deviation (SD) of five mice.
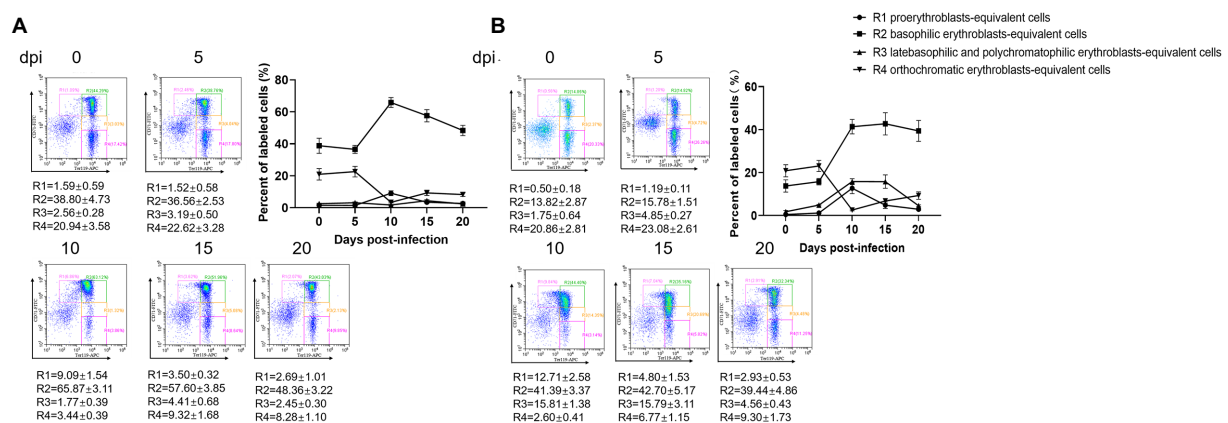
FIGURE 4
Erythropoiesis of red blood cells after infection with *B. microti*. Line graph showing the arithmetic means±SD of the percentage of Ter119-PE and CD71-FITC labeled bone marrow **(A)** and splenocytes **(B)** isolated from mice in the *B. microti*-infected group.

eryptosis, and clarify the roles of the spleen in controlling infection and preventing anemia.

The membranes of erythrocytes can be detrimentally affected under certain physiological or pathological conditions, causing them to undergo programmed cell death, known as eryptosis (Lang et al., 2017). Eryptosis displays some comparable hallmarks, such as cell shrinkage, membrane blebbing, and PS exposure to the cell surface, which is similar to apoptosis (Berg et al., 2001). *Babesia* spp. use gliding motility to migrate and penetrate the erythrocytes. Merozoites of Babesia can sometimes egress from erythrocytes without rupturing the membrane (Asada et al., 2012). Erythrocytes in the *B. microti*-infected group shrunk, and their cell membranes exhibited blebbing, which were typical features of eryptosis. We thus detected the degree of PS surface exposure, ROS level, and calcium ion activity in erythrocytes to confirm if *B. microti* induced eryptosis. Notably,

the level of PS exposure was higher in the *B. microti*-infected group than in the control group at 5, 10, and 15 dpi, suggesting that eryptosis occurred. PS promotes blood coagulation and plays a pivotal role in recognizing and removing defective eryptosis *via* a PS-recognizing receptor on phagocytic cells (Zwaal et al., 2005). The increase in intracellular ROS and calcium entry are also important factors that promote eryptosis (Fink et al., 2019). The ROS activity was also higher in the *B. microti*-infected group than in the control group at 10 dpi. ROS are thought to play a dual role in the physiological functioning of body systems. Though they are toxic byproducts of aerobic metabolism, they are also involved in regulating signal transductions (Mittler, 2017). In malaria, ROS are generated as a byproduct of parasite hemoglobin metabolism in erythrocytes. Anti-oxidative proteins in *B. microti* have been reported as potential targets of anti-parasitic drugs (Huang et al., 2018). Ca^{2+}

plays a key role in erythrocyte invasion; increased calcium concentration stimulates eryptosis (Singh et al., 2012). In this study, calcium concentration did not change significantly during *B. microti* infection, suggesting that the calcium ion transport channel in cell membranes was not activated. However, a morphological comparison of erythrocytes infected with *B. microti* and normal erythrocytes was not performed. The changes in *B. microti* infected-erythrocytes could be elucidated further using the DNA/RNA specific dyes, including Hoechst 33342 (Moles et al., 2015), Syto16 (Brand et al., 2008), and flow cytometry.

Eryptosis functions as a protective mechanism in some cases because it provides the erythrocytes with another form of erythrocyte cell death other than haemolysis (Bartolmäs et al., 2018). Homeostasis between eryptosis and antieryptosis mechanisms is vital in maintaining normal erythrocyte count in the blood, thereby preventing irregularities. Human babesiosis is usually associated with severe hemolytic anemia and splenomegaly (Dumic et al., 2020). Haemolysis of injured or damaged erythrocytes causes the release of erythrocyte contents into the bloodstream. In the same line, the spleen plays an important role in hematopoiesis and erythrocyte clearance (Lewis et al., 2019). We used a splenectomized mice model to observe the differences in parasitemia and hematological parameters between mice in *B. microti*-infected sham and splenectomized groups. Splenectomized mice models have been used to study the functions of splenic T_{reg} cells, the roles of the spleen in decreasing platelet counts, and the filtering functions of the spleen (Manning and McDonald, 1997; Grunewald et al., 2017; Wang et al., 2019). Preliminary results suggest that the integrity of splenic functions affects liver morphology and that the spleen has a protective function in autoimmune hepatitis. In this study, differences between the sham and splenectomized groups were subsequently used to evaluate the anemic condition, and the spleen function in *B. microti-infected* mice. Unlike severe combined immunodeficient (SCID) mice and nonobese diabetic SCID mice, *in vivo* models using BALB/c mice have shown that *B. microti* infection can resolve spontaneously after reaching peak parasitemia (Lu et al., 2012). Parasitemia remained higher in mice in the *B. microti*-infected splenectomized group for several days before gradually decreasing compared to mice in the *B. microti*-infected sham group. Moreover, the extent of splenomegaly was consistent with the level of parasitemia. Apart from the spleen, which is a major site for removal of infected erythrocytes, the liver and lung tissues can also exhibit severe injury as complications of *B. microti* infections (Alvarez De Leon et al., 2019; Hu et al., 2021). It has been reported that a splenectomized patient infected with babesia recovered with only symptomatic treatment (Rosner et al., 1984). This indicates that the spleen is critical, but not the only organ involved, in controlling *B. microti* infection.

The RBCs and HGB values were significantly lower in the *B. microti*-infected splenectomized group compared to the *B. microti*-infected sham group, indicating more severe anemia

occurred in mice of the splenectomized group after *B. microti* infection. Therefore, the absence of a spleen may promote further damage to the erythrocytes. The increases in RDW-CV and RDW-SD at 15 dpi indicate a significant change in the morphology of the erythrocytes. Consistent with a previous report (Park et al., 2015), the cellular volume of the erythrocytes increased as a result of *B. microti* infection when observed under 3D holographic microscopy. Changes in hematological parameters reflect the deregulation of erythrocyte homeostasis and the declining capacity of the spleen to clear abnormal erythrocytes (McKenzie et al., 2018).

Anemia ensues when increased eryptosis results in the loss of circulating erythrocytes without the combined increase in erythropoiesis and sustained increase of reticulocytes (Singh et al., 2012). Erythropoiesis is defined as the generation of erythrocytes from hematopoietic stem and progenitor cells through a series of intermediate progenitors (Nandakumar et al., 2016). Erythroid burst-forming units and erythroid colony-forming units (CFU-E) are early progenitors in the erythroid lineage (Palis and Koniski, 2018). CFU-E progenitors differentiate through several morphologically defined stages which can be grouped into four populations: proerythroblasts, basophilic erythroblasts, polychromatophilic erythroblasts, and orthochromatophilic erythroblasts. Erythropoiesis results showed that the percentage of basophilic erythroblasts-equivalent cells in the bone marrow and spleen dramatically increased, and the percentage of orthochromatic erythroblasts-equivalent cells decreased, suggesting that the main cause of severe anemia in *B. microti* infection might be the loss of erythrocytes coupled with the inability of enhanced erythropoiesis to compensate for this loss fully. Since it is challenging to accurately quantify the absolute number of erythroblasts in the bone marrow or spleen, we did not determine if there were changes in the production of erythrocyte precursors.

Giemsa or Wright's blood smear staining is a useful and convenient method for definitive babesiosis diagnosis. Macrocytic anemia was observed in the *B. microti*-infected group, and the mean corpuscular volume was higher in the infected group than in the non-infected group. However, cytopreps of single-cell suspensions of the bone marrow and spleen from *B. microti*-infected mice and cell morphology analyses using Wright-Giemsa were not performed in this study. The outcome could reveal any alteration in the ratio of erythroid to granulocytic precursors or lymphocytes (Slavova-Azmanova et al., 2013). Additionally, whether *B. microti* infection influences the lifespan of erythrocytes remains unclear. The molecular mechanism underlying *B. microti*-induced eryptosis and spleen modulations need further investigation.

5. Conclusion

Erythrocytes in the *B. microti*-infected group underwent eryptosis. The increased PS exposure and ROS activity in the

B. microti-infected mice model confirmed eryptosis, an erythrocyte's suicidal type of cell death. These results suggest that the spleen plays a protective role in controlling *B. microti* infection and preventing anemia. *Babesia microti* infection could cause a massive loss of late erythroblasts and induce erythropoiesis.

Data availability statement

The raw data supporting the conclusions of this article will be made available by the authors, without undue reservation.

Ethics statement

The animal study was reviewed and approved by the Laboratory Animal Welfare & Ethics Committee (LAWEC), National Institute of Parasitic Diseases of China CDC.

Author contributions

PS and Y-CC: data curation and writing the original manuscript draft. PS, Y-CC, and M-XC: methodology. S-HC and J-XC: writing, review and project supervision. All authors contributed to the article and approved the submitted version.

Funding

Conflict of interest

The authors declare that the research was conducted in the absence of any commercial or financial relationships that could be construed as a potential conflict of interest.

Publisher's note

All claims expressed in this article are solely those of the authors and do not necessarily represent those of their affiliated organizations, or those of the publisher, the editors and the reviewers. Any product that may be evaluated in this article, or claim that may be made by its manufacturer, is not guaranteed or endorsed by the publisher.

Supplementary material

The Supplementary material for this article can be found online at: https://www.frontiersin.org/articles/10.3389/fmicb.2022.1083467/full#supplementary-material

SUPPLEMENTARY FIGURE S1
General features changes of the spleen in non-infected and *Babesia microti*-infected mice. The weights **(A)**, lengths **(B)**, and images **(C)** of spleens in non-infected and *Babesia microti*-infected mice.

SUPPLEMENTARY FIGURE S2
Morphologies of *Babesia microti*-infected erythrocytes in blood smears. Images of erythrocytes infected with *Babesia microti* at 0dpi **(A)**, 5dpi **(B)**, 10dpi **(C)**, 15dpi **(D)**, and 20 dpi **(E)**.

References

Alvarez De Leon, S., Srivastava, P., Revelo, A. E., Kadambi, A., El Khoury, M. Y., Wormser, G. P., et al. (2019). Babesiosis as a cause of acute respiratory distress syndrome: a series of eight cases. *Postgrad. Med.* 131, 138–143. doi: 10.1080/00325481.2019.1558910

An, X., and Chen, L. (2018). Flow cytometry (FCM) analysis and fluorescence-activated cell sorting (FACS) of erythroid cells. *Methods Mol. Biol.* 1698, 153–174. doi: 10.1007/978-1-4939-7428-3_9

Asada, M., Goto, Y., Yahata, K., Yokoyama, N., Kawai, S., Inoue, N., et al. (2012). Gliding motility of Babesia bovis merozoites visualized by time-lapse video microscopy. *PLoS One* 7:e35227. doi: 10.1371/journal.pone.0035227

Bartolmäs, T., Mayer, B., Balola, A. H., and Salama, A. (2018). Eryptosis in autoimmune haemolytic anaemia. *Eur. J. Haematol.* 100, 36–44. doi: 10.1111/ejh.12976

Berg, C. P., Engels, I. H., Rothbart, A., Lauber, K., Renz, A., Schlosser, S. F., et al. (2001). Human mature red blood cells express caspase-3 and caspase-8, but are devoid of mitochondrial regulators of apoptosis. *Cell Death Differ.* 8, 1197–1206. doi: 10.1038/sj.cdd.4400905

Boulet, C., Doerig, C. D., and Carvalho, T. G. (2018). Manipulating Eryptosis of human red blood cells: a novel antimalarial strategy? *Front. Cell. Infect. Microbiol.* 8:419. doi: 10.3389/fcimb.2018.00419

Brand, V., Koka, S., Lang, C., Jendrossek, V., Huber, S. M., Gulbins, E., et al. (2008). Influence of amitriptyline on eryptosis, parasitemia and survival of plasmodium berghei-infected mice. *Cell. Physiol. Biochem.* 22, 405–412. doi: 10.1159/000185482

Brand, V. B., Sandu, C. D., Duranton, C., Tanneur, V., Lang, K. S., Huber, S. M., et al. (2003). Dependence of plasmodium falciparum in vitro growth on the cation permeability of the human host erythrocyte. *Cell. Physiol. Biochem.* 13, 347–356. doi: 10.1159/000075122

De Rosa, M. C., Carelli Alinovi, C., Galtieri, A., Scatena, R., and Giardina, B. (2007). The plasma membrane of erythrocytes plays a fundamental role in the transport of oxygen, carbon dioxide and nitric oxide and in the maintenance of the reduced state of the heme iron. *Gene* 398, 162–171. doi: 10.1016/j.gene.2007.02.048

Djokic, V., Akoolo, L., and Parveen, N. (2018). Babesia microti infection changes host spleen architecture and is cleared by a Th1 immune response. *Front. Microbiol.* 9:85. doi: 10.3389/fmicb.2018.00085

Dumic, I., Madrid, C., Rueda Prada, L., Nordstrom, C. W., Taweesedt, P. T., and Ramanan, P. (2020). Splenic complications of Babesia microti infection in humans: a systematic review. *Can. J. Infect. Dis. Med. Microbiol.* 2020:6934149. doi: 10.1155/2020/6934149

Fink, M., Bhuyan, A. A. M., Nürnberg, B., Faggio, C., and Lang, F. (2019). Triggering of eryptosis, the suicidal erythrocyte death, by phenoxodiol. *Naunyn Schmiedeberg's Arch. Pharmacol.* 392, 1311–1318. doi: 10.1007/s00210-019-01681-8

Ford, J. (2013). Red blood cell morphology. *Int. J. Lab. Hematol.* 35, 351–357. doi: 10.1111/ijlh.12082

Grunewald, S. T. F., Rezende, A. B., Figueiredo, B. B. M., Mendonça, A. C. P., Almeida, C. S., De Oliveira, E. E., et al. (2017). Autotransplantation of spleen

mitigates drug-induced liver damage in Splenectomized mice. *J. Investig. Surg.* 30, 368–375. doi: 10.1080/08941939.2016.1255806

Hakimi, H., Yamagishi, J., Kawazu, S. I., and Asada, M. (2022). Advances in understanding red blood cell modifications by Babesia. *PLoS Pathog.* 18:e1010770. doi: 10.1371/journal.ppat.1010770

Hu, Y., Wang, M., Ren, S., Masoudi, A., Xue, X., Wang, X., et al. (2021). Quantitative proteomics and phosphoproteomic analyses of mouse livers after tick-borne Babesia microti infection. *Int. J. Parasitol.* 51, 167–182. doi: 10.1016/j.ijpara.2020.09.002

Huang, J., Xiong, K., Zhang, H., Zhao, Y., Cao, J., Gong, H., et al. (2018). Molecular characterization of Babesia microti thioredoxin (BmTrx2) and its expression patterns induced by antiprotozoal drugs. *Parasit. Vectors* 11:38. doi: 10.1186/s13071-018-2619-9

Koulnis, M., Pop, R., Porpiglia, E., Shearstone, J. R., Hidalgo, D., and Socolovsky, M. (2011). Identification and analysis of mouse erythroid progenitors using the CD71/TER119 flow-cytometric assay. *J. Vis. Exp.* 5:2809. doi: 10.3791/2809

Krause, P. J., Auwaerter, P. G., Bannuru, R. R., Branda, J. A., Falck-Ytter, Y. T., Lantos, P. M., et al. (2021). Clinical practice guidelines by the Infectious Diseases Society of America (IDSA): 2020 guideline on diagnosis and Management of Babesiosis. *Clin. Infect. Dis.* 72, e49–e64. doi: 10.1093/cid/ciaa1216

Laha, R., Das, M., and Sen, A. (2015). Morphology, epidemiology, and phylogeny of Babesia: an overview. *Trop. Parasitol.* 5, 94–100. doi: 10.4103/2229-5070.162490

Lang, F., Bissinger, R., Abed, M., and Artunc, F. (2017). Eryptosis – the neglected cause of anemia in end stage renal disease. *Kidney Blood Press. Res.* 42, 749–760. doi: 10.1159/000484215

Lang, F., Jilani, K., and Lang, E. (2015). Therapeutic potential of manipulating suicidal erythrocyte death. *Expert Opin. Ther. Targets* 19, 1219–1227. doi: 10.1517/14728222.2015.1051306

Lang, F., and Qadri, S. M. (2012). Mechanisms and significance of eryptosis, the suicidal death of erythrocytes. *Blood Purif.* 33, 125–130. doi: 10.1159/000334163

Lemke, G. (2019). How macrophages deal with death. *Nat. Rev. Immunol.* 19, 539–549. doi: 10.1038/s41577-019-0167-y

Lewis, S. M., Williams, A., and Eisenbarth, S. C. (2019). Structure and function of the immune system in the spleen. *Sci. Immunol.* 4:eaau6085. doi: 10.1126/sciimmunol.aau6085

Lu, Y., Cai, Y. C., Chen, S. H., Chen, J. X., Guo, J., Chen, M. X., et al. (2012). Establishment of the experimental animal model of Babesia microti. *Zhongguo Ji Sheng Chong Xue Yu Ji Sheng Chong Bing Za Zhi* 30, 423–427. (in Chinese).

Maguire, P. A., Prudhomme, J., and Sherman, I. W. (1991). Alterations in erythrocyte membrane phospholipid organization due to the intracellular growth of the human malaria parasite, plasmodium falciparum. *Parasitology* 102, 179–186. doi: 10.1017/s0031182000062466

Manning, K. L., and Mcdonald, T. P. (1997). C3H mice have larger spleens, lower platelet counts, and shorter platelet lifespans than C57BL mice: an animal model for the study of hypersplenism. *Exp. Hematol.* 25, 1019–1024. PMID: 9293898

Matsushita, Y., Ono, W., and Ono, N. (2021). Flow cytometry-based analysis of the mouse bone marrow stromal and perivascular compartment. *Methods Mol. Biol.* 2308, 83–94. doi: 10.1007/978-1-0716-1425-9_7

Mckenzie, C. V., Colonne, C. K., Yeo, J. H., and Fraser, S. T. (2018). Splenomegaly: pathophysiological bases and therapeutic options. *Int. J. Biochem. Cell Biol.* 94, 40–43. doi: 10.1016/j.biocel.2017.11.011

Meliani, P., Khatibi, S., Randazzo, S., Gorenflot, A., and Marchou, B. (2006). Human babesiosis. *Med. Mal. Infect.* 36, 499–504. doi: 10.1016/j.medmal.2006.07.002

Mesarec, L., Góźdź, W., Iglič, A., Kralj-Iglič, V., Virga, E. G., and Kralj, S. (2019). Normal red blood cells' shape stabilized by membrane's in-plane ordering. *Sci. Rep.* 9:19742. doi: 10.1038/s41598-019-56128-0

Mittler, R. (2017). ROS are good. *Trends Plant Sci.* 22, 11–19. doi: 10.1016/j.tplants.2016.08.002

Moles, E., Urbán, P., Jiménez-Díaz, M. B., Viera-Morilla, S., Angulo-Barturen, I., Busquets, M. A., et al. (2015). Immunoliposome-mediated drug delivery to plasmodium-infected and non-infected red blood cells as a dual therapeutic/

prophylactic antimalarial strategy. *J. Control. Release* 210, 217–229. doi: 10.1016/j.jconrel.2015.05.284

Nandakumar, S. K., Ulirsch, J. C., and Sankaran, V. G. (2016). Advances in understanding erythropoiesis: evolving perspectives. *Br. J. Haematol.* 173, 206–218. doi: 10.1111/bjh.13938

Onyiche, T. E., Răileanu, C., Fischer, S., and Silaghi, C. (2021). Global distribution of Babesia species in questing ticks: a systematic review and meta-analysis based on published literature. *Pathogens* 10:230. doi: 10.3390/pathogens10020230

Palis, J., and Koniski, A. (2018). Functional analysis of erythroid progenitors by Colony-forming assays. *Methods Mol. Biol.* 1698, 117–132. doi: 10.1007/978-1-4939-7428-3_7

Pankova-Kholmyansky, I., Dagan, A., Gold, D., Zaslavsky, Z., Skutelsky, E., Gatt, S., et al. (2003). Ceramide mediates growth inhibition of the plasmodium falciparum parasite. *Cell. Mol. Life Sci.* 60, 577–587. doi: 10.1007/s000180300049

Park, H., Hong, S. H., Kim, K., Cho, S. H., Lee, W. J., Kim, Y., et al. (2015). Characterizations of individual mouse red blood cells parasitized by Babesia microti using 3-D holographic microscopy. *Sci. Rep.* 5:10827. doi: 10.1038/srep10827

Pretorius, E., Du Plooy, J. N., and Bester, J. (2016). A comprehensive review on Eryptosis. *Cell. Physiol. Biochem.* 39, 1977–2000. doi: 10.1159/000447895

Qadri, S. M., Bissinger, R., Solh, Z., and Oldenborg, P. A. (2017). Eryptosis in health and disease: a paradigm shift towards understanding the (patho)physiological implications of programmed cell death of erythrocytes. *Blood Rev.* 31, 349–361. doi: 10.1016/j.blre.2017.06.001

Rosner, F., Zarrabi, M. H., Benach, J. L., and Habicht, G. S. (1984). Babesiosis in splenectomized adults. Review of 22 reported cases. *Am. J. Med.* 76, 696–701. doi: 10.1016/0002-9343(84)90298-5

Singh, S., Gudzenko, V., and Fink, M. P. (2012). Pathophysiology of perioperative anaemia. *Best Pract. Res. Clin. Anaesthesiol.* 26, 431–439. doi: 10.1016/j.bpa.2012.11.002

Skariah, S., Arnaboldi, P., Dattwyler, R. J., Sultan, A. A., Gaylets, C., Walwyn, O., et al. (2017). Elimination of Babesia microti is dependent on Intraerythrocytic killing and CD4(+) T cells. *J. Immunol.* 199, 633–642. doi: 10.4049/jimmunol.1601193

Slavova-Azmanova, N. S., Kucera, N., Satiaputra, J., Stone, L., Magno, A., Maxwell, M. J., et al. (2013). Gain-of-function Lyn induces anemia: appropriate Lyn activity is essential for normal erythropoiesis and Epo receptor signaling. *Blood* 122, 262–271. doi: 10.1182/blood-2012-10-463158

Smith, R. P., Hunfeld, K. P., and Krause, P. J. (2020). Management strategies for human babesiosis. *Expert Rev. Anti-Infect. Ther.* 18, 625–636. doi: 10.1080/14787210.2020.1752193

Stein, E., Elbadawi, L. I., Kazmierczak, J., and Davis, J. P. (2017). Babesiosis surveillance – Wisconsin, 2001-2015. *MMWR Morb. Mortal. Wkly Rep.* 66, 687–691. doi: 10.15585/mmwr.mm6626a2

Wang, S., Dale, G. L., Song, P., Viollet, B., and Zou, M. H. (2010). AMPKalpha1 deletion shortens erythrocyte life span in mice: role of oxidative stress. *J. Biol. Chem.* 285, 19976–19985. doi: 10.1074/jbc.M110.102467

Wang, Y., Dembowsky, K., Chevalier, E., Stüve, P., Korf-Klingebiel, M., Lochner, M., et al. (2019). C-X-C motif chemokine receptor 4 blockade promotes tissue repair after myocardial infarction by enhancing regulatory T cell mobilization and immune-regulatory function. *Circulation* 139, 1798–1812. doi: 10.1161/circulationaha.118.036053

Westblade, L. F., Simon, M. S., Mathison, B. A., and Kirkman, L. A. (2017). Babesia microti: from mice to ticks to an increasing number of highly susceptible humans. *J. Clin. Microbiol.* 55, 2903–2912. doi: 10.1128/jcm.00504-17

Xia, Z., Hui, W., Jing-Bo, X., Shang, X., and Xiao-Nong, Z. (2019). Epidemic and research progress of babesiosis. *Zhongguo Xue Xi Chong Bing Fang Zhi Za Zhi* 31, 63–70. doi: 10.16250/j.32.1374.2018293

Xue, X., Ren, S., Yang, X., Masoudi, A., Hu, Y., Wang, X., et al. (2021). Protein regulation strategies of the mouse spleen in response to Babesia microti infection. *Parasit. Vectors* 14:61. doi: 10.1186/s13071-020-04574-5

Yáñez, A., and Goodridge, H. S. (2018). Identification and isolation of Oligopotent and lineage-committed myeloid progenitors from mouse bone marrow. *J. Vis. Exp.* 29: 58061. doi: 10.3791/58061

Zwaal, R. F., Comfurius, P., and Bevers, E. M. (2005). Surface exposure of phosphatidylserine in pathological cells. *Cell. Mol. Life Sci.* 62, 971–988. doi: 10.1007/s00018-005-4527-3

Check for updates

Erratum: Enhanced phosphatidylserine exposure and erythropoiesis in *Babesia microti*-infected mice

Frontiers Production Office*

Frontiers Media SA, Lausanne, Switzerland

An Erratum on

Enhanced phosphatidylserine exposure and erythropoiesis in *Babesia microti*-infected mice

by Song, P., Cai, Y.-C., Chen, M.-X., Chen, S.-H., and Chen, J.-X. (2023). *Front. Microbiol.* 13:1083467. doi: 10.3389/fmicb.2022.1083467

Due to a production error, the DOI for this article was incorrectly registered as 10.3389/fmicb.2023.1083467. The correct DOI for the article is 10.3389/fmicb.2022.1083467. The publisher apologizes for this mistake. The original article has been updated.

Frontiers in **Microbiology**

Retrospective analysis of *Plasmodium vivax* genomes from a pre-elimination China inland population in the 2010s

Ying Liu[1,2,3,4,5†], Tao Zhang[6†], Shen-Bo Chen[1,2,3,4], Yan-Bing Cui[1,2,3,4], Shu-Qi Wang[6], Hong-Wei Zhang[5], Hai-Mo Shen[1,2,3,4]* and Jun-Hu Chen[1,2,3,4,7]*

[1]National Institute of Parasitic Diseases, Chinese Center for Diseases Control and Prevention (Chinese Center for Tropical Diseases Research), Shanghai, China, [2]National Health Commission of the People's Republic of China (NHC) Key Laboratory of Parasite and Vector Biology, Shanghai, China, [3]World Health Organization (WHO) Collaborating Center for Tropical Diseases, Shanghai, China, [4]National Center for International Research on Tropical Diseases, Shanghai, China, [5]Henan Provincial Center for Disease Control and Prevention, Zhengzhou, China, [6]Anhui Provincial Center for Disease Control and Prevention, Hefei, China, [7]School of Global Health, Chinese Center for Tropical Diseases Research, Shanghai Jiao Tong University School of Medicine, Shanghai, China

Introduction: In malaria-free countries, imported cases are challenging because interconnections with neighboring countries with higher transmission rates increase the risk of parasite reintroduction. Establishing a genetic database for rapidly identifying malaria importation or reintroduction is crucial in addressing these challenges. This study aimed to examine genomic epidemiology during the pre-elimination stage by retrospectively reporting whole-genome sequence variation of 10 *Plasmodium vivax* isolates from inland China.

Methods: The samples were collected during the last few inland outbreaks from 2011 to 2012 when China implemented a malaria control plan. After next-generation sequencing, we completed a genetic analysis of the population, explored the geographic specificity of the samples, and examined clustering of selection pressures. We also scanned genes for signals of positive selection.

Results: China's inland populations were highly structured compared to the surrounding area, with a single potential ancestor. Additionally, we identified genes under selection and evaluated the selection pressure on drug-resistance genes. In the inland population, positive selection was detected in some critical gene families, including *sera*, *msp3*, and *vir*. Meanwhile, we identified selection signatures in drug resistance, such as *ugt*, *krs1*, and *crt*, and noticed that the ratio of wild-type *dhps* and *dhfr-ts* increased after China banned sulfadoxine-pyrimethamine (SP) for decades.

Discussion: Our data provides an opportunity to investigate the molecular epidemiology of pre-elimination inland malaria populations, which exhibited lower selection pressure on invasion and immune evasion genes than neighbouring areas, but increased drug resistance in low transmission settings. Our results revealed that the inland population was severely fragmented with low relatedness among infections, despite a higher incidence of multiclonal infections, suggesting that superinfection or co-transmission events are rare in low-endemic circumstances. We identified selective signatures of resistance and found that the proportion of susceptible isolates fluctuated in response to the prohibition of specific drugs. This finding is consistent with the alterations in medication strategies during the malaria elimination campaign in inland China. Such findings could provide a genetic basis for future population studies, assessing changes in other pre-elimination countries.

Introduction

Plasmodium vivax is the most widely distributed human malaria species, with an estimated 350 million Chinese individuals at risk and 30 million cases annually 7 decades ago (Yin et al., 2014). China was declared malaria-free by the World Health Organization in 2021, a remarkable achievement and the outcome of the national malaria program's dedicated efforts (Cao et al., 2021). Despite significant progress in reducing the malaria burden, imported cases have increased due to human settlements and movement activities, cross-border migration, ecological changes, vector population dynamics, and multidrug resistance. Vulnerable populations, such as overseas workers and businessmen, acquire infections due to occupational exposure, including crop plantations, forestry, mining, development projects, and tourism.

Imported cases are especially challenging in malaria-free countries, as connections with neighboring countries with higher transmission rates increase the risk of parasite reintroduction. China reported its last local malaria case in 2016, 6 years after aiming for eradication, but imported malaria will remain a threat until global eradication is achieved (Feng et al., 2014; Lai et al., 2017). Although the Great Mekong Sub-region (GMS including Cambodia, China, Laos, Myanmar, Thailand, and Vietnam) has made significant progress in reducing transmission and is on track to achieve elimination by 2030, border surveillance will be necessary until the target is accomplished. Previous research has identified the risk of malaria transmission in China–Myanmar border areas and cross-border migration as a major source of the potential introduction of malaria into southern China (Zhou et al., 2014; Wang et al., 2015). This importation resulted from human activities involving border trade, businesses, and mass population movement due to political instability. Imported *P. vivax* cases have become a public health concern in malaria-endemic areas where the disease was eradicated many years ago. One of the most important lessons from the malaria elimination plan is to modify the strategy continuously as the malaria situation evolves and programmatic gaps are subsequently filled, allowing for more cost-efficient alternatives reflecting local transmission dynamics (Huang et al., 2022). Moreover, due to the COVID-19 pandemic, many countries have curtailed malaria elimination strategies. The key to addressing these challenges is the establishment of a genetic database for the rapid identification of malaria importation or reintroduction (Arnott et al., 2012). Several genome sequencing projects, such as MalariaGEN, have characterized the genetic diversity of *P. vivax* across populations. It also involves using novel technological advances such as sensitive and accurate genetic tools to trace the likely sources of malaria cases (Preston et al., 2014; Sturrock et al., 2015; Trimarsanto et al., 2019; Fola et al., 2020).

In this study, we retrospectively reported whole-genome sequence variation in 10 *P. vivax* isolates from inland China with high parasite density to provide a view of genomic epidemiology during the pre-elimination stage. Henan reported the last local infection in 2011, and Anhui reported the last two local infection cases in 2013 (our sampling occurred in 2012). Here, we indicate the number of cases in China from 2010 to 2015 to demonstrate the representativeness of our collection (Table 1). The samples were collected in the 2010s from the Anhui and Henan provinces and represented the last inland outbreaks before elimination. Our results revealed that the inland population was severely fragmented with low identity by descent (IBD) relatedness among infections, suggesting that super-infections or co-transmission events are rare in low-endemic areas. We also identified selection signatures in drug resistance and found that the ratio of sensitive isolates changed in response to restricted drugs.

Materials and methods

Ethics statement

The study was approved by the Ethics Committee of the National Institute of Parasitic Diseases (NIPD), Chinese Center for Disease Control and Prevention (China CDC). The participants were informed of the study's procedure, potential risks, and benefits. After the participants agreed to participate in the study, written informed consent was obtained from them.

Collection of genomic data

We used the 2016 genotype call data set (Variant Call Format file) with 228 samples from the following countries: Cambodia, China, India, Indonesia, Laos, Malaysia, Myanmar, Thailand, Vietnam, and Papua New Guinea (Pearson et al., 2016). Information, such as collection location and time, was downloaded from "www.malariagen.net/data/p-vivax-genome-variation-may-2016-data-release." We included published genomic data of six clinical samples collected from the China–Myanmar border (CMB) area (Shen et al., 2017) in our reference dataset. Single-nucleotide polymorphism (SNP) information and allele frequencies were downloaded from the *P. vivax* Genome Variation Project, converted to the Vcftools 012 form, and then merged with our own data. In addition, annotation of the *SaL* I reference database was downloaded from PlasmoDB (Aurrecoechea et al., 2008). For a parallel analysis with PvP01 (Auburn et al., 2016) as mapping targets, we downloaded additional reference sequences from countries around the world for principal component analysis (PCA) and structure analysis: Myanmar (PRJNA603279; Brashear et al., 2020), Brazil (PRJNA240378-98), Columbia (PRJNA240414-44), Mexico (PRJNA240445-64), Peru (PRJNA240367-530), PNG (PRJNA240366-530), and Malagasy (PRJNA175266; Chan et al., 2012), the BioProject and SRA numbers of those samples are listed in the Appendix file (Supplementary Table S5).

Sampling *Plasmodium vivax* parasites and genome sequencing

Blood samples were collected from 10 clinical malaria cases in the Anhui and Henan provinces in 2011–2012 that were microscopically

TABLE 1 Reported malaria cases in China (with Anhui and Henan province) from 2010 to 2015.

Year	No. of cases	Suspected cases	Local cases	Vivax cases ratio (%)	Anhui		Henan	
					Total cases	Local cases	Total cases	Local cases
2010	7,855	34,082*	*	*	1864	*	893	*
2011	4,479	1,311	1,314	56.7	644	526	358	166**
2012	2,718	0	182	39.7	98	30**	151	0
2013	4,128	0	48	22.8	184	2	197	0
2014	3,078	0	56	27.7	144	0	216	0
2015	3,288	0	40	26.9	128	0	184	0

Data were downloaded from the following papers: (Zhou et al., 2011; Xia et al., 2012; Xia et al., 2013; Zhang et al., 2014; Zhang et al., 2015; Zhang et al., 2016).

*China has just promulgated the National Malaria Elimination Plan (NMEP) in 2010, so the previous data have not been fully recorded. In addition, because there was no immediate sampling system at that time, many samples were not retained, which led to many suspected cases.

**This number includes all types of malaria. We collected the local samples from here and used in this study.

positive and PCR-confirmed for a single *P. vivax* infection. Henan reported the last local case in the same year, while Anhui reported the last two local cases the following year. According to the National Malaria Elimination Plan (NMEP) promulgated in 2010, the provincial CDC must go to the hospital for sampling and PCR identification immediately after receiving the case report, which is also how we obtained the samples. Simultaneously, the CDC conducted a detailed on-site investigation to determine if the case was imported. Samples with high parasite density (more than 10,000 parasites/µl) in early records were selected to ensure sequencing integrity. We extracted *P. vivax* genomic DNA from unfiltered infected whole blood (the blood samples could not be filtered because they had been frozen with EDTA at −20°C for too long). We extracted more than 50 ng of total DNA from each sample and ensured that the concentration was greater than 1 ng/µl. Unfortunately, many samples degraded due to long storage times and failed to meet this requirement. Specifically, each frozen blood sample DNA was extracted using a QIAGEN DNeasy Blood & Tissue Kit (Qiagen, United Kingdom). Libraries were prepared using the FC-121-4001 TruSeq Nano DNA LT Sample Preparation Kit (Illumina, United States) and sheared into 500 bp fragments using a Covaris S2 Focus Ultrasonicator. Due to insufficient DNA content in the samples, we could not use the CF11 column for filtration but proceeded directly to sequencing. In a previous study (Chen et al., 2017), we confirmed that direct sequencing did not affect the data. All libraries on Illumina X-10 were sequenced, generating an average of 64 M (46–87 M) paired-end reads of 150 bp. Illumina sequencing raw reads are available in the NCBI Sequence Read Archive under the BioProject accession number PRJNA868867.

Variant identification and filtering

Sequenced reads were filtered using Trimmomatic-3.0 (Bolger et al., 2014) to remove adapter and low-quality sequences and mapped to *P. vivax SaL* I genome using BWA (Li and Durbin, 2010). The Bam file was modified using Picard2.6 tools FixMateInformation and MarkDuplicates, and genotyping was performed using a base quality score recalibration pipeline based on GATK4 workflows (McKenna et al., 2010). We ran GATK BaseRecalibrator on each BAM file to generate a recalibration table based on various covariates and used known-site gvcf files published previously (Pearson et al., 2016) to establish base quality scores. Vcftools (Danecek et al., 2011) was used to

remove indels and filter loci with a MAF of less than 0.05. A variable proportion of reads (8.52–12.6%) from all isolated samples were mapped to the reference genome and aligned to 90% of the reference genome with high fold coverage (12–28x). Excluding SNPs with >5% missing calls from high-quality samples yielded 184,401 high-quality SNPs. Missing calls were defined as positions with fewer than two reads.

We also conducted a parallel analysis using PvP01 as the mapping target. We found that the mapping ratio was lower, resulting in higher FWS and larger SNP differences. When P01 was used as a reference, the FWS values were all greater than 0.95. This suggested that all samples were single-lineage infections, which seemed inconsistent with the general pattern. Here, we exclusively present PCA and structure analysis using the P01 reference and additional reference sequences from around the world to demonstrate the uniqueness of samples from inland China.

Population genetics and structure test

In this study, we restricted the population diversity and divergence analysis to heterozygous major allele calls. In an effort to maintain as many SNPs as possible, many low-quality SNPs were retained but not all of them were used. Only those SNPs of published loci were used for PCA, phylogenetic tree, and structural analysis. Total SNPs were used for selection pressure and single-gene analyses. The within-host infection complexity was assessed by within-sample F-statistic (F_{WS}) values and calculated using the Moimix R package. Pairwise IBD was measured using hmmIBD with default parameters and program-estimated allele frequencies (Schaffner et al., 2018). The pairwise IBD outputs were then determined at 1 kb intervals across each chromosome, and the average fractions of IBD derived from each position in each population were calculated.

We evaluated the population structure using both the surrounding area sample and 10 high-coverage single-infection isolates. For high-quality SNP, we estimated the nucleotide diversity ($\hat{\pi}$), Watterson's estimator ($\hat{\theta}_\omega$), genetic differentiation (F_{ST}), and Tajima's D-value across 4,653 genes on 14 chromosomes in ARLEQUIN-Ver3.5 (Excoffier and Lischer, 2010). PCA was performed using the R package, and the neighbor-joining (NJ) tree was constructed using MEGA (Tamura et al., 2013). The ancestry shared by individual isolates was analyzed using ADMIXTURE software (Alexander et al., 2009), and the optimal K cluster value was determined by running the software multiple times with different *K*-values.

Positive selection tests

The integrated haplotype score (iHS) and cross-population extended haplotype homozygosity (XP-EHH) were used to detect recent or ongoing positive selection in Selscan-Ver1.10a (Szpiech and Hernandez, 2014). These statistical analyses are based on the selective sweep model where mutation occurs in a haplotype and quickly sweeps toward fixation, reducing the locus diversity. Integrated haplotype score (iHS) is the standardized log ratio of the integrated extended haplotype homozygosity (EHH), which is calculated by tracking the decay of haplotype homozygosity for all ancestral and derived haplotypes extending from each SNP site (Sabeti et al., 2002; Voight et al., 2006). SNP with inferred ancestral states and minor allele frequencies of at least 5% were used for iHS. Each raw score was normalized to genome-wide frequency bins. During the EHH computation of each SNP locus, if the start/end of a chromosome arm was reached before EHH <0.05 or if a physical distance (kbp) between two markers >200 was encountered, the calculation was aborted. Cross-population extended haplotype homozygosity (XP-EHH) is the standardized log ratio of the integrated site-specific EHH at core SNP between two populations, which in this study were defined as China inland samples and reference samples (Sabeti et al., 2007). Site-specific EHH does not require polymorphic markers within the population. Therefore, it can detect selective sweeps for alleles that have undergone fixation. In our calculation, the sums in each locus were truncated at the SNP with an EHH value of <0.05 or if the computation extended more than 1 Mbp from the core loci. Previous analyses have suggested that iHS has the maximum capacity to detect selective sweeps that have reached moderate frequency, while XP-EHH can detect selective sweeps at high frequency, thus making the two tests complementary.

Results

Genomic data summary

A total of 10 samples had high-quality genomic data and generated between 46 and 87 million paired-end reads, with an average read length of 150bp. A variable proportion of reads (8.52–12.6%) were mapped to the *P. vivax SaL* I reference. The average coverage of the entire genome by the filtered consensus base calls is 93.16%, and 94.18% of chromosomes were generated (Table 2).

Population structure of China inland samples

The population structure was investigated using PCA and a phylogenetic tree of SNP variations. *Plasmodium vivax* clustered according to their geographic origin, and the Pacific island samples could be distinguished from continental samples (Figure 1A). The major components constituted a distinct inland cluster in China, which was coordinated by a Chinese reference (Pearson et al., 2016). These differences were also evident in the NJ tree (Figure 1B), which divided Asia (Thailand, Myanmar, Cambodia, Vietnam, and China) from the Pacific Islands (Malaysia, Indonesia, and Papua New Guinea). Unexpectedly, eastern Southeast Asian samples (Cambodia and Vietnam) exhibited greater genetic relatedness and were separated by CMB samples. Parallel analysis using PvP01 as a reference revealed substantial differences between the South American and Asian samples in the PCA test (Supplementary Figure S1), confirming that geographic location remains a primary determinant of variance.

The ADMIXTURE analysis identified several major populations that corresponded to Asian samples (Figure 1C). The GMS group, including CMB, resembled a mixture of the Southeast Asian components K7, K5, and K3. K4 represented Pacific island samples and was rare in continental populations. K2 only appeared in the Chinese and CMB groups. In other words, K2 and K4 were highly structured populations with shared ancestry that overcame long geological isolation. China is technically not a Southeast Asian country, and K3 was special and only identified in Thailand and CMB samples, indicating that the complex structure of border malaria was caused by transmission and mixing from both sides. In the parallel structure test with PvP01 strain as the reference, we found (Supplementary Figure S2) that the inland Chinese populations belong to the same potential ancestral taxonomy and are quite different from the Yunnan-collected Chinese border samples.

We calculated within-sample parasite diversity in inland Chinese samples to investigate the complexity of infection. In these samples, F_{WS} values of individual infections ranged from 0.85 to 0.98 (mean 0.925 and median 0.927), whereas, in Thailand and Indonesia, values

TABLE 2 Sequencing and mapping summary statistics for 10 China inland samples.

Sample ID	Total reads	Mapped ratio (%)	Average coverage depth (X)	Genome coverage >1x (%)	Covrage >10x (%)	F_{WS}
M001B	85,817,050	8.89	19.71	94.45	8.38	0.9264
M052B	87,590,464	8.52	28.18	93.70	5.27	0.9398
S2011054	55,480,824	9.80	12.85	92.00	2.42	0.9861
S2011067	83,067,520	8.69	16.42	92.59	4.67	0.9492
S2011068	60,557,874	10.37	15.31	91.81	7.76	0.9056
S2011069	5,3677,630	10.27	13.87	92.26	7.33	0.9119
S2011097	59,224,092	12.63	22.04	96.21	59.21	0.9005
Sample_225	52,169,688	9.68	12.48	90.48	4.52	0.9478
Sample_364	55,316,880	10.52	16.49	95.78	20.93	0.8569
Sample_455	46,641,940	11.92	13.29	92.36	7.09	0.9273
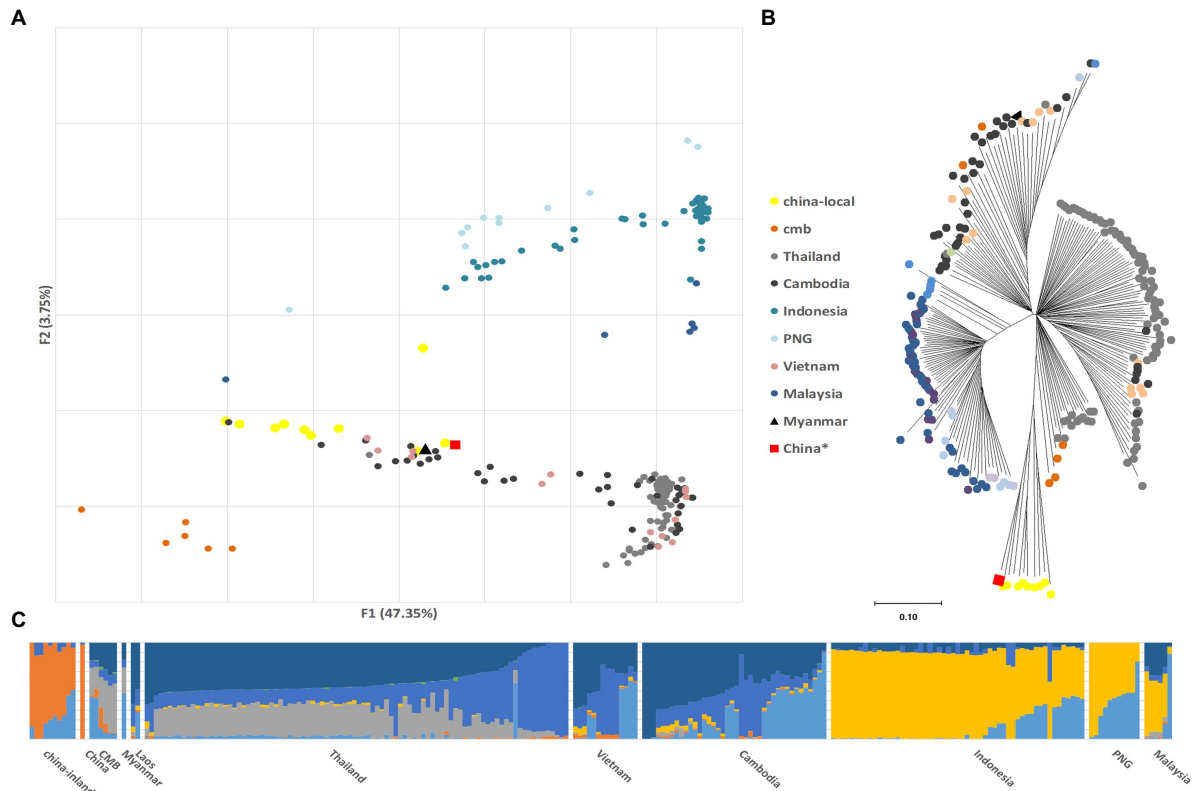
FIGURE 1
Parasite population structure in China inland samples relative to the reference (Cambodia, China*, India, Indonesia, Laos, Malaysia, Myanmar, Thailand, Vietnam, and Papua New Guinea). The China* samples (SAMEA2358527) are also downloaded from the study of Pearson et al. (2016), which was collected from the Yunnan border area, China in 2011, and published on ENA in 2014. **(A)** Principal component analysis (PCA) plots illustrating the genetic differentiation between populations; **(B)** Neighbor-joining tree illustrating the relatedness between the inland *Plasmodium vivax* isolates relative to the reference with 1,000 bootstraps. **(C)** ADMIXTURE bar plot illustrates the population structure within and among populations at an optimized cluster value of $K=7$.

ranged from 0.22 to 0.99 (mean 0.87 and median 0.99) and from 0.28 to 0.99 (mean 0.85 and median 0.91), respectively. An F_{WS} value of 0.95 indicates that an infection predominantly contains a single genotype, even if additional genotypes are present at relatively low proportions. The F_{WS} values revealed a lower proportion of monoclonal infections in the China inland sample (3/10) compared with Thailand (59.78%, 55/92) and other populations (Figure 2A); however, this difference was not statistically significant due to the small sample size. For each segregating allele locus across the low F_{WS} value samples, most of these positions had >5X read depth in major calls but insufficient depth in minority calls, implying that the risk of unrelated parasites from separate mosquito bites was quite low. Without follow-up reports of relapses, it is evident that these cases have neither relapsed nor recurred and that genetic complexity is unlikely to affect the genetic analysis process.

Meanwhile, we checked the chromosome-level structure of inland Chinese isolates with the identity by descent (IBD) fraction, which is widely used to study relatedness among proximal parasite populations (Figure 2B). Although inland China samples exhibited the highest fractions of pairwise IBD (mean value=0.059 in CMB) compared to any other GMS population (0.016 in Cambodia and 0.019 in Thailand) from previous research, the IBD values were still low. This was probably because the sample size was inadequate. In the inland Chinese population, 3,431 IBD regions involving 1,157 genes were identified. Among them, 123 genes contained more than 10 IBD fragments

(Figure 2C), including multigene family members, such as *msp*, *sera*, and *vir*. Remarkably, the gene with the most IBD fragments is the reticulocyte-binding protein (*pvrbp2c*, PVX_090325), which is well-known for its erythrocyte-binding-related conservative regions (Gupta et al., 2018).

Genomic scan for differentiation between inland and border populations

To explore the genomic profile of divergence among *P. vivax* populations, we estimated the fixation index (F_{ST}) of individual genes for the populations separated by differing geographical distances (Supplementary Table S1). Not surprisingly, the Indonesian and Chinese inland populations exhibited considerable differentiation for each gene (mean $F_{ST}=0.26$, median 0.22), which could be attributed to geographic variations between the island and continental samples. In contrast, the average differentiation for each gene in inland China and border samples was lower (mean $F_{ST}=0.18$, median 0.15), and 339 genes had F_{ST} values of >0.5. Gene ontology (GO) term analysis was conducted among these genes to assess which functions were enriched. Genes associated with an intracellular anatomical structure (GO:0005622), RNA binding (GO:0003723), organelles (GO:0043226), and nitrogen compound biosynthetic processes (GO:1901564, GO:0006807, and GO:0044271) were found to be significantly enriched.
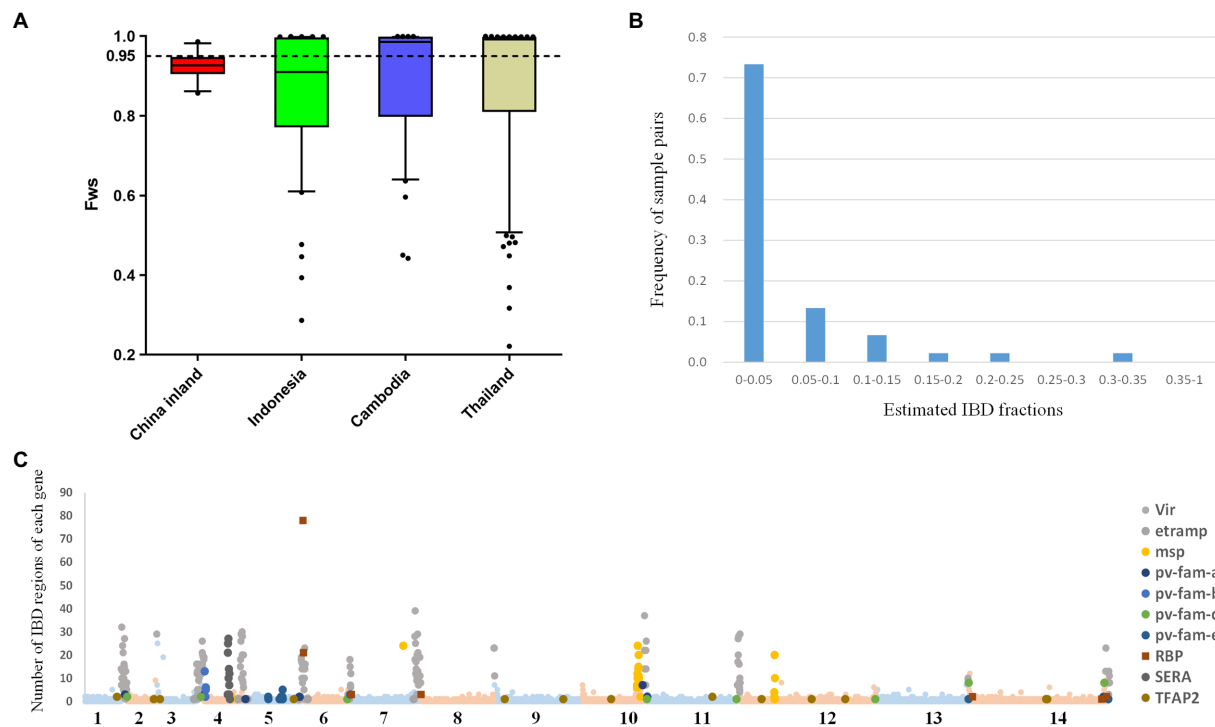
FIGURE 2

F_{WS} and IBD plots illustrate the complexity and relatedness among infections in China's inland population. **(A)** Boxplots illustrating different trends in inland, Indonesia, Cambodia, and Thailand. The dotted line illustrates the $F_{WS}=0.95$, above which infections are essentially monoclonal. **(B)** Patterns of identity by descent (IBD) were explored across the genome of China inland and reference populations. The histogram represents the frequency of sample pairs, each pair with IBD fractions above 0.5 should be considered related. **(C)** 3,431 IBD regions were found and involved 1,157 genes, and 123 genes containing more than 10 IBD fragments including members of multigene families. The *x*-axis of the scatterplot represents the 14 chromosomes of the parasite and the *y*-axis represents the number of IBD regions for each gene.

Identifying signatures of selection in CMB

The analysis focused on the 4,624 genes with at least three SNP each to examine allele frequency distributions for specific genes in the Chinese inland population. Tajima's D-values of inland samples were mostly negative, with a mean of −0.12, which was slightly higher than that of CMB (mean = −0.35 and medium = −0.48); 2,083 genes (27%) had positive Tajima's D-values (Figure 3A). Tajima's D value of 42 orthologs of P. falciparum drug-resistance genes were summarized to reveal the difference between inland and reference populations (Figure 3B). In the other Southeast Asia (SEA) reference population, Thailand samples had 4,865 genes with at least three SNPs, a mean of −1.61, a median of −1.72, and only 88 genes (1.8%) had positive Tajima's D-values. However, there was a clear distinction between *vir* gene families (the average for *vir* was −0.06 in inland and 1.13 in the CMB group separately). This difference corresponded with the disparity in malaria transmission between the two locations in the 2010s. In contrast to the PCA result, the balancing selection of genes did not show consistency in geographic origin. Here, we used Tajima's D-test to distinguish between genes evolving neutrally or during the selection process. The higher the number of genes subject to negative balance selection, the greater the environmental pressure on the population, just as the selection pressure on drug resistance genes can reflect alterations in local drug use strategies. Both belong to the Pacific Islands population, and 4,657 genes with at least three SNPs and 508 genes (10.9%) with positive Tajima's D-values were included in our calculation for the Indonesian population. However, 4,232 available genes in PNG were

included, and 1,284 (30%) had positive values. Consistent with our prior results, the predominantly negative values in SEA isolates indicate a recent population expansion of *P. vivax* in the CMB area (Shen et al., 2018). Compared to highly endemic populations, such as Thailand, inland China samples exhibited a different environment with a lower selection pressure.

Positive selection tests

This study used the integrated haplotype score (iHS) statistic to detect incomplete sweeps and cross-population extended haplotype homozygosity (XP-EHH) in cases where the sweep was near fixation within the population. Using the |iHS| score for all SNPs (MAF of >5%) in the CMB samples, we identified 14 chromosomal regions with SNP values above the top 5% of the randomly expected distribution (Supplementary Table S2). Our previous analyses revealed that positively selected SNP loci are typically associated with genes for red blood cell invasion and immune evasion. The top 1% SNP loci included 127 genes (Figure 4A) whose functions were enriched with membrane-intrinsic components (GO:0031224) and cysteine-type peptidase activity (GO:0008234). Elevated |iHS| values were observed in some important gene families, such as *sera* (four genes, mean |iHS| = 3.49), *msp3* (nine genes, mean |iHS| = 3.7), *vir* (58 genes, mean |iHS| = 3.52), and *Pv-fam-d* (two genes, mean |iHS| = 4.32). The observation of positive selection is similar to the results obtained in previous studies, and the selection of vaccines

FIGURE 3

Balanced selection (Tajima's D-value) of 5,249 genes in inland and border populations. **(A)** Balanced selection (Tajima's D-value) of all genes in both populations. We selected some immune-related genes such as *vir*, *msp.,* and *rbp* to evaluate the differences in environmental stress between China inland and CMB samples. Tajima's D-values of China inland samples were mostly negative with a mean of −0.12, a bit higher than CMB. However, there was a clear difference in *vir* gene families, consistent with the difference in malaria transmission between the two places in the 2010s. **(B)** A balanced selection of 42 orthologs of *P. falciparum* drug-resistance genes summarizing the difference between inland and reference populations. The Southeast Asian population exhibited higher overall pressure levels than Pacific island populations in Tajima's D-test but no significant difference in *pvcrt* and *pvmdr1*. In antifolate-resistance genes, there are positive balance selective pressures in the Southeast Asian population but negative balance selective in island populations.

FIGURE 4

Genome-wide scans to identify regions with extended homozygosity using haplotype-based detecting positive selection. **(A)** Genome-wide scan of standardized |iHS| for *Plasmodium vivax* SNPs with a minor allele frequency of at least 5% in inland samples. Dashed lines indicate the top 1% of |iHS| values (|iHS| score of >2.8). **(B)** Genome-wide scan of standardized XP-EHH for *P. vivax* SNPs with a minor allele frequency of at least 5% in inland samples. Using CMB isolates as the reference population. Dashed lines indicate the top 1% of XP-EHH values (±0.5%, XP-EHH score of >0.78 or<−0.24 in CMB-China).

targeting polymorphic antigens may explain the difficulty in eliciting cross-protective immune responses. The XP-EHH test was applied to compare the average haplotype length of each SNP between inland samples and the CMB references

(Supplementary Table S3). It identifies areas in the genome where destination samples show much longer haplotypes than the reference, indicating recent positive selection in the tested population. These selection signals were stronger in CMB samples

TABLE 3 Putative *Plasmodium falciparum* drug resistance gene orthologous with their associated population genetic statistics.

| Gene | Chr | $\hat{\pi}$ | Tajima's D value | | | | Top 1% \|ihs\| value | Orthology in *P. falciparum* |
			China inland	CMB	Thailand	PNG		
PVX_087980	1	1.01E−03	0.0974	−1.1107	−1.1584	0.3533	1.3021	*crt*
PVX_097025	2	5.02E−04	0.9345	0.3144	−1.9495	−0.9077	1.3703	*mrp*
PVX_089950	5	3.56E−04	−0.1839	2.5562	−1.3701	0.1677	0.2814	*dhfr-ts*
PVX_094580	8	4.66E−04	0.3764	−0.2311	−1.793	−0.373	1.3439	*ap2tf-10*
PVX_091310	9	0.00E+00	0	−1.0365	−1.0863	−1.1285	0.2381	*ugt*
PVX_079990	10	1.20E−03	0.7178	0.1391	−1.6328	−0.0249	0.8844	*acs10*
PVX_080100	10	8.50E−04	1.3814	0.1361	0.365	1.1506	1.6588	*mdr1*
PVX_080480	10	4.08E−04	2.0741	−1.1305	−1.9775	−1.5284	1.1136	*pi3k*
PVX_098050	10	5.23E−04	−1.1766	−0.7887	−0.3258	0.0362	1.439	*pi4k*
PVX_113825	11	3.21E−04	−0.7435	−0.2512	−1.6984	−0.0696	2.1363	*ap2tf-6b*
PVX_113330	11	9.18E−04	0.4449	0.6474	−1.3299	0.3358	0.873	*DHODH*
PVX_083400	12	5.67E−04	0.6242	−0.3317	−0.8159	−1.5999	0.9967	*krs1*
PVX_083080	12	9.35E−05	−1.1117	0	−1.7332	−1.6		*K13*
PVX_118100	12	6.87E−04	−0.2806	−1.9023	−0.2545	−0.1617	1.1937	*mdr2*
PVX_123230	14	5.40E−04	−1.5729	0.6293	−0.8105	−1.2645		*dhps*
PVX_100890	14	7.48E−04	−0.8427	1.5364	−1.5308	0.4126	0.8281	*acs11*
PVX_124085	14	2.50E−04	−1.1895	−0.6429	−0.9771	−0.3874	2.0798	*mrp2*

and included known marker resistance to chloroquine (*crt*) and artemisinin (*pi4k*; Park et al., 2012; Cerqueira et al., 2017). In contrast, only the *vir* and *msp3* gene families exhibited the most positive selection signals in inland isolates (Figure 4B).

Genes associated with drug resistance in the inland isolate

During 2009–2016, molecular surveillance of drug-resistant *Plasmodium vivax* malaria identified chloroquine (CQ) resistance markers in southern and central Myanmar and higher mutation rates of antifolate resistance markers (Nyunt et al., 2017). In this study, we integrated a list of putative drug-resistance genes from earlier research (Gamo et al., 2010; Price et al., 2012; Hupalo et al., 2016; Plouffe et al., 2016) and compared these genes from different sources (Table 3; Supplementary Table S4). In Tajima's D-test, the Southeast Asian population was predicted to exhibit higher overall pressure levels than the Pacific island populations (Figure 3B); however, there was no significant difference in the CQ resistance genes (*pvcrt* and *pvmdr1*). For antifolate resistance genes, we found positive and negative balance selective pressures in Southeast Asian and island populations, respectively, which could be related to the suspension of these drugs in Southeast Asia for almost 20 years. The disparities between China's inland and reference populations were then analyzed. Some genes, such as chloroquine resistance transporter (*crt*), multidrug resistance (*mdr1*), and imidazole piperazine resistance, such as *ugt* and *krs1* (Lim et al., 2016; Saint-Léger et al., 2016), showed higher Tajima's D-values in inland populations but lower in CMB, whereas genes related to sulfadoxine–pyrimethamine (SP) resistance, such as *dhps* and *dhfr-ts*, (Olliaro and Mussano, 2003) were under positive balance selection in the rest of the region.

Discussion

Importing malaria to countries where it has been eradicated is a major barrier to global elimination (Sturrock et al., 2015; Song et al., 2018). The spread of malaria in endemic nations has contributed to the development of drug resistance and hampered long-term eradication goals. Most malaria cases in elimination-stage countries are imported, posing a risk of re-establishing transmission in receptive areas (Hai-Juan et al., 2019). Even in malaria-free countries, imported cases often lead to delays in diagnosis, higher treatment costs, and local secondary transmission.

Recently, the number of imported cases in China has increased dramatically. From 2011 to 2015, 17,745 malaria cases were reported in mainland China; however, only 1,905 (11%) were locally transmitted (Zhou et al., 2016). As overseas investment from China continues to rise, the risk of malaria importation using returning laborers undertaking high-risk outdoor activities without proper protection increases. Parasite diversity is a fundamental predictor of transmission and immunity (Volkman et al., 2007; Manske et al., 2012). An understanding of the parasite population's genetic structure is necessary to comprehend the epidemiology, diversity, distribution, and dynamics of natural *P. vivax* populations. Moreover, studying the population structure of genes under immune selection also reveals the dynamic interplay between transmission and immunity, which is crucial for vaccine development (Neafsey et al., 2012; Batista et al., 2015; Jennison et al., 2015). Therefore, this study aimed to retrospectively identify China's inland malarial population. The genome data provide a unique opportunity to create SNP barcodes with a high tracing ability to identify parasite origin and a unique endemic setting for evaluating the dynamic shifts in transmission and selective pressures during the pre-elimination phase.

Our samples were collected from the last few inland outbreaks from 2011 to 2012 when China initiated a plan to control malaria transmission. Regarding population structure, China inland samples were clustered according to their geographic origin, continental samples differed from Pacific island samples, and the China–Myanmar border (CMB) samples could be regarded as a mixture of China and Myanmar samples with distinct characteristics from both countries. We found that representative sub-populations such as K2 closely matched the published Chinese reference. We observed low fractions of pairwise IBD values in the chromosome-level structure of inland samples, indicating that each infection occurred independently in a low-endemic setting. We conclude that our findings are broadly consistent with the assumptions for a pre-elimination population, except for the monoclonal infection ratio. The high incidence of mosquito bites during the outbreak could explain the lower monoclonal infections than in high transmission areas. Normally, a higher proportion of polyclonal infection reflects more frequent superinfection or co-transmission, which is rarely seen in low-endemic areas (Auburn et al., 2018). Conversely, a high ratio of monoclonal infections in small enclosed spaces such as islands could be due to a low entomological inoculation rate (EIR) or clonal parasite population. For example, recent research from the northeastern Peruvian Amazon revealed that the parasite population showed a high monoclonal ratio and diversity, inconsistent with geographical clustering, reflecting gene flow resulting from frequent travel in this area (Cowell et al., 2018).

Only the most drug-resistant infections survive in the pre-elimination environment, leading to intense drug selection (Maude et al., 2009). The rapidly shrinking population and low transmission rates may foster the emergence of multigenic resistance phenotypes. We suspected that stronger pressure signals could be detected in inland China samples and that the resistance alleles would be common and unlikely to be separated during recombination. Due to the high ratio of co-endemic *Plasmodium falciparum* in China, various artemisinin-based combination therapy (ACT) drugs have been used to shape genetic makeup (Douglas et al., 2010; Price et al., 2011). In our results, we observed selection signals for artemisinin resistance genes orthologous to *pi4k* (|iHS| = 1.44, Tajima's D -1.17) and *atpase6* (|iHS| = 0.78, Tajima's D -1.27). The XP-EHH results also indicated that *pi4k* was under stronger pressure in the CMB than in China. This is a global issue in GMS countries, as migrants may introduce drug-resistant strains to new locations. Meanwhile, Tajima's D-test indicated a balanced selection of the most important drug-resistance genes, such as *crt* and *mdr1*. The data did not confirm our predictions of extended haplotype homozygosity for drug-resistance genes in the top 1% list.

Tajima's D-test revealed that directional selection operating on *dhfr-ts* in China was significantly lower than in Thailand and Cambodia. This finding was expected because SP is only occasionally administered as an intermittent prophylactic treatment for pregnant women. However, we observed stronger pressure on *dhps* than in other GMS countries. We counted the frequency of *dhps* (amino acids 382, 383, 553, and 647) mutations and compared our findings with those reported previously (Na et al., 2005; Lu et al., 2010). We found a higher wild-type ratio, substantially lower than those from the 1990s but consistent with the studies from the 2010s. The remaining infections are drug-resistant, making eradication extremely challenging (Maude et al., 2009). For example, the annual use of ACT increases the proportion of artemisinin-resistant infections.

Conclusion

A genetic database for the rapid identification of any importation or reintroduction of malaria is a critical step in addressing the worldwide and complex challenge of malaria eradication. We retrospectively reported whole-genome sequence variations in 10 *P. vivax* Chinese inland isolates from high parasite density regions to highlight the relevance of genomic epidemiology in the pre-elimination stage. Our results revealed that the inland population was severely fragmented with low relatedness among infections, despite a higher incidence of multiclonal infections, suggesting that superinfection or co-transmission events are rare in low-endemic circumstances. We identified selective signatures of resistance and found that the proportion of susceptible isolates fluctuated in response to the prohibition of specific drugs. This finding is consistent with the alterations in medication strategies during the malaria elimination campaign in inland China. This suggests that *P. vivax* China inland population may face more pressure to survive than around region in the 2010s.

Data availability statement

Illumina sequencing raw reads described here are available at NCBI under accession number PRJNA868867.

Ethics statement

This study was conducted according to the principles expressed in the Declaration of Helsinki. The study protocol, as well as potential risks and benefits, were explained to participants before blood collection, and all adult participants, as well as the parents or legal guardians of children, provided written informed consent. Blood was collected following institutional ethical guidelines reviewed and approved by the Ethics Committee of the National Institute of Parasitic Diseases, Chinese Center for Disease Control and Prevention.

Author contributions

YL, TZ, H-MS, and J-HC conceived and designed the experiments and drafted the manuscript. S-BC and Y-BC conducted the experiments. YL and H-MS analyzed the data. TZ, S-BC, and Y-BC contributed to the reagents, materials, and analysis tools. All authors contributed to the article and approved the submitted version.

Funding

Acknowledgments

We thank the staff of the Anhui and Henan Center for Disease Control and Prevention for collecting blood samples from *Plasmodium vivax*-infected individuals.

Conflict of interest

The authors declare that the research was conducted in the absence of any commercial or financial relationships that could be construed as a potential conflict of interest.

Publisher's note

All claims expressed in this article are solely those of the authors and do not necessarily represent those of their affiliated organizations, or those of the publisher, the editors and the reviewers. Any product that may be evaluated in this article, or claim that may be made by its manufacturer, is not guaranteed or endorsed by the publisher.

Supplementary material

The Supplementary material for this article can be found online at: https://www.frontiersin.org/articles/10.3389/fmicb.2023.1071689/full#supplementary-material

SUPPLEMENTARY FIGURE S1
PCA plots illustrating the parasite population structure in China inland samples relative to reference mapped with the P01 genome. The China* samples are also downloaded from Pearson et al.'s study, which was collected from Yunnan, China in 2011.

SUPPLEMENTARY FIGURE S2
ADMIXTURE structure in China inland samples relative to the reference mapped with the P01 genome. The China* samples are also downloaded from Pearson et al.'s study, which was collected from Yunnan, China in 2011. The ADMIXTURE bar plot illustrates the population structure within and among populations at an optimized cluster value of $K=5$.

References

Alexander, D. H., Novembre, J., and Lange, K. (2009). Fast model-based estimation of ancestry in unrelated individuals. *Genome Res.* 19, 1655–1664. doi: 10.1101/gr.094052.109

Arnott, A., Barry, A. E., and Reeder, J. C. (2012). Understanding the population genetics of *Plasmodium vivax* is essential for malaria control and elimination. *Malar. J.* 11, 1–10. doi: 10.1186/1475-2875-11-14

Auburn, S., Benavente, E. D., Miotto, O., Pearson, R. D., Amato, R., Grigg, M. J., et al. (2018). Genomic analysis of a pre-elimination Malaysian *Plasmodium vivax* population reveals selective pressures and changing transmission dynamics. *Nat. Commun.* 9:2585. doi: 10.1038/s41467-018-04965-4

Auburn, S., Böhme, U., Steinbiss, S., Trimarsanto, H., Hostetler, J., Sanders, M., et al. (2016). A new *Plasmodium vivax* reference sequence with improved assembly of the subtelomeres reveals an abundance of pir genes. *Wellcome Open. Res.* 1:4. doi: 10.12688/wellcomeopenres.9876.1

Aurrecoechea, C., Brestelli, J., Brunk, B. P., Dommer, J., Fischer, S., Gajria, B., et al. (2008). PlasmoDB: a functional genomic database for malaria parasites. *Nucleic Acids Res.* 37, D539–D543. doi: 10.1093/nar/gkn814

Batista, C. L., Barbosa, S., Bastos, M. D. S., Viana, S. A. S., and Ferreira, M. U. (2015). Genetic diversity of *Plasmodium vivax* over time and space: a community-based study in rural Amazonia. *Parasitology* 142, 374–384. doi: 10.1017/S0031182014001176

Bolger, A. M., Lohse, M., and Usadel, B. (2014). Trimmomatic: a flexible trimmer for Illumina sequence data. *Bioinformatics* 30, 2114–2120. doi: 10.1093/bioinformatics/btu170

Brashear, A. M., Fan, Q., Hu, Y., Li, Y., Zhao, Y., Wang, Z., et al. (2020). Population genomics identifies a distinct *Plasmodium vivax* population on the China-Myanmar border of Southeast Asia. *PLoS Negl. Trop. Dis.* 14:e0008506. doi: 10.1371/journal.pntd.0008506

Cao, J., Newby, G., Cotter, C., Hsiang, M. S., Larson, E., Tatarsky, A., et al. (2021). Achieving malaria elimination in China. *Lancet Public Health* 6, e871–e872. doi: 10.1016/S2468-2667(21)00201-2

Cerqueira, G. C., Cheeseman, I. H., Schaffner, S. F., Nair, S., McDew-White, M., Phyo, A. P., et al. (2017). Longitudinal genomic surveillance of *Plasmodium falciparum* malaria parasites reveals complex genomic architecture of emerging artemisinin resistance. *Genome Biol.* 18:78. doi: 10.1186/s13059-017-1204-4

Chan, E. R., Menard, D., David, P. H., Ratsimbasoa, A., Kim, S., Chim, P., et al. (2012). Whole genome sequencing of field isolates provides robust characterization of genetic diversity in *Plasmodium vivax*. *PLoS Negl. Trop. Dis.* 6:e1811. doi: 10.1371/journal.pntd.0001811

Chen, S.-B., Wang, Y., Kassegne, K., Xu, B., Shen, H.-M., and Chen, J.-H. (2017). Whole-genome sequencing of a *Plasmodium vivax* clinical isolate exhibits geographical characteristics and high genetic variation in China-Myanmar border area. *BMC Genomics* 18:131. doi: 10.1186/s12864-017-3523-y

Cowell, A. N., Valdivia, H. O., Bishop, D. K., and Winzeler, E. A. (2018). Exploration of *Plasmodium vivax* transmission dynamics and recurrent infections in the Peruvian Amazon using whole genome sequencing. *Genome Med.* 10:52. doi: 10.1186/s13073-018-0563-0

Danecek, P., Auton, A., Abecasis, G., Albers, C. A., Banks, E., DePristo, M. A., et al. (2011). The variant call format and VCFtools. *Bioinformatics* 27, 2156–2158. doi: 10.1093/bioinformatics/btr330

Douglas, N. M., Anstey, N. M., Angus, B. J., Nosten, F., and Price, R. N. (2010). Artemisinin combination therapy for vivax malaria. *Lancet Infect. Dis.* 10, 405–416. doi: 10.1016/S1473-3099(10)70079-7

Excoffier, L., and Lischer, H. E. (2010). Arlequin suite ver 3.5: a new series of programs to perform population genetics analyses under Linux and windows. *Mol. Ecol. Resour.* 10, 564–567. doi: 10.1111/j.1755-0998.2010.02847.x

Feng, J., Yan, H., Feng, X., Zhang, L., Li, M., Xia, Z., et al. (2014). Imported malaria in China, 2012. *Emerg. Infect. Dis.* 20, 1778–1780. doi: 10.3201/eid2010.140595

Fola, A. A., Kattenberg, E., Razook, Z., Lautu-Gumal, D., Lee, S., Mehra, S., et al. (2020). SNP barcodes provide higher resolution than microsatellite markers to measure *Plasmodium vivax* population genetics. *Malar. J.* 19, 375–385. doi: 10.1186/s12936-020-03440-0

Gamo, F.-J., Sanz, L. M., Vidal, J., de Cozar, C., Alvarez, E., Lavandera, J.-L., et al. (2010). Thousands of chemical starting points for antimalarial lead identification. *Nature* 465, 305–310. doi: 10.1038/nature09107

Gupta, S., Singh, S., Popovici, J., Roesch, C., Shakri, A. R., Guillotte-Blisnick, M., et al. (2018). Targeting a reticulocyte binding protein and Duffy binding protein to inhibit reticulocyte invasion by *Plasmodium vivax*. *Sci. Rep.* 8, 1–10. doi: 10.1038/s41598-018-28757-4

Hai-Juan, D., Li-Yong, W., and Xiao-Nong, Z. (2019). Current status and new challenges of three important imported parasitic diseases. *Zhongguo Xue Xi Chong Bing Fang Zhi Za Zhi* 31, 353–355. doi: 10.16250/j.32.1374.2019207

Huang, F., Feng, X.-Y., Zhou, S.-S., Tang, L.-H., and Xia, Z.-G. (2022). Establishing and applying an adaptive strategy and approach to eliminating malaria: practice and lessons learnt from China from 2011 to 2020. *Emerg. Microbes. Infect.* 11, 314–325. doi: 10.1080/22221751.2022.2026740

Hupalo, D. N., Luo, Z., Melnikov, A., Sutton, P. L., Rogov, P., Escalante, A., et al. (2016). Population genomics studies identify signatures of global dispersal and drug resistance in *Plasmodium vivax*. *Nat. Genet.* 48, 953–958. doi: 10.1038/ng.3588

Jennison, C., Arnott, A., Tessier, N., Tavul, L., Koepfli, C., Felger, I., et al. (2015). *Plasmodium vivax* populations are more genetically diverse and less structured than sympatric *Plasmodium falciparum* populations. *PLoS Negl. Trop. Dis.* 9:e0003634. doi: 10.1371/journal.pntd.0003634

Lai, S., Li, Z., Wardrop, N. A., Sun, J., Head, M. G., Huang, Z., et al. (2017). Malaria in China, 2011–2015: an observational study. *Bull. World Health Organ.* 95, 564–573. doi: 10.2471/BLT.17.191668

Li, H., and Durbin, R. (2010). Fast and accurate long-read alignment with burrows-Wheeler transform. *Bioinformatics* 26, 589–595. doi: 10.1093/bioinformatics/btp698

Lim, M. Y.-X., LaMonte, G., Lee, M. C., Reimer, C., Tan, B. H., Corey, V., et al. (2016). UDP-galactose and acetyl-CoA transporters as *Plasmodium* multidrug resistance genes. *Nat. Microbiol.* 1:16166. doi: 10.1038/nmicrobiol.2016.166

Lu, F., Lim, C. S., Nam, D. H., Kim, K., Lin, K., Kim, T.-S., et al. (2010). Mutations in the antifolate-resistance-associated genes dihydrofolate reductase and dihydropteroate synthase in *Plasmodium vivax* isolates from malaria-endemic countries. *Am. J. Trop. Med. Hyg.* 83, 474–479. doi: 10.4269/ajtmh.2010.10-0004

Manske, M., Miotto, O., Campino, S., Auburn, S., Almagro-Garcia, J., Maslen, G., et al. (2012). Analysis of *Plasmodium falciparum* diversity in natural infections by deep sequencing. *Nature* 487, 375–379. doi: 10.1038/nature11174

Maude, R. J., Pontavornpinyo, W., Saralamba, S., Aguas, R., Yeung, S., Dondorp, A. M., et al. (2009). The last man standing is the most resistant: eliminating artemisinin-resistant malaria in Cambodia. *Malar. J.* 8, 1–7. doi: 10.1186/1475-2875-8-31

McKenna, A., Hanna, M., Banks, E., Sivachenko, A., Cibulskis, K., Kernytsky, A., et al. (2010). The genome analysis toolkit: a MapReduce framework for analyzing next-generation DNA sequencing data. *Genome Res.* 20, 1297–1303. doi: 10.1101/gr.107524.110

Na, B.-K., Lee, H.-W., Moon, S.-U., In, T.-S., Lin, K., Maung, M., et al. (2005). Genetic variations of the dihydrofolate reductase gene of *Plasmodium vivax* in Mandalay division, Myanmar. *Parasitol. Res.* 96, 321–325. doi: 10.1007/s00436-005-1364-0

Neafsey, D. E., Galinsky, K., Jiang, R. H., Young, L., Sykes, S. M., Saif, S., et al. (2012). The malaria parasite *Plasmodium vivax* exhibits greater genetic diversity than *Plasmodium falciparum*. *Nat. Genet.* 44, 1046–1050. doi: 10.1038/ng.2373

Nyunt, M. H., Han, J.-H., Wang, B., Aye, K. M., Aye, K. H., Lee, S.-K., et al. (2017). Clinical and molecular surveillance of drug resistant vivax malaria in Myanmar (2009–2016). *Malar. J.* 16:117. doi: 10.1186/s12936-017-1770-7

Olliaro, P. L., and Mussano, P. (2003). Amodiaquine for treating malaria. *Cochrane Database Syst. Rev.* 2:CD000016. doi: 10.1002/14651858.CD000016

Park, D. J., Lukens, A. K., Neafsey, D. E., Schaffner, S. F., Chang, H.-H., Valim, C., et al. (2012). Sequence-based association and selection scans identify drug resistance loci in the *Plasmodium falciparum* malaria parasite. *Proc. Natl. Acad. Sci. U. S. A.* 109, 13052–13057. doi: 10.1073/pnas.1210585109

Pearson, R. D., Amato, R., Auburn, S., Miotto, O., Almagro-Garcia, J., Amaratunga, C., et al. (2016). Genomic analysis of local variation and recent evolution in *Plasmodium vivax*. *Nat. Genet.* 48, 959–964. doi: 10.1038/ng.3599

Plouffe, D. M., Wree, M., Du, A. Y., Meister, S., Li, F., Patra, K., et al. (2016). High-throughput assay and discovery of small molecules that interrupt malaria transmission. *Cell Host Microbe* 19, 114–126. doi: 10.1016/j.chom.2015.12.001

Preston, M. D., Campino, S., Assefa, S. A., Echeverry, D. F., Ocholla, H., Amambua-Ngwa, A., et al. (2014). A barcode of organellar genome polymorphisms identifies the geographic origin of *Plasmodium falciparum* strains. *Nat. Commun.* 5, 4052–4057. doi: 10.1038/ncomms5052

Price, R. N., Auburn, S., Marfurt, J., and Cheng, Q. (2012). Phenotypic and genotypic characterisation of drug-resistant *Plasmodium vivax*. *Trends Parasitol.* 28, 522–529. doi: 10.1016/j.pt.2012.08.005

Price, R. N., Douglas, N. M., Anstey, N. M., and von Seidlein, L. (2011). *Plasmodium vivax* treatments: what are we looking for? *Curr. Opin. Infect. Dis.* 24, 578–585. doi: 10.1097/QCO.0b013e32834c61e3

Sabeti, P. C., Reich, D. E., Higgins, J. M., Levine, H. Z., Richter, D. J., Schaffner, S. F., et al. (2002). Detecting recent positive selection in the human genome from haplotype structure. *Nature* 419, 832–837. doi: 10.1038/nature01140

Sabeti, P. C., Varilly, P., Fry, B., Lohmueller, J., Hostetter, E., Cotsapas, C., et al. (2007). Genome-wide detection and characterization of positive selection in human populations. *Nature* 449, 913–918. doi: 10.1038/nature06250

Saint-Léger, A., Sinadinos, C., and Ribas de Pouplana, L. (2016). The growing pipeline of natural aminoacyl-tRNA synthetase inhibitors for malaria treatment. *Bioengineered* 7, 60–64. doi: 10.1080/21655979.2016.1149270

Schaffner, S. F., Taylor, A. R., Wong, W., Wirth, D. F., and Neafsey, D. E. (2018). hmmIBD: software to infer pairwise identity by descent between haploid genotypes. *Malar. J.* 17:196. doi: 10.1186/s12936-018-2349-7

Shen, H. M., Chen, S. B., Cui, Y. B., Xu, B., Kassegne, K., Abe, E. M., et al. (2018). Whole-genome sequencing and analysis of *Plasmodium falciparum* isolates from China-Myanmar border area. *Infect. Dis. Poverty* 7:118. doi: 10.1186/s40249-018-0493-5

Shen, H.-M., Chen, S.-B., Wang, Y., Xu, B., Abe, E. M., and Chen, J.-H. (2017). Genome-wide scans for the identification of *Plasmodium vivax* genes under positive selection. *Malar. J.* 16:238. doi: 10.1186/s12936-017-1882-0

Song, L.-G., Zeng, X.-D., Li, Y.-X., Zhang, B.-B., Wu, X.-Y., Yuan, D.-J., et al. (2018). Imported parasitic diseases in mainland China: current status and perspectives for better control and prevention. *Infect. Dis. Poverty* 7:78. doi: 10.1186/s40249-018-0454-z

Sturrock, H. J., Roberts, K. W., Wegbreit, J., Ohrt, C., and Gosling, R. D. (2015). Tackling imported malaria: an elimination endgame. *Am. J. Trop. Med. Hyg.* 93, 139–144. doi: 10.4269/ajtmh.14-0256

Szpiech, Z. A., and Hernandez, R. D. (2014). Selscan: an efficient multi-threaded program to perform EHH-based scans for positive selection. *Mol. Biol. Evol.* 31, 2824–2827. doi: 10.1093/molbev/msu211

Tamura, K., Stecher, G., Peterson, D., Filipski, A., and Kumar, S. (2013). MEGA6: molecular evolutionary genetics analysis version 6.0. *Mol. Biol. Evol.* 30, 2725–2729. doi: 10.1093/molbev/mst197

Trimarsanto, H., Amato, R., Pearson, R.D., Sutanto, E., Noviyanti, R., Trianty, L., et al. (2019). A molecular barcode and online tool to identify and map imported infection with *Plasmodium vivax*. bioRxiv [Preprint]. doi: 10.1101/776781

Voight, B. F., Kudaravalli, S., Wen, X., and Pritchard, J. K. (2006). A map of recent positive selection in the human genome. *PLoS Biol.* 4:e72. doi: 10.1371/journal.pbio.0040072

Volkman, S. K., Sabeti, P. C., DeCaprio, D., Neafsey, D. E., Schaffner, S. F., Milner, D. A., et al. (2007). A genome-wide map of diversity in *Plasmodium falciparum*. *Nat. Genet.* 39, 113–119. doi: 10.1038/ng1930

Wang, D., Li, S., Cheng, Z., Xiao, N., Cotter, C., Hwang, J., et al. (2015). Transmission risk from imported *Plasmodium vivax* malaria in the China–Myanmar border region. *Emerg. Infect. Dis.* 21, 1861–1864. doi: 10.3201/eid2110.150679

Xia, Z.-G., Feng, J., and Zhou, S.-S. (2013). Malaria situation in the People's Republic of China in 2012. *Zhongguo ji sheng chong xue yu ji sheng chong bing za zhi.* 31, 413–418.

Xia, Z.-G., Yang, M.-N., and Zhou, S.-S. (2012). Malaria situation in the People's Republic of China in 2011. *Zhongguo ji sheng chong xue yu ji sheng chong bing za zhi.* 30, 419–422.

Yin, J.-H., Zhou, S.-S., Xia, Z.-G., Wang, R.-B., Qian, Y.-J., Yang, W.-Z., et al. (2014). Historical patterns of malaria transmission in China. *Adv. Parasitol.* 86, 1–19. doi: 10.1016/B978-0-12-800869-0.00001-9

Zhang, L., Feng, J., and Xia, Z.-g. (2014). Malaria situation in the People's Republic of China in 2013. *Zhongguo ji sheng chong xue yu ji sheng chong bing za zhi.* 32, 407–413.

Zhang, L., Feng, J., Zhang, S., Xia, Z., and Zhou, S. (2016). Malaria situation in the People's Republic of China in 2015. *Zhongguo ji Sheng Chong xue yu ji Sheng Chong Bing za zhi.* 34, 477–481.

Zhang, L., Zhou, S.-S., Jun, F., Wen, F., and XIA, Z.-G. (2015). Malaria situation in the People's Republic of China in 2014. *Zhongguo ji sheng chong xue yu ji sheng chong bing za zhi.* 33, 319–326.

Zhou, S., Li, Z., Cotter, C., Zheng, C., Zhang, Q., Li, H., et al. (2016). Trends of imported malaria in China 2010–2014: analysis of surveillance data. *Malar. J.* 15:39. doi: 10.1186/s12936-016-1093-0

Zhou, G., Sun, L., Xia, R., Duan, Y., Xu, J., Yang, H., et al. (2014). Clinical malaria along the China-Myanmar border, Yunnan Province, China, January 2011-august 2012. *Emerg. Infect. Dis.* 20, 675–678. doi: 10.3201/eid2004.130647

Zhou, S.-S., Wang, Y., and Li, Y. (2011). Malaria situation in the People's Republic of China in 2010. *Zhongguo ji sheng chong xue yu ji sheng chong bing za zhi.* 29, 401–403.

A novel *Toxoplasma gondii* TGGT1_316290 mRNA-LNP vaccine elicits protective immune response against toxoplasmosis in mice

Dan Li[1,2], Yizhuo Zhang[1,2], Shiyu Li[1,2] and Bin Zheng[1,2,3]*

[1]School of Basic Medical Sciences and Forensic Medicine, Hangzhou Medical College, Hangzhou, China, [2]Engineering Research Center of Novel Vaccine of Zhejiang Province, Hangzhou Medical College, Hangzhou, China, [3]Key Laboratory of Bio-tech Vaccine of Zhejiang Province, Hangzhou Medical College, Hangzhou, China

Toxoplasma gondii (*T. gondii*) can infect almost all warm-blooded animals and is a major threat to global public health. Currently, there is no effective drug or vaccine for *T. gondii*. In this study, bioinformatics analysis on B and T cell epitopes revealed that TGGT1_316290 (TG290) had superior effects compared with the surface antigen 1 (SAG1). TG290 mRNA-LNP was constructed through the Lipid Nanoparticle (LNP) technology and intramuscularly injected into the BALB/c mice, and its immunogenicity and efficacy were explored. Analysis of antibodies, cytokines (IFN-γ, IL-12, IL-4, and IL-10), lymphocytes proliferation, cytotoxic T lymphocyte activity, dendritic cell (DC) maturation, as well as CD4+ and CD8+ T lymphocytes revealed that TG290 mRNA-LNP induced humoral and cellular immune responses in vaccinated mice. Furthermore, T-Box 21 (T-bet), nuclear factor kappa B (NF-kB) p65, and interferon regulatory factor 8 (IRF8) subunit were over-expressed in the TG290 mRNA-LNP-immunized group. The survival time of mice injected with TG290 mRNA-LNP was significantly longer (18.7±3days) compared with the survival of mice of the control groups (*p*<0.0001). In addition, adoptive immunization using 300μl serum and lymphocytes (5*10⁷) of mice immunized with TG290 mRNA-LNP significantly prolonged the survival time of these mice. This study demonstrates that TG290 mRNA-LNP induces specific immune response against *T. gondii* and may be a potential toxoplasmosis vaccine candidate for this infection.

KEYWORDS
Toxoplasma gondii, TGGT1_316290, mRNA vaccine, lipid nanoparticle, immune response

Introduction

Toxoplasma gondii (*T. gondii*) is an obligate intracellular parasite that threatens one-third of the world's population (Almeria et al., 2021; Smith et al., 2021). It has also become one of the most common zoonotic parasitic protozoa in the world because of its broad host range, high infection rate, and benign coexistence with the host (Montoya and Liesenfeld, 2004). Most people with normally functioning immune system show occult infection without clinical

symptoms of *T. gondii* infection (Pittman and Knoll, 2015; Kochanowsky and Koshy, 2018). However, *T. gondii* seriously affects individuals with impaired immune systems, such as those with AIDS, malignancies, and organ transplant patients, and may cause death (Watts et al., 2015; Flegr and Escudero, 2016). Besides affecting newborns *in utero*, toxoplasmosis can also cause abortion in pregnant women (Robert-Gangneux and Dardé, 2012; Attias et al., 2020). In addition, *T. gondii* infection can be transmitted among livestock and pets, causing miscarriage and stillbirth, suggesting that it is major infection that causes severe economic losses in the livestock industry (Tenter et al., 2000). As a result, toxoplasmosis has attracted much attention in the medical and animal husbandry industry and has become a global public health concern (Montazeri et al., 2018).

Pyrimethamine and sulfadiazine are the current gold standard treatments for *T. gondii* infection (Alday and Doggett, 2017). However, increasing drug resistance has been detected in *T. gondii*, and thus could exacerbate the severity of the disease and lead to treatment failure (Wang et al., 2022). Although drug therapy is effective against *T. gondii* tachyzoites, it is ineffective against the cyst of *T. gondii* (Silva et al., 2021). This calls for development of effective vaccines for the long-term control and prevention of *T. gondii* infection while reducing the side effects and dependence on chemotherapy drugs (Wang et al., 2019).

To date, only one of commercially-licensed live attenuated vaccine were developed based on S48 strain (Toxovax®, MSD, New Zealand). Toxovax® is approved in a few regions (Europe and New Zealand) and can reduce the losses caused by congenital toxoplasmosis in sheep farming, indicating that *T. gondii* vaccine can be successfully exploited and commercially available for human immunization. Nevertheless, Toxovax® vaccine has some limitations, such as short-shelf life, uncertain genetic background, and reverting to the virulent wild type, making them unsuitable for further promotion and use.

Although several studies have employed various vaccination strategies, mainly including DNA vaccines, epitope vaccines, protein vaccines, inactivated vaccines, live vector-based vaccines, live attenuated vaccines, exosome vaccines, nanoparticle vaccines, and carbohydrate vaccines, to develop an effective toxoplasmosis vaccine (Wang et al., 2019), there is no safe and effective vaccine for *T. gondii* (Chu and Quan, 2021). mRNA vaccines are promising alternatives to conventional vaccines because of their high potency, low manufacturing cost, and short preparation period (Bok et al., 2021; Chaudhary et al., 2021). Nevertheless, only a few researches have analyzed mRNA vaccines against parasites.

This study aimed to explore a novel mRNA vaccine candidate against *T. gondii*. Furthermore, BALB/c mice were intramuscularly given TGGT1_316290 (TG290, ToxoDB accession number: TGGT1_316290) mRNA-LNP vaccine to evaluate its immunogenicity and immunoprotective effect.

Materials and methods

Epitope prediction

The potency of vaccine candidate antigens against *T. gondii* was assessed using PROTEAN program in DNASTAR software (Madison, Wisconsin, United States) based on its surface probability, flexible regions, antigenic index, and hydrophilicity. Additionally, the predicted half maximal inhibitory concentration (predicted IC50) values of polypeptides that bind to the major histocompatibility complex (MHC) class II molecules of vaccine candidate antigens were determined using Immune Epitope Database (IEDB, http://tools.immuneepitope.org/mhcii/).

Mice, parasites, and cells

Specific-pathogen-free (SPF) male BALB/c mice (seven-week-old) were obtained from the Zhejiang Experimental Animal Center (Zhejiang province, China) and kept under standard routine conditions. Some mice were used in challenge test after immunization with mRNA vaccine, and others were used in challenge test after adoptive immunization. This study was approved by Hangzhou Medical College Institutional Animal Care and Use Committee (No: 2021-152) and followed the Chinese legislation regarding the use and care of research animals (GB/T35823-2018).

The *T. gondii* RH strain (type I) was stored at the laboratory for the extraction of total RNA, challenge experiments, and preparation of soluble tachyzoite antigens (STAg), as previously described (Zheng et al., 2017).

Vero, HEK293, and C2C12 cells preserved in the research group and maintained in DMEM containing 10% fetal bovine serum (FBS; Gibco, New Zealand) in an incubator with 5% CO_2 at 37°C, were used for *T. gondii* generation and *in vitro* transfections.

Expression of the recombinant TG290 (rTG290) protein and preparation of rabbit anti-TG290 polyclonal antibodies (rabbit anti-TG290 pAb)

The TG290 gene was amplified by PCR using *T. gondii* cDNA as template. TG290 and plasmid pET-28a were digested with BamHI and XhoI restriction enzymes. Then, it was separated by agarose gel electrophoresis and purified by AxyPrep™ DNA Gel Extraction Kit (Axygen, California, United States). T4 DNA ligase (Takara, Dalian, China) was used to ligate the digested DNA and pET-28a. The ligated products were transformed into TOP10 competent cells. Kanamycin was used to screen positive colonies. Finally, the positive plasmids were identified by sequencing. The constructed recombinant pET28a-TG290 vector was transformed into *E. coli* BL21 (DE3) to induce rTG290 expression overnight at 37°C *in vitro* using 0.1 mM/L isopropyl-beta-D-Thiogalactoside (IPTG). The bacteria were centrifuged at $12,000 \times g$, 4°C for 15 min and resuspended with PBS. Cells were cracked by ultrasound at low temperature (power: 200 W, 5 s ultrasonic interval 10s, 100 times), and supernatant was collected. Purified rTG290 was obtained using $Ni2^+$-NTA agarose columns (Sangon Biotech, Shanghai, China) *via* affinity chromatography, then stored at −80°C for further use. The purified rTG290 was utilized to generate rabbit anti-TG290 polyclonal antibodies as described by Zheng et al. (2019).

Formulation of TG290 mRNA and TG290 mRNA-LNP

Wild-type constructs encoding TG290 [containing a T7 promoter site for *in vitro* transcription (IVT) of mRNA, 5′ and 3′ UTRs] were synthesized by GenScript Biotech Corporation (Nanjing, China). The −300 bp upstream and 300 bp downstream sequences of the TG290 gene were used for the 5′ UTR and 3′ UTR, respectively. The T7 RNA polymerase promoter site upstream of the 5′ UTR is used to transcribe mRNA *in vitro*. Standard mRNA was synthesized from linearized DNA using the T7 *in vitro* transcription kit with unmodified nucleotides (CELLSCRIPT™, Wisconsin, United States). Incognito mRNA Synthesis Kit (CELLSCRIPT™, Wisconsin, United States) was used to generate RNA encapsulated in lipid nanoparticles with pseudouridine instead of uridine. NanoAssemblr® Benchtop system (Precision Nanosystems Inc., PNI, British Columbia, Canada) was used to encapsulate enzymatically added structures of 5′ cap-1 and 3′ poly (A). The mRNA was solubilized with PNI formulation buffer (PNI, British Columbia, Canada). mRNA-LNPs were generated at a 3:1 flow rate ratio (RNA in PNI buffer; GenVoy-ILM™) through a laminar flow cassette at 12 ml/min. Quant-iT™ RiboGreen™ RNA Reagent and Kit (Invitrogen, California, United States) was used to assess the encapsulation efficiency and mRNA concentration of mRNA-LNPs.

In vitro transfections

HEK293 and C2C12 cells were transfected with TG290 mRNA using Lipo2000 reagent (Invitrogen, California, United States) following the manufacturer's protocol. Cells were seeded in 12-well plates until they reached 70–90% confluence after transfection. They were transferred to a fresh DMEM medium. 4 μl Lipo 2000 liposomes were added to 100 μl Gibco Opti MEM medium and mixed well for 5 min at room temperature. 2 μg mRNA was added to 100 μl Opti MEM medium and mix well for 5 min at room temperature. The mRNA-lipid complexes were mixed together at room temperature for 20 min and then carefully added to the culture medium. The cell supernatant and whole cell lysate were collected 24 h after transfection for subsequent experiments. The cells were washed with phosphate-buffered saline (PBS) and lysed with radioimmunoprecipitation (RIPA) buffer (Biotime, Haimen, China), then centrifuged at $16,000 \times g$, 4°C for 10 min. The supernatant was purified *via* ultracentrifugation at $140,000 \times g$ overnight (16 h) at 4°C using a 20% sucrose cushion. Protein complexes were resuspended in 50 μl of PBS containing 1% bovine serum albumin (BSA) and stored at −20°C for subsequent analysis. Lysates or purified supernatant samples (10 μl) were detected *via* western blotting.

Immunization and *Toxoplasma gondii* challenge

Seven-week-old male BALB/c mice ($n = 60$) were randomly divided into three groups (experimental group, negative group, and blank group) to evaluate the prophylactic efficacy of TG290 mRNA-LNP. The mice in the experimental group ($n = 20$) were intramuscularly given 10 μg TG290 mRNA-LNP vaccine once every 2 weeks (thrice),

while the mice in the negative group ($n = 20$) were injected with empty LNP. The mice in the blank group were not given any treatment ($n = 20$). Blood was collected from each mouse on days 0, 13, 27, and 41, and the serum was stored at − 20°C. The mice were intraperitoneally challenged with 100 tachyzoites of highly virulent *T. gondii* RH strain at 2 weeks after final administration (15 mice per group), then survival time was monitored daily.

Furthermore, serum was collected from each group ($n = 5$) in the immunization section to assess the protective effect of serum transfer immunization. The naive mice ($n = 30$) were divided into three groups, then injected with TG290 mRNA-LNP-immunized serum ($n = 10$), LNP-immunized serum (negative group, $n = 10$), and the naive serum (blank group, $n = 10$) *via* (100 μl of serum per mice) tail vein daily for 5 days. The mice were also intraperitoneally injected with 100 RH tachyzoites and the survival time was monitored.

Splenocytes were obtained from each group of mice ($n = 5$) in the immunization section to evaluate the preventive effect of splenocyte transfer immunization. The naive mice ($n = 30$) were divided into three groups. The mice were injected with TG290 mRNA-LNP-immunized splenocytes or LNP-immunized splenocytes, or naive splenocytes *via* the tail vein ($5*10^8$ splenocytes per mouse). The mice were also given *T. gondii* RH strain (100 tachyzoites) intraperitoneally at 24 h post injection, and the survival time was monitored daily.

Indirect ELISA

Each hole in the ELISA board was coated with rTG290 (20 μg/ml) and incubated overnight in a 2–8°C wet box. The plates were washed five times with PBST (0.05% Tween-20 in PBS) and blocked with 1% bovine serum albumin (BSA) at room temperature for 2 h. 100 μl diluted serum (1:100) was added to each well and incubated at room temperature for 2 h. The plates were washed five times with PBST (0.05% Tween-20), then the samples were incubated with 100 μl 1:100000 diluted horseradish peroxidase (HRP) labeled Goat Anti-Mouse IgG, IgG1, or IgG2a (Abcam, Cambridge, United Kingdom) at 37°C for 1 h in each well. The plates were washed again, and the samples were incubated with 100 μl tetramethylbenzidine substrate reaction solution at room temperature and away from light for 15 min in each well. An automatic ELISA reader (BioTek, Virginia, United States) was used to determine the OD value of the sample at 450 nm. Meanwhile, the corresponding blank control group and negative control group were set up. All samples were in triplicates.

Preparation of spleen cell suspension

Spleen was removed from five mice in each group after 2 weeks of the last vaccination, then ground with nylon sieve to obtain splenocytes. Red blood cell lysis buffer (Sigma, Melbourne, United States) was added to remove blood cells. The spleen cells were resuspended in Dulbecco's modified Eagle's medium with 10% FBS (Gibco, New Zealand). The suspension of 45 μl splenic lymphocytes was mixed with 5 μl 0.4% trypan blue dye and stained under a microscope (count of viable cells should be above 95% before the next experiment).

Lymphocyte proliferation assay

Cell Counting Kit-8 (CCK-8, Dojindo, Kumamoto, Japan) was used to determine the proliferation activity of spleen lymphocytes following the manufacturer's instructions. About $2*10^5$ purified spleen lymphocytes per well were incubated into 96-well microplates. The lymphocytes were stimulated with rTG290 ($10\,\mu g/ml$). Concanavalin A (ConA; $5\,\mu g/ml$; Sigma) was added as a positive control, and Dulbecco's modified Eagle's medium alone was added as a negative control. CCK-8 (Dojindo, Kumamoto, Japan) was added to each well after 4 days, then incubated at $37°C$ for 4h for lymphocyte proliferation. The stimulation index was calculated as follows: stimulation index (SI) = (OD_{570} rTG290 − OD_{570} Control): (OD_{570} ConA − OD_{570} Control).

Cytokine measurement

Splenic lymphocytes ($100\,\mu l$: adjusted density of $5*10^6$ cells/mL) were added to each well with 96-well plates, followed by ConA ($5\,\mu g/$ ml) or rTG290 ($10\,\mu g/ml$) addition. The cells were then cultured in a 5% CO_2 incubator at $37°C$. Each BABL/c mouse in each group had three parallel wells. The cell supernatants were used to evaluate the level of IL-4 at 24h, IL-10 at 72h, and IFN-γ and IL-12 at 96h. Mouse ELISA Kit with Pre-coated Plates series (eBioscience, California, United States) was used to for cytokine measurement following the manufacturer's instructions.

Cytotoxic T lymphocyte activity assays

Cytotoxic T-lymphocyte (CTL) assay was performed *via* lactate dehydrogenase-release assay using CytoTox 96® Non-Radioactive Cytotoxicity Assay Kit (Promega, Wisconsin, United States). Lymphocytes were cultured with 100 U/ml recombinant mouse IL-12 (eBioscience, California, United States) for 5 days to act as effector cells, while Sp2/0 cells were transfected with TG290 mRNA-LNP to serve as target cells. Effector cells and target cells were mixed at a scale of 10:1, 20:1, 40:1, 80:1, and incubated at $37°C$ for 6h. Cytotoxicity was calculated as follows: %Cytotoxicity = (Experimental -Effector Spontaneous-Target Spontaneous)/(Target Maximum-Target Spontaneous) × 100.

Flow cytometry assay

The percentages of CD4+ and CD8+ T cells of mice in the TG290 mRNA-LNP, LNP, and blank groups were detected using flow cytometry. Splenic lymphocytes were harvested and dead cells were first removed using the Dead Cell Removal Kit (Miltenyi Biotec, no. 130-090-101) following the manufacturer's instructions. Surviving cells were counted and single cell suspensions were prepared by resuspending them at 1×10^7 cells/ml in cell staining buffer. They were then pre-incubated with TruStain FcX™ PLUS (anti-mouse CD16/32) antibody at $2.5\,\mu g$ per 10^7 cells in a volume of $100\,\mu l$ for 5–10 min on ice to block the Fc receptor. Subsequently, the cells were incubated with anti-mouse CD3e-FITC + anti-mouse CD8-PE and anti-mouse CD3e-FITC + anti-mouse CD4-PE antibodies (Abcam, Cambridge,

United Kingdom) in the dark at $4°C$ for 30 min. For CD83, CD86, and MHC molecule changes in splenic DCs, the separated lymphocytes were double-stained with CD11c-FITC + CD83-PE, CD11c-FITC + CD86-PE, CD11c-FITC + MHC-I-PE, and CD11c-FITC + MHC-II-PE (eBioscience, California, United States) in the dark at $4°C$ for 30 min. Cell populations were analyzed *via* flow cytometry using FACScan flow cytometer (Becton Dickinson, New Jersey, United States) and CellQuest software (Becton Dickinson, New Jersey, United States).

Cytokine-related transcription factor assay

qRT-PCR and western blotting were used to assess the expression levels of interferon regulatory factor 8 (IRF8), T-Box 21 (T-bet), and nuclear factor kappa B (NF-kB) p65 in prepared splenocyte lymphocytes. Total RNA was isolated from the cells using a RNAsimple Total RNA kit (TaKaRa, Dalian, China). It was then used to synthesize cDNA with the ReverTra Ace -a-™ (Toyobo, Osaka, Japan) kit whereas the KOD SYBR® qPCR Mix (Toyobo, Osaka, Japan) was used to quantify mRNA expression following the manufacturer's protocol. The qPCR program was as follows: pre-denaturation at $98°C$ for 2 min, denaturation at $98°C$ for 10s, annealing at $60°C$ for 10s, and extension at $68°C$ for 30s (40 cycles). The primers utilized are shown in Table 1. Western blotting was used to analyze transcription factors (IRF8, T-bet, NF-kB p65) in the nucleus *via* the Nuclear and cytoplasmic Isolation Kit (Biotime, Haimen, China). The antibodies used in this study were source from Cell Signaling Technology, Inc. (Danvers, MA, United States) with the following catalog numbers: #5628 for IRF8, #13232 for T-bet, #8242 for NF-kB p65, and #4499 for H3 Histone.

Statistical analysis

GraphPad Prism 8.0 (GraphPad, California, United States) was used for statistical analyses. One-way ANOVA with multiple comparisons (compare the mean of each group with the mean of every other group) was used to assess the differences in antibody levels, cytokine levels, lymphocyte proliferation, and flow cytometry assays

TABLE 1 RT -PCR primers used to amplify the NF-κB p65, T-bet, IRF8, and β-actin genes designed by primer premier 6.0.

Primer name	Sequence
NF-κB p65-F	5′-GAACCAGGGTGTGTCCATGT-3′
NF-κB p65-R	5′-TCCGCAATGGAGGAGAAGTC-3′
T -bet-F	5′-GCCAGGGAACCGCTTATATG-3′
T -bet-R	5′-TGGAGAGACTGCAGGACGAT-3′
IRF8-F	5′-GCTGATCAAGGAACCTTGTG-3′
IRF8-R	5′-CAGGCCTGCACTGGGCTG-3′
β-Actin-F	5′-GCTTCTAGGCGGACTGTTAC-3′
β-Actin-R	5′-CCATGCCAATGTTGTCTCTT-3′

among all the groups. Log-rank tests were used to evaluate the survival time. $p < 0.05$ was considered statistically significant.

Results

Bright B cell and T cell epitopes prediction of TG290

Antigenic epitopes generally have high hydrophilicity, flexibility, antigen index and multi-surface probability (Lyn et al., 1991). Hydrophilic amino acids are enriched on the surface of the hydrophilic region, and these sites have evolutionary been used as the main amino acid insertion sites for protein, which also lays a foundation for the secretion of the protein into the cytoplasm and extracellular. The amino acid residues with strong flexibility are the sites with high plasticity, which can easily form antigenic epitopes. Surface probability illustrates the probability that the antigenic point is located in the exposed area of the protein surface. The antigen index can reflect the antigenicity scale by analyzing the amino acids of the continuous sites of the well-studied proteins, and the value can be derived by dividing the frequency of each amino acid in all proteins by the frequency at which each amino acid appears in the antigen region. PROTEAN program in DNASTAR software was used to analyze B cell epitopes of TG290 and SAG1. The regions with hydrophilicity (the critical value is 0) of TG290 are 1–10, 15–16, 17–23, 36–51, 52–67, 75–83, 88–98, 103–106, 115–127, 128–134, 136–140, 141–148, 149–151, 153–162, 164–165, 166–187, 200–232, 235–240. The surface probability regions (the critical value is 1) of TG290 are 3–9, 15–20, 35–47, 50–51, 54–60, 76–79, 89–94, 105, 116–122, 126–127, 129–134, 140–144, 149, 157–159, 168–181, 208–213, 218–230, 238–240. The antigen index regions of TG290 (the critical value is 0) are 1–10, 13–29, 34–62, 64–70, 77–111, 115–161, 167–181, 187–189, 195–206, 209–232, 237–240. The flexibility regions of TG290 are 5–12, 15–22, 24–26, 34–53, 56–63, 74–82, 89–95, 106–108, 117–123, 127–135, 143–148, 156–179, 199–207, 211–214, 218–233. TG290 linear-B cell epitopes were more excellent than SAG1 in terms of surface probability, antigenic index, flexibility, and hydrophilicity (Figure 1). In addition, IEDB online service was used to evaluate T cell epitopes of TG290 and SAG1 as the published article (Fleri et al., 2017). Although the predicted half-maximal inhibitory concentration (predicted IC50) of H2-IAb of TG290 was higher than that of SAG1, the predicted IC50 of H2-Iad and H2-Ied of TG290 was significantly lower than that of SAG1. The predicted IC50 values of HLA-DRB 1*01:01 were similar for both TG290 and SAG1. The results revealed that TG290 protein may have strong binding to MHCII (Table 2). Bioinformatic analysis showed that TG290 peptides had an ideal score of linear-B cell epitopes and a lower percentile of predicted IC50 values than SAG1, suggesting that TG290 has a promising prospect for generating vaccine.

In addition, we used BepiPred-2.0 and NetChop for further analysis of TG290 and SAG1 epitopes. The phylogenetic tree of TG290 was constructed using MEGA software. SWISS – MODEL[1] to build TG290 protein structure. The structural models of mouse BCR(No.8EMA), TCR (No.8D5P) and MHCII-TCR complex (No.3C60) were obtained from the RCSB PDB.[2] Cluspro 2.0[3] protein–protein Docking was used to construct the spatial interaction between TG290 and BCR, TCR and MHCII-TCR. We have provided these results in the Supplementary materials.

Preparation and delivery of TG290 mRNA-LNP

Mature mRNAs similar to host mRNAs were generated. The essential structure of TG290 mRNA consists of the 5′, 3′ UTRs, 5′ cap-1 structure, and a 3′ poly (A) tail (Figure 2A).

The rabbit anti-TG290 pAb can pick out rTG290 (Figure 2B). Meanwhile, the native TG290 was explicitly recognized in STAg. *In vitro*-synthesized mRNA was transfected into HEK293 cells, and the cell lysate and supernatant were collected to further identify mRNA expression. The purified supernatants did not contain β-actin band, demonstrating that any cytoplasmic contamination was removed *via* ultracentrifugation (Figure 2B). In addition, a single specific TG290 band was detected in lysate and supernatant of cells transfected with TG290 mRNA, while no band was detected in the blank control group (Figure 2B). Taken together, these findings show that mRNAs synthesized *in vitro* can induce TG290 protein expression.

Invitrogen's Quant-iTRibogreen RNA assay kit (Invitrogen, California, United States) detected encapsulation efficiency of 95.8%. Furthermore, protein expression in muscle cells was characterized after administration of TG290 mRNA-LNP *via* intramuscular injection to differentiated skeletal myoblasts C2C12 cells, which induced TG290 expression (Figure 2C).

TG290 mRNA-LNP facilitates the production of TG290-specific total IgG and subtype IgG1, IgG2a antibodies

The levels of TG290-specific total IgG, IgG1, and IgG2a were determined *via* enzyme-linked immunosorbent (ELISA) assays to evaluate whether TG290 mRNA-LNP can elicit specific humoral immune response. The TG290-specific total IgG antibody titer increased with the number of injections (Figures 2A, 3A). Furthermore, serum antibody titers were substantially higher in mice vaccinated with TG290 mRNA-LNP than in the control groups ($p < 0.0001$, Figure 3A). The levels of TG290-specific IgG1 and IgG2a were considerably increased in mice immunized with TG290 mRNA-LNP vaccine compared with the blank and LNP groups ($p < 0.0001$, Figure 3B). Notably, the IgG2a levels (0.86 ± 0.01, $p < 0.0001$, Figure 3B) were significantly higher than IgG1 level (0.47 ± 0.01, $p < 0.0001$, Figure 3B).
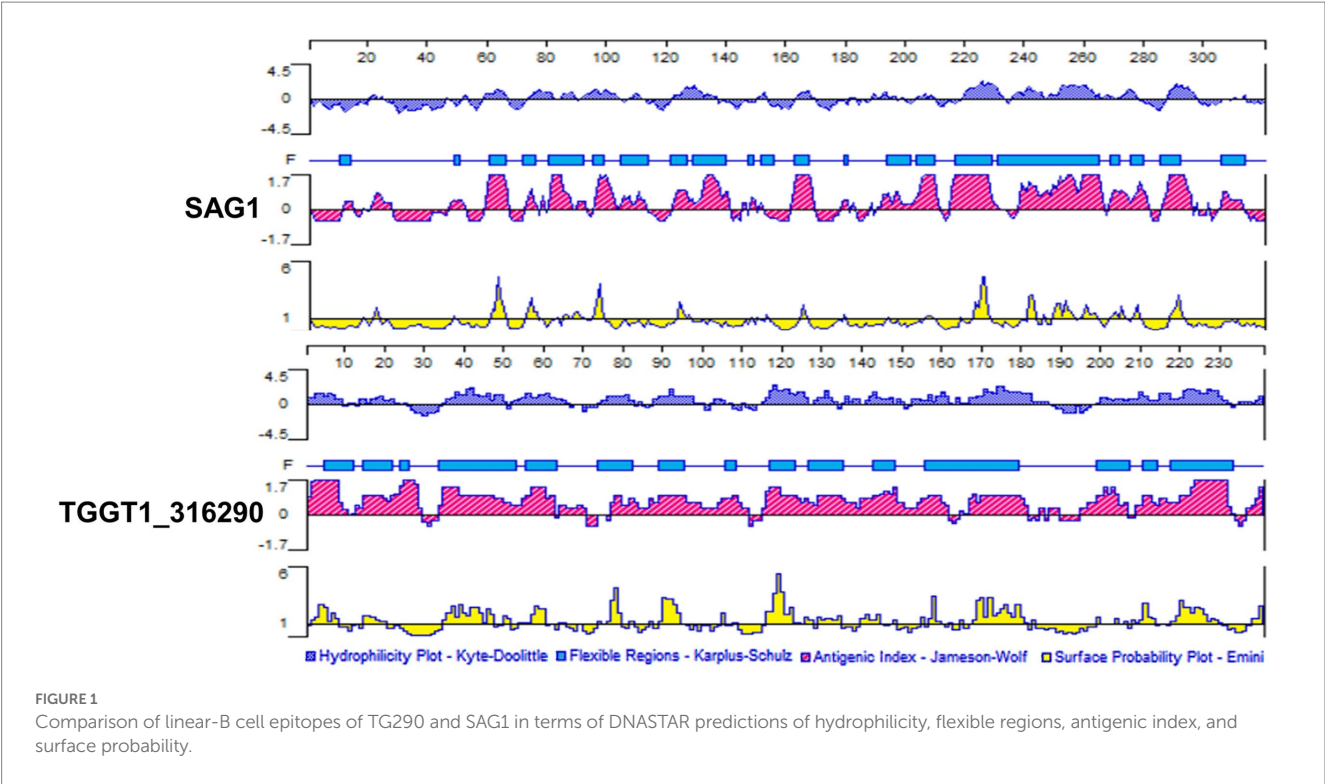
---

[1] https://swissmodel.expasy.org/

[2] https://www.rcsb.org/

[3] https://cluspro.bu.edu/

FIGURE 1
Comparison of linear-B cell epitopes of TG290 and SAG1 in terms of DNASTAR predictions of hydrophilicity, flexible regions, antigenic index, and surface probability.

TABLE 2 Predicted IC50 values from IEDB[a] for TG290 and SAG1 binding to MHC class II molecules.

MHC II alblele[b]	Start-stop[c]		Percentile rank[d]	
	SAG1	TG290	SAG1	TG290
H2-IAb	26–40	28–42	0.95	3.6
H2-IAd	170–184	48–62	2.45	0.49
H2-IEd	14–28	18–32	3.35	0.51
HLA-DRB 1*01:01	12–26	16–30	1.8	2.1

[a]The immune epitope database (http://tools.immuneepitope.org/mhcii).
[b]H2-IAb, H2-IAd, and H2-IEd alleles are mouse MHC class II molecules; the HLA-DRB1*01:01 allele is a human MHC class II molecule.
[c]15 amino acids were chosen for analysis.
[d]Low percentile indicates high level binding according to the software instructions.

TG290 mRNA-LNP vaccination enhances lymphocyte proliferation ability and CTL activity

Splenocytes were obtained at 2 weeks post-final immunization to assess whether the splenic T lymphocytes were validly activated. Lymphocyte proliferation was measured with rTG290 as a stimulator, medium only as a negative control, and ConA as positive control. The stimulation index (SI) of lymphocytes was considerably higher in BALB/c mice vaccinated with TG290 mRNA-LNP (SI: 2.1 ± 0.06, Figure 5A, $p < 0.0001$) than mice in the blank and LNP groups.

CTL responses are crucial for efficient protection against *T. gondii*. Herein, CTL activity of splenic lymphocytes was higher in mice vaccinated with TG290 mRNA-LNP than in the control group when effector target ratio was 40:1 and CTL activity was highest at 80:1 (Figure 5B, $p < 0.0001$).

Generation of high levels cytokines (IFN-γ, IL-12, IL-4, and IL-10) in mice vaccinated with TG290 mRNA-LNP

The levels of Cytokines (IFN-γ, IL-12, IL-4, and IL-10) were measured to determine the type of T helper cell response. The levels of IFN-γ (874.6 ± 27.1 pg./ml), IL-12 (790.6 ± 9.8 pg./ml), IL-4 (138.8 ± 1.7 pg./ml), and IL-10 (265.9 ± 2.3 pg./ml) were significantly elevated in mice immunized with TG290 mRNA-LNP vaccine compared with the control groups ($p < 0.0001$; Figure 4). Collectively, these results reveal that TG290 mRNA-LNP elicits a mixed Th1/Th2 response.

Augmentation in splenic T lymphocytes and dendritic cells levels post TG290 mRNA-LNP vaccine immunization

The splenic lymphocytes were harvested at 2 weeks after the last immunization to investigate the effect of TG290 mRNA-LNP on T Lymphocytes. The levels of CD4+CD8− (Figure 6A) and CD8+CD4− (Figure 6B) T lymphocytes were higher in mice vaccinated with TG290 mRNA-LNP than in the blank and LNP groups ($p < 0.0001$).

Meanwhile, CD83 (Figure 6C) and CD86 (Figure 6D) levels on the surfaces of DCs were higher in mice inoculated with TG290
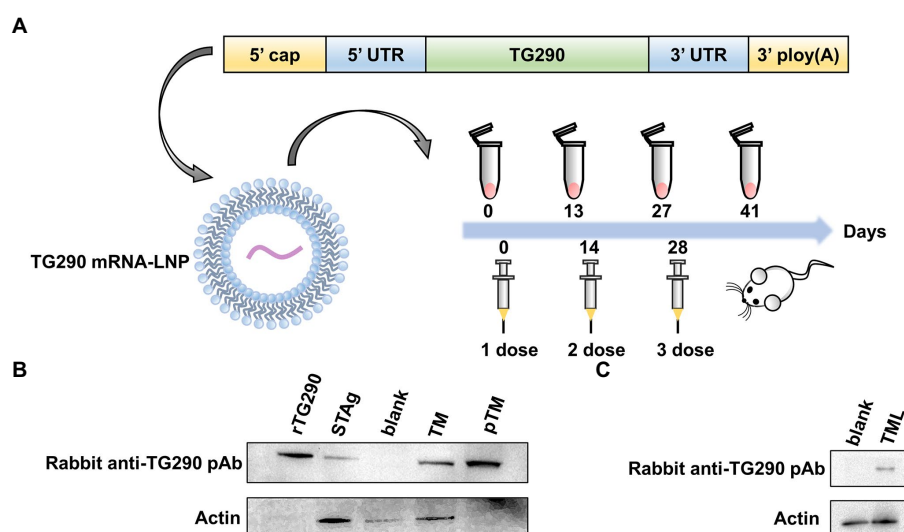
FIGURE 2
The construction, protein expression and delivery of TG290 mRNA-LNP vaccine. **(A)** The engineered mRNA construct. An mRNA encoding the TG290 was designed with 5' and 3' untranslated regions (UTRs) flanking the coding sequence, a 5' cap-1 structure and a 3' poly(A) tail. *In vitro*-synthesized mRNA encapsulated in a lipid nanoparticle to be applied in *in vitro* and *in vivo* experiments. **(B)** The expression of TG290 in HEK293 cell lysates and STAg was determined by Western blot. rTG290 served as a positive control; STAg: (soluble antigen of *T. gondii*); Blank: non-transfected cells; Unpurified cell lysate from TG290 mRNA-transfected cells ©; Purified supernatant from TG290 mRNA-transfected cells (pTM). **(C)** *In vitro*-synthesized TG290 mRNA was encapsulated in a lipid nanoparticle and administered to C2C12 cells. Lysate was analyzed by Western blotting with Rabbit anti-TG290 pAb. Blank: empty transfected cells; TG290 mRNA-LNP transfected cells (TML).
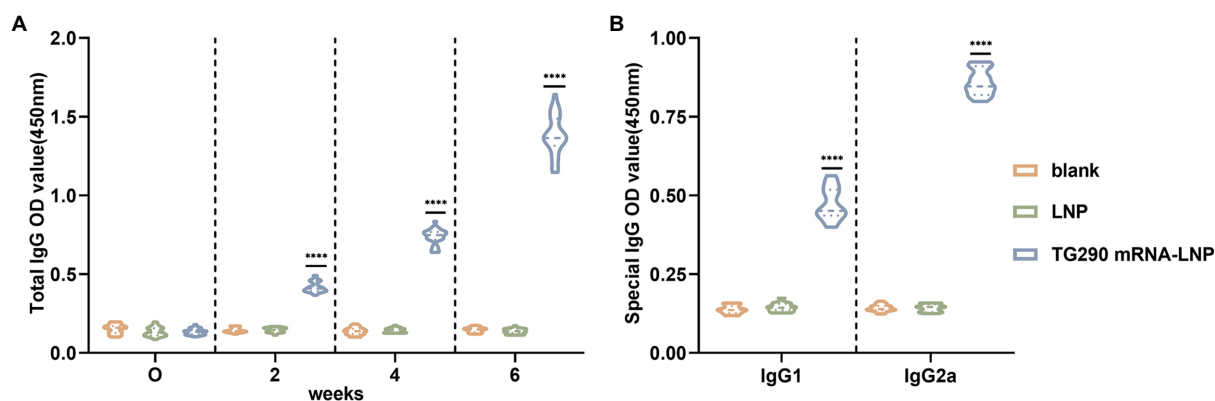
FIGURE 3
TG290 mRNA-LNP vaccine elicited humoral immunity response in BALB/c mice. **(A)** Total TG290-specific IgG; **(B)** TG290-specific IgG1, IgG2a. The OD450 value of total TG290-specific IgG was recorded at 0-, 2-, 4-, and 6-weeks post-vaccination (*n*=10). The OD450 value of TG290-specific IgG subclass (IgG1, IgG2a) was recorded at 6weeks post-vaccination (*n*=5). ****$p<0.0001$, analyzed by One-way ANOVA with multiple comparisons (compare the mean of each group with the mean of every other group).

mRNA-LNP than in the blank and LNP groups ($p<0.0001$). Additionally, TG290 mRNA-LNP vaccination significantly promoted increased levels of MHC-I (Figure 6E) and MHC-II (Figure 6F) molecules ($p<0.0001$). Taken together, these results indicate that TG290 mRNA-LNP elicits higher levels of the CD83 and CD86 molecules of DCs and plays a critical role in the antigen presentation effects of DCs.

TG290 mRNA-LNP immunization increases expression of cytokine-related transcription factors

The mRNA and protein expression levels of IRF8, T-bet, and p65 were determined by qPCR and western blot, respectively. The expression levels of T-bet, p65, and IRF8 were markedly higher in
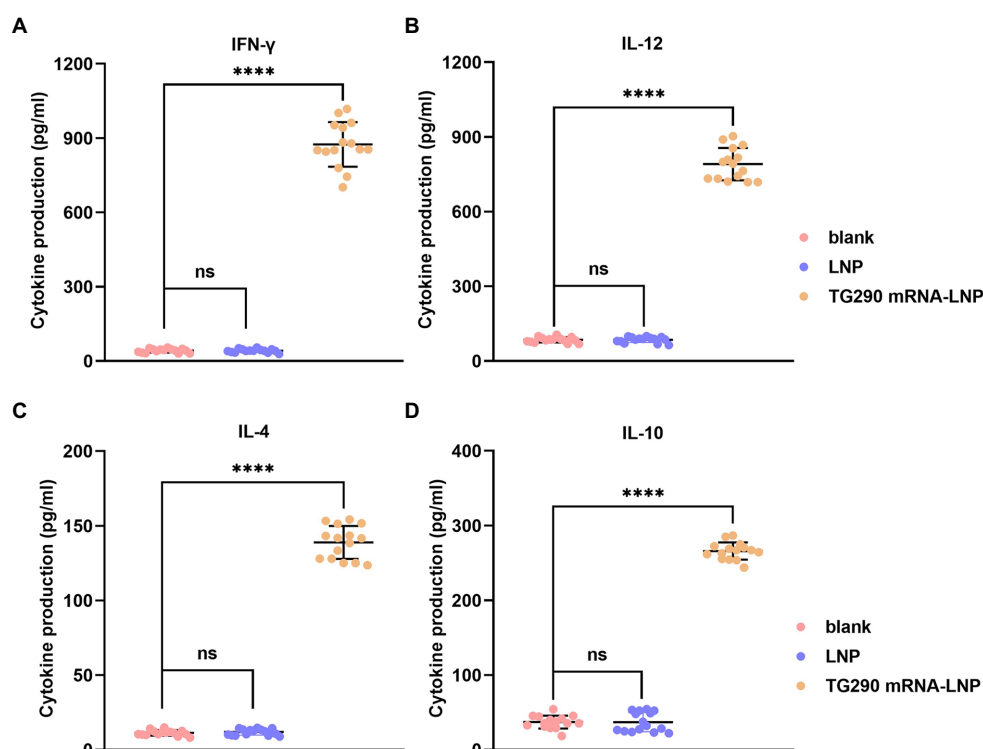
FIGURE 4
The determination of cytokines. The prepared spleen cell suspension was obtained from mice 2weeks of the last vaccination. The levels of **(A)** IFN-γ and **(B)** IL-12 and **(C)** IL-4 and **(D)** IL-10 in BALB/c mice immunized with TG290 mRNA-LNP vaccine. Data were obtained from triplicate independent experiments and are presented as means $\pm$ SD (n=5). ****p<0.0001, analyzed by one-way ANOVA multiple comparisons (compare the mean of each group with the mean of every other group).

FIGURE 5
Proliferation and CTL activity of lymphocytes in immunized BALB/c mice. **(A)** The proliferative responses of splenocytes in immunized BALB/c mice. SI, stimulation index. **(B)** CTL activity of spleen lymphocytes in TG290 mRNA-LNP immunized mice. The horizontal axis indicates the effector-to-target cell ratios. The vertical axis shows the percentage of *T. gondii*-specific lysis. Data were obtained from triplicate independent experiments and are presented as means$\pm$SD (n=5). ****p<0.0001, analyzed by One-way ANOVA with multiple comparisons (compare the mean of each group with the mean of every other group).

FIGURE 6
Flow cytometry analysis. The percentage of CD4+ **(A)** and CD8+ T lymphocytes **(B)** in splenic lymphocytes. The percentage of CD83 **(C)** and CD86 molecules **(D)** on splenic DCs. The percentage of MHC-I **(E)** and MHC-II molecules **(F)** on splenic DCs. $n=5$; ****$p<0.0001$, analyzed by One-way ANOVA with multiple comparisons (compare the mean of each group with the mean of every other group).

mice vaccinated with TG290 mRNA-LNP than in the blank and LNP groups (Figure 7, $p<0.0001$). These results demonstrated that TG290 mRNA-LNP can stimulate the expression of T-bet, p65, and IRF8.

TG290 mRNA-LNP vaccination prolongs the survival time

The survival curve (Figure 8) showed that TG290 mRNA-LNP-vaccinated mice (Figure 8A, 18.5 ± 3 days, $p<0.0001$) had prolonged survival time than mice in the blank and LNP groups (The mice in the two groups died within 8 days). Meanwhile, the survival time of mice adoptively transferred using serum (Figure 8B, 11.9 ± 2.6 days, $p<0.0001$) and splenocytes (Figure 8C, 14.4 ± 2.5 days, $p<0.0001$) was longer than that of mice in the control group (died within 8 days). These datas demonstrated that TG290 mRNA-LNP vaccine prolonged the survival time of mice.

Discussion

T. gondii is a major opportunistic pathogen infecting nearly more than two billion people worldwide (Hakimi et al., 2017). Vaccination can effectively prevent zoonoses (Rahman et al., 2020), especially mRNA vaccines since they have low insertional mutagenesis risk, safe delivery, low manufacturing cost, accelerated development cycles, and high potency. Various mRNA vaccines are at the clinical trial stage and can combat the emergence and re-emergence of infectious diseases, including rabies, Zika, and influenza (Le et al., 2022). Furthermore, mRNA vaccines have recently been successfully used against COVID-19, validating the platform and showing that mRNA vaccines can prevent infectious diseases in the future (Greaney et al., 2021). Various studies have shown that LNP technology can significantly boost the delivery of mRNA, thus providing intrinsic adjuvant activity and enhancing antigen expression.
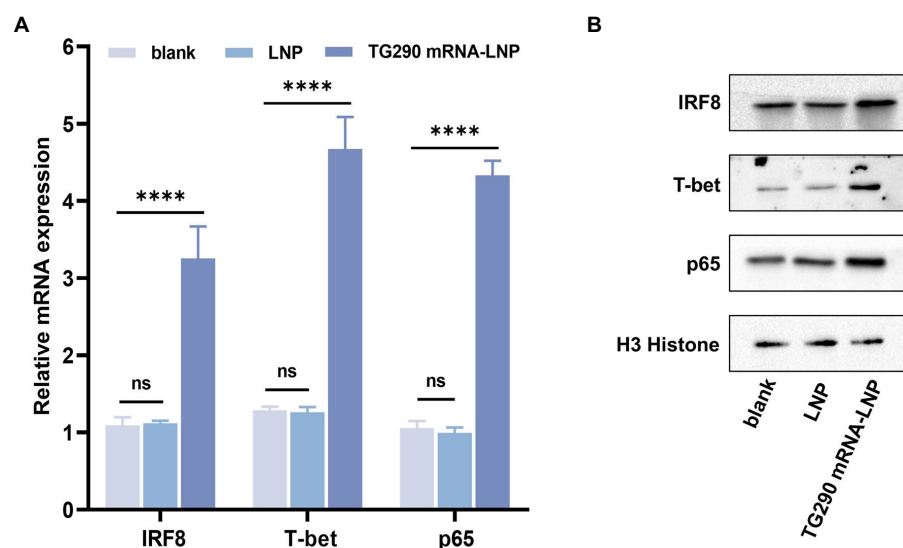
FIGURE 7
The mRNA and protein expression levels of IRF8, T-bet, and p65 in splenocytes. **(A)** The mRNA expression levels of IRF8, T-bet, and p65. **(B)** The protein expression levels of IRF8, T-bet, and p65. Data were obtained from triplicate independent experiments and are presented as means±SD (*n*=5). ****$p<0.0001$, analyzed by One-way ANOVA with multiple comparisons (compare the mean of each group with the mean of every other group).
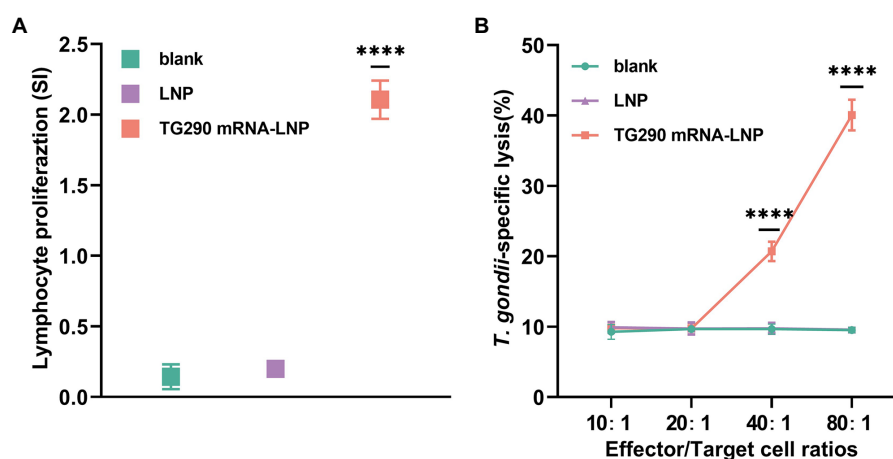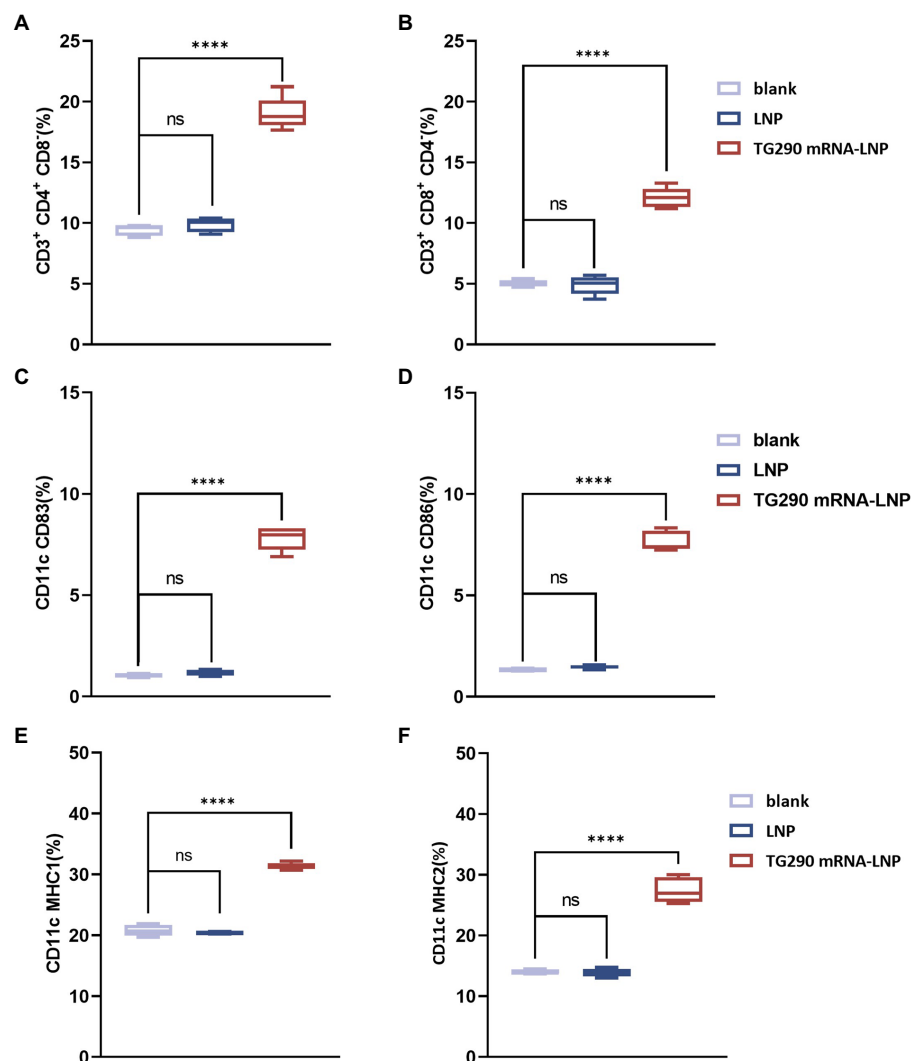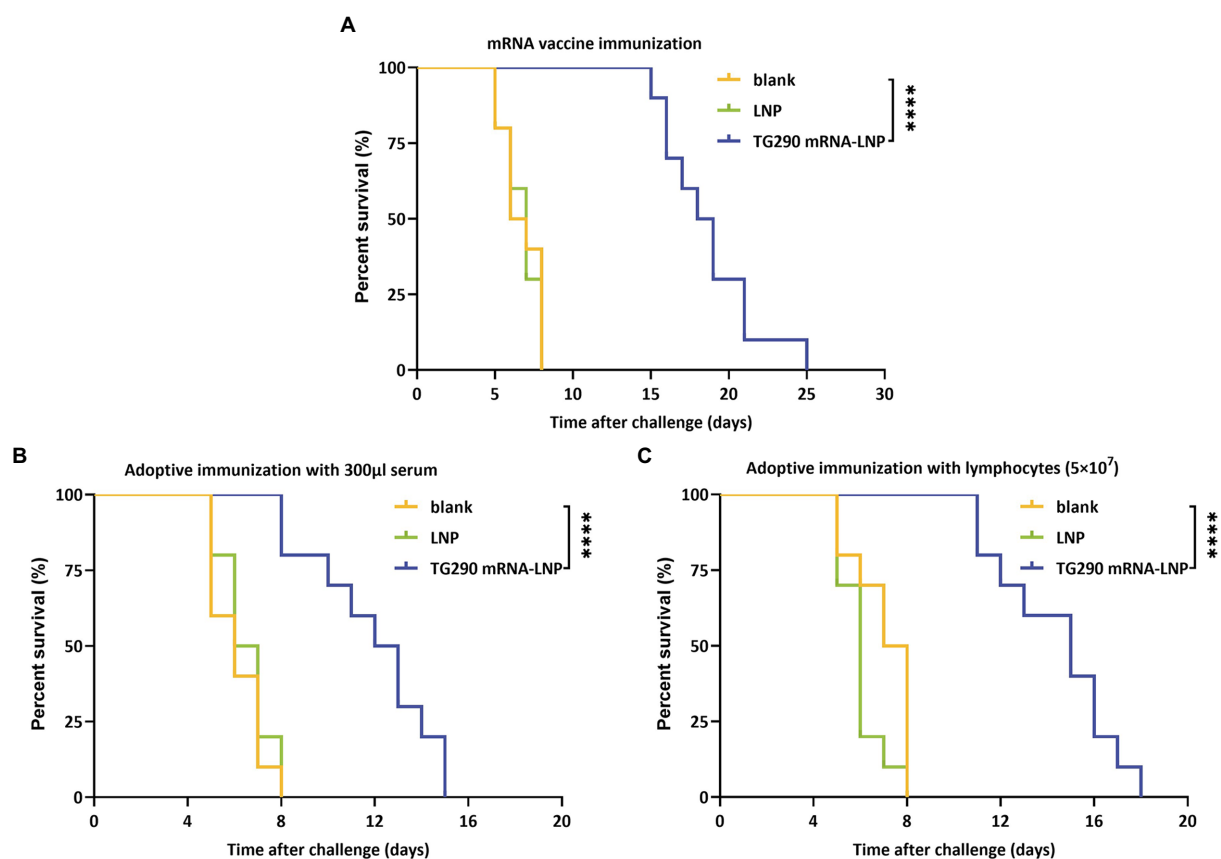

FIGURE 8
Survival curves of BALB/c mice after challenge. **(A)** TG290 mRNA-LNP vaccine protected against the lethal challenge (15 mice per group). **(B)** Adoptive immunization with serum protected against the lethal challenge (10 mice per group). **(C)** Adoptive immunization with lymphocytes protected against the lethal challenge (10 mice per group). ****$p<0.0001$ by the log rank tests.

Many antigens have already been found to be potential vaccine candidates against *T. gondii* like TgSAGs, TgROPs, TgMICs, among others (Mamaghani et al., 2023). However, the efficacy of different vaccine candidates cannot be compared because they were administered *via* different routes, animal types, vaccination doses, and vaccine production processes, all of which affect immunization efficacy (Zhang et al., 2022). In addition, there is lack of a uniform and standardized protocol for analysis of *T. gondii* vaccine efficacy. Previous studies have found that SAG1 is the predominant antigen on the surface of *T. gondii*, with strong immunogenicity and immunoprotective effects, and is considered a promising vaccine candidate (Pagheh et al., 2020). Hence, we chose SAG1 as a reference and compared efficacy of the predicted secreted antigens with linear B-cell epitopes and T-cell epitopes of SAG1 using a bioinformatics approach.

The search for vaccine candidate molecules were focused on the predicted *T. gondii* secretory proteins because of the essential role of these proteins in host-pathogen interactions (Xu et al., 2014). Secretory proteins containing transmembrane domains and signal peptides at the genome-wide level were screened on the *T. gondii* database (ToxoDB, http://ToxoDB.org). The screened candidates were then further analyzed for T/B cell epitopes.

Acquired immunity relies on T and B cells, which provide immune protection by recognizing antigen epitopes capable of forming pathogen-specific memory (Sasai et al., 2018; Khan and Moretto, 2022). The decoding of the whole genome of *T. gondii* provides a basis for subsequent analysis of T/B cell epitopes. Bioinformatics methods have been used to predict the epitopes of numerous *T. gondii* vaccine molecules, such as SAG4 (Zhou and Wang, 2017) and ROP21 (Zhang Z. et al., 2018). Herein, bioinformatics data showed that TG290 had a higher epitope score for linear B cells than SAG1 and a lower predicted IC50 value than SAG1, theoretically showing that TG290 is a promising vaccine candidate.

Humoral immunity is essential in resisting *T. gondii* infection. Antibodies can provide protective immunity response by regulating parasite phagocytosis, resisting invasion, and activating antibody-mediated classical complement pathway (Pifer and Yarovinsky, 2011). In this study, the levels of TG290-specific total IgG were increased in the serum of mice vaccinated with TG290 mRNA-LNP. In addition, TG290 mRNA-LNP significantly increased the levels of TG290-specific IgG1 and IgG2a antibodies, suggesting that TG290 mRNA-LNP can induce a mixed immune response of Th1/Th2.

IFN-γ improves host resistance to *T. gondii* infection (Park and Hunter, 2020). IFN-γ can also inhibit the propagation of *T. gondii*, activate macrophages, up-regulate NK cells, and promote the secretion of specific antibodies against *T. gondii* IgG1 and IgG2a *via* B cells (Boehm et al., 1997). IL-12 promotes IFN-γ production and T cell proliferation (Sun et al., 2020; Yu et al., 2021), while IL-4 promotes IFN-γ production late in infection (Tian et al., 2021). IL-10 can promote inhibition of inflammation and CD4 + T cells-mediated immunopathology (Wang et al., 2017). In this study, the levels of cytokines IFN-γ, IL-12, IL-4, and IL-10 were increased in mice inoculated with TG290 mRNA-LNP, consistent with previous studies (detection of *T. gondii* GRA24-based DNA vaccine; Zheng et al., 2019).

T-cell-mediated immune responses significantly prevent *T. gondii* invasion into host cell. Activating CD4+T lymphocytes depends on co-stimulators and MHC-II molecules, while the activation of CD8+T cells relies on APC or CD4+T helper cells (Verdon et al., 2020). T

lymphocytes proliferate and differentiate after activation. Notably, T lymphocyte proliferation is widely used to reflect immune status (Luo et al., 2017). In this study, mice inoculated with TG290 mRNA-LNP vaccine produced significant T lymphocyte proliferation. Additionally, the type of immune response depends on the differentiation of T lymphocytes (Zhu et al., 2010). Cytotoxic T lymphocytes (CTLs) are differentiated from activated CD8+T cells by producing IFN-γ or perforin-mediated cytolysis (Halle et al., 2017). Activated CD4+T lymphocytes promote the activation of macrophages, recruitment of macrophages, and release of cytokines (Tubo and Jenkins, 2014). A previous study showed that vaccination with pVAX-MIC16 or pVAX-MIC5 induces T lymphocyte proliferation. In this study, immunization with pVAX-MIC16, pVAX-MIC5 or pVAX-MIC16 + pVAX-MIC15 significantly increased the percentage of CD4+ and CD8+ T cells compared with the control group (Zhu et al., 2021). Furthermore, the proportion of CD4+ and CD8+T lymphocytes significantly increased in mice vaccinated with the TG290 mRNA-LNP vaccine, consistent with previous studies.

DCs is a vital antigen-presenting cell crucial in activating innate and acquired immunity (Schraml, 2015). As an essential checkpoint of surface expression of mature DC, CD83 plays a pivotal role in regulating immunity and inducing inflammation regression (Grosche et al., 2020). Studies have also shown that CD83 significantly influence T cell stimulation (Pinho et al., 2014). CD86 is a key co-stimulatory molecule that binds to the CD28 molecule on the surface of T cells and provides a co-stimulatory signal to T cells, thus lowering the activated threshold of the initial T cells (Greenwald et al., 2005). Furthermore, CD86 molecules can regulate antigen presentation (Baravalle et al., 2011). Mature DC can also produce MHC-II molecules and mainly activate CD4+T cells (Fooksman, 2014). Meanwhile, MHC-I molecules are expressed in all nucleated cells and are crucial in antigen presentation at the endogenous level, thus promoting CD8+T cell activation (Lyons et al., 2001). MHC-I molecules can also deliver exogenous antigenic peptides to the cell surface *via* the cross-presentation pathway, thereby activating CD8+T cells (Colbert et al., 2020). In addition, the upregulation of MHC-I molecules may enhance IFN-γ secretion (Zhou, 2009). TgP2-pVAX1/PLGA and TgP2-pVAX1/CS increase the levels of CD83, CD86, MHC-II, and MHC-I molecules (Yu et al., 2022). In this study, the levels of CD83 and CD86 molecules were significantly increased in TG290 mRNA-LNP immunized mice, indicating that TG290 mRNA-LNP can promote DC maturity and enhance the expression of some co-stimulatory molecules. Moreover, the levels of MHC-II and MHC-I molecules were significantly elevated in mice immunized with TG290 mRNA-LNP. These results show that TG290 mRNA-LNP can facilitate DC maturation and stimulate MHC-I and MHC-II-dependent antigen presentation.

IRF8 is a crucial transcription factor that can modulate the expression of IL-12p40 and IL-12p35 in response to TLR11 and MYD88 activation (Tailor et al., 2006). In this study, the levels of IRF8 were significantly increased in mice immunized with TG290 mRNA-LNP, suggesting that TG290 mRNA-LNP vaccination may elicit IL-12 expression *via* IRF8 pathway. NF-κB is analogous to the IRF8 signaling pathway and is crucial in the generation of IL-12 or IFN-γ (Sangaré et al., 2019). In this study, the levels of NF-κB in Splenocytes were significantly increased in TG290 mRNA-LNP-immunized mice, indicating that TG290 mRNA-LNP immunity can induce the expression of IL-12 or IFN-γ through NF-kB signal pathway. T-bet

regulates Th0-specific differentiation, which promotes Th1/Th2 exchange. Meanwhile, Th1 cells are selectively expressed by T-bet. In this study, TG290 mRNA-LNP immunologically evoked T-bet expression. These findings demonstrate that activation of the IRF8 and NF-κB pathways and T-Bet-mediated activation of CD4 + T cells and NK cells may elevate IFN-γ, similar to previous studies (Zhang N. Z. et al., 2018).

The percentage survival of vaccinated mice under a lethal challenge with *T. gondii* RH tachyzoites can be used to evaluate potential vaccine candidates. In this study, the mice vaccinated with TG290 mRNA-LNP had significantly extended survival time, while mice in the control group died within 8 days post challenge with type I RH tachyzoites (Figure 8A, 18.5 ± 3 days, $p < 0.0001$). Nevertheless, all mice eventually died. Similarly, a previous study also showed that TgCDPK1 can significantly prolong the survival time of mice (20% of these survived for 17 days) compared with the control groups (died within 8 days; Huang et al., 2019). Moreover, pVAX-MIC6 (11.5 ± 0.8 days), pVAX-GRA24 (8.1 ± 0.5 days), pVAX-GRA25 (9.4 ± 0.7 days), pVAX-GRA24 + pVAX-GRA25 (13.8 ± 0.9 days) and pVAX-GRA24 + PVAX-GRA25 + pVAX-MIC6 (18.7 ± 1.3 days) can significantly prolong the survival time of mice under lethal challenge (Xu et al., 2019). Notably, combination of vaccines may enhance the protective efficacy against *T. gondii*.

Furthermore, the survival time of mice adoptively immunized with serum (Figure 8B, 11.9 ± 2.6 days, $p < 0.0001$) and splenocytes (Figure 8C, 14.4 ± 2.5 days, $p < 0.0001$) was significantly prolonged compared with mice in the control groups (died within 8 days). Similarly, a previous study showed that vaccine-evoked immune serum and splenocytes can enhance resistance to *T. gondii* infection (Wang et al., 2020).

Bioinformatics analysis indicated that most regions of TG290 protein were flexible. Hydrophilicity plots showed that TG290 protein had an ideal antigenic index and surface probability, indicating that TG290 is a promising vaccine candidate. Further results also indicated that TG290 mRNA-LNP could elicit humoral and cellular immune responses, enhance cytokine production, evoke DCs and T lymphocytes, thus prolonging the survival time of mice vaccinated with TG290 mRNA-LNP. In summary, TG290 is a potential candidate molecule for the production of anti-*T. gondii* vaccine, providing a basis for the further design of TG290-based multi-epitope vaccines.

Data availability statement

The datasets presented in this study can be found in online repositories. The names of the repository/repositories and accession number(s) can be found in the article/Supplementary material.

Ethics statement

This study was approved by Hangzhou Medical College Institutional Animal Care and Use Committee (No: 2021-152) and followed the Chinese legislation regarding the use and care of research animals (GB/T35823-2018).

Author contributions

BZ oversaw and conceptualized the project, designed the study, and edited and reviewed manuscript. DL, YZ, and SL performed experiments and raw data pre-processing. DL and YZ performed data analysis and drafted the manuscript. SL performed literature search. All authors contributed to the article and approved the submitted version.

Funding

Conflict of interest

The authors declare that the research was conducted in the absence of any commercial or financial relationships that could be construed as a potential conflict of interest.

Publisher's note

All claims expressed in this article are solely those of the authors and do not necessarily represent those of their affiliated organizations, or those of the publisher, the editors and the reviewers. Any product that may be evaluated in this article, or claim that may be made by its manufacturer, is not guaranteed or endorsed by the publisher.

Supplementary material

The Supplementary material for this article can be found online at: https://www.frontiersin.org/articles/10.3389/fmicb.2023.1145114/full#supplementary-material

References

Alday, P. H., and Doggett, J. S. (2017). Drugs in development for toxoplasmosis: advances, challenges, and current status. *Drug Des. Devel. Ther.* 11, 273–293. doi: 10.2147/DDDT.S60973

Almeria, S., Murata, F. H. A., Cerqueira-Cézar, C. K., Kwok, O. C. H., Shipley, A., and Dubey, J. P. (2021). Epidemiological and public health significance of *Toxoplasma gondii* infection in wild rabbits and hares: 2010-2020. *Microorganisms* 9, 597–604. doi: 10.3390/microorganisms9030597

Attias, M., Teixeira, D. E., Benchimol, M., Vommaro, R. C., Crepaldi, P. H., and De Souza, W. (2020). The life-cycle of *Toxoplasma gondii* reviewed using animations. *Parasit. Vectors* 13:588. doi: 10.1186/s13071-020-04445-z

Baravalle, G., Park, H., McSweeney, M., Ohmura-Hoshino, M., Matsuki, Y., Ishido, S., et al. (2011). Ubiquitination of CD86 is a key mechanism in regulating antigen presentation by dendritic cells. *J. Immunol.* 187, 2966–2973. doi: 10.4049/jimmunol.1101643

Boehm, U., Klamp, T., Groot, M., and Howard, J. C. (1997). Cellular responses to interferon-gamma. *Annu. Rev. Immunol.* 15, 749–795. doi: 10.1146/annurev.immunol.15.1.749

Bok, K., Sitar, S., Graham, B. S., and Mascola, J. R. (2021). Accelerated COVID-19 vaccine development: milestones, lessons, and prospects. *Immunity* 54, 1636–1651. doi: 10.1016/j.immuni.2021.07.017

Chaudhary, N., Weissman, D., and Whitehead, K. A. (2021). mRNA vaccines for infectious diseases: principles, delivery and clinical translation. *Nat. Rev. Drug Discov.* 20, 817–838. doi: 10.1038/s41573-021-00283-5

Chu, K. B., and Quan, F. S. (2021). Advances in *Toxoplasma gondii* vaccines: current strategies and challenges for vaccine development. *Vaccines* 9, 413–429. doi: 10.3390/vaccines9050413

Colbert, J. D., Cruz, F. M., and Rock, K. L. (2020). Cross-presentation of exogenous antigens on MHC I molecules. *Curr. Opin. Immunol.* 64, 1–8. doi: 10.1016/j.coi.2019.12.005

Flegr, J., and Escudero, D. Q. (2016). Impaired health status and increased incidence of diseases in Toxoplasma-seropositive subjects - an explorative cross-sectional study. *Parasitology* 143, 1974–1989. doi: 10.1017/S0031182016001785

Fleri, W., Paul, S., Dhanda, S. K., Mahajan, S., Xu, X., Peters, B., et al. (2017). The immune epitope database and analysis resource in epitope discovery and synthetic vaccine design. *Front. Immunol.* 8:278. doi: 10.3389/fimmu.2017.00278

Fooksman, D. R. (2014). Organizing MHC Class II presentation. *Front. Immunol.* 5:158. doi: 10.3389/fimmu.2014.00158

Greaney, A. J., Loes, A. N., Gentles, L. E., Crawford, K. H. D., Starr, T. N., Malone, K. D., et al. (2021). Antibodies elicited by mRNA-1273 vaccination bind more broadly to the receptor binding domain than do those from SARS-CoV-2 infection. *Sci. Transl. Med.* 13. doi: 10.1126/scitranslmed.abi9915

Greenwald, R. J., Freeman, G. J., and Sharpe, A. H. (2005). The B7 family revisited. *Annu. Rev. Immunol.* 23, 515–548. doi: 10.1146/annurev.immunol.23.021704.115611

Grosche, L., Knippertz, I., König, C., Royzman, D., Wild, A. B., Zinser, E., et al. (2020). The CD83 molecule - an important immune checkpoint. *Front. Immunol.* 11:721. doi: 10.3389/fimmu.2020.00721

Hakimi, M. A., Olias, P., and Sibley, L. D. (2017). Toxoplasma effectors targeting host signaling and transcription. *Clin. Microbiol. Rev.* 30, 615–645. doi: 10.1128/CMR.00005-17

Halle, S., Halle, O., and Förster, R. (2017). Mechanisms and dynamics of T cell-mediated cytotoxicity in vivo. *Trends Immunol.* 38, 432–443. doi: 10.1016/j.it.2017.04.002

Huang, S. Y., Chen, K., Wang, J. L., Yang, B., and Zhu, X. Q. (2019). Evaluation of protective immunity induced by recombinant calcium-dependent protein kinase 1 (TgCDPK1) protein against acute toxoplasmosis in mice. *Microb. Pathog.* 133:103560. doi: 10.1016/j.micpath.2019.103560

Khan, I. A., and Moretto, M. (2022). Immune responses to *Toxoplasma gondii*. *Curr. Opin. Immunol.* 77:102226. doi: 10.1016/j.coi.2022.102226

Kochanowsky, J. A., and Koshy, A. A. (2018). Toxoplasma gondii. *Curr. Biol.* 28, R770–R771. doi: 10.1016/j.cub.2018.05.035

Le, T., Sun, C., Chang, J., Zhang, G., and Yin, X. (2022). mRNA vaccine development for emerging animal and zoonotic diseases. *Viruses* 14, 401–420. doi: 10.3390/v14020401

Luo, L., Qin, T., Huang, Y., Zheng, S., Bo, R., Liu, Z., et al. (2017). Exploring the immunopotentiation of Chinese yam polysaccharide poly(lactic-co-glycolic acid) nanoparticles in an ovalbumin vaccine formulation in vivo. *Drug Deliv.* 24, 1099–1111. doi: 10.1080/10717544.2017.1359861

Lyn, D., Gill, D. S., Scroggs, R. A., and Portner, A. (1991). The nucleoproteins of human parainfluenza virus type 1 and Sendai virus share amino acid sequences and antigenic and structural determinants. *J. Gen. Virol.* 72, 983–987. doi: 10.1099/0022-1317-72-4-983

Lyons, R. E., Anthony, J. P., Ferguson, D. J., Byrne, N., Alexander, J., Roberts, F., et al. (2001). Immunological studies of chronic ocular toxoplasmosis: up-regulation of major histocompatibility complex class I and transforming growth factor beta and a protective role for interleukin-6. *Infect. Immun.* 69, 2589–2595. doi: 10.1128/IAI.69.4.2589-2595.2001

Mamaghani, A. J., Fathollahi, A., Arab-Mazar, Z., Kohansal, K., Fathollahi, M., Spotin, A., et al. (2023). Toxoplasma gondii vaccine candidates: a concise review. *Ir. J. Med. Sci.* 192, 231–261. doi: 10.1007/s11845-022-02998-9

Montazeri, M., Mehrzadi, S., Sharif, M., Sarvi, S., Tanzifi, A., Aghayan, S. A., et al. (2018). Drug resistance in *Toxoplasma gondii*. *Front. Microbiol.* 9:2587. doi: 10.3389/fmicb.2018.02587

Montoya, J. G., and Liesenfeld, O. (2004). Toxoplasmosis. *Lancet* 363, 1965–1976. doi: 10.1016/S0140-6736(04)16412-X

Pagheh, A. S., Sarvi, S., Sharif, M., Rezaei, F., Ahmadpour, E., Dodangeh, S., et al. (2020). *Toxoplasma gondii* surface antigen 1 (SAG1) as a potential candidate to develop vaccine against toxoplasmosis: a systematic review. *Comp. Immunol. Microbiol. Infect. Dis.* 69:101414. doi: 10.1016/j.cimid.2020.101414

Park, J., and Hunter, C. A. (2020). The role of macrophages in protective and pathological responses to *Toxoplasma gondii*. *Parasite Immunol.* 42:e12712. doi: 10.1111/pim.12712

Pifer, R., and Yarovinsky, F. (2011). Innate responses to *Toxoplasma gondii* in mice and humans. *Trends Parasitol.* 27, 388–393. doi: 10.1016/j.pt.2011.03.009

Pinho, M. P., Migliori, I. K., Flatow, E. A., and Barbuto, J. A. (2014). Dendritic cell membrane CD83 enhances immune responses by boosting intracellular calcium release in T lymphocytes. *J. Leukoc. Biol.* 95, 755–762. doi: 10.1189/jlb.0413239

Pittman, K. J., and Knoll, L. J. (2015). Long-term relationships: the complicated interplay between the host and the developmental stages of *Toxoplasma gondii* during

acute and chronic infections. *Microbiol. Mol. Biol. Rev.* 79, 387–401. doi: 10.1128/MMBR.00027-15

Rahman, M. T., Sobur, M. A., Islam, M. S., Ievy, S., Hossain, M. J., El Zowalaty, M. E., et al. (2020). Zoonotic diseases: etiology, impact, and control. *Microorganisms* 8, 1405–1439. doi: 10.3390/microorganisms8091405

Robert-Gangneux, F., and Dardé, M. L. (2012). Epidemiology of and diagnostic strategies for toxoplasmosis. *Clin. Microbiol. Rev.* 25, 264–296. doi: 10.1128/CMR.05013-11

Sangaré, L. O., Yang, N., Konstantinou, E. K., Lu, D., Mukhopadhyay, D., Young, L. H., et al. (2019). Toxoplasma GRA15 activates the NF-κB pathway through interactions with TNF receptor-associated factors. *MBio* 10, 808–19. doi: 10.1128/mBio.00808-19

Sasai, M., Pradipta, A., and Yamamoto, M. (2018). Host immune responses to *Toxoplasma gondii*. *Int. Immunol.* 30, 113–119. doi: 10.1093/intimm/dxy004

Schraml, B. U. (2015). Reis e Sousa C. Defining dendritic cells. *Curr. Opin. Immunol.* 32, 13–20. doi: 10.1016/j.coi.2014.11.001

Silva, M. D., Teixeira, C., Gomes, P., and Borges, M. (2021). Promising drug targets and compounds with anti-*Toxoplasma gondii* activity. *Microorganisms*. 9, 1960–1980. doi: 10.3390/microorganisms9091960

Smith, N. C., Goulart, C., Hayward, J. A., Kupz, A., Miller, C. M., and van Dooren, G. G. (2021). Control of human toxoplasmosis. *Int. J. Parasitol.* 51, 95–121. doi: 10.1016/j.ijpara.2020.11.001

Sun, H., Li, J., Xiao, T., Huang, X. D., Wang, L. J., Huang, B. C., et al. (2020). Protective immunity induced by a DNA vaccine cocktail expressing TgSAG1, TgROP2, and the genetic adjuvant HBsAg against *Toxoplasma gondii* infection. *Microb. Pathog.* 147:104441. doi: 10.1016/j.micpath.2020.104441

Tailor, P., Tamura, T., and Ozato, K. (2006). IRF family proteins and type I interferon induction in dendritic cells. *Cell Res.* 16, 134–140. doi: 10.1038/sj.cr.7310018

Tenter, A. M., Heckeroth, A. R., and Weiss, L. M. (2000). *Toxoplasma gondii*: from animals to humans. *Int. J. Parasitol.* 30, 1217–1258. doi: 10.1016/S0020-7519(00)00124-7

Tian, D., Liu, X., Li, X., Xu, L., Yan, R., and Song, X. (2021). Eimeria maxima rhomboid-like protein 5 provided partial protection against homologous challenge in forms of recombinant protein and DNA plasmid in chickens. *Vaccines* 10, 32–49. doi: 10.3390/vaccines10010032

Tubo, N. J., and Jenkins, M. K. (2014). CD4+ T cells: guardians of the phagosome. *Clin. Microbiol. Rev.* 27, 200–213. doi: 10.1128/CMR.00097-13

Verdon, D. J., Mulazzani, M., and Jenkins, M. R. (2020). Cellular and molecular mechanisms of CD8(+) T cell differentiation, dysfunction and exhaustion. *Int. J. Mol. Sci.* 21, 7357–7385. doi: 10.3390/ijms21197357

Wang, J. L., Elsheikha, H. M., Zhu, W. N., Chen, K., Li, T. T., Yue, D. M., et al. (2017). Immunization with *Toxoplasma gondii* GRA17 deletion mutant induces partial protection and survival in challenged mice. *Front. Immunol.* 8:730. doi: 10.3389/fimmu.2017.00730

Wang, Y. L., Jin, L. L., Cheng, X., Yan, W. F., Deng, H., Shen, Q. K., et al. (2022). Synthesis and evaluation of in vitro and in vivo anti-*Toxoplasma gondii* activity of tetraoxane-substituted ursolic acid derivatives. *Nat. Prod. Res.* 1-9, 1–9. doi: 10.1080/14786419.2022.2098497

Wang, J. L., Liang, Q. L., Li, T. T., He, J. J., Bai, M. J., Cao, X. Z., et al. (2020). *Toxoplasma gondii* tkl1 deletion mutant is a promising vaccine against acute, chronic, and congenital toxoplasmosis in mice. *J. Immunol.* 204, 1562–1570. doi: 10.4049/jimmunol.1900410

Wang, J. L., Zhang, N. Z., Li, T. T., He, J. J., Elsheikha, H. M., and Zhu, X. Q. (2019). Advances in the development of anti-*Toxoplasma gondii* vaccines: challenges, opportunities, and perspectives. *Trends Parasitol.* 35, 239–253. doi: 10.1016/j.pt.2019.01.005

Watts, E., Zhao, Y., Dhara, A., Eller, B., Patwardhan, A., and Sinai, A. P. (2015). Novel approaches reveal that *Toxoplasma gondii* bradyzoites within tissue cysts are dynamic and replicating entities *in vivo*. *MBio* 6, e01155–e01115. doi: 10.1128/mBio.01155-15

Xu, X. P., Liu, W. G., Xu, Q. M., Zhu, X. Q., and Chen, J. (2019). Evaluation of immune protection against toxoplasma gondii infection in mice induced by a multi-antigenic DNA vaccine containing TgGRA24, TgGRA25 and TgMIC6. *Parasite* 26:58. doi: 10.1051/parasite/2019050

Xu, X., Zhang, Y., Lin, D., Zhang, J., Xu, J., Liu, Y. M., et al. (2014). Serodiagnosis of *Schistosoma japonicum* infection: genome-wide identification of a protein marker, and assessment of its diagnostic validity in a field study in China. *Lancet Infect. Dis.* 14, 489–497. doi: 10.1016/S1473-3099(14)70067-2

Yu, Z., Cao, W., Gao, X., Aleem, M. T., Liu, J., Luo, J., et al. (2021). With chitosan and PLGA as the delivery vehicle, *Toxoplasma gondii* oxidoreductase-based DNA vaccines decrease parasite burdens in mice. *Front. Immunol.* 12:726615. doi: 10.3389/fimmu.2021.726615

Yu, Z., He, K., Cao, W., Aleem, M. T., Yan, R., Xu, L., et al. (2022). Nano vaccines for *T. gondii* ribosomal P2 protein with nanomaterials as a promising DNA vaccine against toxoplasmosis. *Front. Immunol.* 13:839489. doi: 10.3389/fimmu.2022.839489

Zhang, N. Z., Gao, Q., Wang, M., Elsheikha, H. M., Wang, B., Wang, J. L., et al. (2018). Immunization with a DNA vaccine cocktail encoding TgPF, TgROP16, TgROP18, TgMIC6, and TgCDPK3 genes protects mice against chronic toxoplasmosis. *Front. Immunol.* 9:1505. doi: 10.3389/fimmu.2018.01505

Zhang, Y., Li, D., Lu, S., and Zheng, B. (2022). Toxoplasmosis vaccines: what we have and where to go? *NPJ Vaccines* 7:131. doi: 10.1038/s41541-022-00563-0

Zhang, Z., Li, Y., Wang, M., Xie, Q., Li, P., Zuo, S., et al. (2018). Immune protection of Rhoptry protein 21 (ROP21) of *Toxoplasma gondii* as a DNA vaccine against toxoplasmosis. *Front. Microbiol.* 9:909. doi: 10.3389/fmicb.2018.00909

Zheng, B., Ding, J., Chen, X., Yu, H., Lou, D., Tong, Q., et al. (2017). Immuno-efficacy of a *T. gondii* secreted protein with an altered thrombospondin repeat (TgSPATR) as a novel DNA vaccine candidate against acute toxoplasmosis in BALB/c mice. *Front. Microbiol.* 8:216. doi: 10.3389/fmicb.2017.00216

Zheng, B., Lou, D., Ding, J., Zhuo, X., Ding, H., Kong, Q., et al. (2019). GRA24-based DNA vaccine prolongs survival in mice challenged with a virulent *Toxoplasma gondii* strain. *Front. Immunol.* 10:418. doi: 10.3389/fimmu.2019.00418

Zhou, F. (2009). Molecular mechanisms of IFN-gamma to up-regulate MHC class I antigen processing and presentation. *Int. Rev. Immunol.* 28, 239–260. doi: 10.1080/08830180902978120

Zhou, J., and Wang, L. (2017). SAG4 DNA and peptide vaccination provides partial protection against *T. gondii* infection in BALB/c mice. *Front. Microbiol.* 8:1733. doi: 10.3389/fmicb.2017.01733

Zhu, Y. C., Ma, L. J., Zhang, J. L., Liu, J. F., He, Y., Feng, J. Y., et al. (2021). Protective immunity induced by TgMIC5 and TgMIC16 DNA vaccines against toxoplasmosis. *Front. Cell. Infect. Microbiol.* 11:686004. doi: 10.3389/fcimb.2021.686004

Zhu, J., Yamane, H., and Paul, W. E. (2010). Differentiation of effector CD4 T cell populations. *Annu. Rev. Immunol.* 28, 445–489. doi: 10.1146/annurev-immunol-030409-101212

Coalescing disparate data sources for the geospatial prediction of mosquito abundance, using Brazil as a motivating case study

Anwar Musah[1]*, Ella Browning[2,3], Aisha Aldosery[2],
Iuri Valerio Graciano Borges[4], Tercio Ambrizzi[4], Merve Tunali[5],
Selma Başibüyük[5], Orhan Yenigün[5,6],
Giselle Machado Magalhaes Moreno[4], Clarisse Lins de Lima[7],
Ana Clara Gomes da Silva[8], Wellington Pinheiro dos Santos[8],
Tiago Massoni[9], Luiza Cintra Campos[10] and Patty Kostkova[2]

[1]Department of Geography, University College London, London, United Kingdom, [2]Centre for Digital Public Health and Emergencies, Institute for Risk and Disaster Reduction, University College London, London, United Kingdom, [3]Centre for Biodiversity and Environment Research, Department of Genetics, Evolution and Environment, University College London, London, United Kingdom, [4]Department of Atmospheric Sciences, Institute of Astronomy, Geophysics and Atmospheric Sciences (IAG), University of São Paulo, São Paulo, Brazil, [5]Institute of Environmental Sciences, Boğaziçi University, Istanbul, Türkiye, [6]School of Engineering, European University of Lefke, Lefke, Cyprus, [7]Polytechnic School of Pernambuco, University of Pernambuco (Poli-UPE), Recife, PE, Brazil, [8]Department of Biomedical Engineering, Federal University of Pernambuco, Recife, PE, Brazil, [9]Department of Systems and Computing, Federal University of Campina Grande, Campina Grande, PB, Brazil, [10]Department of Civil, Environmental and Geomatic Engineering, University College London, London, United Kingdom

One of the barriers to performing geospatial surveillance of mosquito occupancy or infestation anywhere in the world is the paucity of primary entomologic survey data geolocated at a residential property level and matched to important risk factor information (e.g., anthropogenic, environmental, and climate) that enables the spatial risk prediction of mosquito occupancy or infestation. Such data are invaluable pieces of information for academics, policy makers, and public health program managers operating in low-resource settings in Africa, Latin America, and Southeast Asia, where mosquitoes are typically endemic. The reality is that such data remain elusive in these low-resource settings and, where available, high-quality data that include both individual and spatial characteristics to inform the geospatial description and risk patterning of infestation remain rare. There are many online sources of open-source spatial data that are reliable and can be used to address such data paucity in this context. Therefore, the aims of this article are threefold: (1) to highlight where these reliable open-source data can be acquired and how they can be used as risk factors for making spatial predictions for mosquito occupancy in general; (2) to use Brazil as a case study to demonstrate how these datasets can be combined to predict the presence of arboviruses through the use of ecological niche modeling using the maximum entropy algorithm; and (3) to discuss the benefits of using bespoke applications beyond these open-source online data sources, demonstrating for

how they can be the new "gold-standard" approach for gathering primary entomologic survey data. The scope of this article was mainly limited to a Brazilian context because it builds on an existing partnership with academics and stakeholders from environmental surveillance agencies in the states of Pernambuco and Paraiba. The analysis presented in this article was also limited to a specific mosquito species, i.e., *Aedes aegypti*, due to its endemic status in Brazil.

1 Introduction

In an age when global viruses such as COVID-19 are an urgent public health priority for research, overshadowing vector-borne diseases, the World Health Organization (WHO) has emphasized the critical need for continued efforts to prevent the transmission of vector-borne diseases, such as malaria, dengue or Zika, which are spread by mosquitoes. While focusing on digital solutions for pandemics, the WHO has implored the global community to not relent nor allow the current pandemic to eclipse the global agenda of reducing the burden of vector-borne diseases (1).

In the context of vector-borne disease surveillance and research, residential entomologic survey data are essential for understanding the geographical and temporal variability in mosquito occupancy in residential locations. Information gathered from entomologic surveys can be used to formulate control strategies for combating mosquito populations effectively. The spatially precise and fine-scale data collected under these surveys are one of the most sought-after pieces of information by health researchers and key policy makers in the field of overlooked tropical disease epidemiology. Such data can be utilized for supporting the decision-making process when determining which high-priority areas are in need of an intervention (i.e., mosquito/larvicidal campaigns or bed nets) (2). From a Global South perspective, although many surveys have been conducted (which have been diligently documented in notable open source websites, e.g., the Malaria Atlas Project (3) and the Global Aedes Aegypti & Albopictus Compendium (4)), such residential property-level survey data with information on physical and environmental characteristics are hard to come by. Such data in most cases remain inaccessible to health researchers, policy makers, and public health program managers. This problem of data paucity is due to the lack of a systematic approach for standardizing the collation of information into a digital format that was initially recorded on paper. The timely entry of data into an electronic registry is a challenge, and this issue is especially true for many low-resource settings in countries in sub-Saharan Africa (5–7) and Latin America (8) which is a hinderance in developing a more satisfactory dashboard for infectious disease surveillance.

Mosquitoes are sensitive to changes in environment and climate that impact their movement potential and survivability. In addition, the abundance of surface water in the form of a stagnated reservoir can have a positive or adverse effect on breeding habits and populations. These serve as risk factors that can have either a positive or negative influence on mosquito abundance in an environment. For example, many cities in the northeastern region of Brazil were hit hard by the Zika virus outbreak in 2015 (9–11). Zika virus, an arboviral infection, is transmitted by the *Aedes* mosquito genus (i.e., via two common species known as the *Aedes aegypti* and *Aedes albopictus*), which are endemic to that region. Their increased abundance in the northeast of Brazil is typically associated with standing water, which serves as a reservoir hotspot for breeding. Apart from the presence of standing water in human dwellings, a restricted set of climatic conditions such as land-surface temperature, humidity, precipitation, and seasonality, in addition to area-level socioeconomic deprivation risk factors, interact with each other to create an environment that is tenable for the mosquito's survival (12).

To predict the spatial and spatiotemporal distribution of illnesses such as dengue, Zika, and chikungunya, in two northeasten Brazilian cities, Recife and Campina Grande, local environmental health authorities routinely carry out surveys on a bimestrial basis. The community health workers (CHWs) from these cities are deployed to high-risk neighborhoods to visit residential properties to inspect seven different types of breeding sources to detect the presence of the *Aedes* mosquito and its larvae (13–17). The CHWs collect other important information that describes the property's physical characteristics (e.g., type of building structure and presence of a garden) and waste management practices (e.g., mode of waste disposal, presence of landfill, etc.) that contribute to the proliferation of mosquitoes (18, 19). A key challenge faced by these CHWs is the use of paper-based tools to document "thousands upon thousands" of pages of entomological information collected directly from the field. The data recorded on the paper forms must then be manually input into an electronic database by the CHWs; and ultimately increases the risk of passing incomplete data to policy makers and public health managers. This problem occurs in Recife and Campina Grande and was addressed

by Aldosery et al. (18), who have developed a system for handling primary data with state-of-the-art bespoke smartphone applications (18). Considering these aforementioned issues (i.e., paucity of survey data due to how they are collected at the residential premises level), the CHWs are faced with challenges of linking primary information with other broader secondary sources of data that may contain wider indicators for water sanitation and hygiene (WASH) and weather parameters which may contribute to mosquito occupancy in residential premises (4, 20, 21).

A significant number of highly reliable open-source datasets are available. These open-source data can be linked to spatially referenced survey records to augment the mosquito surveillance effort. The authors argue that these sources remain elusive to many researchers in this line of research. Therefore, the primary objectives of this research article are threefold: (1) to point out to readers where these reliable open-source data can be acquired and explain how they can be used as risk factors for making spatial predictions for mosquito occupancy in general; (2) to use Brazil as a case study to demonstrate how these datasets can be brought together to predict the presence of arboviruses through ecological niche modeling using the maximum entropy algorithm; and (3) to discuss the benefits of using bespoke technologies (smartphone applications, the Internet of Things, etc.), and to explain how these can be the new "gold-standard" approach for gathering primary entomologic survey data. The scope of this paper was limited to a Brazilian context because the research builds on an existing partnership with academics and stakeholders from environmental surveillance agencies in Recife (State of Pernambuco) and Campina Grande (State of Paraiba). We also chose the *Aedes* genus as the mosquito of focus due to its endemic status in Brazil and restricted the analysis specifically to the *Aedes aegypti* mosquito, since it is more commonly found than *Aedes albopictus*. Nevertheless, this article was written to build capacity for and awareness of data sources and methods, and thus

it is applicable to different mosquito species and other areas in the Global South with similar circumstances.

2 Description of data sources

In this section, we highlight the various sources of data that can be obtained online. We have provided a detailed description of how to use the data for causal inference and predictive analytics for mosquito occupancy. This included shapefiles for countries as well as point and raster grids for weather and environmental data, respectively. For raster data, we particularly highlighted the most reliable and updated sources available at a high spatial resolution.

2.1 Obtaining spatial boundaries for study areas from GADM

Shapefiles can be obtained from the Global Administrative Areas Database (GADM) (https://gadm.org/index.html). The GADM is a high-resolution database that contains information on administrative areas for all countries, at all sub-divisional levels (e.g., national, state, municipal, district, and sub-district levels), and is freely accessible for research (22). For example, the shapefiles for Brazil (see https://gadm.org/download_country.html) are available at four levels (see Figure 1):

- Level 0: the country's border ("gadm36_BRA_0.shp")
- Level 1: boundaries for the 27 states ("gadm36_BRA_1.shp")
- Level 2: boundaries for the 5,504 municipalities ("gadm36_BRA_2.shp")
- Level 3: boundaries for the 10,195 districts ("gadm36_ BRA_3.shp").

FIGURE 1
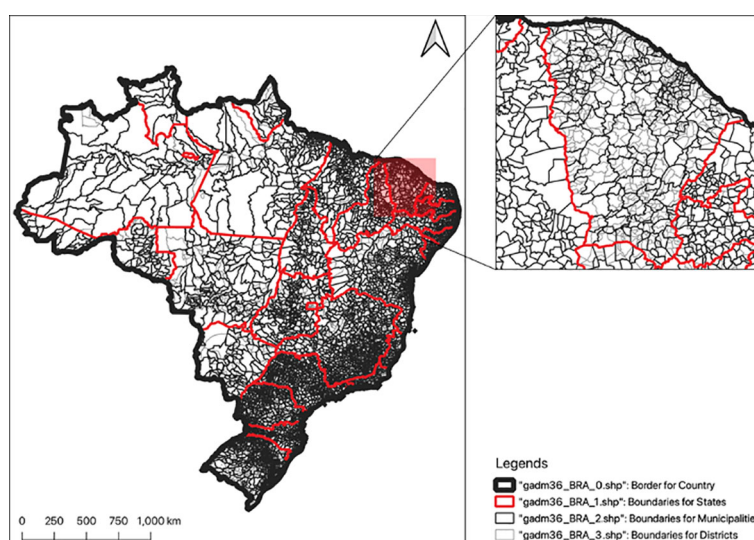Shapefile (available from https://gadm.org/index.html) plotting the spatial configuration of Brazil. The administrative levels of Brazil are divided into four (0, 1, 2, and 3); however, for certain countries (especially those classified as low- or middle-income countries) the breakdown of administrative levels may differ.

2.2 Obtaining various environmental data

2.2.1 Vegetation cover from the USGS Earth Explorer

Vegetation cover is one of the prominent risk factors for mosquito-borne transmission. For some species, it provides a suitable condition for its movement potential and survivability. One important metric that is often used in the prediction of vector-borne diseases is the Normalized Difference Vegetation Index (NDVI), which is easy to derive on a raster grid (23). This metric describes whether a gridded value in a geographic space contains high or low levels of vegetation. An excellent source is the USGS Earth Explorer (https://earthexplorer.usgs.gov/), which provides users with access to several selectable aerial satellite images (e.g., via Landsat, Sentinel-2, MODIS, and radar instruments) that can be downloaded and cropped according to the spatial extent and temporal resolution of the study area of interest. The images are downloaded as bands ranging from 1 to 12. To derive the NDVI as a gridded layer, one can use the satellite data that correspond to band 4 (i.e., red) and band 5 [i.e., near infrared (NIR)]. The NDVI indices are generated as a raster image by taking the image of bands 4 (red) and 5 (NIR) using the formula (NIR - RED)/(NIR + RED). The length of the pixel (i.e., grid cell) is derived at 90.0 m, whereby each pixel contains an estimate that refers to the intensity of vegetation at a given location. A higher value shows that the presence of vegetation at a location is greater and *vice versa*. Readers should note that the USGS Earth Explorer has already packaged the NDVI data into several products [i.e., MOD13A1 (500 m), MOD13Q1 (250 m), MYD13A1 (500 m), and MYD13Q1 (250 m)], which are hosted on the Google Earth Engine (https://earthengine.google.com). With bespoke Python code, the NDVI data can be extracted through Google Earth Engine's code editor (see section on data availability).

2.2.2 Obtaining land-surface elevation data from the STRM Digital Elevation Database

Elevation is often used as an important predictor for determining environmental suitability for mosquito abundance. High-altitude areas (i.e., those averaging above 1,200 m) adversely affect survival rates for most mosquitoes (24–26). The land-surface elevation layer can be obtained from the STRM 90.0 m DEM Digital Elevation Database (https://srtm.csi.cgiar.org): it is possible to select and download the tiled raster that contains land-surface elevation estimates for the study area. The user can crop (or "cookie cut") the tile to the spatial extents of the study area of interest. The resolution for the layer is 90.0 m, where a grid cell value contains a positive (or negative) continuous measurement in meters to reflect the height of the land's surface above (or below) sea level.

2.2.3 Obtaining aridity data from the GAI–PECD database

The Global Aridity Index & Potential Evapotranspiration Climate Database (GAI-PECD) (version 2) (see https://cgiarcsi.community/2019/01/24/global-aridity-index-and-potential-evapotranspiration-climate-database-v2/) provides high-resolution (approximately 1 km) global raster climate information

for levels of environmental dryness, measured as the Aridity Index (AI) (27). Aridity is a significant environmental risk factor for determining environmental suitability for mosquito survivability (28, 29). Mosquitoes are unable to survive in harsh areas that are hyper-arid or arid and thus are completely absent in such environments; however, they can thrive in semi-arid and dry subhumid environments. The raster contains numerically derived estimates for AI (ranging from 0.0 to 0.65) describing the degree of dryness of the climate at a given location. The raster values for AI can be reclassified accordingly to four dryland subtypes: < 0.05 (hyper-arid), 0.06 to 0.20 (arid), 0.21 to 0.50 (semi-arid), and 0.51 to 0.65 (dry subhumid). Since mosquitoes cannot survive in hyper-arid and arid areas (i.e., AI 0.20), it is possible to limit the area of analysis to semi-arid and dry subhumid areas (i.e., AI > 0.20) and create a binary raster constraining the analysis to areas where they will survive (i.e., AI > 0.20).

2.3 Obtaining various anthropogenic data from WorldPop.org

An ensemble of several anthropogenic-related risk factors stored as gridded data at a high-resolution of 100 m can be accessed from Worldpop.org (https://www.worldpop.org/). WorldPop.org is an open-source spatial demographic database.

2.3.1 Built settlements

Several studies have demonstrated that the degree of urbanization in a study area is correlated with a significantly increased risk of mosquito occupancy, as urbanization inadvertently yields breeding sites within human dwellings (30, 31). The built settlements raster layer can therefore be used to model the risk of infestation. This raster layer contains binary information that defines an area as either an urban (1) or non-urban (0) location. These data can be implemented in the spatial analysis for mosquito surveillance in two ways. First, for point analysis, the data can be used to classify point features (e.g., communities, villages, and points of individual houses or residential premises) as "urban" or "non-urban" through simple overlays and pixel extraction to spatial points. Second, for area-level spatial analysis, one can calculate the fraction of surface defined to be urban or non-urban. For each country, WorldPop.org has mapped the trajectory of how built settlements have expanded over the years (32), and these raster data are available from 2010 to 2020.

2.3.2 Population density

Human population characteristics are an important feature to account for in the modeling of mosquito-borne transmission (33). The population density raster can be used to estimate counts of inhabitants at point locations. For areal analysis, these grids can be aggregated within a boundary to derive an estimate for the total number of inhabitants in an area, which is useful, as a denominator is necessary to obtain measures of disease (or infestation) frequency (e.g., prevalence or incidence rates). WorldPop.org provides a large number of raster layers that all contain discrete values that

represent the estimated number of inhabitants within a given pixel and are available for many countries in the Global South from 2010 to 2020. The resource also provides raster data that are gender- and age-group-specific, which is very useful for deriving age- and sex-adjusted estimates. The details of how these layers were created are explained by Lloyd et al. (34).

2.3.3 Night-time lighting of areas

Worldpop.org (https://www.worldpop.org/) provides resampled gridded data to show the intensity and detection of non-natural lighting on the Earth's surface to signify the presence of anthropogenic activity, or land occupied by human settlements. Artificial lighting is an important risk factor to account for in the prediction of mosquito occupancy for two reasons: (1) as shown in a recent review, there is a growing body of literature indicating that it significantly impacts mosquito feeding behavior (i.e., mosquitoes have a preference for feeding during the night, when non-natural lighting is pronounced) (35); and (2) in the Global South, especially in sub-Saharan Africa, extensive lighting is a strong indicator of a city's economic and structural development. Therefore, these data can be modeled as a direct risk factor; alternatively, they can be used to generate a composite for socioeconomic deprivation (36). The spatial resolution for this dataset is 100 m by 100 m.

2.4 Weather variables

Land surface temperature, humidity, and rainfall are typical weather-related risk factors that must be taken into consideration for the spatial prediction of breeding hotspots for mosquitoes, irrespective of species. The joint contribution of climatic variables plays an immense role in creating an environment that is suitable for the mosquitoes' survivability and for its breeding and feeding habits. A group of such climatic risk factors stored as high-resolution gridded data can be accessed from several sources. Here, we describe two prominent sources: WorldClim and OpenWeatherMap API.

2.4.1 Obtaining weather-related information from WorldClim

WorldClim (https://www.worldclim.org) is a comprehensive spatial database containing high-resolution weather and climate data on a global scale (37, 38). It provides two datasets. First, it provides historical monthly weather data from 1960 to 2018, specifically for the following climate variables: minimum temperature (°C), maximum temperature (°C) (which can be recalculated to obtain either a median or mean temperature), and total precipitation (mm). It should be noted that the highest spatial resolution for these data is 2.5′ (approximately 4.5 km). Downloading the parameters will produce a highly compressed zip file containing several GeoTiff (.tif) files (i.e., the raster) for each month of the year (where January is 1 and December is 12) for a 10-year period. Second, WorldClim provides projected monthly estimates for climate data for the time periods 2021–2040, 2040–2060, 2061–2080, and 2081–2100 at four different spatial resolutions [30″ (approximately 900 m), 2.5′ (approximately 4.5 km), 5′ (approximately 9 km), and 10′ (approximately 18 km)]. The projected version provides monthly values of minimum temperature (°C), maximum temperature (°C), precipitation (mm), and 19 other bioclimatic variables, which were all derived from 23 climate models.

2.4.2 Obtaining weather-related data from the OpenWeatherMap API

Data can be downloaded from an online meteorological service called the OpenWeatherMap application program interface (API) (https://openweathermap.org/api). It provides an API with JSON endpoints to make free and unlimited calls for extracting weather values (i.e., for temperature, relative humidity (%), pressure, cloud cover, and weather description) that are current estimates; users can also extract projected estimates or "short-term" 3-hourly forecasts stretching up to 5 days in the future, which is a useful feature if the user wants to incorporate data for predicting mosquito occupancies over a short period. It should be noted that extracting data from this source is challenging. One must first register to gain access to an API key, then set up a "scheduled" extraction script to extract the current analysis and 3-hourly forecasts (for up to the next 5 days) at the selected location (i.e., using the GPS centroids of cities) *via* OpenWeatherMap (the information is compiled in a JSON file). This can be done *via* a local server (i.e., personal computer) using a crontab (https://crontab.guru/every-5-minutes) or preferably on a cloud-based online server such as the MongoDB (https://www.mongodb.com). The data extraction is performed through the following API address, with the given API key provided by the OpenWeatherMap service (the selected city's ID number is inserted in the "ID" part of the API address): http://api.openweathermap.org/data/2.5/forecast?id=ID&APPID=KEY. It should be noted that this resource provides weather measurements only at a city level. For example, suppose we wanted to extract the weather data for Recife and Campina Grande (in Brazil) (39): we can perform this action by using the API key provided by the OpenWeatherMap API services, and then setting the API to the selected cities' IDs by inserting the values of 3390760 (i.e., Recife, longitude −34.8811 and latitude −8.0539) and 3403642 (i.e., Campina Grande, longitude −35.8811 and latitude −7.2306) into the above link through a timed recursive loop to continuously compile the records into a local server or into a cloud-based online platform. Details of this resource were explained extensively by Musah et al. (39).

3 Materials and methods

In this section, we describe the implementation of a population-based ecological study design using spatially referenced point survey records on presence-only mosquito data, using Brazil as a case study for this demonstration. We will discuss the implementation of the maximum entropy model (MAXENT) for predicting the probability of mosquito occurrence across the whole of Brazil while accounting for other environmental attributes that impact mosquito habitats.

3.1 Data extraction from the global compendium of *Aedes aegypti* and *Albopictus* occurrence

The global compendium of the *Aedes* species is an open source database that is accessible *via* the Global Biodiversity Information Facility (GBIF) (https://www.gbif.org) (4). For this demonstration, we have restricted the analysis to the *Aedes aegypti* species points in Brazil. This file contains a grand total of 19,929 spatially referenced occurrence points across the world. Brazil has 5,057 survey points spanning from 1979 to 2013 that contribute to this database. The majority of the survey points for Brazil were documented in 2013 (4,410; 87%), while the remaining survey points (i.e., 594; 12%) were unevenly spread across 1979 to 2011, with 53 survey points having missing information for the year. Therefore, to determine the possible distribution of the *Aedes aegypti* species in Brazil, a total of 4,410 occurrence locations for the *Aedes aegypti* species were extracted from this database for the year 2013 only.

3.2 Study design

A country-scale ecological study design within a cross-sectional framework was used on 2013 data to retrospectively determine the following outcomes: (1) the probability of the *Aedes aegypti* species being present at a location in Brazil; (2) the likely areas that are environmentally suitable for *Aedes aegypti*; and (3) the set of restricted variables (i.e., temperature, precipitation, natural lighting, urbanization, NDVI, population density, and land surface elevation) that yields the highest contribution to mosquito occurrence prediction in a Brazilian context.

3.2.1 Gridded environmental variables

As described in section 3.2, seven predictor variables, of which two are climate related (annual temperature and precipitation in 2013), three describe the physical environment (averaged NDVI and natural lighting in 2013, and land surface elevation), and the remaining two describe the anthropogenic conditions (i.e., overall population density and urbanization, both measured for 2013), constituted the gridded data used as risk factors for mosquito occupancy. These raster grids were combined accordingly into a single multiband raster object with dimensions of 4.5 km by 4.5 km resolution to enable the following actions needed for the analysis: (1) the extraction of all environmental raster values from all seven variables onto the occurrence and absence points (see section 3.2.2); and (2) the feeding of the entire multiband raster object into the MAXENT model after it is trained for the country-scale estimation and spatial prediction for *Aedes aegypti* occupancy in Brazil.

3.2.2 Statistical analysis using the maximum entropy algorithm (MAXENT)

The maximum entropy algorithm is a classification algorithm that falls under the umbrella of ecological niche models, which are used to estimate the relationship between species records at sites and the environmental and spatial characteristics of those sites (40). In other words, these are distributional models that use occurrence point data in conjunction with environmental data to make a correlative model of the environmental conditions that meet an outcome's environmental (or ecological) requirements, which, in turn, can infer zones for the relative suitability (or predictability) of an outcome. They have many applications in ecology, epidemiology, and disaster risk reduction and have been widely used for country-scale mapping for determining habitat suitability for the *Aedes* species in South America (41–43).

As described in section 3.1, 4,410 location data points for *Aedes aegypti* in 2013 in Brazil were compiled and used as presence points. Background data for twice the number of the presence points (i.e., 8,820) were generated within the extent of the study area to serve as proxy locations for pseudo-absences of *Aedes aegypti*. The presence and pseudo-absence points were rendered into a binary indicator that takes a Bernoulli function to model probabilities in geographic space. It should be noted that all 4,410 occurrence points were coded as 1 to signify the presence of *Aedes aegypti*, while the assumed background points (i.e., pseudo-absences) were coded as 0 to signify the absence of *Aedes aegypti* (40) (Figure 2). These points were used to extract all environmental raster values as described in section 3.2.1.

Before constructing the predictive model, we performed a fourfold cross-validation analysis by randomly withholding 25% of the presence and pseudo-absence locations as test data, and retaining the remaining 75% as training data for mapping the predictions. This meant that the model was fitted four times while withholding a separate quarter of the data – each cross-validation would churn a key indicator that was averaged to allow for overall model validation, i.e., the area under the curve (AUC) and maximum true-positive rate and true-negative rate (max TPR + TNR). AUC is an indicator of model performance where higher values indicate greater accuracy in our predictions; an AUC value of 0.5 is a common cut-off point used for assessing model performance. Hence, an AUC value of 0.5 or lower is an indication of our predictions being unreliable, while values above 0.5 and toward 1.0 indicate that our predictions are more reliable and accurate. Max TPR + TNR denotes the probability threshold at which our model maximizes the TPR and the TNR for correctly classifying a grid cell as a presence feature. It is generally accepted that this is the optimum value at which to set the threshold for the binary classification of a grid cell and the predicted probability is a reflection of the level of certainty of the classification that was mapped. We used the max TPR + TNR threshold to reclassify the region's predicted probabilities accordingly as "suitable" and "not suitable", whereby any value above max TPR + TNR was deemed as environmentally suitable for the *Aedes* species and *vice versa*.

All statistical analysis, including GIS mapping and MAXENT modeling, was performed in RStudio (version 2022.07.1 Build 554). All datasets along with scripts were provided for reproducible research (see section on data availability).
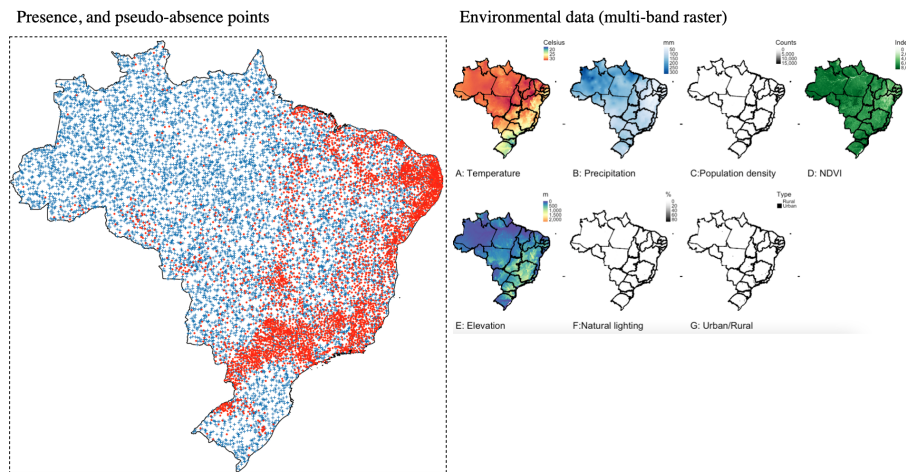
FIGURE 2

The right panel shows point locations with a known presence (red dots) of *Aedes aegypti* in 2013 in Brazil, whereas the blue crosses correspond to pseudo-absence points. The left panel shows the following Brazilian covariate data measured for 2013: **(A)** annual temperature; **(B)** annual precipitation; **(C)** population density; **(D)** NDVI; **(E)** land surface elevation; **(F)** natural lighting; and **(G)** urban/rural classification.

4 Results

4.1 Mapping the predicted probabilities and suitability regions for Brazil

After performing the fourfold cross-validation analysis, we found that the overall AUC estimate was 0.8376 (83.76%), which was obtained after averaging AUC-specific estimates for each cross-validation, i.e., 0.8435 (84.35%), 0.8403 (84.03%), 0.8333 (83.33%), and 0.8331 (83.31%). This value is greater than 0.5, thus indicating the model's predictive reliability (Figure 3).

The optimal threshold (i.e., max TPR + TNR) at which the MAXENT model was able to correctly classify a grid cell as a presence feature for mosquito occupancy was 0.4953. Hence, we will use a predicted probability threshold of 0.4953 to reclassify areas as suitable for mosquito occupancy (Figure 4). The expected outputs are shown in Figure 4: the left panel (A) shows the predicted probability distribution of mosquito occupancy for the *Aedes aegypti* species throughout Brazil, retrospectively, in 2013, while the right panel (B) shows the delineated areas where they are more likely to thrive.

The predictions were adjusted with seven different environmental covariates (Figure 3); here, we report the overall variable contributions. The population density, an anthropogenic indicator, has the highest contribution to the prediction, estimated at 75.75%, followed by natural lighting (10.29%), precipitation (6.79%), NDVI (4.18%), temperature
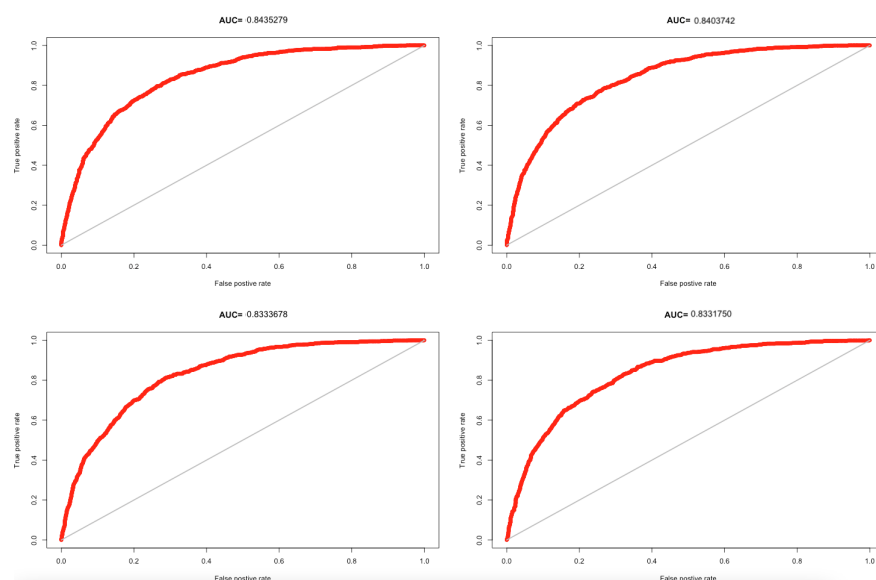
FIGURE 3

AUC curves from fourfold cross-validation analysis; the four estimates were averaged to 0.8376 (> 0.5) with a max TPR + TNR of 0.4953.

FIGURE 4
MAXENT modeling results showing **(A)** the predicted probability map of mosquito (*Aedes aegypti*) occupancy and **(B)** the suitability map based on the max TPR + TNR to illustrate where *Aedes aegypti* will thrive in Brazil.

(2.55%), land surface elevation (0.421%), and urbanization (negligible; < 0.0001%).

5 Discussion

In this article, we described a broad range of open data sources that can be harnessed for the spatial prediction of mosquito populations. We used the whole of Brazil as a moti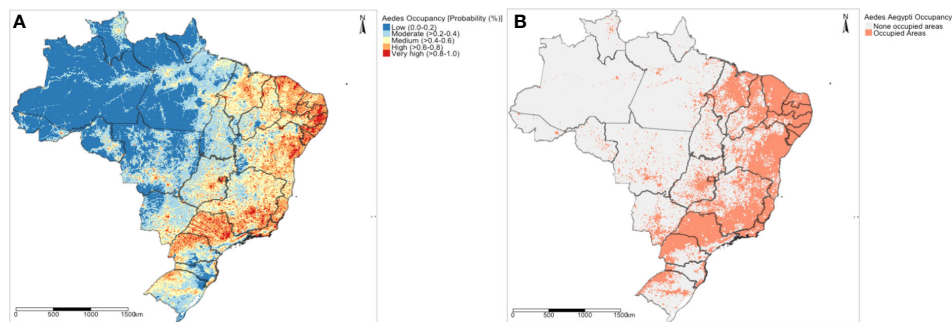vational case study to demonstrate how these datasets can be brought together for predicting the intensity of mosquito occupancy for *Aedes aegypti* in a data-sparse context using the MAXENT algorithm, which showed that population density, natural lighting, and precipitation made the biggest contributions to mosquito occupancy. While this approach was rigorous and should be used when data remains elusive, the author(s) concede that there are flaws in this approach. First, the research design of this case study was retrospective, using open entomologic data that were mostly available for 2013. The predictions shown in Figure 3 are not at all representative of the current climate situation when this research article was written (i.e., 2023). However, it would be possible to use the projected climate and population-based data for 2023 (which could have been done here, but this article is simply a demonstration), which could be fed into our trained MAXENT model and would have produced the predicted probability values for a future scenario. Second, the study design itself relies upon an ecological study design within a retrospective cross-sectional framework. In this study, the data used were a combination of both point and gridded information that is at a high geographic resolution but not at an individual level, e.g., at the level of household or property. This meant that the interpretation of the predictions needed to be done with the ecological fallacy in mind. These biases limit the research's ability to achieve both internal and external validity. To combat these biases, we argue the case for using bespoke applications for acquiring accurate entomologic data.

Our case study demonstrated the combining of open-source data to crudely map areas of mosquito habitat suitability, analytically and in an unsupervised scenario (and where data paucity is an issue). However, the authors stand by the opinion that point-level mosquito surveillance data that recorded observations at either a residential premise or property level would be the "gold standard" approach for collecting primary data at a granular resolution. This provides ample opportunity to collect more detailed information describing property characteristics that promote infestation, which was absent from our case study. In addition, it provides point-level data used in point-process models for making spatial predictions regarding infestation burden, which in turn can be integrated into an early warning system for outbreaks (44–46). We propose that the use of smartphone applications that are developed for the main purpose of collecting surveillance data to show the infestation risk and at the same time the geographic burden of such infestations is the best way to support vector control campaigns. There is now a shift toward using such applications for this purpose, especially in Central and South America, with three examples given here. First, VectorPoint is an excellent mobile surveillance application for reporting Chagas disease and infestations in Arequipa, Peru (47). The application provides a risk map based on data collected during fieldwork. Second, Chaak is a smartphone-based application system interlinked with a dashboard (for managers) dedicated to mosquito-borne disease surveillance that captures data related to the immature stages of dengue virus mosquito vectors in Mérida, Mexico (48). Third, VazaDengue is akin to VectorPoint and Chaak; however, it is only a smartphone-based system that integrates social media with citizen science to guide surveillance agents in controlling mosquitoes (49).

The authors have developed a robust surveillance system, which is cloud based, that improves the surveillance of mosquitoes by providing timely and geolocated reports regarding the presence and absence of mosquitoes in properties along with other entomological characteristics (i.e., eggs or larvae) in north-east Brazilian cities, limited specifically to Recife and Campina Grande. This was done by taking everything the CHWs use in their mosquito control campaign [i.e., surveillance reporting cards (data collection sheets) and the spatial configuration of block areas as scanned maps] and digitizing them into a format supported by the MEWAR application (a full description of its development is provided by Aldosery et al. (18) (see Figure 5). The application seeks to collect
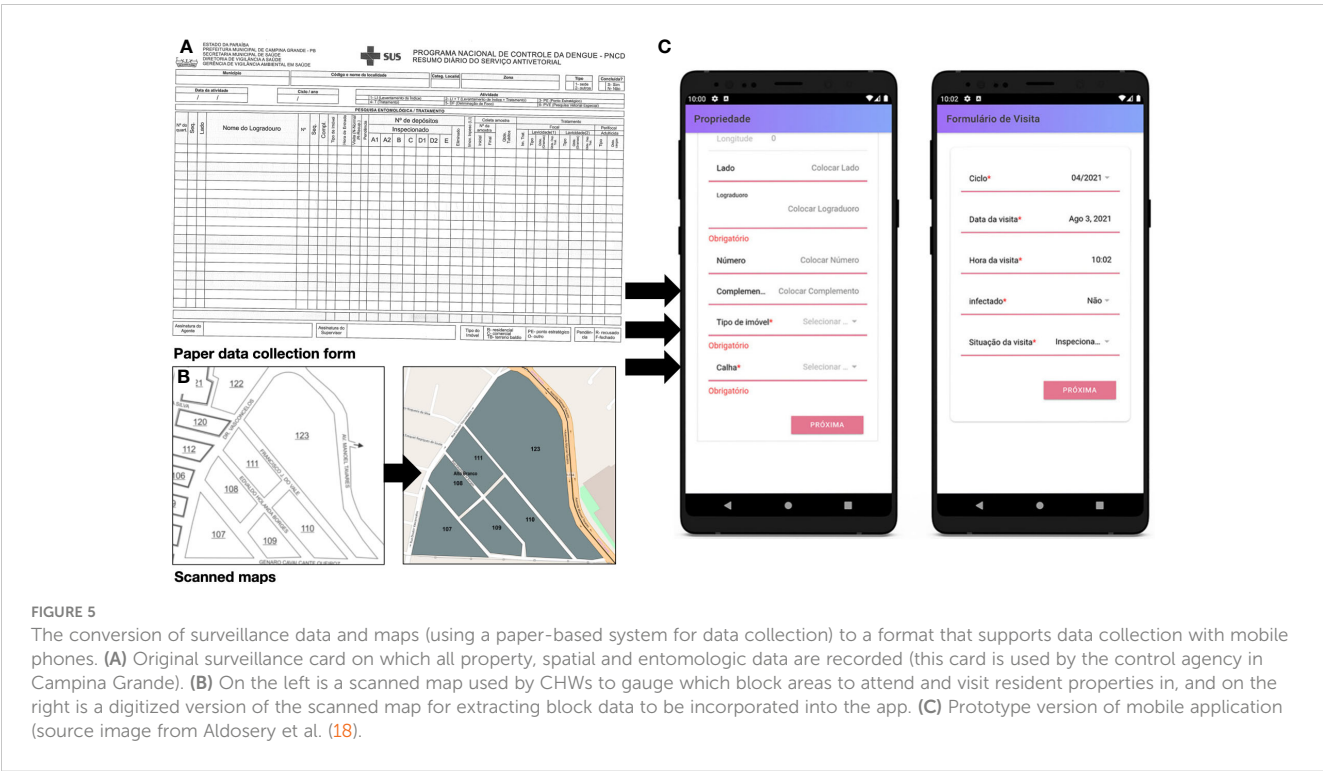
FIGURE 5

The conversion of surveillance data and maps (using a paper-based system for data collection) to a format that supports data collection with mobile phones. **(A)** Original surveillance card on which all property, spatial and entomologic data are recorded (this card is used by the control agency in Campina Grande). **(B)** On the left is a scanned map used by CHWs to gauge which block areas to attend and visit resident properties in, and on the right is a digitized version of the scanned map for extracting block data to be incorporated into the app. **(C)** Prototype version of mobile application (source image from Aldosery et al. (18)).

general parameters linked to infestation, ranging from spatial information to property-level characteristics such as land use, waste disposal practices, and key entomologic infestation and treatment indicators (see Table 1).

The list of data sources that are raster based is malleable for area-level analysis—most mosquito surveillance data tend to be released at an area level; hence, these pixels can be aggregated within areal boundaries and matched to observed units to be used

TABLE 1 General summary of the type of information collected through the MEWAR smartphone application mapped from Environmental Health Agents (EHA) from Recife and Campina Grande (see details in Aldosery et al. (18)).

Variable name	Indicator type	Description
Full address	Character	• Full address details of the building, which includes the following: door number, street name, neighborhood, district, and state
GPS (in decimal degrees)	Spatial	• Longitude • Latitude
Land use type	Property	• Residential • Commercial • Other building type (abandoned properties)
Waste disposal practice	Sanitation	• Proper disposal (i.e., collected directly by waste management) • Improper disposal [i.e., collected indirectly, burnt, buried, thrown on landfill, thrown on ground, thrown in a body of water (e.g., river, stream, or lake)]
Sources for mosquito breeding (six-tier classification)	Entomological	• A1 (water tanks) • A2 (large indoor domestic containers, e.g., barrels, bathtubs, and cisterns) • B (indoor small domestic containers, e.g., vases, dishes, and flowerpots) • C (fixed outdoor objects, e.g., gutters, slabs, swimming pools, and ornamental fountains) • D1 (discarded objects found outside property, e.g., tires) • D2 (discarded garbage, e.g., plastic food containers, bottles, and cans)
Infestation status	Outcome	• Infested • Not infested
Treatment status	Performance	• Inspected • Treated (i.e., with larvicidal application, mechanically, chemically, etc.) • Not treated

as risk factors. Appropriate rasters that are good candidates for aggregation include population density, climate data from WorldClim, and aridity—these can produce proxy measures for area units such as totals and other useful summary statistics (medians, averages, etc.) that can be implemented in a variety of spatial risk models at an area level [notable examples of spatial models for risk prediction include Bayesian hierarchical modeling (46, 50, 51) and machine learning (e.g., boosted regressions (52)]. Users rendering their data to this level and implementing this kind of approach should keep in mind the various biases that can occur when reporting results, and hence a pronounced bias, such as the ecological fallacy, should therefore be considered carefully. However, the use of individual-level data (i.e., residential premises) collected through primary surveys can be augmented with the open-source environmental spatial data highlighted in this article by linking their GPS coordinates by using a spatial join, overlapping the raster pixels with the surveillance points and assigning the raster values to the survey points to facilitate a much more precise and granular modeling approach. This would be invaluable, as the point-process approach for mapping is the gold standard for making spatial risk predictions for households, and the results can be further interpolated over a grid for risk coverage. There are many models that enable this kind of analysis—notable examples include Bayesian modeling frameworks such as stochastic partial differential equations using integrated nested Laplace approximations (SPDE-INLA) (53–55). These are valuable options for risk prediction and creating an early warning system for mosquito outbreaks; whereby such information can be fed into a dashboard to provide digital solutions for surveillance manager and policy makers (56, 57).

6 Conclusion

To conclude, we have identified a broad range of open-source data sources that can be harnessed as risk factors for the spatial prediction of mosquito occupancy or infestation, and we have demonstrated in a reproducible way how they can be brought together and implemented using the MAXENT algorithm within a Brazilian context. We explicitly note that this approach should be utilized within a data-sparse context. However, we also discussed the use of novel bespoke technologies, such as smartphone applications, that should be considered the better method for collecting primary entomologic data, to address the problems of data paucity and avoid potential biases that are typically found in studies using open source datasets—doing so will improve a study's internal and external validity. This article was written to build capacity for and awareness of various data sources, demonstrating their use with reproducible methods, and thus it is applicable to different mosquito species and other areas in the Global South with similar environmental and socioeconomic conditions.

Data availability statement

The original contributions presented in the study are included in the article. All datasets, script files and instructions for reproducing the analysis shown in this original article are made freely available through our GitHub repository (https://github.com/UCLPG-MSC-SGDS/Data-Sources).

Author contributions

Conceptualization: AM and PK; data management, extraction, and analysis: AM; original draft: AM; supervision and funding acquisition: PK, WPdS, TM, LCC, OY, and TA; revision of manuscript: PK, WPdS, TM, LCC, OY, TA, IVGB, MT, SB, EB, GMMM, ACGdS, CLdL, and AA. All authors contributed to the article and approved the submitted version.

Funding

Conflict of interest

The authors declare that the research was conducted in the absence of any commercial or financial relationships that could be construed as a potential conflict of interest.

Publisher's note

All claims expressed in this article are solely those of the authors and do not necessarily represent those of their affiliated organizations, or those of the publisher, the editors and the reviewers. Any product that may be evaluated in this article, or claim that may be made by its manufacturer, is not guaranteed or endorsed by the publisher.

References

1. Seelig F, Bezerra H, Cameron M, Hii J, Hiscox A, Irish S, et al. The COVID-19 pandemic should not derail global vector control efforts. *PloS Negl Trop Dis* (2020) 14 (8):e0008606. doi: 10.1371/journal.pntd.0008606

2. Benelli G. Research in mosquito control: current challenges for a brighter future. *Parasitol Res* (2015) 114(8):2801–5. doi: 10.1007/s00436-015-4586-9

3. Hay SI, Snow RW. The malaria atlas project: developing global maps of malaria risk. *PloS Med* (2006) 3(12):e473. doi: 10.1371/journal.pmed.0030473

4. Kraemer MUG, Sinka ME, Duda KA, Mylne A, Shearer FM, Brady OJ, et al. The global compendium of Aedes aegypti and Ae. *albopictus* occurrence. *Sci Data* (2015) 2 (1):150035. doi: 10.1038/sdata.2015.35

5. Brooker S, Kabatereine NB, Smith JL, Mupfasoni D, Mwanje MT, Ndayishimiye O, et al. An updated atlas of human helminth infections: the example of East Africa. *Int J Health Geogr* (2009) 8(1):42. doi: 10.1186/1476-072X-8-42

6. Brooker S, Hotez PJ, Bundy DAP. The global atlas of helminth infection: mapping the way forward in neglected tropical disease control. *PloS Negl Trop Dis* (2010) 4(7): e779. doi: 10.1371/journal.pntd.0000779

7. Hay SI, George DB, Moyes CL, Brownstein JS. Big data opportunities for global infectious disease surveillance. *PloS Med* (2013) 10(4):e1001413. doi: 10.1371/journal.pmed.1001413

8. Maciel-de-Freitas R, Aguiar R, Bruno RV, Guimarães MC, Lourenço-de-Oliveira R, Sorgine MH, et al. Why do we need alternative tools to control mosquito-borne diseases in Latin America? *Mem Inst Oswaldo Cruz* (2012) 107:828–9. doi: 10.1590/S0074-02762012000600021

9. Magalhaes T, Braga C, Cordeiro MT, Oliveira ALS, Castanha PMS, Maciel APR, et al. Zika virus displacement by a chikungunya outbreak in recife, Brazil. *PloS Negl Trop Dis* (2017) 11(11):e0006055. doi: 10.1371/journal.pntd.0006055

10. Lowe R, Barcellos C, Brasil P, Cruz OG, Honório NA, Kuper H, et al. The zika virus epidemic in Brazil: from discovery to future implications. *Int J Environ Res Public Health* (2018) 15(1):96. doi: 10.3390/ijerph15010096

11. Souza AI, de Siqueira MT, Ferreira ALCG, de Freitas CU, Bezerra ACV, Ribeiro AG, et al. Geography of microcephaly in the zika era: a study of newborn distribution and socio-environmental indicators in recife, Brazil, 2015-2016. *Public Health Rep* (2018) 133(4):461–71. doi: 10.1177/0033354918777256

12. Tunali M, Radin AA, Başıbüyük S, Musah A, Borges IVG, Yenigun O, et al. A review exploring the overarching burden of zika virus with emphasis on epidemiological case studies from Brazil. *Environ Sci pollut Res Int* (2021) 28 (40):55952–66. doi: 10.1007/s11356-021-15984-y

13. da Silva CC, de Lima CL, da Silva ACG, Moreno GMM, Musah A, Aldosery A, et al. Spatiotemporal forecasting for dengue, chikungunya fever and zika using machine learning and artificial expert committees based on meta-heuristics. *Res BioMed Eng* (2022) 38:499–537. doi: 10.1007/s42600-022-00202-6

14. de Lima CL, da Silva ACG, da Silva CC, Moreno GMM, da Silva Filho AG, Musah A, et al. Intelligent systems for dengue, chikungunya, and zika temporal and spatio-temporal forecasting: a contribution and a brief review. In: Pani SK, Dash S, dos Santos WP, Chan Bukhari SA, Flammini F, editors. *Assessing COVID-19 and other pandemics and epidemics using computational modelling and data analysis*. Cham: Springer International Publishing (2022). p. 299–331. doi: 10.1007/978-3-030-79753-9_17

15. Silva CCda, Lima CLde, Silva A CGda, Moreno GMM, Musah A, Aldosery A, et al. Forecasting dengue, chikungunya and zika cases in recife, Brazil: a spatio-temporal approach based on climate conditions, health notifications and machine learning. *Res Soc Dev* (2021) 10(12):e452101220804–e452101220804. doi: 10.33448/rsd-v10i12.20804

16. Musah A, Rubio-Solis A, Birjovanu G, dos Santos WP, Massoni T, Kostkova P. (2019). Assessing the relationship between various climatic risk factors & mosquito abundance in recife, Brazil. In: *DPH'19 Proceedings of the 9th International Conference on Digital Public Health*, Marseille, France. (20th to 23rd November 2019). (2019) pp. 97–101. doi: 10.1145/3357729.3357744

17. Rubio-Solis A, Musah A, Dos Santos W, Massoni T, Birjovanu G, Kostkova P. (2019). ZIKA virus: prediction of aedes mosquito larvae occurrence in recife (Brazil) using online extreme learning machine and neural networks. In: *DPH'19 Proceedings of the 9th International Conference on Digital Public Health*, (20th to 23rd November 2019). Marseille, France: Association for Computing Machinery (2019) pp. 101–10. doi: 10.1145/3357729.3357738

18. Aldosery A, Musah A, Birjovanu G, Moreno G, Boscor A, Dutra L, et al. MEWAR: development of a cross-platform mobile application and web dashboard system for real-time mosquito surveillance in northeast Brazil. *Front Public Health* (2021) 9:1623. doi: 10.3389/fpubh.2021.754072

19. Beltrán JD, Boscor A, dos Santos WP, Massoni T, Kostkova P. ZIKA: a new system to empower health workers and local communities to improve surveillance protocols by e-learning and to forecast zika virus in real time in Brazil. *DH'18: Proceedings of the 2018 International Conference on Digital Health*, (Lyon, France) (23rd to 26th April). (2018) pp. 90–4. doi: 10.1145/3194658.3194683

20. Leta S, Beyene TJ, De Clercq EM, Amenu K, Kraemer MUG, Revie CW. Global risk mapping for major diseases transmitted by aedes aegypti and aedes albopictus. *Int J Infect Dis* (2018) 67:25–35. doi: 10.1016/j.ijid.2017.11.026

21. Sallam MF, Fizer C, Pilant AN, Whung PY. Systematic review: land cover, meteorological, and socioeconomic determinants of aedes mosquito habitat for risk mapping. *Int J Environ Res Public Health* (2017) 14(10):1230. doi: 10.3390/ijerph14101230

22. *Global administrative areas. GADM database of global administrative areas (Version 2.0)* (2012). Available at: www.gadm.org.

23. Kofidou M, de Courcy Williams M, Nearchou A, Veletza S, Gemitzi A, Karakasiliotis I. Applying remotely sensed environmental information to model mosquito populations. *Sustainability* (2021) 13(14):7655. doi: 10.3390/su13147655

24. Attaway DF, Jacobsen KH, Falconer A, Manca G, Waters NM. Risk analysis for dengue suitability in Africa using the ArcGIS predictive analysis tools (PA tools). *Acta Trop* (2016) 158:248–57. doi: 10.1016/j.actatropica.2016.02.018

25. Asigau S, Hartman DA, Higashiguchi JM, Parker PG. The distribution of mosquitoes across an altitudinal gradient in the Galapagos islands. *J Vector Ecol* (2017) 42(2):243–53. doi: 10.1111/jvec.12264

26. Attaway DF, Jacobsen KH, Falconer A, Manca G, Rosenshein Bennett L, Waters NM. Mosquito habitat and dengue risk potential in Kenya: alternative methods to traditional risk mapping techniques. *Geospatial Health* (2014) 9(1):119–30. doi: 10.4081/gh.2014.10

27. *Global aridity index and potential evapotranspiration (ET0) climate database v2. figshare* (2019). Available at: https://figshare.com/articles/dataset/Global_Aridity_Index_and_Potential_Evapotranspiration_ET0_Climate_Database_v2/7504448/3.

28. Paz S. Effects of climate change on vector-borne diseases: an updated focus on West Nile virus in humans. *Emerg Top Life Sci* (2019) 3(2):143–52. doi: 10.1042/ETLS20180124

29. Sinka ME, Golding N, Massey NC, Wiebe A, Huang Z, Hay SI, et al. Modelling the relative abundance of the primary African vectors of malaria before and after the implementation of indoor, insecticide-based vector control. *Malar J* (2016) 15(1):142. doi: 10.1186/s12936-016-1187-8

30. Kolimenakis A, Heinz S, Wilson ML, Winkler V, Yakob L, Michaelakis A, et al. The role of urbanisation in the spread of aedes mosquitoes and the diseases they transmit–a systematic review. *PloS Negl Trop Dis* (2021) 15(9):e0009631. doi: 10.1371/journal.pntd.0009631

31. Čabanová V, Miterpáková M, Valentová D, Blažejová H, Rudolf I, Stloukal E, et al. Urbanization impact on mosquito community and the transmission potential of filarial infection in central Europe. *Parasit Vectors* (2018) 11(1):261. doi: 10.1186/s13071-018-2845-1

32. Nieves JJ, Sorichetta A, Linard C, Bondarenko M, Steele JE, Stevens FR, et al. Annually modelling built-settlements between remotely-sensed observations using relative changes in subnational populations and lights at night. *Comput Environ Urban Syst* (2020) 80:101444. doi: 10.1016/j.compenvurbsys.2019.101444

33. Shaw WR, Catteruccia F. Vector biology meets disease control: using basic research to fight vector-borne diseases. *Nat Microbiol* (2019) 4(1):20–34. doi: 10.1038/s41564-018-0214-7

34. Lloyd CT, Sorichetta A, Tatem AJ. High resolution global gridded data for use in population studies. *Sci Data* (2017) 4(1):170001. doi: 10.1038/sdata.2017.1

35. Barghini A, de Medeiros BAS. Artificial lighting as a vector attractant and cause of disease diffusion. *Environ Health Perspect* (2010) 118(11):1503–6. doi: 10.1289/ehp.1002115

36. O'Hanlon SJ, Slater HC, Cheke RA, Boatin BA, Coffeng LE, Pion SDS, et al. Model-based geostatistical mapping of the prevalence of onchocerca volvulus in West Africa. *PloS Negl Trop Dis* (2016) 10(1):e0004328. doi: 10.1371/journal.pntd.0004328

37. Fick SE, Hijmans RJ. WorldClim 2: new 1-km spatial resolution climate surfaces for global land areas. *Int J Climatol* (2017) 37(12):4302–15. doi: 10.1002/joc.5086

38. Harris I, Jones PD, Osborn T j., Lister D h. Updated high-resolution grids of monthly climatic observations – the CRU TS3.10 dataset. *Int J Climatol* (2014) 34 (3):623–42. doi: 10.1002/joc.3711

39. Musah A, Dutra LMM, Aldosery A, Browning E, Ambrizzi T, Borges IVG, et al. An evaluation of the OpenWeatherMap API versus INMET using weather data from two Brazilian cities: recife and campina grande. *Data* (2022) 7(8):106. doi: 10.3390/data7080106

40. Elith J, Phillips SJ, Hastie T, Dudík M, Chee YE, Yates CJ. A statistical explanation of MaxEnt for ecologists. *Divers Distrib* (2011) 17(1):43–57. doi: 10.1111/j.1472-4642.2010.00725.x

41. Estallo EL, Sangermano F, Grech M, Ludueña-Almeida F, Frías-Cespedes M, Ainete M, et al. Modelling the distribution of the vector aedes aegypti in a central Argentine city. *Med Vet Entomol* (2018) 32(4):451–61. doi: 10.1111/mve.12323

42. Arboleda S, Jaramillo- ON, Peterson AT. Spatial and temporal dynamics of aedes aegypti larval sites in bello, Colombia. *J Vector Ecol* (2012) 37(1):37–48. doi: 10.1111/j.1948-7134.2012.00198.x

43. Portilla Cabrera CV, Selvaraj JJ. Geographic shifts in the bioclimatic suitability for aedes aegypti under climate change scenarios in Colombia. *Heliyon* (2020) 6(1): e03101. doi: 10.1016/j.heliyon.2019.e03101

44. Racloz V, Ramsey R, Tong S, Hu W. Surveillance of dengue fever virus: a review of epidemiological models and early warning systems. *PloS Negl Trop Dis* (2012) 6(5): e1648. doi: 10.1371/journal.pntd.0001648

45. Semenza JC. Prototype early warning systems for vector-borne diseases in Europe. *Int J Environ Res Public Health* (2015) 12(6):6333–51. doi: 10.3390/ijerph120606333

46. Lowe R, Bailey TC, Stephenson DB, Jupp TE, Graham RJ, Barcellos C, et al. The development of an early warning system for climate-sensitive disease risk with a focus on dengue epidemics in southeast Brazil. *Stat Med* (2013) 32(5):864–83. doi: 10.1002/sim.5549

47. Gutfraind A, Peterson JK, Rose EB, Arevalo-Nieto C, Sheen J, Condori-Luna GF, et al. Integrating evidence, models and maps to enhance chagas disease vector surveillance. *PloS Negl Trop Dis* (2018) 12(11):e0006883. doi: 10.1371/journal.pntd.0006883

48. Lozano–Fuentes S, Wedyan F, Hernandez–Garcia E, Sadhu D, Ghosh S, Bieman JM, et al. Cell phone-based system (Chaak) for surveillance of immatures of dengue virus mosquito vectors. *J Med Entomol* (2013) 50(4):879–89. doi: 10.1603/ME13008

49. Sousa L, de Mello R, Cedrim D, Garcia A, Missier P, Uchôa A, et al. VazaDengue: an information system for preventing and combating mosquito-borne diseases with social networks. *Inf Syst* (2018) 75:26–42. doi: 10.1016/j.is.2018.02.003

50. Lowe R, Bailey TC, Stephenson DB, Graham RJ, Coelho CAS, Sá Carvalho M, et al. Spatio-temporal modelling of climate-sensitive disease risk: towards an early warning system for dengue in Brazil. *Comput Geosci* (2011) 37(3):371–81. doi: 10.1016/j.cageo.2010.01.008

51. Lowe R, Coelho CA, Barcellos C, Carvalho MS, Catão RDC, Coelho GE, et al. Evaluating probabilistic dengue risk forecasts from a prototype early warning system for Brazil. *eLife* (2016) 5:e11285. doi: 10.7554/eLife.11285

52. Ashby J, Moreno-Madriñán MJ, Yiannoutsos CT, Stanforth A. Niche modeling of dengue fever using remotely sensed environmental factors and boosted regression trees. *Remote Sens* (2017) 9(4):328. doi: 10.3390/rs9040328

53. Moraga P, Dean C, Inoue J, Morawiecki P, Noureen SR, Wang F. Bayesian Spatial modelling of geostatistical data using INLA and SPDE methods: a case study predicting malaria risk in Mozambique. *Spat Spatio-Temporal Epidemiol* (2021) 39:100440. doi: 10.1016/j.sste.2021.100440

54. Alegana VA, Macharia PM, Muchiri S, Mumo E, Oyugi E, Kamau A, et al. Plasmodium falciparum parasite prevalence in East Africa: updating data for malaria stratification. *PloS Glob Public Health* (2021) 1(12):e0000014. doi: 10.1371/journal.pgph.0000014

55. Juan P, Díaz-Avalos C, Mejía-Domínguez NR, Mateu J. Hierarchical spatial modeling of the presence of chagas disease insect vectors in Argentina. *A Comp approach Stoch Environ Res Risk Assess* (2017) 31(2):461–79. doi: 10.1007/s00477-016-1340-5

56. Kostkova P. Disease surveillance data sharing for public health: the next ethical frontiers. *Life Sci Soc Policy* (2018) 14:16. doi: 10.1186/s40504-018-0078-x

57. Kostkova P, Garbin S, Moser J, Pan W Integration and visualization public health dashboard: the medi+board pilot project. *Proceedings of the 23rd International Conference on World Wide Web* (2014). p. 657–662. doi: 10.1145/2567948.2579276

Dirofilariasis mouse models for heartworm preclinical research

A. E. Marriott[1†], J. L. Dagley[1†], S. Hegde[1], A. Steven[1], C. Fricks[2], U. DiCosty[2], A. Mansour[2], E. J. Campbell[3], C. M. Wilson[3], F. Gusovsky[4], S. A. Ward[1], W. D. Hong[5], P. O'Neill[5], A. Moorhead[3], S. McCall[2], J. W. McCall[2,3], M. J. Taylor[1] and J. D. Turner[1]*

[1]Department of Tropical Disease Biology, Centre for Drugs and Diagnostics, Liverpool School of Tropical Medicine, Pembroke Place, Liverpool, United Kingdom, [2]TRS Laboratories Inc, Athens, GA, United States, [3]Department of Infectious Diseases, College of Veterinary Medicine, University of Georgia, Athens, GA, United States, [4]Eisai Global Health, Cambridge, MA, United States, [5]Department of Chemistry, University of Liverpool, Liverpool, United Kingdom

Introduction: Dirofilariasis, including heartworm disease, is a major emergent veterinary parasitic infection and a human zoonosis. Currently, experimental infections of cats and dogs are used in veterinary heartworm preclinical drug research.

Methods: As a refined alternative *in vivo* heartworm preventative drug screen, we assessed lymphopenic mouse strains with ablation of the interleukin-2/7 common gamma chain (γc) as susceptible to the larval development phase of *Dirofilaria immitis*.

Results: Non-obese diabetic (NOD) severe combined immunodeficiency (SCID)γc$^{-/-}$ (NSG and NXG) and recombination-activating gene (RAG)2$^{-/-}$γc$^{-/-}$ mouse strains yielded viable *D. immitis* larvae at 2−4 weeks post-infection, including the use of different batches of *D. immitis* infectious larvae, different *D. immitis* isolates, and at different laboratories. Mice did not display any clinical signs associated with infection for up to 4 weeks. Developing larvae were found in subcutaneous and muscle fascia tissues, which is the natural site of this stage of heartworm in dogs. Compared with *in vitro*-propagated larvae at day 14, *in vivo*-derived larvae had completed the L4 molt, were significantly larger, and contained expanded *Wolbachia* endobacteria titres. We established an *ex vivo* L4 paralytic screening system whereby assays with moxidectin or levamisole highlighted discrepancies in relative drug sensitivities in comparison with *in vitro*-reared L4 *D. immitis*. We demonstrated effective depletion of *Wolbachia* by 70%−90% in *D. immitis* L4 following 2- to 7-day oral *in vivo* exposures of NSG- or NXG-infected mice with doxycycline or the rapid-acting investigational drug, AWZ1066S. We validated NSG and NXG *D. immitis* mouse models as a filaricide screen by *in vivo* treatments with single injections of moxidectin, which mediated a 60%−88% reduction in L4 larvae at 14−28 days.

Discussion: Future adoption of these mouse models will benefit end-user laboratories conducting research and development of novel heartworm preventatives via increased access, rapid turnaround, and reduced costs and may simultaneously decrease the need for experimental cat or dog use.

Introduction

Dirofilaria immitis is a major veterinary filarial nematode causing chronic heartworm disease (HWD) in dogs. Dirofilariasis is spread primarily by mosquito species of the *Culicidae* family, including the invasive tiger mosquito, *Aedes albopictus* (Cancrini and Kramer, 2001). HWD develops following the establishment of adult nematodes in the right chambers of the heart-associated vessels following larval migrations in subcutaneous and muscle tissues. Adult infections can persist in the heart for >5 years (McCall et al., 2008). Pathology is chronic-progressive, associated with enlargement and hyper-proliferation of endocardium and physical blockage of adult worms in the pulmonary artery contributing to vessel narrowing, hypertension, and ultimately heart failure (Simón et al., 2012). *Dirofilaria immitis* causes a more acute immunopathology in cats where the arrival of immature worms often triggers an overt inflammatory reaction in the lungs leading to heartworm-associated respiratory disease (McCall et al., 2008). Both cats and dogs are at risk of acute, fatal thromboembolisms when dead adult worms lodge in pulmonary vasculature (Simón et al., 2012). *Dirofilaria* spp. can also cause abbreviated zoonotic infections in humans, whereby the arrested development of immature adults can cause subcutaneous nodules and lung parenchyma disease (Reddy, 2013). *Dirofilaria repens* is the most widely reported dirofilarial zoonosis, noted to be increasing across Europe, Asia, and Sri Lanka, although, *D. immitis*, *Dirofilaria striata, Dirofilaria tenuis, Dirofilaria ursi,* and *Dirofilaria spectans* also infect humans (Litster and Atwell, 2008). In 2012, 48,000 dogs tested positive for heartworm in the United States (US), and in 2016, over one million pets were estimated to carry the disease.[1] Incidence of HWD in the US is increasing both within endemic areas and into erstwhile HW-free, westerly and northerly regions, including Canada (Simón et al., 2012). A similar epidemiological pattern of increased dirofilariae incidence has also been documented in the Mediterranean, which has spread into the northern latitudes of Central and Western Europe (Morchón et al., 2012; Genchi and Kramer, 2017).

Heartworm disease is controlled by preventative chemotherapy and curative treatment of diagnosed cases. Chemo-prophylaxis with macrocyclic lactones (ML), namely ivermectin, milbemycin oxime, moxidectin, and selamectin, is effective at targeting L3–L4 larvae during subcutaneous tissue development and before immature adults reach the pulmonary artery to establish pathological adult infection (Wolstenholme et al., 2015; Prichard and Geary, 2019). After more than 40 years of use in veterinary medicine, ML drug resistance is prevalent in veterinary nematode parasites, with several *D. immitis* isolates formally determined as resistant to ML, whereby timed experimental infections and accurate prophylactic dosing have failed to prevent the development of fecund adult HW infections (Prichard and Geary, 2019).

The only regulatory-approved cure available for HWD is the injectable, melarsomine dihydrochloride. However, issues with this therapy include lengthy treatment regimens requiring in-clinic administrations, potential steroid pre-treatment, exercise

restriction, and the risk of severe adverse events. Melarsomine is unsafe for use in cats, with no alternative curative therapies currently approved. Alternative curative therapies include the use of moxidectin and doxycycline ("moxi-doxy") (Jacobson and DiGangi, 2021) with the latter antibiotic validated as a curative drug targeting the filarial endosymbiont, *Wolbachia*, demonstrable in human filariasis clinical trials (Johnston et al., 2021). However, due to concerns with doxycycline use within veterinary applications, such as long treatment time frames, dysbiosis side effects, and antibiotic stewardship of a human essential medicine, the development of short-course narrow-spectrum anti-*Wolbachia* heartworm therapeutics, without general antibiotic properties, may offer a potential future alternative (Turner et al., 2020).

ML preventatives, costing typically between $266 and $329 a year for a pet's treatment in the US, represent a potential multi-billion dollar global market (Mwacalimba et al., 2021). Due to the emergent spread of *D. immitis* infections, the growing concerns of ML prophylactic failure in the US, and the current inadequacies of curative treatments, new therapeutic strategies are being intensively investigated.

Until recently, the only fully validated *in vivo* screens available for heartworm anti-infectives were laboratory-reared cats and dogs. Lymphopenic and type-2 immunodeficient mice have been developed and validated as *in vivo* and *ex vivo* drug screens for medically important filarial parasite genera: *Brugia, Onchocerca,* and *Loa* (Halliday et al., 2014; Pionnier et al., 2019; Johnston et al., 2021; Marriott et al., 2022). Advantages of immunodeficient mouse models for filariasis drug screening include increased throughput, ease of maintenance, potential for international commercial supply, standardization with murine pharmacology models, reduced costs, and, potentially, a reduction in the use of "specially protected," highly sentient animal species (cats, dogs, and non-human primates). Considering these advantages, academic investigators and animal healthcare companies have latterly begun to research rodent infection models of *D. immitis,* including the application of immunodeficient mice as potential drug screens (Noack et al., 2021; Hess et al., 2023). Here, we demonstrate that multiple lymphopenic immunodeficient mouse strains with ablation of the interleukin-2/7 common gamma chain (γc) are susceptible to the initial tissue larval development phase of *D. immitis*. *In vivo* larvae are morphologically superior to *in vitro*-propagated larvae (including *Wolbachia* endobacteria content), and can be successfully utilized in a variety of drug screening applications for the evaluation of direct-acting preventatives and anti-*Wolbachia* therapeutics.

Materials and methods

Animals

Male NOD.SCIDγc$^{-/-}$ (NSG; NOD.Cg-*Prkdc^{scid} Il2rg^{tm1Wjl}*/SzJ) and BALB/c RAG2$^{-/-}$γc$^{-/-}$ (RAG2ɣc; C;129S4-*Rag2$^{tm1.1Flv}$ Il2rg$^{tm1.1Flv}$*/J) mice were purchased from Charles River, UK. Male NXG mice (NOD-*Prkdc^{scid}-IL2rg^{Tm1}*/Rj) were purchased from Janvier Labs, France. Mice were group housed under specific pathogen-free (SPF) conditions at the biomedical services unit (BSU), University of Liverpool, Liverpool, UK. Male NSG mice used at TRS laboratories were purchased from The

Jackson Laboratory, US, and group housed within filter-top cages. Mice were aged 5–7 weeks and weighed 21–32 g at the start of experiments. Animals had continuous access to fresh sterile food and water throughout experiments. Weight was monitored twice weekly and welfare behavior monitored daily. Study protocols were approved in the UK by LSTM & University of Liverpool Animal Welfare and Ethics Review Boards and licensed by The UK Home Office Animals in Science Regulation Unit. In the US, studies were approved by the TRS Institutional Animal Care and Use Committee.

Dirofilaria immitis parasite production

Missouri isolate (MO) *D. immitis* microfilariae in dog blood (NR-48907, provided by the NIH/NIAID Filariasis Research Reagent Resource Center, FR3, for distribution through BEI Resources) were fed to female *Aedes aegypti* mosquitoes (Liverpool strain) at a density of 5,000 mf/ml through an artificial membrane feeder (Hemotek, UK). Blood-fed mosquitoes were reared for 15 days with daily sugar-water feeding to allow development to the L3 stage. At day 15, *Di*L3 were collected from infected mosquitoes by crushing and concentration using a Baermann apparatus and Roswell Park Memorial Institute (RPMI) 1640 with 1% penicillin–streptomycin (both Sigma-Aldrich, UK). For validation studies at TRS Labs, US, an in-house Georgia III (GAIII) isolate of *D. immitis* was utilized. *Dirofilaria immitis* mf were used to infect female *A. aegypti* mosquitoes (Liverpool strain) in dog blood using a glass feeder at a density of 1,000–2,500 mf/ml. At day 14, *Di*L3 were collected from infected mosquitoes using crushing and straining with RPMI 1640 and 1% penicillin–streptomycin.

Dirofilaria immitis experimental infections

Highly motile infectious stage larvae (*Di*L3) retrieved from mosquitoes were washed in RPMI 1640 with 1% penicillin–streptomycin and 1% amphotericin B (Sigma-Aldrich, UK) and injected subcutaneously into the flank of male NSG, NXG, or RAG2ɣc mice at a density of 200 *Di*L3 per mouse. Cohorts of mice also received a single intraperitoneal injection of 2 mg methylprednisolone acetate (MPA; Sigma-Aldrich, UK) immediately prior to infection and after 1-week post-infection. Mice were humanely culled between 14 and 28 days post-infection. To retrieve parasites, skins were removed and subcutaneous tissue was scarified with a sharp scalpel blade. Muscle tissues were similarly scarified. Visceral organs were dissected and viscera, skin (pellet side-up), muscle tissues, and carcass were soaked in warm Eagle's minimum essential media (EMEM; Sigma-Aldrich, UK) with 1% penicillin–streptomycin and 1% amphotericin B for 2 h to allow active larvae to migrate from the tissues. Skin, muscle, and carcasses were incubated for a further 24-h period allowing residual larvae to migrate out of tissues.

In vitro larval cultures

Madin-Darby Canine Kidney (MDCK) cells and rhesus monkey kidney epithelial (LLCMK2) cells were passaged in T-75 flasks in EMEM with 10% fetal bovine serum (FBS), 1% penicillin–streptomycin, 1% amphotericin B, and 1% non-essential amino acid solution (NEAAS; Sigma-Aldrich, UK). Cells were seeded onto 12-well plates to reach confluent monolayers 24–48 h prior to parasite addition. For parasite cultures, washed MO *Di*L3 from mosquitoes were plated onto cell monolayers, or the cell-free media (EMEM) control at a density of 10–20 iL3 per well with 4 ml media. Larvae were monitored over a 35-day time point for survival and motility and at 14 days post-culture to evaluate development, length, and *Wolbachia* titres.

In vitro and *ex vivo* drug screening assays

MO *Di*L3 larvae were transferred onto MDCK monolayers and allowed to develop to 14- (early-mid L4) or 28 (mid-late L4)-day-old larvae. For comparative *ex vivo* assays, L4 stage larvae were recovered from male NSG mice 14 days post-infection and washed in sterile EMEM prior to the addition of drugs. All larval stages were plated into 12-well plates at densities of 3–5 larvae per well per drug concentration in 4 ml of EMEM with 10% FBS, 1% penicillin–streptomycin, 1% NEAAS, and 1% amphotericin B for drug screening assays. Moxidectin (Sigma-Aldrich, UK) was solubilised in phosphate-buffered saline (PBS, Fisher Scientific), and 10-fold serial dilutions ranging from 0.0001 to 100 μM were prepared in EMEM with 1% penicillin–streptomycin, 1% NEAAS, and 1% amphotericin B. Vehicle controls were included using the equivalent percentage PBS added to the cultures. Assays were incubated for 6 days in which larvae were continuously exposed to the drug at 37°C, 5% CO_2 and scored daily for motility and survival.

In vivo drug screening validation

Paired groups of 1–5 male NSG mice were subcutaneously inoculated with 200 *Di*L3 into the right flank on day 0. They were then randomized into treatment groups with a single subcutaneous dose of moxidectin prepared at 2.5 mg/kg in saline, or a saline-only control, in the nape of the neck on day 1. Mice were monitored daily for weight change and culled at day 14 to evaluate efficacy based on parasite recoveries. Alternatively, immediately following infection, groups of 4–6 mice were randomized into a 7-day oral regimen of doxycycline at 50 mg/kg prepared in ddH₂O followed by a 7-day washout period, and a 2-day oral bi-daily regime of AWZ1066S prepared in standard suspension vehicle (SSV; PEG300/propylene glycol/H₂O (55/25/20), or matching vehicle controls. Mice were monitored daily (weight and welfare) and culled between days 14 and 28 post-infection to evaluate parasitology, L4 length, and/or *Wolbachia* depletion using qPCR.

Wolbachia titer analysis

To assess *Wolbachia* titres across different developmental time points (2, 3, and 4 weeks post-infection), to compare *in vitro*-reared larvae in parallel to *in vivo* reared controls, and to investigate drug activity against *Wolbachia*, individual larvae were taken, and their DNA was extracted using previously published methods (Halliday et al., 2014). *Wolbachia* single copy *Wolbachia surface protein* (*wsp*) gene quantification was undertaken by qPCR using the following primer pair: F-TTGGTATTGGTGTTGGCGCA and R-AGCCAAAATAGCGAGCTCCA, under conditions used to determine *Brugia malayi wsp* copy numbers (Halliday et al., 2014).

Fluorescence *in situ* hybridization

Fluorescence *in situ* hybridization (FISH) was used for detecting *Wolbachia in Di*L3 and L4 larvae using two different DNA probes specific for *Wolbachia* 16S rRNA: W1—/5ATTO 590N/AATCCGGC-GARCCGACCC and W2—/5ATTO590N/C TTCTGTGAGTACCGTCATTATC, as previously described by Walker et al. (2021). L3 and L4 larvae were stored in 50% ethanol at room temperature until further processing. For FISH staining, frozen larvae were fixed using 4% paraformaldehyde (PFA) and incubated with 10 μg/ml pepsin for 10 min at 37°C. After a thorough wash using PBS, the samples were hybridized overnight in hybridization buffer with probes (or without probes for negative controls). Hybridisation buffer consisted of 50% formamide, 5×SCC, 0.1 M dithiothreitol (DTT), 200 g/L dextran sulfate, 250 mg/L poly(A), 250 mg/L salmon sperm DNA, 250 mg/L tRNA, and 0.5× Denhardt's solution. Larvae were then washed twice in 1×SSC and 0.1×SSC 10 Mm DDT before mounting with VECTASHIELD antifade mounting medium containing DAPI (4′,6-diamindio-2-phenylinole;Vector laboratories). L4 larvae were visualized using bright-field microscopy for length measurements, calculated using Fiji (ImageJ), USA. FISH-stained larvae were imaged using a Zeiss laser scanning confocal microscope, and changes in larval morphology were visualized using bright-field and DAPI nuclear staining.

Statistical analysis

Continuous data were tested for normality using the D'Agostino & Pearson omnibus Shapiro–Wilk normality tests. In case the data were skewed, non-parametric analyses were used to compare statistical differences between groups using Dunn's *post hoc* tests. In case the data passed the normality tests, Tukey's *post hoc* tests were applied. Categorical data were analyzed using Fisher's exact tests. Survival of larvae in culture (frequency motile vs. immotile) was evaluated using the log-rank (Mantel–Cox) test. Moxidectin/levamisole IC_{50} values were derived from the percentage of immotile larvae per drug concentration on day 6 of the assay. Non-linear curves were generated using the three-parameter least squares fit with [IC_{50}] calculated. All the tests were performed using GraphPad

Prism 9.1.2 software. Significance is indicated at or below alpha = 0.05.

Results

Selection of a susceptible mouse model of tissue-phase heartworm infection

NSG and RAG2γc mouse strains were initially selected to investigate permissiveness to *D. immitis* tissue-phase larval infections, based on our previous success in establishing long-term infections of the related filarial species, *Brugia malayi, Loa loa,* and *Onchocerca ochengi,* utilizing lymphopenic immunodeficient mice (Halliday et al., 2014; Pionnier et al., 2019). In these models, the additional knockout of the interleukin-2/7 common gamma chain within lymphopenic mice is essential for susceptibility to *L. loa* adult development in subcutaneous tissues and bolsters both *B. malayi* and *O. ochengi* adult infections within the peritoneal cavity (Pionnier et al., 2022). We also trialed methylprednisolone acetate (MPA) administrations to evaluate whether steroid suppression of residual innate immune responses could increase survival and yields of *D. immitis* larvae *in vivo,* as has been reported for experimental *Strongyloides stercoralis* infections (Patton et al., 2018). Initially, we used a Missouri (MO) isolate of *D. immitis* (NR-48907, provided by the NIH/NIAID Filariasis Research Reagent Resource Center, FR3, for distribution through BEI Resources). Infectious L3 were isolated 15 days after membrane feeding of *D. immitis* mf in dog blood to *A. aegypti* at LSTM, and infection experiments were undertaken at the University of Liverpool, UK (Figure 1A). Following inoculations of 200 L3 under the skin, at 14 days post-infection, we successfully recovered *D. immitis* parasites from subcutaneous and muscle fascia tissues in all (5/5) NSG and RAG2γc + MPA infected mice (Figure 1B). Multiple tissues were dissected to locate parasites (heart, lungs, peritoneal cavity, gastrointestinal tract, liver, and spleen), but no evidence of infection was found in these ectopic locations. Infection success was lower in NSG + MPA (3/4 mice) and RAG2γc (4/5) mouse groups. Yields significantly varied between groups with RAG2γc + MPA mice yielding higher numbers of *D. immitis* developing larvae (L4) compared with either RAG2γc or NSG + MPA groups (Kruskal–Wallis one-way ANOVA *P* = 0.0033 and Dunn's *post hoc* tests *P* < 0.05). Median recovery rates were similar between NSG and RAG2γc + MPA groups (median recovery 9 vs. 12%, ns).

Due to the simpler infection regimen in NSG mice, the international commercial availability of the model, the potential for further humanization, and the potential to avoid welfare or drug-drug interactions arising due to long-term MPA administrations, we selected this immunodeficient mouse model for extensive characterization. We evaluated the infection success and yields of *D. immitis* L4 across multiple independent experiments utilizing different batches of MO isolate *D. immitis* shipped from the US to the UK as mf in dog blood and passaged to the infectious L3 stage in *A. aegypti* mosquitoes (Figure 1C). In six independent experiments, using a total of 21 mice, we were reproducibly able to recover *D. immitis* larvae at 14 dpi (21/21 mice) with a 5% median yield of the initial 200 L3 infectious
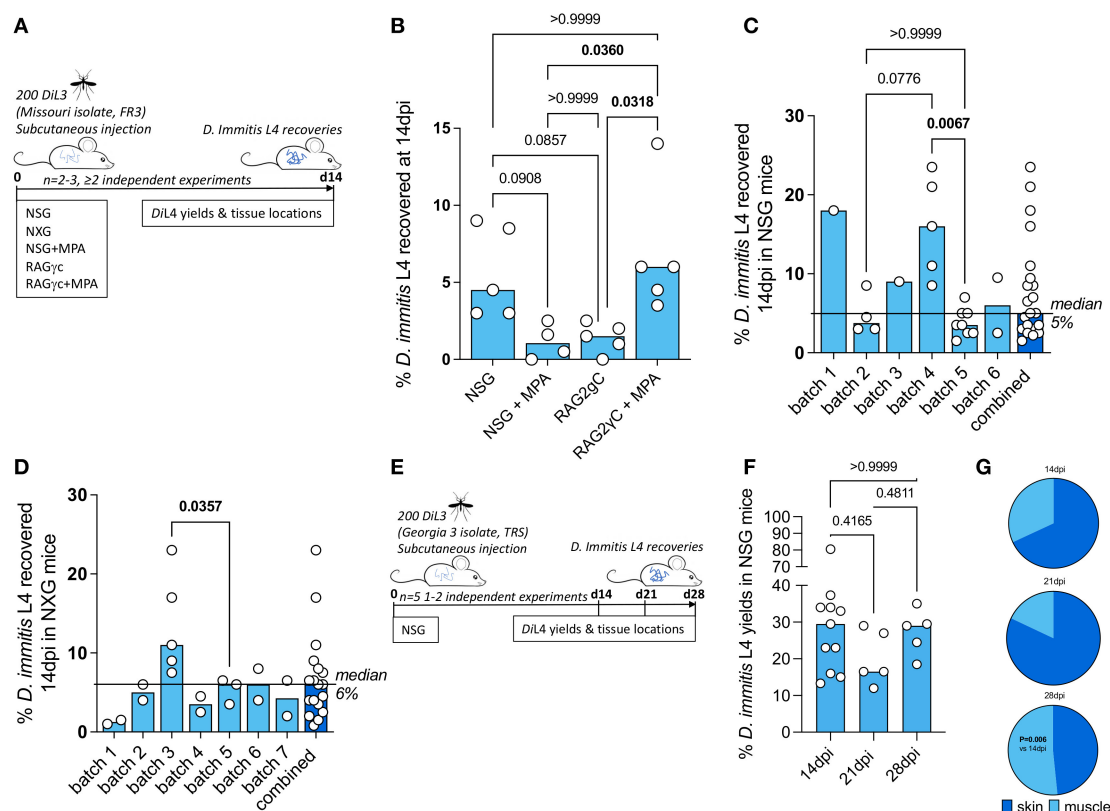
FIGURE 1

Susceptibility of compound immunodeficient mouse strains to *Dirofilaria immitis*. Experimental schematic using Missouri (MO) isolate *D. immitis* **(A)**. Percentage recovery of initial infectious load of *D. immitis* L4 at 14 days post-infection in indicated immunodeficient mice **(B–D)**. Experimental schematic using Georgia (GA)-III isolate *D. immitis* **(E)**. Percentage recovery of initial infectious load **(F)** and tissue distributions **(G)** of *D. immitis* L4 at indicated time points in NSG mice. Bars indicate median values with individual mouse data plotted. Significant differences were assessed by Kruskal–Wallis one-way ANOVA with Dunn's multiple comparison's tests except **(G)** where the difference in proportions was tested by Fisher's exact test. Significant differences (*P*-values < 0.05) are indicated in bold. Data are combined from two or more independent experiments **(B–D, F)** or individual experiments **(C, D, F)** with between 1 and 5 mice per group and per batch of L3 inoculated.

inoculate (range 1.5%−23.5%). In experiments where >2 mice were infected, we compared yields between batches and determined that batch-to-batch variability of the initial L3 infectious inoculate significantly influenced the yields of larvae recovered at 14 dpi in NSG mice (Kruskal–Wallis one-way ANOVA $P = 0.0017$ and Dunn's *post hoc* tests $P < 0.01$). We then measured recoveries utilizing NXG mice; a similar severe combined immunodeficient mouse line on the non-obese diabetic strain background with additional γc ablation developed independently and recently commercialized by Janvier Laboratories[2] (Figure 1D). As with the NSG mouse line, in seven independent experiments, with a total of 18 experimental mouse infections (run at LSTM/University of Liverpool), we consistently recovered developing larvae at 14 dpi (18/18 NXG mice) with a 6% median proportion of the initial 200 L3 infectious inoculate (range 1%−23%). Similar to NSG infections, in individual experiments where >2 NXG mice were available for analysis, batch-to-batch variability of the initial L3 infectious inoculate significantly influenced the yields of larvae recovered at 14 dpi (Mann–Whitney $P < 0.05$).

We then repeated experiments with NSG mice in TRS Labs (Georgia, USA), accessing an in-house parasite life cycle and using a unique "Georgia III" (GAIII) isolate of *D. immitis*. We infected batches of five mice and evaluated yields of L4 at 14, 21, or 28 days post-inoculation with 200 L3 (Figure 1E). All mice, irrespective of time point post-inoculation, yielded GAIII *D. immitis* developing larvae. Yields were six-fold higher on average than those derived at the LSTM laboratory at 14 days post-infection (median = 29.5%, range 13.3%−80.5%, Figure 1F). Yields did not significantly deviate between 14, 21, and 28 days post-infection (Figure 1F). However, the distribution of larvae in mouse tissues changed between 14 and 28 days post-infection, with relatively more larvae recovered in muscle tissues by 28 dpi ($P < 0.01$, Fisher's exact test, Figure 1G). These experiments demonstrate that lymphopenic mice with additional IL-2 gamma chain deficiency are susceptible to *D. immitis* tissue-stage infection with reproducible success using different isolates of heartworm in independent laboratories and when shipping larvae internationally between sites (details of which are summarized in Supplementary Table 1). Our time-course data indicate that tissue-phase heartworm larvae persist without significant decline in yields within NSG mice whilst initiating their natural migratory route

---

2   JANVIER (2019).

through subcutaneous and muscle tissues over the first 28 days of infection.

Mouse-derived developing larvae demonstrate superior morphogenesis, *Wolbachia* content, and reduced drug assay sensitivities compared with *in vitro* cultured *D. immitis*

Mosquito-derived infectious L3 larvae are traditionally utilized in serum-supplemented 37°C mammalian cultures to induce molting and morphogenesis into fourth-stage developing larvae (Lok et al., 1984; Devaney, 1985; Abraham et al., 1987). This technique has been utilized to study *D. immitis* larval biology and for applied applications such as biomarker and preventative drug discovery (Long et al., 2020; Hübner et al., 2021; Tritten et al., 2021). The survival of various filarial parasite life cycle stages can be extended when utilizing co-cultures with mammalian "feeder cell" monolayers or trans-well compartments (Townson et al., 1986; Evans et al., 2016; Zofou et al., 2018; Njouendou et al., 2019; Gandjui et al., 2021; Marriott et al., 2022). We, therefore, compared the survival and motility of MO isolate *D. immitis* larvae between cell-free and LL-MCK2 (monkey) or MDCK (dog) kidney cell co-cultures in 10% calf-serum cultures (Figure 2A). The 50% survival time of cell-free cultures was day 18, and subsequently, all larvae had died by day 28 in culture (Figure 2B). Conversely, co-cultures with both LL-MCK2 and MDCK cells significantly increased survival, whereby >80% of *D. immitis* larvae were viable up to day 28 ($P < 0.0001$, Mantel–Cox survival analysis). We noted a reduction in motility in all larval cultures after the first week in culture, which persisted to end point, apart from MDCK co-cultures which returned to full motility by day 32 in culture (Supplementary Figure 1). Selecting MDCK co-cultures as supportive of long-term larval motility and survival, we directly compared morphogenesis, growth, and *Wolbachia* endobacteria expansions between *in vitro*-propagated MO *D. immitis* larvae and MO larvae derived from NSG mouse infections at the 14-day time point (Figure 2A). Both *in vitro*- and *in vivo*-derived d14 *D. immitis* larvae displayed the blunted and widened anterior extremities characteristic of the L4 developmental stage (Orihel, 1961; Kotani and Powers, 1982), compared with the tapered, narrow anterior of filariform infectious L3 (Figure 2C). However, anterior morphogenesis was partially arrested *in vitro* compared with NSG mouse-derived larvae (Figure 2C). In the dog, larvae complete the L3–L4 molt rapidly, the vast majority by 3 days post-infection (Lichtenfels et al., 1985). In our cultures, ~50% of the day 14 L4 had completed molting, with cuticle casts evident in the culture media. The other ~50% of *in vitro* cultured larvae displayed partial molting of the third-stage cuticle (Figure 2C). There were obvious microscopic degenerative features of the *in vitro* larvae by day 14 compared with *in vivo* larvae, including malformed cuticle, hypodermis, buccal cavity, esophagus, and intestine (Figure 2C). Despite their high survival rate and continued motility, 14-day-old *in vitro*-propagated larvae were also significantly stunted compared with larvae derived from

NSG mice (mean = 1020 vs. 1880 μM, one-way ANOVA $F = 57.7$, $P < 0.0001$, Tukey's multiple comparisons test) and had not grown significantly in comparison with the L3 infectious stage (mean = 870 μm; Figure 2D). *Wolbachia* titer analysis using qPCR further highlighted disparities between *in vitro* and *in vivo* reared larvae (Figure 2E). The MO *D. immitis in vivo* larvae had undergone a significant, 66-fold average *Wolbachia* expansion during the 14-day NSG mouse (Figure 2E) infection in comparison with iL3 (median = 4.2×10^4 vs 6.2×10^2 *Wolbachia*/larva, Kruskal–Wallis one-way ANOVA 26.4, $P < 0.0001$ Dunn's multiple comparisons test), whereas MO larvae cultured for 14 days *in vitro* had failed to expand *Wolbachia* content (median = 8.7×10^2 *Wolbachia*/larvae).

Utilizing GAIII *D. immitis*, we further examined length and *Wolbachia* expansions between day 14 and day 28 post-infection in NSG mice (Figure 2F). GAIII L4 continued to grow in length between day 14, day 21, and day 28 post-infection in NSG mice (Figure 2G; means = 1,335, 1,713, and 2,211 μm, respectively, one-way ANOVA $F = 87.4$, $P < 0.05$–$P < 0.0001$, Tukey's multiple comparisons tests). Similarly, *Wolbachia* titres continued to expand within the NSG-derived GAIII *D. immitis* larvae (Figure 2H) with significant differences evident between day 14 and day 28 (median = 1.7×10^5 vs. 3.1×10^6 *Wolbachia*/larva, Kruskal–Wallis statistic = 8.5, $P < 0.05$ Dunn's multiple comparisons test). We corroborated qPCR *Wolbachia* data, visualizing that time-dependent *Wolbachia* multiplication was occurring within the hypodermal chord cell syncytia from a posterior to anterior direction in mouse-derived, but not *in vitro* cultured, *D. immitis* L4 specimens, utilizing fluorescent *in situ* hybridization (FISH) of *Wolbachia* 16S rRNA and confocal microscopy (Figure 2I). We then examined the *in vitro* vs. *ex vivo* paralytic susceptibilities of MO isolate *D. immitis* L4 following 6-day exposures to the standard preventative drug, moxidectin, using cultured L3-L4 larvae at 0–6 days, 15–21 days, or 28–35 days compared with NSG mouse L4 larvae isolated at 14 dpi and exposed to drug *ex vivo* between 15–21 days in matching culture conditions (Figure 2J). The IC_{50} concentrations inhibiting motility of *D. immitis* were 1.7 μM for 0–6 days L3–L4 larvae (Figure 2K). Sensitivity to moxidectin had increased in day 14–day 35 larvae with IC_{50} ranging between 300 and 330 nM (Figures 2L, M). In comparison, *ex vivo* larvae derived from mice were relatively insensitive to the *in vitro* paralytic activity of moxidectin with IC_{50} ranging between 48 and 66 μM (Figure 2N). This equated to a >28-fold decrease in moxidectin susceptibility compared with *D. immitis* L3–L4 cultures and >140-fold decreased sensitivity compared with long-term L4 cultures. We further examined relative paralytic susceptibilities of *D. immitis* MO *in vitro* vs. *ex vivo* L4 to 6-day exposures of the anthelmintic, levamisole, commencing at 15 days after iL3 culture/infection (Supplementary Figure 2). Whilst *in vitro* larvae were susceptible to high doses of levamisole (IC_{50} 13.2 μM), *ex vivo* L4 maintained full motility for 6 days in the presence of the top dose of the drug (100 μM). These data demonstrate the developmental superiority of *D. immitis* larvae derived from the subcutaneous and muscle tissues of NSG mice compared with standard *in vitro* cultures, reflected in a lowered sensitivity to moxidectin and levamisole when used in *ex vivo* drug titration assays.
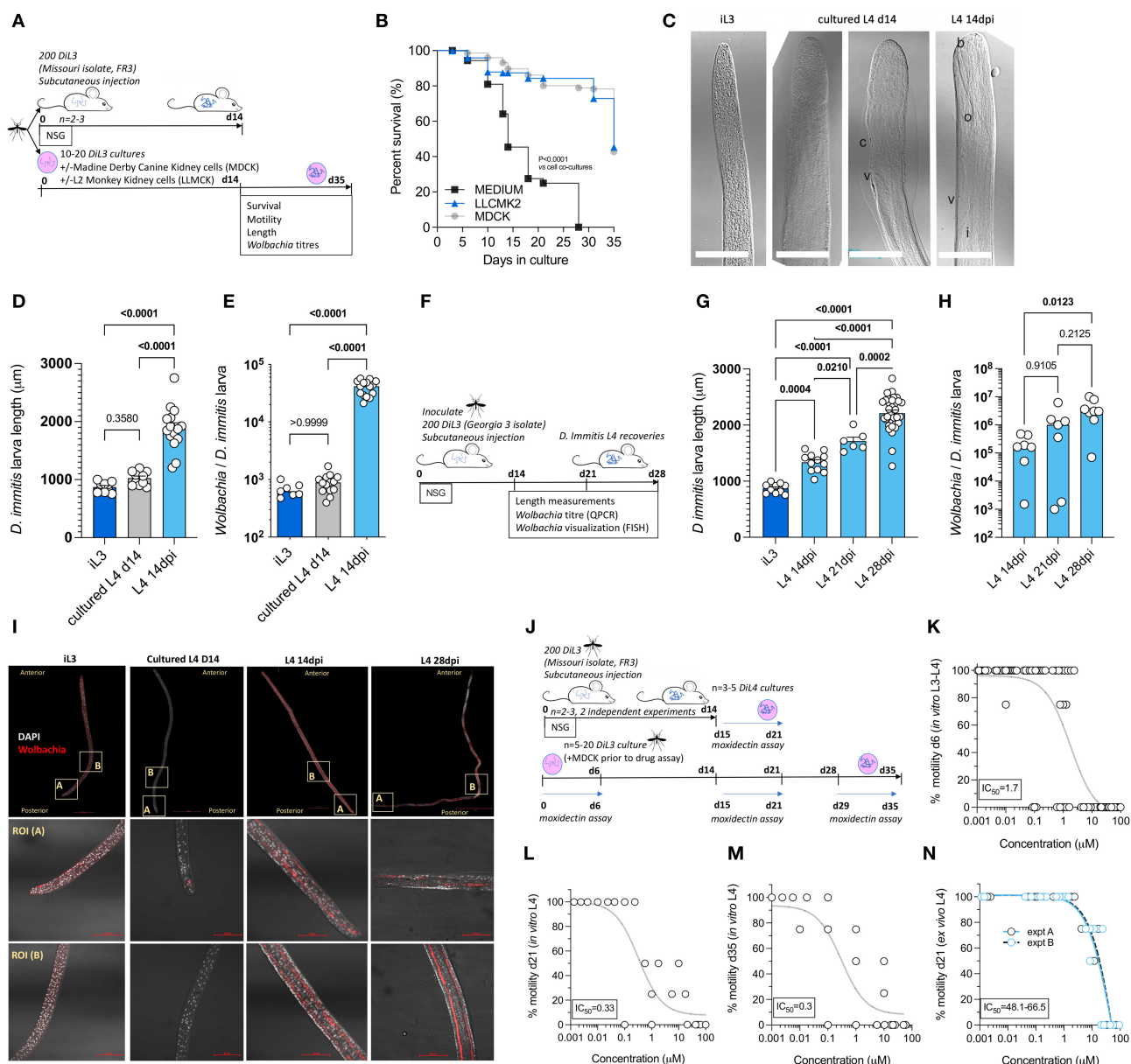
FIGURE 2

Comparative morphogenesis, *Wolbachia* expansions, and drug assay sensitivities of mouse-derived larvae compared with *in vitro* cultured *Dirofilaria immitis*. Experimental schematic using MO isolate *D. immitis* L3 **(A)**. Survival analysis of cultured larvae in indicated conditions **(B)** representative photomicrographs of iL3, d14 L4 cultures or L4 recovered from NSG mice at 14 dpi [**(C)**; b, buccal cavity; c, cuticle; i, intestine; o, esophagus; v, vulva, and scale bars = 50 μM]. Length **(D)** and *Wolbachia* content **(E)** of iL3, d14 L4 cultures or L4 recovered from NSG mice at 14 dpi. Experimental schematic using GAIII isolate *D. immitis* L3 **(F)**. Length **(G)** and *Wolbachia* content **(H)** of NSG mouse-derived L4 larvae at indicated time points. Representative FISH photomicrographs of iL3, d14 L4 cultures or L4 recovered from NSG mice at 14 or 28 dpi (*Wolbachia* 16SrRNA red, DAPI gray, scale bars = 50 μM) **(I)**. Experimental schematic of drug assays utilizing MO isolate *D. immitis* cultures or *ex vivo* larvae from NSG mice **(J)**. Moxidectin concentration *D. immitis* motility inhibition analysis after 6-day exposures when using cultured *D. immitis* for periods between 0 and 6 days L3/L4 **(K)**, 15–21 days L4 **(L)**, 28–35 days L4 **(M)**, or 15–21 days L4 derived from 14 dpi NSG mice **(N)**. In **(K–N)**, non-linear curves are three-parameter least squares fit with [IC$_{50}$] calculated in Prism 9.1.2. Bars represent mean ± SEM **(D, G)** or median **(E, H)** values with individual larva data plotted. Significant differences were determined by the Mantel−Cox log-rank tests **(B)**. One-way ANOVA with Tukey's multiple comparisons tests **(D, G)** or Kruskal−Wallis with Dunn's multiple comparisons tests **(E, H)**. Significant differences (*P*-values <0.05) are indicated in bold. Data are one individual experiment except **(N)** which is two independent experiments.

Dirofilaria immitis NSG or NXG mouse infections can be used to evaluate anti-*Wolbachia* drugs

Because we established rapid *Wolbachia* expansions occur during the L4 tissue development phase of *D. immitis* following infections of NSG or NXG mice, we next investigated the validity of these models as anti-*Wolbachia* drug screens. We initially infected batches of 4–6 NSG mice with MO isolate *D. immitis* iL3 and randomized animals into 7-day 50 mg/kg oral treatment with doxycycline or matching vehicle controls, commencing at infection with a further 7-day washout period to 14 dpi (Figure 3A).

FIGURE 3

Validation of *Dirofilaria immitis* NSG and NXG mouse models as *in vivo* anti-*Wolbachia* drug screening systems. Experimental schematic using MO or GAIII isolates of *D. immitis* L3 **(A)**. *Wolbachia* loads determined by qPCR on day 14 MO *D. immitis* larvae exposed to doxycycline **(B)** or AWZ1066S **(C)**. Length changes in day 14 MO *D. immitis* larvae exposed to doxycycline **(D)** or AWZ1066S **(E)**. *Wolbachia* loads determined by qPCR on day 14 GAIII *D. immitis* larvae exposed to doxycycline **(F)**. Visualization of *Wolbachia* depletion in hypodermis of day 14 GAIII *D. immitis* larvae exposed to doxycycline by FISH **(G)**. Length cha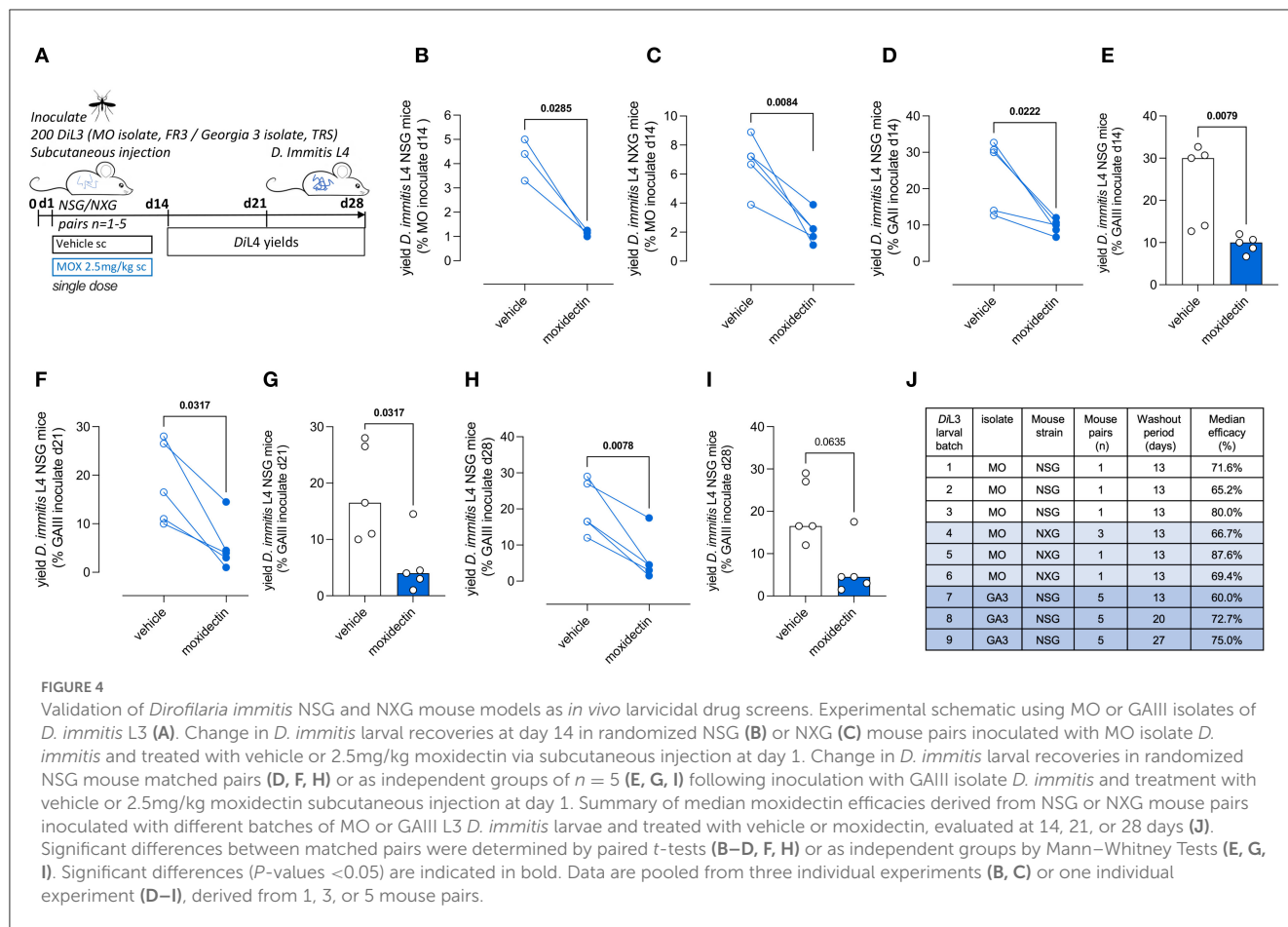nges in day 14 GAIII *D. immitis* larvae exposed to doxycycline **(H)**. Bars represent median **(B, C, F)** or mean ± SEM **(D, E, H)** values with individual larva data plotted. Significant differences were determined by Mann−Whitney tests **(B, C, F)** or unpaired Student's *t*-tests **(D, E, H)**. Significant differences (*P*-values <0.05) are indicated in bold. Data are one individual experiment with larvae derived from 2 to 5 NSG **(B, D, F, G)** or NXG **(C, E)** mice per group.

We selected this regimen and timing of dose based on proven significant depletion of *B. malayi* L3-L4 *Wolbachia in vivo* in a SCID mouse model (Jacobs et al., 2019). We subsequently randomized four NXG-infected mice into a 2-day bi-daily 200 mg/kg treatment of our fast-acting anti-*Wolbachia* azaquinazoline clinical candidate, AWZ1066S (Hong et al., 2019) or vehicle control, to compare relative anti-*Wolbachia* activity. Doxycycline treatment mediated a 70% median reduction in *Wolbachia* titres in day 14 MO *D. immitis* larvae when compared against vehicle control levels (0.29×10^4 vs. 9.5×10^4 *Wolbachia*/larva, Mann−Whitney test $P = 0.014$, Figure 3B). The short-course AWZ1066S 2-day oral treatment mediated a more profound 90% median efficacy in depletion of *Wolbachia* from day 14 MO *D. immitis* larvae (0.49×10^4 vs. $4.5 \times 10^{4-}$ *Wolbachia*/larva, Mann−Whitney test $P < 0.0001$, Figure 3C). The effect of *Wolbachia* depletion via doxycycline and AWZ1066S on larval growth was also evaluated (Figures 3D, E). We found that depletions of *Wolbachia* by 7-day doxycycline or 2-day AWZ1066S were associated with a 15.9 and 15.3% mean stunting effect on 14-day MO *D. immitis* larvae, which was significant for doxycycline treatment (Student's *t*-test, $P = 0.0182$). We repeated the validation of the *D. immitis* NSG mouse model as an anti-*Wolbachia* drug screening system

in an independent laboratory, utilizing GAIII isolate *D. immitis* (Figure 3A). In this dosing study, the 7-day oral regimen of doxycycline mediated a significant, 89% median depletion of *Wolbachia* in day 14 GAIII larvae (0.25×10^5 vs. 2.4×10^5 *Wolbachia*/larva, Mann−Whitney test, $P = 0.0098$, Figure 3F). We corroborated the clearance of *Wolbachia* from posterior hypodermal chord cells by FISH staining (Figure 3G). Stunting of GAIII *D. immitis* larvae was also apparent following 7-day doxycycline exposures in NSG mice (mean reduction in length 30%, Figure 3H). Together, these data demonstrate the utility of the *D. immitis* tissue-phase NSG or NXG mouse models to screen for the efficacy of oral anti-*Wolbachia* regimens *in vivo*.

Dirofilaria immitis NSG and NXG mouse infections can be used to evaluate preventative drug efficacy

Moxidectin is a front-line ML preventative used in various oral, topical, or injectable formulations as monthly, biannual, or annual heartworm prophylaxis in dogs (Savadelis et al., 2022). We

FIGURE 4
Validation of *Dirofilaria immitis* NSG and NXG mouse models as *in vivo* larvicidal drug screens. Experimental schematic using MO or GAIII isolates of *D. immitis* L3 **(A)**. Change in *D. immitis* larval recoveries at day 14 in randomized NSG **(B)** or NXG **(C)** mouse pairs inoculated with MO isolate *D. immitis* and treated with vehicle or 2.5mg/kg moxidectin via subcutaneous injection at day 1. Change in *D. immitis* larval recoveries in randomized NSG mouse matched pairs **(D, F, H)** or as independent groups of *n* = 5 **(E, G, I)** following inoculation with GAIII isolate *D. immitis* and treatment with vehicle or 2.5mg/kg moxidectin subcutaneous injection at day 1. Summary of median moxidectin efficacies derived from NSG or NXG mouse pairs inoculated with different batches of MO or GAIII L3 *D. immitis* larvae and treated with vehicle or moxidectin, evaluated at 14, 21, or 28 days **(J)**. Significant differences between matched pairs were determined by paired *t*-tests **(B–D, F, H)** or as independent groups by Mann–Whitney Tests **(E, G, I)**. Significant differences (*P*-values <0.05) are indicated in bold. Data are pooled from three individual experiments **(B, C)** or one individual experiment **(D–I)**, derived from 1, 3, or 5 mouse pairs.

selected a single high-dose subcutaneous injection of moxidectin (2.5 mg/kg) for the evaluation of larvicidal efficacy in NSG or NXG mice (emulating route of delivery and dose of long-acting injectable formulations of moxidectin in dogs). Matched pairs of mice were infected with batches of 200 *D. immitis* MO or GAIII isolate larvae, and the next day these were randomized into vehicle control or moxidectin treatment (Figure 4A). After 14 days post-infection (13 days post-treatment), we recorded 65%−80% reductions in MO *D. immitis* L4 in NSG mice (*n* = 3 pairs, *P* = 0.03, paired *t-test*, Figure 4B). A similar range of larvicidal efficacy was evident in NXG mice 14 days after infection with MO isolate *D. immitis* and treatment with a single injection of moxidectin (range 46%−88% *n* = 6 pairs, *P* = 0.008, Figure 4C). When using the GAIII isolate of *D. immitis* for NSG infections, the level of moxidectin efficacy ranged between 29 and 73%, evaluated at 14 days post-infection (*P* = 0.022, *n* = 5 pairs, Figure 4D). The availability of groups of five mice infected with the same batch of L3 allowed for unpaired group testing, rather than matched pairs, whereby the significance of moxidectin efficacy was confirmed (*P* = 0.008, Mann–Whitney Test, Figure 4E). We examined extended washout periods after moxidectin single dosing in NSG mice infected with GAIII *D. immitis*. At 21 days post-infection, the range of moxidectin efficacy was 45%−94% (*P* = 0.037, *n* = 5 paired analysis and Mann–Whitney tests Figures 4F, G) whilst at 28 days post-infection, efficacy ranged between 35 and 91% (*P* = 0.0078, *n* = 5 paired analysis, *P* = 0.064, Mann–Whitney tests, Figures 4H, I). The

median efficacy for all studies is shown in Figure 4J. In summary, a single injection of moxidectin delivered a median efficacy between 65 and 80% at 2 weeks in NSG/NXG mice infected with MO isolate, and 60%, 73%, and 75% efficacy at 2, 3, or 4 weeks in NSG infected with GAIII isolate (Figure 4J). All mice in the drug studies displayed typical behavior and gained weight over the 2- to 4-week period of infection and dosing (Supplementary Figure 3).

Discussion

We have determined that ablation of both the B and T lymphocyte compartments and additional cytokine signaling via the IL-2/7 common gamma chain receptor in mice allows permissiveness to *D. immitis* tissue-phase larval development for at least the first 28 days of infection. This confirms the study of Hess et al. (2023) who recently reported the NSG strain as a *D. immitis* mouse model but also highlights that other commercially available mouse strains with similar deficiencies (NXG and BALB/c RAG2$^{-/-}$γc$^{-/-}$) are susceptible to *D. immitis* tissue-phase L4 infections. A polarized type-2 adaptive immune response with associated type-2 tissue macrophage activation leads to eosinophil entrapment and degranulation as the basis of immune-mediated filarial larvicidal activity in mice (Specht et al., 2006; Turner et al., 2018; Pionnier et al., 2020; Ehrens et al., 2021). However, experimental infections with *B. malayi, L. sigmodontis,* and *O.*

ochengi in lymphopenic mouse strains (SCID/RAG2$^{-/-}$) with additive γc gene ablations have illustrated bolstered chronic susceptibility (Layland et al., 2015; Pionnier et al., 2022), whilst in *L. loa* subcutaneous infections, only combination of lymphopenia and γc deficiency is sufficient to allow permissiveness to adult infections (Pionnier et al., 2019). Thus, an additional layer of innate immune resistance operates which can reduce or eliminate establishing larval filarial infections. In *B. malayi* infections, p46$^+$ NK cells with an activated/memory phenotype and residual eosinophilia are implicated in the innate immune resistance to chronic infection in RAG2$^{-/-}$ mice (Pionnier et al., 2022), whereas in *Litomosoides* infections, CD45$^-$/TCRβ$^-$/CD90.2$^+$/Sca-1$^+$/IL-33R$^+$/GATA-3$^+$ type-2 innate lymphoid cells (ILC2) are required for innate immune resistance to microfilarial blood infections (Reichwald et al., 2022). It remains to be determined which of these multiple innate and adaptive immune processes are operating to control the larval establishment of *D. immitis* in mice. Because we detected increases in *D. immitis* larval burdens in NOD.SCID- vs. BALB/c RAG2$^{-/-}$-γc$^{-/-}$ mice which could be improved by steroid treatments in the latter model, this may indicate residual innate immune differences between background strains. For instance, NOD mice are deficient in complement humoral immunity due to a 2-bp deletion in the haemolytic complement (Hc) gene, which encodes the C5 complement protein (Verma et al., 2017). Our models now afford an opportunity for reconstitution of innate or adaptive immune cell types and humoral immune components to dissect the mechanisms of immunity to *D. immitis* migrating larvae, as has recently been attempted for *L. sigmodontis* with CD4$^+$ T cell transfers into RAG2$^{-/-}$γc$^{-/-}$ mice (Wiszniewsky et al., 2021). This application may be useful in determining minimally sufficient immune pathways necessary to mediate sterilizing immunity. Similarly, the new *D. immitis* mouse models may be valuable in evaluating the efficacy of neutralizing sub-unit vaccine target antibody responses (e.g. via passive transfer of purified specific antibodies or isolated B-cell clones adoptively transferred from immunocompetent NOD mice).

Our initial evaluations of immunodeficient mouse susceptibility utilized MO isolate *D. immitis* mf shipped from the FR3 repository, Athens, USA, to Liverpool, UK, before being reared to infectious stage L3s within Liverpool Strain *A. aegypti*. Following the selection of the NSG and NXG mouse lines for further evaluations, when we repeated experiments in an independent laboratory (TRS, Georgia) with NSG mice infected with an on-site *A. aegypti* generated GAIII isolate of *D. immitis,* the yields of L4 at 2 weeks were improved on average by ~six-fold. The latter yields were more in line with those achieved by Hess et al. (2023) (16%−29% recoveries), utilizing the FR3 MO isolate whereby L3s were generated locally. We currently do not know the factor or factors causing variable susceptibility between laboratories, but they could include the impact of international shipping of mf, disparities in L3 larval infectivity following passage in different colonies of mosquitoes, or variances in the maintenance of immunodeficient mice between facilities altering host microbiome and modifying host innate response to infection. Because we recorded significant batch-to-batch variability in L3 inoculations in terms of L4 recovered at 14 days, the quality of infectious stage L3 produced by mosquito colonies is likely to be

a major influencing factor, and experiments should be carefully controlled to account for this potential source of batch variation.

We evaluated that *D. immitis* larval parasitism and development in immunodeficient mice accurately tract the natural course of infection in definitive hosts over the 1st month. All larvae were recovered from the subcutaneous tissues and muscle fascia, in line with previous observations of natural parasite locations in both ferret and dog infections of *D. immitis* at this time interval (Orihel, 1961; Supakorndej et al., 1994). We demonstrate that *in vivo* larvae complete cuticle molting and undergo 4th stage larval morphogenesis. L4 growth lengths in NSG or NXG mice were within the range of those prior documented in dog and ferret infections at matching point of infection, at 14–15 days (NSG = 1.2–2.8 mm, NXG = 1.2–2.5 mm, dog = 1.7–2.2 mm, ferret = 1.6–2.7 mm) (Orihel, 1961; Supakorndej et al., 1994). These lengths also emulate those recently reported (1.5–1.8 mm) after 14 days of infection of NSG mice by Hess et al. (2023).

We also demonstrate that *D. immitis* expand *Wolbachia* titres significantly during parasitism of NSG or NXG mice. From PCR analysis, we ascertain that *Wolbachia* are doubling approximately every 42 h for MO isolate to every 55 h for GAIII isolate over the first 14-day infection time-course of *D. immitis* L3–L4 larvae *in vivo*. This is the first record of early *Wolbachia* expansions in *D. immitis* developing larvae and is comparatively slower compared with the average doubling time (32 h) over the first 14 days of L3–L4 development *in vivo* for the human filariae, *B. malayi* (McGarry et al., 2004). The establishment of *D. immitis* mouse models now allows for tractable comparative endosymbiotic biology of this clade C nematode *Wolbachia* (also found in the causative agent of river blindness, *O. volvulus*) vs. the clade D *Wolbachia* of human lymphatic filariae, most commonly used in basic and applied nematode *Wolbachia* research.

Before the establishment of *D. immitis* immunodeficient mouse models, a ready source of *in vivo D. immitis* L4 propagations for onward "*ex vivo*" basic and translational research has been unavailable. Mosquito stage L3 can be induced to molt rapidly into the early L4 stage, with as much as 95% molting success, and survive for 3 weeks in calf serum–supplemented cultures (Abraham et al., 1987). We recapitulated this early L4 morphogenesis and improved L4 longevity to >1 month in culture if larvae were co-cultured with dog or monkey kidney cells. However, comparisons with *in vivo* reared larvae highlighted several defects in growth, incomplete morphogenesis, and, most strikingly, an almost complete failure to expand *Wolbachia* endosymbiont titres. Therefore, the failure of larvae to thrive *in vitro* may be linked with a deficit in *Wolbachia*-produced haem, riboflavin, nucleotides, or other biosynthetic pathways identified as relevant in the *Wolbachia*–nematode symbiosis (Lefoulon et al., 2020). Whether environmental cues are lacking *in vitro* for *Wolbachia* expansion is currently not known. Sub-optimal neo-glucogenesis in cultured *D. immitis* larvae could lower available carbon energy sources necessary for *Wolbachia* expansion (Voronin et al., 2019). Alternatively, because autophagic induction in filariae regulates *Wolbachia* populations residing within host vacuoles (Voronin et al., 2012), failure of *Wolbachia* growth may be the result of starvation/stress in culture-inducing autophagy. Certainly, filarial stress responses are demonstrably

upregulated in *ex vivo* adult worm culture systems (Ballesteros et al., 2016).

We demonstrate that the use of sub-optimal L3/L4 grown *in vitro* for pharmacological screening leads to significantly >28-fold increased sensitivities to the paralytic activities of two nematodicidal agents, namely moxidectin and levamisole, compared with larvae of the same age derived from NSG or NXG mouse infections. Our data are currently limited to comparisons of two drugs, and more evaluations are required to determine how consistently *ex vivo* vs. *in vitro* larvae diverge in terms of drug sensitivity. However, our data suggest that a reliance on *in vitro* larvae may lead to artificial sensitivities to new preventatives in development and thus might lead to incorrect selection of candidates or dose levels for *in vivo* preclinical evaluations with consequences for incorrect cat and dog usage. The mouse models now afford a facile method of generating more physiologically relevant L4 larvae which should offer more accurate pharmacological assessments prior to a decision to advance into *in vivo* preclinical screening justifying protected animal use.

Our data determining the failure of *Wolbachia* to expand *in vitro* within *D. immitis* developing larvae preclude the use of cultured L3/L4 in evaluating the activities of novel anti-*Wolbachia* compounds. We thus demonstrate the utility of the NSG and NXG mouse models as an *in vivo* anti-*Wolbachia* drug screen. L4 larvae could be reproducibly depleted of *Wolbachia* using a 7-day regimen of the established anti-*Wolbachia* antibiotic, doxycycline, with confirmatory experiments run in an independent laboratory with a different *D. immitis* isolate. The levels of anti-*Wolbachia* efficacy we observed (70%−89%) are aligned to those measured against *B. malayi* day 14 larval *Wolbachia* following identical doxycycline regimen treatment of infected CB.17 SCID mice (76%) (Jacobs et al., 2019). Excitingly, we demonstrate that a 2-day *in vivo* treatment with the novel investigational azaquinazoline drug, AWZ1066S, is a rapid and profound *D. immitis Wolbachia* depleting agent with 90% efficacy achieved. This benchmark of 90% efficacy has been determined as clinically relevant in terms of sustained *Wolbachia* reductions and subsequent long-term anti-parasitic activities in human filariasis clinical trials (Johnston et al., 2021). The unique rapid activity of AWZ1066S has been previously determined through time-kill assays with *B. malayi Wolbachia,* whereby a near maximum kill rate can be achieved with 1-day exposure compared with 6 days for standard classes of antibiotics, including tetracyclines (Hong et al., 2019). Thus, azaquinazolines or other novel anti-*Wolbachia* chemistry with similar rapid killing activity, as identified in high-throughput industrial screening (Clare et al., 2019), might hold promise as new heartworm preventative or curative candidates and now can be triaged for activity utilizing our novel *D. immitis* mouse models.

We used a high single parenteral dose of moxidectin, mimicking extended-release formulations used in dogs (Savadelis et al., 2022), to evaluate the *D. immitis* NSG and NXG mouse models as a preventative drug screen. We demonstrated, using multiple batches of different ML-susceptible *D. immitis* isolates, in different evaluating laboratories, that injected moxidectin mediated significant 65%−89% reductions in larvae assessed between 13 and 27 days post-exposure. Hess et al. also measured ivermectin

and moxidectin responses in infected NSG mice following oral doses ranging between 0.001 and 3mg/kg given on days 0, 15, and 30 post-infection (Hess et al., 2023). Their studies determine that the MO isolate and an ivermectin-resistant JYD-34 isolate of *D. immitis* were equally sensitive to moxidectin with high but incomplete efficacy demonstrable after 0.01 mg/kg dosing. They also show high levels of ivermectin efficacy against the MO, but not JYD-34 isolate, in dose titrations ranging between 0.01 and 3 mg/kg. Thus, we conclude *D. immitis* NSG and NXG models are robustly validated by multiple independent laboratories as screening tools for assessing direct-acting nematodicidal agents over at least a 28-day infection window. Our *ex vivo* and *in vivo* drug response evaluations of *D. immitis* L3/L4 in NSG or NXG mice demonstrate the flexibility to establish this model in independent laboratories with different commercially available NSG or NXG lines. Furthermore, we determine feasibility of international shipping of live mf in dog blood to produce L3s for onward experimental infections in lymphopenic mice. Mouse infections utilizing shipped L3s may allow for increased accessibility to expand experimental *D. immitis* research out of the few specialist reference centers which maintain the full life cycle of the parasite and/or the mosquito vector.

Main limitations of our study are (1) lack of data on full permissiveness to adult infections within murine cardiopulmonary vasculature, (2) lack of validation within female lymphopenic mice, and (3) <100% achievable moxidectin preventative efficacy response. In Hess et al., evaluation periods were extended and, whilst larvae continued to grow and mature within NSG mice, a divergence in growth compared with comparative dog studies was apparent after the 1st month of infection. Furthermore, there was no evidence of immature adults arriving in the heart and lungs by 15 weeks (Hess et al., 2023). The authors conclude either physiological or anatomical deficiencies may prevent the full development of *D. immitis* in mice. However, full development of the highly-related subcutaneous filaria, *Loa loa,* is possible in both NSG and RAG2$^{-/-}$γc$^{-/-}$ mice after 5–6 months (Pionnier et al., 2019), and thus, it remains to be tested whether full *D. immitis* development may be achieved over an extended time frame. We selected the use of male mice due to observations that even in immunodeficient systems (Rajan et al., 1994), as well as in outbred gerbils (Ash, 1971), male-biased sex-specific susceptibility is a feature of rodent filarial infections. For future pharmacological investigations, to fully enable the characterization of interactions between sex and the drug pharmacokinetic–pharmacodynamic (PK-PD) relationship, it would be useful to assess whether *D. immitis* are able to develop within female lymphopenic mouse strains. In natural hosts, injectable formulations of moxidectin are proven to mediate 100% preventative efficacies (Savadelis et al., 2022). The substantial yet incomplete moxidectin responses in our NSG and NXG *D. immitis* models may reflect that complete efficacy evolves over an extended time period, particularly considering that ML can depot in fatty subcutaneous tissues to deliver a long-tail of systemic exposure, detectable over 1 month (Al-Azzam et al., 2007; Arisov et al., 2019). Alternatively, an immunopharmacological mode of action involving decreased immunosuppressive secretions and an activated host-immune response has been proffered as one rationale why filarial larvae are differentially sensitive to ML

drugs at physiological levels *in vitro* vs. *in vivo* (Moreno et al., 2010). Thus, we currently cannot rule out a potential synergy with adaptive immune-mediated responses (such as the development of opsonising or neutralizing antibodies) contributing to the complete efficacy of moxidectin. As previously discussed, passive transfer of antibodies into lymphopenic mice may determine whether such a mechanism contributes to ML preventative efficacy at physiologically relevant dose levels.

It is widely accepted that the use of specially protected, highly sentient species in preclinical research, including cats and dogs, should be strictly minimized wherever possible. This has not been plausible for veterinary heartworm preventative R&D due to a lack of a tractable small animal laboratory model. Typical drug screening has relied on *in vitro* potency testing against *D. immitis* larvae, potentially combined with initial preclinical evaluation in a surrogate rodent filarial infection model, before deciding to proceed into experimental dog infection challenge studies. Vulnerabilities of this approach include differential drug sensitivities between larvae being tested *in vitro* vs. *in vivo*, differences in filarial species larval migration routes/parasitic niches, and variability in drug target expression/essentiality across different filarial parasite species and life cycle stages, all of which may drive artifactual efficacy information. Our models, with the international commercial supply of lymphopenic strains and shipping of mf or L3 from donating laboratories, provide universal access to accurate and facile PK-PD assessments of preventative *D. immitis* drug candidate responses against the prophylactic L3–L4 larval target. Evaluations of drug larvicidal activities over the 1st month of infection, whilst larvae are developing in subcutaneous and muscle tissue, allow for rapid assessments whilst avoiding the risk of welfare issues associated with the arrival of adult parasites in the cardiovascular system. We observed no overt welfare issues in mice after parasitism, with mice gaining weight and displaying typical behavior. If adopted, our models should accelerate drug research timelines and enable more precise dose-fractionation studies for clinical selection into cat or dog studies. We conclude that *D. immitis* immunodeficient mouse models are preliminarily established for more efficient heartworm drug discovery which may, in the future, reduce the requirements for long-term cat and dog experimentation with the risk to cause severe harm, in line with an ethos of "replacement, refinement, and reduction" of animals in scientific research.

Data availability statement

The original contributions presented in the study are included in the article/Supplementary material, further inquiries can be directed to the corresponding author.

Ethics statement

The study protocols were approved in the UK by LSTM & University of Liverpool Animal Welfare and Ethics Review Boards and licensed by the UK Home Office Animals in Science Regulation Unit. In the USA, studies were approved by TRS Institutional Animal Care and Use Committee.

Author contributions

JT: conceptualization. AMar and JD: data curation. AMar, JD, SH, and JT: formal analysis. MT and JT: funding acquisition. AMar, JD, SH, AS, CF, UD, AMan, CW, and EC: investigation. AMar, JD, and SH: methodology. JT, AMo, SM, and JM: project administration. FG, SW, WH, PO'N, MT, and JT: resources. AMar, JD, and JT: writing—original draft. AMar, JD, CF, JM, SM, AMo, and JT: writing—reviewing and editing. All authors contributed to the article and approved the submitted version.

Conflict of interest

CF, UD, AMan, SM, and JM are employed by TRS Laboratories Inc. FG is employed by Eisai Global Health.

The remaining authors declare that the research was conducted in the absence of any commercial or financial relationships that could be construed as a potential conflict of interest.

Publisher's note

All claims expressed in this article are solely those of the authors and do not necessarily represent those of their affiliated organizations, or those of the publisher, the editors and the reviewers. Any product that may be evaluated in this article, or claim that may be made by its manufacturer, is not guaranteed or endorsed by the publisher.

Supplementary material

The Supplementary Material for this article can be found online at: https://www.frontiersin.org/articles/10.3389/fmicb.2023.1208301/full#supplementary-material

References

Abraham, D., Mok, M., Mika-Grieve, M., and Grieve, R. B. (1987). *In vitro* culture of *Dirofilaria immitis* third- and fourth-stage larvae under defined conditions. *J. Parasitol.* 73, 377–383. doi: 10.2307/3282093

AHS (2016). *Heartworm by the Numbers*. Available online at: https://www.heartwormsociety.org/resources/vet/infographics/633-heartworm-by-the-numbers (accessed June 11, 2023).

Al-Azzam, S. I., Fleckenstein, L., Cheng, K. J., Dzimianski, M. T., and McCall, J. W. (2007). Comparison of the pharmacokinetics of moxidectin and ivermectin after oral administration to beagle dogs. *Biopharm. Drug Dispos.* 28, 431–438. doi: 10.1002/bdd.572

Arisov, M. V., Indyuhova, E. N., and Arisova, G. B. (2019). Pharmacokinetics of combination antiparasitic drug preparation for dogs and cats in the form of spot-on solution. *J. Adv. Vet. Anim. Res.* 6, 25–32. doi: 10.5455/javar.2019.f308

Ash, L. R. (1971). Preferential susceptibility of male jirds (*Meriones unguiculatus*) to infection with Brugia pahangi. *J. Parasitol.* 57, 777–780. doi: 10.2307/3277796

Ballesteros, C., Tritten, L., O'Neill, M., Burkman, E., Zaky, W. I., Xia, J., et al. (2016). The Effect of *in vitro* cultivation on the transcriptome of adult *Brugia malayi*. PLoS Negl. Trop. Dis. 10, e0004311. doi: 10.1371/journal.pntd.0004311

Cancrini, G., and Kramer, L. H. (2001). "Insect vectors of *Dirofilaria* spp.," in *Heartworm Infection in Humans and Animals*, eds F. Simon, and C. Genchi (Salamanca:Universidad Salamanca), 63–82.

Clare, R. H., Bardelle, C., Harper, P., Hong, W. D., Börjesson, U., Johnston, K. L., et al. (2019). Industrial scale high-throughput screening delivers multiple fast acting macrofilaricides. *Nat. Commun.* 10, 11. doi: 10.1038/s41467-018-07826-2

Devaney, E. (1985). *Dirofilaria immitis*: the moulting of the infective larva *in vitro*. *J. Helminthol.* 59, 47–50. doi: 10.1017/S0022149X00034477

Ehrens, A., Lenz, B., Neumann, A. L., Giarrizzo, S., Reichwald, J. J., Frohberger, S. J., et al. (2021). Microfilariae trigger eosinophil extracellular DNA traps in a dectin-1-dependent manner. *Cell Rep.* 34, 108621. doi: 10.1016/j.celrep.2020.108621

Evans, H., Flynn, A. F., and Mitre, E. (2016). Endothelial cells release soluble factors that support the long-term survival of filarial worms *in vitro*. *Exp. Parasitol.* 170, 50–58. doi: 10.1016/j.exppara.2016.08.004

Gandjui, N. V. T., Njouendou, A. J., Gemeg, E. N., Fombad, F. F., Ritter, M., Kien, C. A., et al. (2021). Establishment of an *in vitro* culture system to study the developmental biology of Onchocerca volvulus with implications for anti-Onchocerca drug discovery and screening. *PLoS Negl. Trop. Dis.* 15, e0008513. doi: 10.1371/journal.pntd.0008513

Genchi, C., and Kramer, L. (2017). Subcutaneous dirofilariosis (*Dirofilaria repens*): an infection spreading throughout the old world. *Parasit. Vectors* 10, 517. doi: 10.1186/s13071-017-2434-8

Halliday, A., Guimaraes, A. F., Tyrer, H. E., Metuge, H. M., Patrick, C. N., Arnaud, K. O., et al. (2014). A murine macrofilaricide pre-clinical screening model for onchocerciasis and lymphatic filariasis. *Parasit. Vectors* 7, 472. doi: 10.1186/s13071-014-0472-z

Hess, J. A., Eberhard, M. L., Segura-Lepe, M., Grundner-Culemann, K., Kracher, B., Shryock, J., et al. (2023). A rodent model for *Dirofilaria immitis*, canine heartworm: parasite growth, development, and drug sensitivity in NSG mice. *Sci. Rep.* 13, 976. doi: 10.1038/s41598-023-27537-z

Hong, W. D., Benayoud, F., Nixon, G. L., Ford, L., Johnston, K. L., Clare, R. H., et al. (2019). AWZ1066S, a highly specific anti-*Wolbachia* drug candidate for a short-course treatment of filariasis. *Proc. Natl. Acad. Sci. USA.* 116, 1414–1419. doi: 10.1073/pnas.1816585116

Hübner, M. P., Townson, S., Gokool, S., Tagboto, S., Maclean, M. J., Verocai, G. G., et al. (2021). Evaluation of the *in vitro* susceptibility of various filarial nematodes to emodepside. *Int. J. Parasitol. Drugs Drug Resist.* 17, 27–35. doi: 10.1016/j.ijpddr.2021.07.005

Jacobs, R. T., Lunde, C. S., Freund, Y. R., Hernandez, V., Li, X., Xia, Y., et al. (2019). Boron-pleuromutilins as anti-*Wolbachia* agents with potential for treatment of onchocerciasis and lymphatic filariasis. *J. Med. Chem.* 62, 2521–2540. doi: 10.1021/acs.jmedchem.8b01854

Jacobson, L. S., and DiGangi, B. A. (2021). An accessible alternative to melarsomine: "moxi-doxy" for treatment of adult heartworm infection in dogs. *Front. Vet. Sci.* 8, 702018. doi: 10.3389/fvets.2021.702018

JANVIER (2019). *NXG Immunodeficient Mouse*. France: Le Genest-Saint-Isle. Available online at: https://janvier-labs.com/en/fiche_produit/1-nxg-immunodeficient-mouse/ (accessed June 11, 2023).

Johnston, K. L., Hong, W. D., Turner, J. D., O'Neill, P. M., Ward, S. A., Taylor, M. J., et al. (2021). Anti-*Wolbachia* drugs for filariasis. *Trends Parasitol.* 37, 1068–1081. doi: 10.1016/j.pt.2021.06.004

Kotani, T., and Powers, K. G. (1982). Developmental stages of *Dirofilaria immitis* in the dog. *Am. J. Vet. Res.* 43, 2199–2206.

Layland, L. E., Ajendra, J., Ritter, M., Wiszniewsky, A., Hoerauf, A., Hübner, M. P., et al. (2015). Development of patent Litomosoides sigmodontis infections in semi-susceptible C57BL/6 mice in the absence of adaptive immune responses. *Parasit. Vectors* 8, 396. doi: 10.1186/s13071-015-1011-2

Lefoulon, E., Clark, T., Guerrero, R., Cañizales, I., Cardenas-Callirgos, J. M., Junker, K., et al. (2020). Diminutive, degraded but dissimilar: *Wolbachia* genomes from filarial nematodes do not conform to a single paradigm. *Microb. Genom.* 6, mgen000487. doi: 10.1099/mgen.0.000487

Lichtenfels, J. R., Pilitt, P. A., Kotani, T., and Powers, K. G. (1985). *Morphogenesis of Developmental Stages of Dirofilaria immitis (Nematoda) in the Dog*. Mexico: Universidad Nacional Autonoma de Mexico.

Litster, A. L., and Atwell, R. B. (2008). Feline heartworm disease: a clinical review. *J. Feline Med. Surg.* 10, 137–144. doi: 10.1016/j.jfms.2007.09.007

Lok, J. B., Mika-Grieve, M., Grieve, R. B., and Chin, T. K. (1984). *In vitro* development of third- and fourth-stage larvae of *Dirofilaria immitis*: comparison of basal culture media, serum levels and possible serum substitutes. *Acta Trop.* 41, 145–154.

Long, T., Alberich, M., André, F., Menez, C., Prichard, R. K., Lespine, A., et al. (2020). The development of the dog heartworm is highly sensitive to sterols which activate the orthologue of the nuclear receptor DAF-12. *Sci. Rep.* 10, 11207. doi: 10.1038/s41598-020-67466-9

Marriott, A. E., Furlong Silva, J., Pionnier, N., Sjoberg, H., Archer, J., Steven, A., et al. (2022). A mouse infection model and long-term lymphatic endothelium co-culture system to evaluate drugs against adult *Brugia malayi*. *PLoS Negl. Trop. Dis.* 16, e0010474. doi: 10.1371/journal.pntd.0010474

McCall, J. W., Genchi, C., Kramer, L. H., Guerrero, J., and Venco, L. (2008). Heartworm disease in animals and humans. *Adv. Parasitol.* 66, 193–285. doi: 10.1016/S0065-308X(08)00204-2

McGarry, H. F., Egerton, G. L., and Taylor, M. J. (2004). Population dynamics of *Wolbachia* bacterial endosymbionts in Brugia malayi. *Mol. Biochem. Parasitol.* 135, 57–67. doi: 10.1016/j.molbiopara.2004.01.006

Morchón, R., Carretón, E., González-Miguel, J., and Mellado-Hernández, I. (2012). Heartworm disease (*Dirofilaria immitis*) and their vectors in europe - new distribution trends. *Front. Physiol.* 3, 196. doi: 10.3389/fphys.2012.00196

Moreno, Y., Nabhan, J. F., Solomon, J., Mackenzie, C. D., and Geary, T. G. (2010). Ivermectin disrupts the function of the excretory-secretory apparatus in microfilariae of *Brugia malayi*. *Proc. Natl. Acad. Sci. USA.* 107. doi: 10.1073/pnas.1011983107

Mwacalimba, K., Amodie, D., Swisher, L., Moldavchuk, M., Brennan, C., Walther, C., et al. (2021). Pharmacoeconomic analysis of heartworm preventive compliance and revenue in veterinary practices in the United States. *Front. Vet. Sci.* 8, 602622. doi: 10.3389/fvets.2021.602622

Njouendou, A. J., Kien, C. A., Esum, M. E., Ritter, M., Chounna Ndongmo, W. P., Fombad, F. F., et al. (2019). *In vitro* maintenance of *Mansonella perstans* microfilariae and its relevance for drug screening. *Exp. Parasitol.* 206, 107769. doi: 10.1016/j.exppara.2019.107769

Noack, S., Harrington, J., Carithers, D. S., Kaminsky, R., and Selzer, P. M. (2021). Heartworm disease - Overview, intervention, and industry perspective. *Int. J. Parasitol. Drugs Drug Resist.* 16, 65–89. doi: 10.1016/j.ijpddr.2021.03.004

Orihel, T. C. (1961). Morphology of the larval stages of *Dirofilaria immitis* in the dog. *J. Parasitol.* 47, 251–262. doi: 10.2307/3275301

Patton, J. B., Bonne-Année, S., Deckman, J., Hess, J. A., Torigian, A., Nolan, T. J., et al. (2018). Methylprednisolone acetate induces, and Δ7-dafachronic acid suppresses. *Proc. Natl. Acad. Sci. USA.* 115, 204–209. doi: 10.1073/pnas.1712235114

Pionnier, N., Furlong-Silva, J., Colombo, S. A. P., Marriott, A. E., Chunda, V. C., Ndzeshang, B. L., et al. (2022). NKp46+ natural killer cells develop an activated/memory-like phenotype and contribute to innate immunity against experimental filarial infection. *Front. Immunol.* 13, 969340. doi: 10.3389/fimmu.2022.969340

Pionnier, N., Sjoberg, H., Furlong-Silva, J., Marriott, A., Halliday, A., Archer, J., et al. (2020). Eosinophil-mediated immune control of adult filarial nematode infection can proceed in the absence of IL-4 receptor signaling. *J. Immunol.* 205, 731–740. doi: 10.4049/jimmunol.1901244

Pionnier, N. P., Sjoberg, H., Chunda, V. C., Fombad, F. F., Chounna, P. W., Njouendou, A. J., et al. (2019). Mouse models of *Loa loa*. *Nat. Commun.* 10, 1429. doi: 10.1038/s41467-019-09442-0

Prichard, R. K., and Geary, T. G. (2019). Perspectives on the utility of moxidectin for the control of parasitic nematodes in the face of developing anthelmintic resistance. *Int. J. Parasitol. Drugs Drug Resist.* 10, 69–83. doi: 10.1016/j.ijpddr.2019.06.002

Rajan, T. V., Nelson, F. K., Shultz, L. D., Shultz, K. L., Beamer, W. G., Yates, J., et al. (1994). Influence of gonadal steroids on susceptibility to Brugia malayi in scid mice. *Acta Trop.* 56, 307–314. doi: 10.1016/0001-706X(94)90102-3

Reddy, M. V. (2013). Human dirofilariasis: an emerging zoonosis. *Trop. Parasitol.* 3, 2–3.

Reichwald, J. J., Risch, F., Neumann, A. L., Frohberger, S. J., Scheunemann, J. F., Lenz, B., et al. (2022). ILC2s control microfilaremia during litomosoides sigmodontis infection in Rag2(-/-) mice. *Front. Immunol.* 13, 863663. doi: 10.3389/fimmu.2022.863663

Savadelis, M. D., Mctier, T. L., Kryda, K., Maeder, S. J., and Woods, D. J. (2022). Moxidectin: heartworm disease prevention in dogs in the face of emerging macrocyclic lactone resistance. *Parasit. Vectors* 15, 82. doi: 10.1186/s13071-021-05104-7

Simón, F., Siles-Lucas, M., Morchón, R., González-Miguel, J., Mellado, I., Carretón, E., et al. (2012). Human and animal dirofilariasis: the emergence of a zoonotic mosaic. *Clin. Microbiol. Rev.* 25, 507–544. doi: 10.1128/CMR.00012-12

Specht, S., Saeftel, M., Arndt, M., Endl, E., Dubben, B., Lee, N. A., et al. (2006). Lack of eosinophil peroxidase or major basic protein impairs defense against murine filarial infection. *Infect. Immun.* 74, 5236–5243. doi: 10.1128/IAI.00329-06

Supakorndej, P., McCall, J. W., and Jun, J. J. (1994). Early migration and development of *Dirofilaria immitis* in the ferret, *Mustela putorius furo*. *J. Parasitol.* 80, 237–244. doi: 10.2307/3283753

Townson, S., Connelly, C., and Muller, R. (1986). Optimization of culture conditions for the maintenance of Onchocerca gutturosa adult worms *in vitro*. *J. Helminthol.* 60, 323–330. doi: 10.1017/S0022149X00008579

Tritten, L., Burkman, E. J., Clark, T., and Verocai, G. G. (2021). Secretory microRNA profiles of third- and fourth-stage. *Pathogens* 10, 786. doi: 10.3390/pathogens10070786

Turner, J. D., Marriott, A. E., Hong, D., O'Neill, P., Ward, S. A., Taylor, M. J., et al. (2020). Novel anti-*Wolbachia* drugs, a new approach in the treatment and prevention of veterinary filariasis? *Vet. Parasitol.* 279, 109057. doi: 10.1016/j.vetpar.2020.109057

Turner, J. D., Pionnier, N., Furlong-Silva, J., Sjoberg, H., Cross, S., Halliday, A., et al. (2018). Interleukin-4 activated macrophages mediate immunity to filarial helminth

infection by sustaining CCR3-dependent eosinophilia. *PLoS Pathog* 14, e1006949. doi: 10.1371/journal.ppat.1006949

Verma, M. K., Clemens, J., Burzenski, L., Sampson, S. B., Brehm, M. A., Greiner, D. L., et al. (2017). A novel hemolytic complement-sufficient NSG mouse model supports studies of complement-mediated antitumor activity *in vivo*. *J. Immunol. Methods* 446, 47–53. doi: 10.1016/j.jim.2017.03.021

Voronin, D., Cook, D. A., Steven, A., and Taylor, M. J. (2012). Autophagy regulates *Wolbachia* populations across diverse symbiotic associations. *Proc. Natl. Acad. Sci. USA.* 109, E1638–E1646. doi: 10.1073/pnas.1203519109

Voronin, D., Schnall, E., Grote, A., Jawahar, S., Ali, W., Unnasch, T. R., et al. (2019). Pyruvate produced by Brugia spp. via glycolysis is essential for maintaining the mutualistic association between the parasite and its endosymbiont, *Wolbachia*. *PLoS Pathog.* 15, e1008085. doi: 10.1371/journal.ppat.1008085

Walker, T., Quek, S., Jeffries, C. L., Bandibabone, J., Dhokiya, V., Bamou, R., et al. (2021). Stable high-density and maternally inherited *Wolbachia* infections in *Anopheles moucheti* and *Anopheles demeilloni* mosquitoes. *Curr. Biol.* 31, 2310–2320.e5. doi: 10.1016/j.cub.2021.03.056

Wiszniewsky, A., Layland, L. E., Arndts, K., Wadephul, L. M., Tamadaho, R. S. E., Borrero-Wolff, D., et al. (2021). Adoptive transfer of immune cells into RAG2IL-2Rγ-deficient mice during litomosoides sigmodontis infection: a novel approach to investigate filarial-specific immune responses. *Front. Immunol.* 12, 777860. doi: 10.3389/fimmu.2021.777860

Wolstenholme, A. J., Evans, C. C., Jimenez, P. D., and Moorhead, A. R. (2015). The emergence of macrocyclic lactone resistance in the canine heartworm, *Dirofilaria immitis*. *Parasitology* 142, 1249–1259. doi: 10.1017/S003118201500061X

Zofou, D., Fombad, F. F., Gandjui, N. V. T., Njouendou, A. J., Kengne-Ouafo, A. J., Chounna Ndongmo, P. W., et al. (2018). Evaluation of *in vitro* culture systems for the maintenance of microfilariae and infective larvae of *Loa loa*. *Parasit. Vectors* 11, 275. doi: 10.1186/s13071-018-2852-2

Check for updates

The efficacy of the benzimidazoles oxfendazole and flubendazole against *Litomosoides sigmodontis* is dependent on the adaptive and innate immune system

Frederic Risch[1], Johanna F. Scheunemann[1], Julia J. Reichwald[1], Benjamin Lenz[1], Alexandra Ehrens[1,2], Joséphine Gal[3], Frédéric Fercoq[3], Marianne Koschel[1], Martina Fendler[1], Achim Hoerauf[1,2], Coralie Martin[3] and Marc P. Hübner[1,2]*

[1]Institute for Medical Microbiology, Immunology and Parasitology, University Hospital Bonn, Bonn, Germany, [2]German Center for Infection Research (DZIF), Partner Site Bonn-Cologne, Bonn, Germany, [3]Unité Molécules de Communication et Adaptation des Microorganismes, Sorbonne Université, Muséum national d'Histoire naturelle, CNRS, Paris, France

Filarial nematodes can cause debilitating diseases such as lymphatic filariasis and onchocerciasis. Oxfendazole (OXF) is one promising macrofilaricidal candidate with improved oral availability compared to flubendazole (FBZ), and OXF is currently under preparation for phase 2 clinical trials in filariasis patients. This study aimed to investigate the immune system's role during treatment with OXF and FBZ and explore the potential to boost the treatment efficacy via stimulation of the immune system. Wild type (WT) BALB/c, eosinophil-deficient *ΔdblGata1*, *IL-4r/IL-5*⁻/⁻, antibody-deficient µMT and B-, T-, NK-cell and ILC-deficient *Rag2/IL-2rγ*⁻/⁻ mice were infected with the rodent filaria *Litomosoides sigmodontis* and treated with an optimal and suboptimal regimen of OXF and FBZ for up to 5 days. In the second part, WT mice were treated for 2−3 days with a combination of OXF and IL-4, IL-5, or IL-33. Treatment of WT mice reduced the adult worm burden by up to 94% (OXF) and 100% (FBZ) compared to vehicle controls. In contrast, treatment efficacy was lower in all immunodeficient strains with a reduction of up to 90% (OXF) and 75% (FBZ) for *ΔdblGata1*, 50 and 92% for *IL-4r/IL-5*⁻/⁻, 64 and 78% for µMT or 0% for *Rag2/IL-2rγ*⁻/⁻ mice. The effect of OXF on microfilariae and embryogenesis displayed a similar pattern, while FBZ's ability to prevent microfilaremia was independent of the host's immune status. Furthermore, flow cytometric analysis revealed strain-and treatment-specific immunological changes. The efficacy of a shortened 3-day treatment of OXF (−33% adult worms vs. vehicle) could be boosted to a 91% worm burden reduction via combination with IL-5, but not IL-4 or IL-33. Our results suggest that various components of the immune system support the filaricidal effect of benzimidazoles *in vivo* and present an opportunity to boost treatment efficacy.

Introduction

Parasitic filarial nematodes are the causative agents of several diseases such as lymphatic filariasis (*Wuchereria bancrofti*, *Brugia malayi*, and *Brugia timori*), onchocerciasis (*Onchocerca volvulus*), loiasis (*Loa loa*) and mansonelliasis (*Mansonella perstans*, *Mansonella streptocerca*, and *Mansonella ozzardi*). The WHO includes lymphatic filariasis and onchocerciasis in its list of neglected tropical diseases (NTD) (WHO, 2020). Lymphatic filariasis may manifest with symptoms like lymphedema, hydrocele or elephantiasis and is prevalent in 72 countries with an estimated 51.4 million people infected in 2018 (Taylor et al., 2010; WHO, 2020). Patients with onchocerciasis can develop symptoms like dermatitis, visual impairment and blindness (Taylor et al., 2010). Onchocerciasis, also known as river blindness, is responsible for an estimated 1.3 million disability-adjusted life years, with roughly 21 million people infected in sub-Saharan Africa and minor foci in South America (James et al., 2018; WHO, 2020).

Both lymphatic filariasis and onchocerciasis are mainly treated via mass drug administration (MDA) campaigns which consist of (bi-) annual community-wide treatment efforts (WHO, 2020). The current recommendations for MDA of lymphatic filariasis are a combination of ivermectin, albendazole and diethylcarbamazine (Irvine et al., 2017; King et al., 2018; Ehrens et al., 2022a). However, this triple therapy may cause severe adverse events in patients co-infected with loiasis and onchocerciasis (Francis et al., 1985; Boussinesq et al., 2003; Wanji et al., 2018). Thus, in areas co-endemic for onchocerciasis, the WHO recommends treatment with ivermectin alone (WHO, 2020). In areas co-endemic for loiasis, ivermectin and albendazole are used. However, people with high *L. loa* microfilariae loads have to be excluded from the treatment (test-and-not-treat) due to the risk of developing life-threatening adverse events. Moreover, the current treatment strategies have severe limitations as ivermectin, albendazole and diethylcarbamazine are mainly microfilaricidal, i.e., they target and eliminate the filarial progeny, the microfilariae, of the parasites (Geary et al., 2019; Hawryluk, 2020). Thus, the current treatment strategies temporarily interrupt the transmission of the parasite. However, eliminating the diseases will require continuous, community-wide administrations for decades as the adult worms can be reproductively active for at least 5–8 years (Taylor et al., 2010; McLure et al., 2022; Fuller et al., 2023). In addition, as the prevalence of lymphatic filariasis or onchocerciasis decreases, community-wide treatment strategies become less cost-effective, and the transition to more targeted approaches that cure the disease, i.e., clear the adult worms (=macrofilaricidal), rather than prevent transmission become more relevant (Irvine et al., 2017). As a result, the WHO has outlined the development of novel macrofilaricidal compounds or treatment strategies as one of the critical actions to combat onchocerciasis in the 2030 NTD roadmap (WHO, 2020). Potential macrofilaricidal compounds that are currently being tested in phase II clinical trials include flubentylosin (ABBV4083), emodepside, and oxfendazole (OXF) (Ehrens et al., 2022a).

OXF, as well as the related compound flubendazole (FBZ), are two benzimidazoles that selectively target the β-tubulin subunits of nematodes and both compounds have shown macrofilaricidal activities against different filarial species (Lacey, 1990; Geary et al., 2019; Gonzalez et al., 2019). Animal studies have reported on the macrofilaricidal efficacy of FBZ against *Brugia pahangi* and

Litomosoides sigmodontis (Denham et al., 1979; Surin and Denham, 1990; Hübner et al., 2019). However, FBZ has limited oral bioavailability, and early studies in humans have reported severe side effects such as abscess formations and inflammation after parenteral administrations in humans (Dominguez-Vazquez et al., 1983). Studies that attempted to address the issues of FBZ have resulted in an amorphous solid dispersion formulation of FBZ with increased oral bioavailability (Hübner et al., 2019; Lachau-Durand et al., 2019). However, this formulation had only limited efficacy on adult worms of *Onchocerca ochengi* and *Brugia pahangi*, microfilariae of *B. malayi* and caused genotoxicity in an *in vivo* micronucleus test (Fischer et al., 2019; Lachau-Durand et al., 2019; Sjoberg et al., 2019). OXF, on the other hand, is not only effective after subcutaneous injection but also has improved bioavailability compared to FBZ (Ehrens et al., 2022a). OXF has been used in veterinary medicine as a broad-spectrum anthelmintic for over 30 years (Gonzalez et al., 2019; Hawryluk, 2020). Recent studies have shown that OXF is also effective against adult worms of *Onchocerca gutturosa*, L5 stages of *O. volvulus* and adult worms of the rodent filaria *Litomosoides sigmodontis* but possesses limited to no effect against microfilariae (Hübner et al., 2020). Phase I clinical studies with multiple ascending dosages for OXF have been completed and shown no adverse reactions (Bach et al., 2020). Additional bioavailability studies in humans with an OXF field applicable tablet formulation have been tested through the Helminth Elimination Platform (HELP),[1] and Phase II clinical trials of OXF as a pan-nematode drug against *O. volvulus*, *L. loa*, *M. perstans*, and the intestinal human whipworm *Trichuris trichiura* through the EU-funded eWHORM project[2] are currently in preparation (Specht and Keiser, 2022).

Despite these advances in developing macrofilaricidal candidates, additional preclinical research may further improve treatment options. One potential avenue to improve the efficacy of anti-filarial treatment is the combination of chemotherapy with immunostimulatory compounds (Murthy et al., 1992; Rahdar et al., 2020; Silva et al., 2020). Thus, this study aimed to characterize the role of the immune system during anti-filarial treatment with OXF and FBZ using the *L. sigmodontis* rodent model and evaluate the potential of boosting the macrofilaricidal activity of OXF via a combination therapy of OXF with various cytokines.

Materials and methods

Animals and natural infection with *Litomosoides sigmodontis*

Six-week old female and male BALB/cJ WT mice were purchased from Janvier Labs, Saint-Berthevin, France. BALB/c *ΔdblGata1*, BALB/c *IL-4r/IL-5⁻/⁻*, BALB/c μMT, and C57BL/6 *Rag2/IL-2rγ⁻/⁻* were bred at the animal facility "Haus für Experimentelle Therapie" of the University Hospital Bonn. *ΔdblGata1* and μMT mice were originally obtained from Jackson Laboratory (Bar Harbor, United States), *IL-4r/IL-5⁻/⁻* from Prof. Dr.

---

1 https://eliminateworms.org/

2 https://www.ewhorm.org/

Klaus Matthaei (Matthaei, Stem Cell & Gene Targeting Laboratory, ANU College of Medicine, Biology and Environment, Canberra, Australia) and *Rag2/IL-2rγ*$^{-/-}$ from Taconic Biosciences Inc. (Cologne, Germany).

For the experiments, mice were housed in individually ventilated cages with unlimited access to food and water and a 12-h day/night cycle within the animal facility at the Institute for Medical Microbiology, Immunology and Parasitology (IMMIP), University Hospital Bonn. All animal experiments were performed according to EU Directive 2010/63/EU and approved by the appropriate state authorities Landesamt für Natur-, Umwelt- und Verbraucherschutz, Recklinghausen, Germany (AZ: 84–02.04.2015.A507, 81–02.04.2020. A244, 81–02.05.40.18.057).

Six to twenty week old male and female mice were naturally infected with *L. sigmodontis* via exposure to the tropical rat mite, *Ornithonyssus bacoti*, carrying the infective L3 larvae as described elsewhere (Reichwald et al., 2022). In short, mice were placed in cages with bedding material containing the mites. After 24 h, the bedding material containing the mites was removed, and the cages were placed on top of a plastic tub with disinfectant below the cages and no direct contact with the mice. After an additional 24 h, mice were moved into standard cages, and the bedding material was exchanged daily for 5 days to remove any remaining mites.

Treatment

For the OXF treatment, a commercially available formulation of OXF (Dolthene) was used and dissolved in corn oil (Sigma-Aldrich, St. Louis, United States). Vehicle controls received only corn oil. For all experiments, treatment with OXF was performed orally, twice per day, 8 h apart starting 35 days post infection (dpi) after the development of adult worms (28–35 dpi) but before the onset of microfilaremia (50–56 dpi) (Hübner et al., 2009). For the experiments with immunodeficient strains, mice received either 5 or 12.5 mg/kg OXF in a total volume of 5 mL/kg per treatment for 5 days (see Supplementary Table S1 for a detailed breakdown of treatments in immunodeficient mice) (Hübner et al., 2020). For the 3-day combination therapy, mice received 12.5 mg/kg OXF for 3 or 5 days, and for the 2-day combination therapy, mice received either 12.5 or 25 mg/kg OXF per treatment for 2 or 5 days. For the 3-day combination therapy, 2 μg of interleukin-4 (IL-4), IL-5 or IL-33 were given intranasally in a volume of 10 μL under short anesthesia induced with 2% isoflurane (AbbVie, Wiesbaden, Germany) once per day for 3 days (Johansson et al., 2018; Beckert et al., 2020). For the 2-day combination therapy, 2 μg of IL-5 was given intranasally in a volume of 10 μL under short anesthesia induced with 2% isoflurane (AbbVie, Wiesbaden, Germany) once per day for 2 days.

For the FBZ treatment, FBZ (Sigma-Aldrich, St. Louis, United States) was dissolved in distilled water with 0.1% v/v tween80 (Sigma-Aldrich, St. Louis, United States) and 0.5% w/v hydroxyethyl cellulose (Sigma-Aldrich, St. Louis, United States). Vehicle controls received only distilled water with 0.1% v/v tween80 and 0.5% w/v hydroxyethyl cellulose. Treatment was performed 35 dpi for 2 or 5 days once per day via subcutaneous injections (Hübner et al., 2019). All mice received 2 mg/kg FBZ in a volume of 5 mL/kg per treatment (see Supplementary Table S1 for a detailed breakdown of treatments in immunodeficient mice).

Parasite recovery and quantification

Necropsies were performed to quantify the adult worm burden and the number of microfilariae in the peripheral blood at 70 dpi. Mice were euthanized with an overdose of isoflurane, and adult worms were isolated via lavage of the thoracic cavity with 8–10 mL PBS (Thermo Fisher Scientific, Waltham, United States). Isolated worms were counted and the gender was determined. To quantify the microfilariae burden at 56 and 70 dpi, 50 μL of peripheral blood was drawn from the facial vein into EDTA tubes (Sarstedt AG & Co. KG, Nümbrecht, Germany) and incubated with 950 μL red blood cell lysis buffer (Thermo Fisher Scientific, Waltham, United States) for 10 min at room temperature (RT). The blood was centrifuged at $400 \times g$ for 5 min at RT, the supernatant was discarded, and microfilariae in the pellet were counted with a bright-field microscope (Zeiss, Göttingen, Germany) as previously described (Reichwald et al., 2022).

To quantify the embryonal stages, intact, female adult worms were fixed with 4% formaldehyde (Sigma-Aldrich, St. Louis, United States) in PBS (Thermo Fisher Scientific, Waltham, United States) for 24 h and then stored in 60% v/v ethanol in distilled water at RT until further analysis. Worms were then transferred into 1.5 mL Eppendorf tubes (Eppendorf SE, Hamburg, Germany) containing 100 μL Hinkelmann solution (0.5% eosin yellow, 0.5% phenol, 0.185% formaldehyde in distilled water) and crushed with a mortar. Embryonal stages [oocyte, morula, pretzel, stretched microfilaria, degenerated early stage (altered oocyte/morula) and degenerated late stage (altered pretzel/microfilaria)] were then quantified with a bright-field microscope (Zeiss, Göttingen, Germany) as previously described (Ziewer et al., 2012).

Histology

Lungs from *L. sigmodontis*-infected WT BALB/c mice ($n = 6$–7 per group) were inflated and fixed twice in 4% formalin for 24 h each. Lungs were then dehydrated in ethanol baths of increasing concentrations from 70 to 100% and placed in toluene before paraffin embedding. All sections were cut deep enough to see the main bronchi and perivascular adventitial spaces (PVS). Seven-micron-thick serial sections were prepared and various stainings were performed. (i) Hematoxylin and eosin staining was used to visualize lung structure and performed as follows: Sections were incubated with Mayer's hematoxylin solution for 5 min, rinsed with tap water for 20 s and then incubated with 1% eosin solution for 1 min. (ii) Alcian Blue—Periodic Acid Schiff (AB-PAS) staining to visualize mucus-producing cells was performed as follows: Sections were incubated with 1% Alcian blue in 3% acetic acid for 20 min, rinsed with tap water and distilled water for 2 min each, incubated with 0.5% periodic acid for 5 min and again rinsed with distilled water. Next, sections were counterstained with Schiff's reagent for 10 min, rinsed with tap water for 5 min and stained with hematoxylin for 1 min. Finally, sections were rinsed again with tap water for 2 min and then differentiated with acid alcohol. (iii) Luxol Fast Blue staining to visualize eosinophils was performed as follows: Sections were incubated with Luxol blue for 20 min, rinsed with running tap water for 2 min and then counterstained with Mayer's hematoxylin for 10 s. The number of Luxol blue positive eosinophils was determined in 15 fields of view with an ×100 objective using Olympus BH2. The other sections were scanned at the MNHN

light microscopy facility (CeMIM, Centre de Microscopie et d'IMagerie numerique, MNHN Paris) with a NanoZoomer S60 digital slide scanner (Hamamatsu) and images were analyzed with QuPath 0.3 software (Bankhead et al., 2017). For cell infiltration in PVS, 3–5 PVS areas per mouse were segmented manually, Hematoxylin positive nucleus detection was done using the "Cell detection" tool in QuPath and results were expressed as "number of nuclei/mm^2 of PVS." Minimal thickness of bronchial arteries (in micrometer) was measured from 3 to 6 arteries of similar diameter per mouse.

Preparation of organs for flow cytometry analysis

The thoracic cavity lavage was performed with 8–10 mL PBS. The lavage was centrifuged at $400 \times g$ for 5 min at 4°C and the supernatant was discarded. The pellet was resuspended in 1 mL red blood cell lysis buffer (Thermo Fisher Scientific, Waltham, United States). Cells were then washed with PBS containing 1% v/v FCS (PAN Biotech, Aidenbach, Germany) and 2 mM EDTA (Carl Rohe, Karlsruhe, Germany), resuspended in PBS containing 1% v/v FCS and 2 mM EDTA and counted with a CasyR TT Cell Counter (Schärfe Systems, Reutlingen, Germany). 1×10^6 cells were used for flow cytometric analysis.

To isolate splenocytes, spleens were perfused with 3 mL of a 0.5 mg/mL collagenase VIII solution (Roche, Basel, Switzerland), cut into small pieces and incubated at 37°C for 30 min on a shaker with 200 rpm. Five milliliter PBS containing 1% v/v FCS and 2 mM EDTA were then added and the minced spleens were pushed through a 70 μm metal sieve to generate single-cell suspensions. Cells were then centrifuged at $400 \times g$ for 5 min at 4°C and the supernatant was discarded. Red blood cell lysis was performed by incubating the pellet in 1 mL red blood cell lysis buffer (Thermo Fisher Scientific, Waltham, United States). Cells were then washed with PBS containing 1% v/v FCS (PAN Biotech, Aidenbach, Germany) and 2 mM EDTA (Carl Rohe, Karlsruhe, Germany), resuspended in PBS containing 1% v/v FCS and 2 mM EDTA and counted with a CasyR TT Cell Counter (Schärfe Systems, Reutlingen, Germany). 1×10^6 cells were used for flow cytometric analysis.

Flow cytometry

Cells from the thoracic cavity and spleen were analyzed with one surface staining to identify lymphoid cells and two intracellular stainings to identify T helper cell subsets and myeloid cells. For the surface staining, cells were incubated for 20 min on ice in a mastermix in PBS with 1% v/v FCS, 0.1% v/v rat IgG (Sigma-Aldrich, St. Louis, United States) containing the following antibodies: anti-CD3 (Al700, clone GK1.5, BioLegend), anti-CD4 (BV605, clone RM4-5, BioLegend), anti-CD5 (PerCP Cy5.5, 53–7.3, BioLegend), anti-CD8 (PE, 53–6.7, BioLegend), and anti-CD19 (APC, eBio1D3, Thermo Fisher Scientific). Cells were then washed twice with PBS containing 1% v/v FCS, resuspended in 200 μL PBS containing 1% v/v FCS and 2 mM EDTA and filtered through 70 μm gauze (Labomedic, Bonn, Germany) before measurement with a CytoFLEX S (Beckmann Coulter, Brea, United States) and further analysis with FlowJo V10 (FlowJo, Ashland, United States).

For the intracellular staining, cells were incubated in a fixation/permeabilization buffer (Thermo Fisher Scientific, Waltham, United States) for 20 min at RT. Cells were then centrifuged at $400 \times g$ for 5 min at 4°C and incubated overnight in PBS containing 1% w/v bovine serum albumin fraction V (PAA Laboratories, Cölbe, Germany) and 0.1% v/v rat IgG (Sigma-Aldrich, St. Louis, United States) at 4°C. The following day, cells were centrifuged at $400 \times g$ for 5 min at 4°C and incubated in a permeabilization buffer (Thermo Fisher Scientific, Waltham, United States) for 20 min at RT. Cells were again centrifuged at $400 \times g$ for 5 min at 4°C and stained with master mixes in PBS containing 1% w/v bovine serum albumin fraction V (PAA Laboratories, Cölbe, Germany) and the following antibodies for 45 min at 4°C in the dark: anti-CD3 (BV510, clone 145-2C11, BioLegend), anti-CD4 (Al700, clone 17A2, BioLegend), anti-CD8 (PerCP Cy5.5, clone 53–6.7, BioLegend), anti-CD11b (Al700, clone M1/70, BioLegend), anti-CD11c (BV605, clone N418, BioLegend), anti-CD25 (BV421, PC61, BioLegend), anti-GATA-3 (Al488, clone 16E10A23, BioLegend), anti-FOXP3 (PE-Cy7, FJK-16S, Thermo Fisher Scientific), anti-I-ab (BV421, M5/114.15.2, BioLegend), anti-Ly6C (APC-Cy7, clone HK1.4, BioLegend), anti-Ly6G (PE-Cy7, clone 1A8, BioLegend), anti-RELM-α (APC, clone DS8RELM, Thermo Fisher Scientific), anti-RORγT (PE, clone AFKJS-9, Thermo Fisher Scientific), Siglec-F (PE, clone E50-2440, BD Biosciences) and anti-T-bet (APC, clone 4B10, BioLegend). Cells were then washed twice with PBS containing 1% v/v FCS, resuspended in 200 μL PBS containing 1% v/v FCS and 2 mM EDTA and filtered through 70 μm gauze (Labomedic, Bonn, Germany) before measurement with a CytoFLEX S (Beckmann Coulter, Brea, United States) and further analysis with FlowJo V10 (FlowJo, Ashland, United States).

Statistical analysis

Statistical analysis was performed with GraphPad Prism software version 8/9 (GraphPad Software, San Diego, United States). The choice of statistical analysis was based on sample size and distribution of samples. Normality was assessed via the Shapiro–Wilk test. For normally distributed data, a One-Way ANOVA with Dunnet's multiple comparison test was performed. For non-parametric data, the Kruskal-Wallis test followed by Dunn's multiple comparisons test was used to assess significant differences between 3 or more groups or the Mann–Whitney-U test for differences between two groups. Data for adult worms, microfilariae, immune cells and histological analysis are shown as median with interquartile range. Data for embryonal stages in stacked bar graphs are shown as mean with standard error of mean. $p < 0.05$ were considered to be significant.

Results

Treatment efficacy of oxfendazole against *Litomosoides sigmodontis* is reduced in immunocompromised mice

To characterize the role of the immune system during anti-filarial treatment, we naturally infected WT BALB/c mice and several immunodeficient strains, i.e., *ΔdblGata1*, *IL-4r/IL-5$^{-/-}$*, μMT, and

Rag2/IL-2rγ⁻/⁻, with *Litomosoides sigmodontis* and treated them orally with 5 or 12.5 mg/kg OXF twice per day for 5 days after the development of adult worms (35 dpi) but before the appearance of microfilariae at 50–56 dpi. Necropsies were performed 70 dpi to quantify worm burden and immunological changes.

Treatment with both 5 and 12.5 mg/kg OXF led to a statistically significant reduction of the median adult worm burden only in BALB/c WT (88 and 94% respectively) and *ΔdblGata1* mice (80 and 90%) (Figure 1A). The reduction of the adult worm burden in the other strains was either not statistically significant with a median reduction of up to 50% or only statistically significant for one treatment condition, i.e., a reduction of 64% in μMT mice after treatment with 5 mg/kg OXF (Figure 1A). Interestingly, the strain with the most severe immunodeficiency (*Rag2/IL-2rγ⁻/⁻*) displayed no reduction of the adult worm burden after treatment at all (Figure 1A). The effect of the treatment on the numbers of microfilariae in the peripheral blood presented a different picture (Figure 1B). Here we could observe a median reduction of 100% in BALB/c WT mice as well as the mature B cell-and antibody-deficient μMT mice whereas all other strains displayed no (*ΔdblGata1*) or only impaired effects on microfilariae numbers (*IL-4r/IL-5⁻/⁻, Rag2/IL-2rγ⁻/⁻*) (Figure 1B). Accordingly, treatment in immunodeficient mice led to fewer adult worm or microfilariae-negative animals (with the exception of μMT mice) compared to the treatment in BALB/c WT animals (Table 1). Importantly, the treatment was performed 35–39 dpi while microfilariae are only detectable in the peripheral blood after 49–56 days indicating that the effect of OXF was based on changes in the embryogenesis of adult worms rather than a direct effect against microfilariae.

To further assess the fertility of female worms, we analyzed drug effects on embryogenesis. Therefore, female worms were homogenized and stained with Hinkelmann solution and different embryonal stages, i.e., oocyte, morulae, pretzel, stretched microfilariae as well as degenerated early (oocyte, morulae) and degenerated late stages (pretzel, microfilariae), were counted with a bright field microscope (Figure 1C). Here, *IL-4r/IL-5⁻/⁻* and *Rag2/IL-2rγ⁻/⁻* mice had significantly more embryonal stages in the untreated mice than the other strains and treatment with OXF led to a substantial reduction of embryonal stages in all tested strains (Figures 1D–H). In line with the microfilariae numbers (Figure 1B), a closer examination of the treatment effect revealed a nearly complete elimination of late stages (<10 pretzel or stretched microfilariae per worm) only in BALB/c WT and μMT mice but not the other immunodeficient strains (Supplementary Table S2). Taken together, the macrofilaricidal efficacy of OXF appears to be influenced by the innate and adaptive immune system with a more substantial decrease in effectiveness in more severe immunodeficient strains. In contrast, the effect on microfilaremia appears to be influenced by components of innate and adaptive immunity but independent of mature B cells or antibodies and mediated via a reduction in fertility of adult female worms.

Macrofilaricidal efficacy of flubendazole is reduced in immunocompromised mice

Next, we analyzed the efficacy of FBZ in immunodeficient mice by treating mice that were naturally infected with *L. sigmodontis* with 2 mg/kg FBZ subcutaneously for 2 or 5 days once per day starting

treatment at 35 dpi. Necropsies were again performed 70 dpi to investigate the worm burden and immunological changes.

Similar to OXF, the macrofilaricidal efficacy of FBZ was reduced in all immunodeficient strains (Figure 2A). Treatment with FBZ in BALB/c WT mice led to a median reduction of 100% with 56 or 93% of animals cleared of all adult worms after 2 and 5 days of treatment, respectively (Table 2). By contrast, reductions in the immunodeficient strains ranged from 0 to 92% with significant reductions only in μMT mice after 2 days of FBZ and *IL-4r/IL-5⁻/⁻* mice after 5 days of FBZ treatment (Figure 2A). In addition, FBZ treatment only achieved a partial clearance of adult worms in the immunodeficient strains with the most significant effect in *ΔdblGata1* mice with 27 and 30% of animals being adult worm free, respectively (Table 2). Interestingly, the effect of FBZ on microfilariae was drastically different compared to the effect of OXF (Figure 2B). All mice with the exception of one *IL-4r/IL-5⁻/⁻* mouse had no microfilariae detectable in the peripheral blood after FBZ treatment (Table 2). Results from the analysis of the embryonal development supported the microfilariae data showing significant reductions in all embryonal stages after treatment (Figures 2C–G). Furthermore, late stages were almost completely eliminated in all strains, and only early or degenerated stages could be detected (Supplementary Table S3). Hence we conclude that the macrofilaricidal efficacy of FBZ is dependent on the immune system. However, the prevention of microfilaremia is immune system-independent.

Distinct patterns of immunological changes in different strains after benzimidazole treatment

Next, we aimed to further characterize the impact of the host's immune status by analyzing changes in immune cell populations in the thoracic cavity, the site of adult worm residency, and the spleen, which plays a crucial role in the elimination of microfilariae, after treatment (see Supplementary Figures S1, S2 for gating strategies). OXF and FBZ treatment led to distinct, strain-and compound-specific changes in both spleen (Figures 3A–D) and thoracic cavity (Figures 3E–H) compared to corresponding vehicle controls.

In BALB/c WT mice (shown in green in Figure 3), treatment with both OXF and FBZ induced only limited changes in cell frequencies in the spleen, with the strongest reductions observed for eosinophils, Ly6C(hi) monocytes and cDC2s after OXF treatment (Figure 3A) and Th1 cells, cDCs2 and pDCs after FBZ treatment (Figure 3C) while the total cell count was reduced for almost all cell types (Figures 3B,D). By contrast, treatment with OXF led to an overall increase in cell frequencies and total cell counts in *ΔdblGata1* mice (blue, Figures 3A,B). Treatment with FBZ in *ΔdblGata1* mice, on the other hand, led to broadly similar changes as in BALB/c WT mice with decreases in Th1, cDC2, and pDC frequencies and overall decreased total cell counts (Figures 3C,D). For *IL-4r/IL-5⁻/⁻* mice, treatment with OXF led to no significant changes in cell frequencies or total counts (red, Figures 3A,B), whereas FBZ treatment reduced frequencies and total cell counts of lymphocytes (except Tregs) while myeloid cells except for cDC2s and pDCs were increased (Figures 3C,D). *Rag2/IL-2rγ⁻/⁻* had overall decreased frequencies and total cell counts after both OXF and FBZ treatment (purple, Figures 3A–D). μMT mice had decreased lymphocyte frequencies after OXF treatment, but
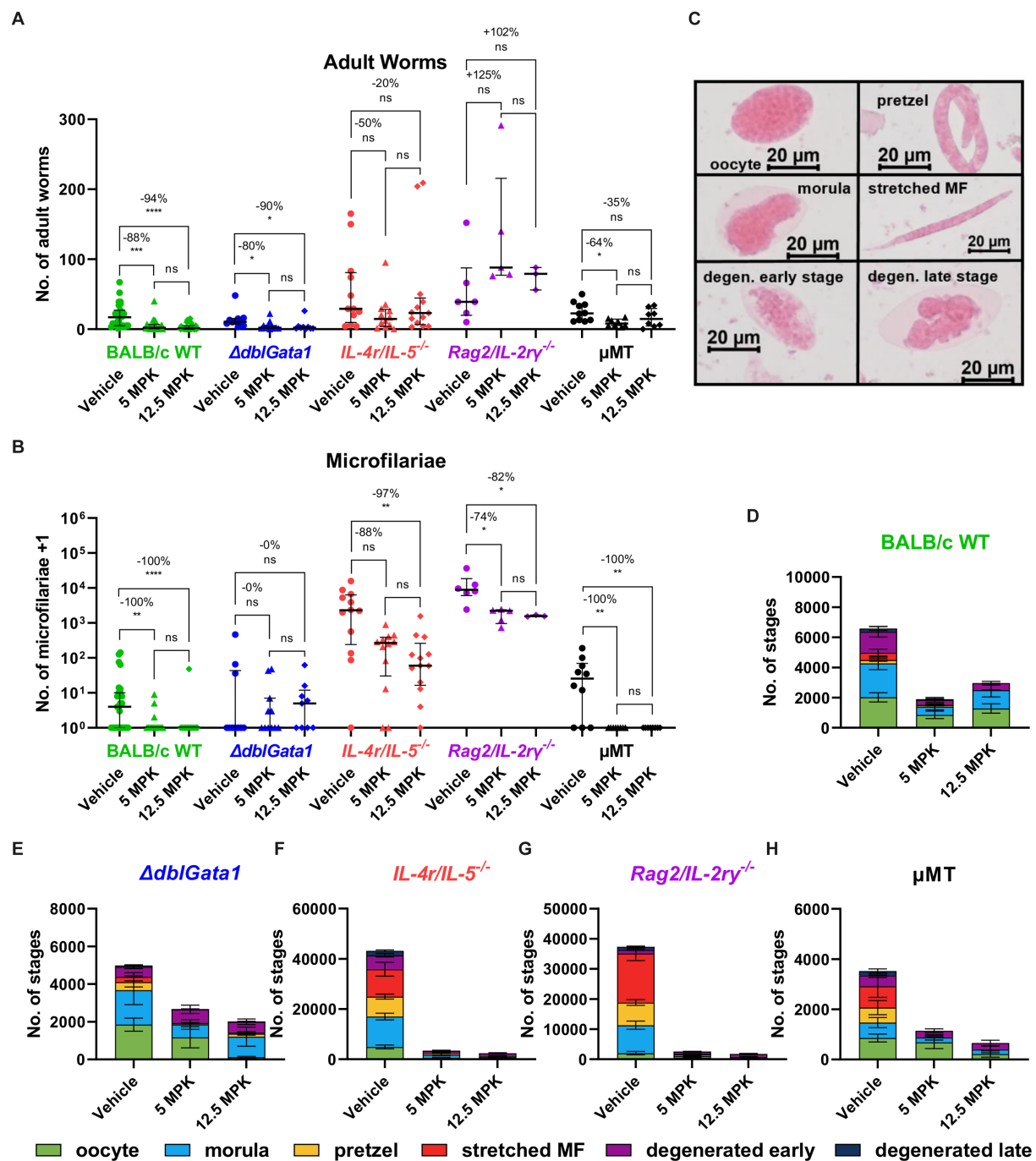
FIGURE 1

Reduced treatment efficacy of oxfendazole in immunodeficient mice. **(A–H)** Indicated mouse strains were naturally infected with *Litomosoides sigmodontis* and treated orally with 5 or 12.5mg/kg oxfendazole twice per day for 5 days starting 35 days after the infection. Necropsies were performed 70 days after the infection. **(A)** Adult worm burden. **(B)** Microfilariae per 50µL peripheral blood +1. **(C)** Representative images of embryonal stages. **(D–H)** Average number of embryonal stages per female worm in **(D)** BALB/c (green), **(E)** *ΔdblGata1* (blue), **(F)** *IL-4r/IL-5⁻/⁻* (red), **(G)** *Rag2/IL-2rγ⁻/⁻* (purple), and **(H)** µMT mice (black). **(A,B)** Data shown as median with interquartile range. Numbers show reduction of median in comparison to corresponding vehicle control. **(D–H)** Data shown as mean±SEM. **(A,B,D–H)** Data for BALB/c pooled from 6 experiments, *IL-4r/IL-5⁻/⁻* pooled from 3 experiments, *ΔdblGata1, Rag2/IL-2rγ⁻/⁻* and µMT pooled from 2 experiments. Statistical analysis using Kruskal-Wallis with Dunn's *post-hoc* test, *$p<0.05$, **$p<0.01$, ***$p<0.001$, ****$p<0.0001$.

unchanged or slightly elevated cell counts (black, Figures 3A,B) and overall increased lymphocyte numbers after FBZ treatment (Figures 3C,D). Interestingly, myeloid cell numbers were mostly increased after OXF treatment, whereas FBZ treatment reduced

neutrophils, eosinophils and cDC numbers, while other myeloid cells were increased in µMT mice (Figures 3C,D).

In the thoracic cavity of WT mice, treatment with both OXF and FBZ led to an increase in most lymphocyte numbers except for Th1

TABLE 1 Clearance of adult worms and microfilariae after OXF treatment.

	Adult worm negative mice			Microfilariae negative mice		
	Vehicle	5 mg/kg OXF	12.5 mg/kg OXF	Vehicle	5 mg/kg OXF	12.5 mg/kg OXF
BALB/c	0.0%	23.8%	44.4%	44.4%	85.7%	96.2%
	(0/27)	(5/21)	(12/27)	(12/27)	(18/21)	(26/27)
$\Delta dblGata1$	0.0%	9.0%	11.1%	70.0%	54.5%	44.4%
	(0/10)	(1/11)	(1/9)	(7/10)	(6/11)	(4/9)
$IL\text{-}4r/IL\text{-}5^{-/-}$	0.0%	8.3%	0.0%	8.3%	16.60%	7.6%
	(0/12)	(1/12)	(0/13)	(1/12)	(2/12)	(1/13)
$Rag2/IL\text{-}2r\gamma^{-/-}$	0.0%	0.0%	0.0%	0.0%	0.0%	0.0%
	(0/6)	(0/5)	(0/3)	(0/6)	(0/5)	(0/3)
μMT	0.0%	0.0%	12.5%	30.0%	100%	100%
	(0/10)	(0/8)	(1/8)	(3/10)	(8/8)	(8/8)

BALB/c WT mice and immunodeficient strains ($\Delta dblGata1$, $IL\text{-}4r/IL\text{-}5^{-/-}$, μMT, and $Rag2/IL\text{-}2r\gamma^{-/-}$) were naturally infected with *Litomosoides sigmodontis* and treated with 5 or 12.5 mg/kg OXF twice per day for 5 days starting 35 dpi. Number of adult worms in the thoracic cavity and number of microfilariae per 50 μL blood were quantified 70 dpi. Data is pooled from 2 to 6 experiments. Shown is the number and frequency of animals that were free of adult worms and microfilariae at 70 dpi.

cells (green, Figures 3E–H). Myeloid cells, on the other hand, were mostly decreased after OXF treatment or essentially unchanged, except for strongly decreased eosinophils after FBZ treatment (Figures 3E–H). For both $\Delta dblGata1$ and $IL\text{-}4r/IL\text{-}5^{-/-}$ mice, OXF treatment had only minor effects on cell numbers in the thoracic cavity, whereas treatment with FBZ led to a significant decrease in CD4$^+$ (especially Th1) and CD8$^+$ T cell numbers (blue and red, Figures 3E–H). For $Rag2/IL\text{-}2r\gamma^{-/-}$, OXF treatment induced only limited changes in thoracic cavity cell numbers while treatment with FBZ strongly reduced total cell numbers (purple, Figures 3E–H). By contrast, treatment in μMT mice revealed more extensive changes after OXF rather than FBZ treatment (black, Figures 3E–H). Overall, OXF and FBZ induced marked differences in both spleen and thoracic cavity cell compositions with distinct differential patterns in each strain.

Combination of oxfendazole with interleukin-5 improves macrofilaricidal efficacy against *Litomosoides sigmodontis*

Based on the reduced treatment efficacy of OXF and FBZ observed in immunodeficient mice, we hypothesized that stimulating the immune system during drug treatment might improve the efficacy or enable an equally effective treatment using a shorter treatment regimen. To investigate this, we naturally infected BALB/c WT mice with *L. sigmodontis* and treated them with 12.5 mg/kg OXF for 3 days (suboptimal time) with or without additional intranasal application of IL-4, IL-5, or IL-33 starting 35 dpi (Figure 4). The cytokines were given intranasally to induce a local immune response at the site of infection, i.e., the thoracic cavity (Jackson-Jones et al., 2016).

Treatment with OXF for 3 days alone led to no statistically significant difference of the adult worm burden, with a 33% median reduction compared to the vehicle controls (Figure 4A). Addition of

IL-4 and IL-33 improved the median adult worm burden reduction to 58%. The combination with IL-5 boosted the efficacy to 91% achieving a similar reduction as a 5-day OXF treatment even though all three combination therapies did not lead to statistically significant differences in comparison to the vehicle control (Dunn's *post-hoc* test). However, the combination with IL-5 did lead to significant differences compared to both the vehicle control ($p = 0.025$) as well as the 3-day OXF treatment ($p = 0.004$) via direct comparison (Mann–Whitney U test). Treatment with the cytokines alone did not lead to a reduction of the adult worm burden (Figure 4A). Besides the improved macrofilaricidal efficacy, the combination of OXF with IL-5 reduced the number of microfilariae-positive animals from 4/13 to 1/13 compared to OXF alone (Figure 4B). Analysis of the embryonal development showed a substantial reduction of all stages after OXF treatment (Figure 4C). Importantly, significant numbers of late stages remained after 3-day OXF treatment (137.1 ± 61.8 pretzel stages, 36.7 ± 24.9 stretched microfilariae, mean ± SEM) which were almost completely eliminated in the OXF + IL-5 group (5.8 ± 4.3 pretzel stages, 0.0 ± 0.0 stretched microfilariae) (Supplementary Table S4). Based on these results, we also tested a treatment regimen of only 2 days. However, a combination therapy of 12.5 or 25 mg/kg OXF with IL-5 for only 2 days failed to significantly reduce the adult worm burden or microfilariae numbers (Supplementary Figure S3).

Interestingly, flow cytometric analysis of the 3-day OXF combination therapy revealed a reduction in eosinophil frequencies in the spleen in mice treated with OXF, cytokines (IL-4, IL-5, IL-33) or a combination thereof compared to the vehicle controls (Figure 4D). The composition of immune cells in the thoracic cavity was mostly unchanged after treatment with an intriguing increase in monocyte numbers after 3-day OXF treatment (Figures 4F,G). To assess any pathological changes in adjacent organs caused by the combination therapy, we analyzed histological changes in the lungs of treated mice (Figure 5). Here, we observed that the treatment with IL-33 appeared to cause vascular inflammation with increased cell infiltration into the pulmonary vascular stroma (Figures 5A,B) and increased thickness of bronchial arteries (Figures 5C,D). Apart from these pathological changes, treatment with OXF, the combination of OXF with cytokines and the cytokines by themselves led to a reduction in mucus covering the surfaces of bronchioles (Figures 5E,F). Lastly, as expected, treatment with IL-5 led to an infiltration of eosinophils into the lung (Figures 5G,H).

Overall, the combination of OXF with IL-5 improved the macrofilaricidal efficacy, reduced the number of microfilariae-positive animals, and no pathological changes were observed in the lungs of treated mice.

Discussion

In the present study, we characterized the role of the immune system during anti-filarial treatment in the *L. sigmodontis* rodent model and investigated the potential of a combination therapy approach to improve the macrofilaricidal efficacy of OXF.

In the first part, we compared the treatment efficacy and immunological changes after treatment with two different benzimidazole compounds, OXF and FBZ, in BALB/c WT mice with immunodeficient mouse strains, i.e., $\Delta dblGata1$ mice lacking eosinophils, $IL\text{-}4r/IL\text{-}5^{-/-}$ mice lacking eosinophils as well as RELMα$^+$
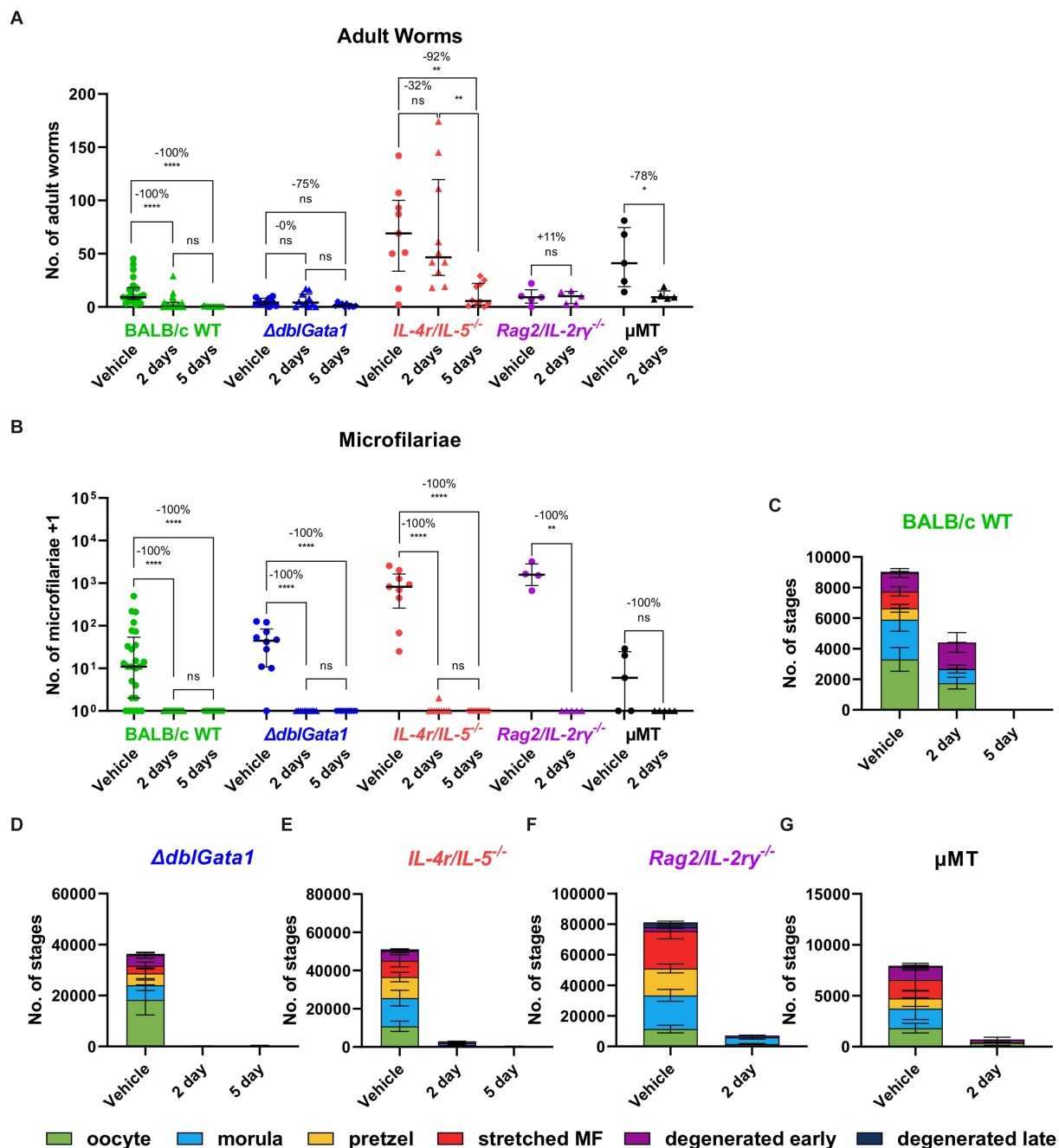
FIGURE 2

Reduced macrofilaricidal efficacy of flubendazole in immunodeficient mice. **(A–G)** Indicated mouse strains were naturally infected with *Litomosoides sigmodontis* and treated subcutaneously with 2 mg/kg flubendazole once per day for 2 or 5 days starting 35 days after the infection. Necropsies were performed 70 days after the infection. **(A)** Adult worm burden. **(B)** Microfilariae per 50 μL peripheral blood +1. **(C–G)** Average number of embryonal stages per female worm in **(C)** BALB/c (green), **(D)** *ΔdblGata1* (blue), **(E)** *IL-4r/IL-5⁻/⁻* (red), **(F)** *Rag2/IL-2rγ⁻/⁻* (purple) and **(G)** μMT mice (black). **(A,B)** Data shown as median with interquartile range. Numbers show reduction of median in comparison to corresponding vehicle control. **(C–G)** Data shown as mean±SEM. **(A–G)** Data for BALB/c pooled from 5 experiments, *ΔdblGata1* and *IL-4r/IL-5⁻/⁻* pooled from 2 experiments, *Rag2/IL-2rγ⁻/⁻* and μMT from 1 experiment. Statistical analysis using Kruskal-Wallis with Dunn's *post-hoc* test, *$p < 0.05$, **$p < 0.01$, ****$p < 0.0001$.

and mature F4/80 (high) macrophages, μMT mice lacking mature B cells and antibodies and *Rag2/IL-2rγ⁻/⁻* mice lacking T cells, B cells, NK cells and ILCs. The macrofilaricidal efficacy of both OXF and FBZ was reduced in all tested immunodeficient strains, and treatment efficacy was lowest in strains with more severe immunodeficiency, i.e., *IL-4r/IL-5⁻/⁻* vs. *ΔdblGata1* mice, or completely abrogated in *Rag2/IL-2rγ⁻/⁻* mice. Interestingly, the effect on microfilariae, the filarial

progeny, which are released into the peripheral blood, were markedly different for both drugs 70 dpi. While treatment with FBZ led to a complete absence of microfilariae in all strains 70 dpi, treatment with OXF prevented microfilaremia only in BALB/c WT and μMT mice 70 dpi, indicating that the effect of OXF on microfilaremia is dependent on the immune system overall but independent of mature B cells and antibodies. At 56 dpi, mice treated with either OXF or FBZ

TABLE 2 Clearance of adult worms and microfilariae after FBZ treatment.

	Adult worm negative mice			Microfilariae negative mice		
	Vehicle	2 days FBZ	5 days FBZ	Vehicle	2 days FBZ	5 days FBZ
BALB/c	0.0%	56.0%	93.3%	20.0%	100%	100%
	(0/25)	(14/25)	(14/15)	(5/25)	(25/25)	(15/15)
ΔdblGata1	10.0%	27.2%	30.0%	10.0%	100%	100%
	(1/10)	(3/11)	(3/10)	(1/10)	(11/11)	(10/10)
IL-4r/IL-5⁻/⁻	0.0%	0.0%	10.0%	0.0%	90%	100%
	(0/9)	(0/10)	(1/10)	(0/9)	(9/10)	(10/10)
Rag2/IL-2rγ⁻/⁻	0.0%	0.0%	n/a	0.0%	100%	n/a
	(0/5)	(0/5)		(0/5)	(5/5)	
μMT	0.0%	0.0%	n/a	20.0%	100%	n/a
	(0/5)	(0/5)		(2/5)	(5/5)	

BALB/c WT mice and immunodeficient strains (*ΔdblGata1*, *IL-4r/IL-5⁻/⁻*, μMT and *Rag2/IL-2rγ⁻/⁻*) were naturally infected with *Litomosoides sigmodontis* and treated with 2 mg/kg FBZ once per day for 2 or 5 days starting 35 dpi. Number of adult worms in the thoracic cavity and number of microfilariae per 50 μL blood were quantified 70 dpi. Data is pooled from 1 to 5 experiments. Shown is the number and frequency of animals that were free of adult worms and microfilariae at 70 dpi.

presented with 0 microfilariae in the peripheral blood except for two *ΔdblGata1* mice (Supplementary Figure S4). Analysis of embryonal development supported these results with a near complete absence of late stages after FBZ treatment in all strains or only BALB/c and μMT mice after OXF treatment.

Notably, treatment with FBZ and OXF was performed between 35 and 39 dpi, i.e., after the final molt into adult worms (~30 dpi) but before the development of microfilariae (~50 dpi) (Petit et al., 1992; Hübner et al., 2009; Risch et al., 2021). In addition, FBZ was injected subcutaneously while OXF was given orally. Prior studies in jirds (*Meriones unguiculatus*) have shown that subcutaneously injected FBZ is slowly released, and FBZ remains stable and detectable in the plasma for >50 days after injection (Hübner et al., 2019). Orally given OXF, on the other hand, is rapidly metabolized with a $T_{1/2}$ of 2.8 h in mice (Hübner et al., 2020). Therefore, OXF only interacted with the adult worms and prevented microfilaremia purely via an impact on the fertility of adult worms, whereas FBZ may have affected both adult worms and microfilariae. It is, however, relevant to note that both OXF and FBZ have been reported to be relatively ineffective against the microfilarial stage of *L. sigmodontis* and *B. malayi*, respectively. Prior studies have posited the damage to adult worms and subsequent negative impact on fertility as the leading cause for the reduced microfilariae burden for both parasites (Hübner et al., 2019; Sjoberg et al., 2019).

Previous studies have reported that *ΔdblGata1* mice present with a higher susceptibility to *L. sigmodontis* infection than BALB/c WT mice with an increased adult worm burden and >70% of mice developing microfilaremia (Fercoq et al., 2019; Frohberger et al., 2019). In the current study, we have observed a significantly lower number of microfilariae-positive animals only in the controls for the OXF treatment but not the FBZ treatment (Figures 1B, 2B). A more detailed analysis of the data sets revealed that this discrepancy is due to a strong sexual dimorphism in *ΔdblGata1* mice, with female mice significantly more susceptible to develop patent infections (Supplementary Figure S5).

The flow cytometry data analysis revealed significant changes after treatment in all strains with distinct strain-specific patterns in both the spleen and thoracic cavity. The thoracic cavity, which contains the adult worms of *L. sigmodontis,* is filled with a variety of immunologically active components such as lysozymes, antibodies, complement factors and different immune cells depending on the stage of infection (Miserocchi, 1997; Charalampidis et al., 2015; Finlay and Allen, 2020). Of note, eosinophils are absent from the thoracic cavity in naïve mice but recruited during the infection starting from day 11 after the infection (Finlay and Allen, 2020; Ehrens et al., 2022b). Flow cytometry analysis showed decreased eosinophil frequencies and total cell counts after OXF treatment in the thoracic cavity in BALB/c but an increase in *Rag2/IL-2rγ⁻/⁻* and μMT mice. As eosinophils are critical effectors in controlling the adult worm burden (Ehrens et al., 2022b), it is possible that this strain-dependent difference can be explained by the clearance of adult worms in BALB/c mice and the continuous presence of the adult worms in the immunodeficient strains. Similarly, BALB/c mice presented with markedly increased B and Th2 cell numbers which were either absent or less pronounced in the other strains. Both T and B cells play important roles in worm killing and mediating protection against secondary infections (Al-Qaoud et al., 1997, 1998; Martin et al., 2001; Finlay and Allen, 2020). Overall, the data set highlights several intriguing immunological changes after treatment in both immunocompetent WT and immunodeficient KO mice.

Based on the results from the immunodeficient mice, we next investigated the potential of a combination therapy of OXF with three cytokines (IL-4, IL-5, and IL-33). The cytokines were chosen based on the reduced treatment efficacy in *ΔdblGata1* and *IL-4r/IL-5⁻/⁻* mice and to boost the type 2 immune response typically associated with helminth infections (Finlay and Allen, 2020; Ehrens et al., 2022b). The combination with IL-5 achieved the most promising results with improved macrofilaricidal efficacy, reduction in microfilariae-positive animals and no pathological changes in the lungs of treated mice. The combination of anthelmintics with immunostimulatory compounds has already been tested for the treatment of several different helminths including *Angiostrongylus cantonensis* (mebendazole with IL-12), *B. malayi* (diethylcarbamazine with tuftsin, mebendazole with Freund's complete adjuvant), *Echinococcus granulosus* (albendazole with IL-12, IFN-α, and IFN-γ), *Echinococcus multilocularis* (albendazole with transfer factor), *L. sigmodontis* (ivermectin with various immunomodulators), *Schistosoma mansoni* (praziquantel with various immunomodulators) and *Toxocara canis* (albendazole with glucan); most studies reported an overall improvement of the treatment efficacy (Murthy et al., 1992; Fatma et al., 1994; Hrckova and Velebny, 2001; Du et al., 2003; Owais et al., 2003; Dvoroznakova et al., 2009; Zhang et al., 2017; Rahdar et al., 2020; Silva et al., 2020). For example, Zhang et al. demonstrated a significantly stronger reduction of the number, size and weight of *E. granulosus* cysts in mice treated with albendazole + IFN-α compared to mice treated with albendazole alone. In addition, they reported structural modifications of cysts associated with the combination therapy (Zhang et al., 2017). Murthy et al. showed that mebendazole given intraperitoneally, along with Freund's complete adjuvant, was four times more effective as a filaricide than mebendazole alone (Murthy et al., 1992). To the best of the authors' knowledge, the current study is the first to investigate the potential of improving the anti-filarial activity of OXF via a combination with immunostimulatory compounds and may serve as a proof of concept study for further research in this area.
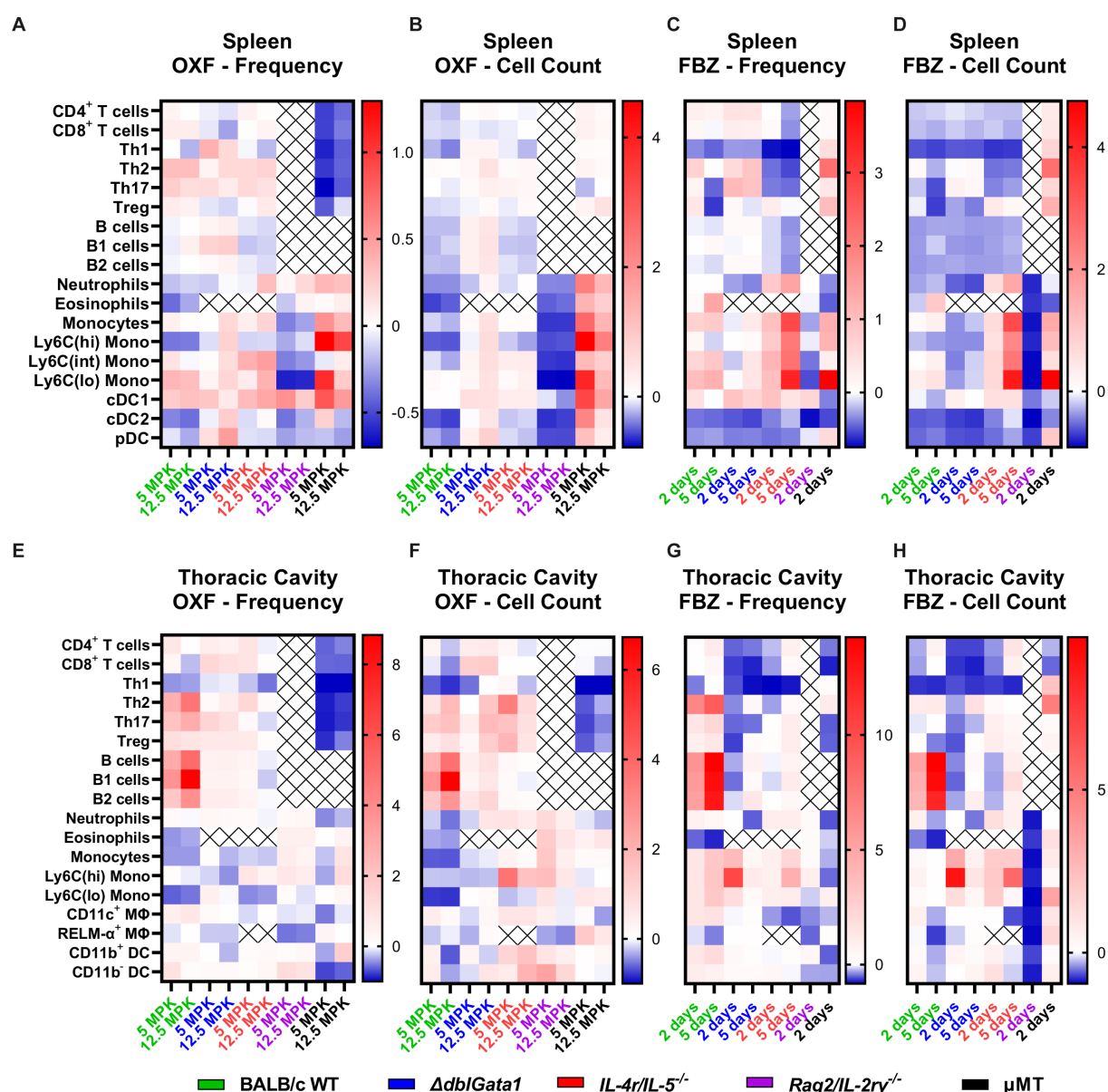
FIGURE 3

Distinct immunological changes in different immunodeficient strains after anti-filarial treatment. **(A−H)** Indicated mouse strains were naturally infected with *Litomosoides sigmodontis* and treated with **(A,B,E,F)** oxfendazole or **(C,D,G,H)** flubendazole 35 days after the infection. Necropsies were performed 70 days after the infection and immune cell populations in **(A−D)** spleen and **(E−H)** thoracic cavity were analyzed via flow cytometry. Heat maps show fold change of **(A,C,E,G)** mean of immune cell frequencies and **(B,D,F,H)** mean of total cell counts after treatment in comparison to corresponding vehicle controls. **(A,B,E,F)** Data for BALB/c (green) pooled from 6 experiments, *IL-4r/IL-5−/−* (red) pooled from 3 experiments, *ΔdblGata1* (blue), *Rag2/IL-2rγ−/−* (purple) and µMT (black) pooled from 2 experiments. **(C,D,G,H)** Data for BALB/c pooled from 5 experiments, *ΔdblGata1* and *IL-4r/IL-5−/−* pooled from 2 experiments, *Rag2/IL-2rγ−/−* and µMT from 1 experiment.

OXF has been used as a broad-spectrum anthelmintic in the veterinary market since the 1990s (Gonzalez et al., 2019). However, concerted efforts by academia and the Drugs for Neglected Disease initiative (DNDi) have investigated the potential to repurpose OXF as a pan-nematode compound for use in humans [Specht and Keiser, 2022; Ehrens et al., 2022a, Helminth Elimination Platform (HELP)][3]. We have

previously shown the activity of OXF against *L. sigmodontis* adult worms, *O. gutturosa* adult worms and *O. volvulus* pre-adult stages (Hübner et al., 2020). In addition, first tolerability and safety studies in humans have shown OXF to be well tolerated at relevant dosages (Bach et al., 2020). OXF is currently transitioning into phase II clinical trials and will be evaluated as a potential pan-nematode drug for *O. volvulus*, *L. loa*, *M. perstans*, and *Trichuris trichiura* in the Democratic Republic of the Congo, Gabon, Cameroon and Tanzania as part of the recently launched EU-EDCTP3 project eWHORM (enabling the WHO Road Map, see text footnote 2).
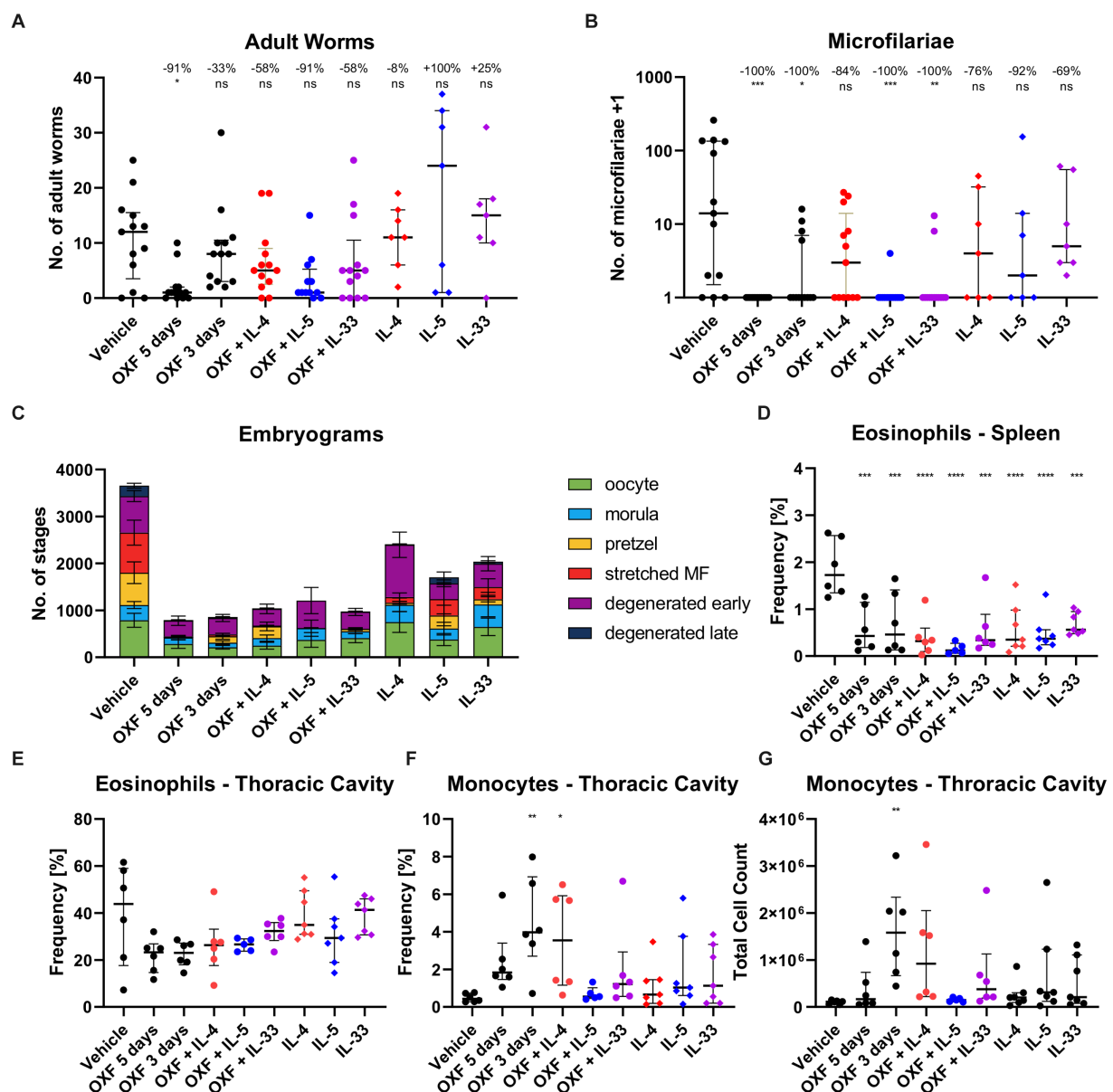
FIGURE 4
Combination of oxfendazole with interleukin-5 improves macrofilaricidal treatment efficacy in shortened treatment regimen. **(A–G)** Six-week old female BALB/c mice were naturally infected with *Litomosoides sigmodontis* and treated with 12.5mg/kg oxfendazole twice per day for 5 days (positive control) or 3 days (shortened treatment) with or without addition of intranasal application of 2μg IL-4, IL-5, or IL-33 once per day. Necropsies were performed 70 days after the infection. **(A)** Adult worm burden. **(B)** Microfilariae per 50μL peripheral blood +1. **(C)** Average number of embryonal stages per female worm. **(D)** Frequency of eosinophils [CD8⁻, CD11b⁻, Ly6G⁻, Siglec-F⁺] in spleen. **(E)** Frequency of eosinophils [CD8⁻, CD11b⁺, Siglec-F⁻] in thoracic cavity. **(F)** Frequency of monocytes [CD8⁻, CD11b⁺, Siglec-F⁻, RELMα⁻, Ly6G⁻, I-ab⁽ˡᵒ⁾] in thoracic cavity. **(G)** Total cell count of monocytes in thoracic cavity. **(A,B,D–G)** Data shown as median with interquartile range. Numbers show reduction of median in comparison to vehicle control. **(C)** Data shown as mean±SEM. **(A–C)** Data for IL-4, IL-5, IL-33 from 1 experiment, data for other groups pooled from 2 experiments (n=6−7 per group per experiment). **(D–G)** Representative data for two experiments. **(A-C,E)** Statistical analysis using Kruskal-Wallis with Dunn's *post-hoc* test, **(D,F,G)** Statistical analysis using One-Way ANOVA with Dunnett's multiple comparisons test, *p<0.05, **p<0.01, ***p<0.001, ****p<0.0001.

In light of this, further research into a combination of OXF with immunostimulatory compounds may yield additional treatment options. However, several open questions remain. One particular area that requires further research is the choice of immunostimulant. The cytokines utilized in this proof of concept study (IL-4, IL-5, and IL-33) are not likely to be applicable in the human setting as (1) recombinant cytokines are too expensive for anti-filarial treatment in the affected regions and (2) recombinant

cytokines would require a lengthy regulatory approval. On the other hand, the combination of OXF with already approved immunostimulatory compounds/treatments such as pidotimod (used mainly for respiratory diseases) or commonly used vaccine adjuvants may allow a more cost-effective treatment, shorter treatment regimens and lower drug concentrations and a faster translation of basic research to human patients and therefore contribute to the critical actions outlined in the WHO NTD
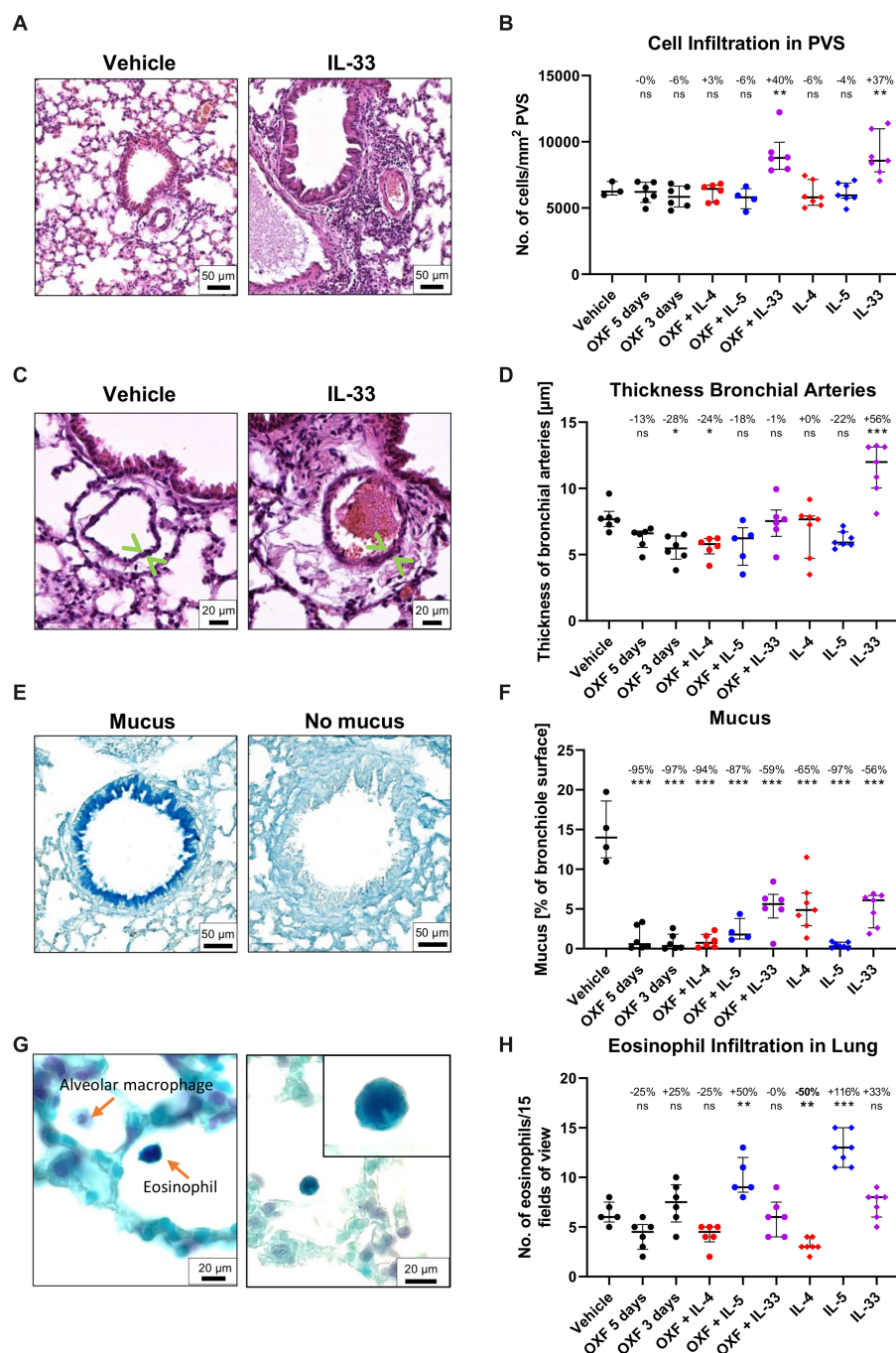
FIGURE 5
Histological changes in the lung after combination therapy. **(A–H)** Six-week old female BALB/c mice were naturally infected with *Litomosoides sigmodontis* and treated with 12.5mg/kg oxfendazole twice per day for 5 days (positive control) or 3 days (shortened treatment) with or without addition of intranasal application of 2µg IL-4, IL-5, or IL-33 once per day. Necropsies were performed 70 days after the infection and lungs were processed for histological analysis. **(A)** H&E staining of perivascular spaces (PVS). **(B)** Quantification of Hematoxylin positive nuclei per mm² in the PVS. **(C)** H&E staining of bronchial arteries. Arrows indicate the artery boundaries. **(D)** Quantification of bronchial vein thickness. **(E)** Alcian blue staining of mucus in bronchial epithelium. **(F)** Quantification of mucus on bronchiole surface. **(G)** Luxol fast blue staining of eosinophils. Left image displays a Luxol blue positive eosinophil and an alveolar macrophage. The corner zoom on the right image highlights the eosinophil lobed nucleus. **(H)** Quantification of eosinophil infiltration in the lung. **(A–H)** Results are expressed as median with interquartile of $n=3-7$ mice per group (1 experiment). Numbers show reduction of median in comparison to vehicle control. Statistical analysis using One-way ANOVA followed by Dunnett's Multiple Comparison Tests, $*p<0.05$, $**p<0.01$, $***p<0.001$.

roadmap 2021–2030 (Mahashur et al., 2019; WHO, 2020). One other yet unanswered question is the role of the immune system during anti-*Wolbachia* treatment.

Overall, in this study, we have demonstrated the significant contributions of the immune system during anti-filarial treatment. Using various immunodeficient mouse strains, we have highlighted

how the absence of different immune cells or components affects treatment efficacy against adult worms, microfilariae and embryogenesis of *L. sigmodontis*. In addition, we have shown how the combination of OXF with immunostimulatory compounds can improve treatment efficacy, and further research may yield more treatment options for human filarial patients.

Data availability statement

The original contributions presented in the study are included in the article/Supplementary material, further inquiries can be directed to the corresponding author.

Ethics statement

The animal study was reviewed and approved by the Landesamt für Natur-, Umwelt-und Verbraucherschutz, AZ: 84–02.04.2015.A507, 81–02.04.2020.A244, 81–02.05.40.18.057.

Author contributions

FR, CM, AH, and MH: conceptualization. FR, JG, FF, and MH: data curation. FR, JS, JR, BL, AE, JG, FF, MK, MF, and CM: experimentation. CM, AH, and MH: resources. CM and MH: supervision. FR and MH: writing—original draft. All authors: writing—review and editing. All authors contributed to the article and approved the submitted version.

Funding

Acknowledgments

Conflict of interest

The authors declare that the research was conducted in the absence of any commercial or financial relationships that could be construed as a potential conflict of interest.

Publisher's note

All claims expressed in this article are solely those of the authors and do not necessarily represent those of their affiliated organizations, or those of the publisher, the editors and the reviewers. Any product that may be evaluated in this article, or claim that may be made by its manufacturer, is not guaranteed or endorsed by the publisher.

Supplementary material

The Supplementary material for this article can be found online at: https://www.frontiersin.org/articles/10.3389/fmicb.2023.1213143/full#supplementary-material

References

Al-Qaoud, K. M., Fleischer, B., and Hoerauf, A. (1998). The Xid defect imparts susceptibility to experimental murine filariosis--association with a lack of antibody and IL-10 production by B cells in response to phosphorylcholine. *Int. Immunol.* 10, 17–25. doi: 10.1093/intimm/10.1.17

Al-Qaoud, K. M., Taubert, A., Zahner, H., Fleischer, B., and Hoerauf, A. (1997). Infection of BALB/c mice with the filarial nematode *Litomosoides sigmodontis*: role of CD4+ T cells in controlling larval development. *Infect. Immun.* 65, 2457–2461. doi: 10.1128/iai.65.6.2457-2461.1997

Bach, T., Galbiati, S., Kennedy, J. K., Deye, G., Nomicos, E. Y. H., Codd, E. E., et al. (2020). Pharmacokinetics, safety, and tolerability of Oxfendazole in healthy adults in an open-label phase 1 multiple ascending dose and food effect study. *Antimicrob. Agents Chemother.* 64:e01018-20. doi: 10.1128/AAC.01018-20

Bankhead, P., Loughrey, M. B., Fernandez, J. A., Dombrowski, Y., Mcart, D. G., Dunne, P. D., et al. (2017). QuPath: open source software for digital pathology image analysis. *Sci. Rep.* 7:16878. doi: 10.1038/s41598-017-17204-5

Beckert, H., Meyer-Martin, H., Buhl, R., Taube, C., and Reuter, S. (2020). Single and synergistic effects of type 2 cytokines on eosinophils and asthma hallmarks. *J. Immunol.* 204, 550–558. doi: 10.4049/jimmunol.1901116

Boussinesq, M., Gardon, J., Gardon-Wendel, N., and Chippaux, J. P. (2003). Clinical picture, epidemiology and outcome of Loa-associated serious adverse events related to mass ivermectin treatment of onchocerciasis in Cameroon. *Filaria J.* 2 Suppl 1:S4. doi: 10.1186/1475-2883-2-S1-S4

Charalampidis, C., Youroukou, A., Lazaridis, G., Baka, S., Mpoukovinas, I., Karavasilis, V., et al. (2015). Pleura space anatomy. *J. Thorac. Dis.* 7, S27–S32. doi: 10.3978/j.issn.2072-1439.2015.01.48

Denham, D. A., Samad, R., Cho, S. Y., Suswillo, R. R., and Skippins, S. C. (1979). The anthelmintic effects of flubendazole on *Brugia pahangi*. *Trans. R. Soc. Trop. Med. Hyg.* 73, 673–676. doi: 10.1016/0035-9203(79)90018-x

Dominguez-Vazquez, A., Taylor, H. R., Greene, B. M., Ruvalcaba-Macias, A. M., Rivas-Alcala, A. R., Murphy, R. P., et al. (1983). Comparison of flubendazole and diethylcarbamazine in treatment of onchocerciasis. *Lancet* 1, 139–143. doi: 10.1016/s0140-6736(83)92753-8

Du, W. Y., Liao, J. W., Fan, C. K., and Su, K. E. (2003). Combined treatment with interleukin-12 and mebendazole lessens the severity of experimental eosinophilic meningitis caused by *Angiostrongylus cantonensis* in ICR mice. *Infect. Immun.* 71, 3947–3953. doi: 10.1128/IAI.71.7.3947-3953.2003

Dvoroznakova, E., Porubcova, J., and Sevcikova, Z. (2009). Immune response of mice with alveolar echinococcosis to therapy with transfer factor, alone and in combination with albendazole. *Parasitol. Res.* 105, 1067–1076. doi: 10.1007/s00436-009-1520-z

Ehrens, A., Hoerauf, A., and Hubner, M. P. (2022a). Current perspective of new anti-Wolbachial and direct-acting macrofilaricidal drugs as treatment strategies for human filariasis. *GMS Infect. Dis.* 10:Doc02. doi: 10.3205/id000079

Ehrens, A., Hoerauf, A., and Hubner, M. P. (2022b). Eosinophils in filarial infections: inducers of protection or pathology? *Front. Immunol.* 13:983812. doi: 10.3389/fimmu.2022.983812

Fatma, N., Mathur, K. B., and Chatterjee, R. K. (1994). Chemotherapy of experimental filariasis: enhancement of activity profile of ivermectin with immunomodulators. *Acta Trop.* 57, 55–67. doi: 10.1016/0001-706x(94)90093-0

Fercoq, F., Remion, E., Frohberger, S. J., Vallarino-Lhermitte, N., Hoerauf, A., Le Quesne, J., et al. (2019). IL-4 receptor dependent expansion of lung CD169+ macrophages in microfilaria-driven inflammation. *PLoS Negl. Trop. Dis.* 13:e0007691. doi: 10.1371/journal.pntd.0007691

Finlay, C. M., and Allen, J. E. (2020). The immune response of inbred laboratory mice to *Litomosoides sigmodontis*: a route to discovery in myeloid cell biology. *Parasite Immunol.* 42:e12708. doi: 10.1111/pim.12708

Fischer, C., Ibiricu Urriza, I., Bulman, C. A., Lim, K. C., Gut, J., Lachau-Durand, S., et al. (2019). Efficacy of subcutaneous doses and a new oral amorphous solid dispersion formulation of flubendazole on male jirds (*Meriones unguiculatus*) infected with the filarial nematode *Brugia pahangi*. *PLoS Negl. Trop. Dis.* 13:e0006787. doi: 10.1371/journal.pntd.0006787

Francis, H., Awadzi, K., and Ottesen, E. A. (1985). The Mazzotti reaction following treatment of onchocerciasis with diethylcarbamazine: clinical severity as a function of infection intensity. *Am. J. Trop. Med. Hyg.* 34, 529–536. doi: 10.4269/ajtmh.1985.34.529

Frohberger, S. J., Ajendra, J., Surendar, J., Stamminger, W., Ehrens, A., Buerfent, B. C., et al. (2019). Susceptibility to *L. sigmodontis* infection is highest in animals lacking IL-4R/IL-5 compared to single knockouts of IL-4R, IL-5 or eosinophils. *Parasit. Vectors* 12:248. doi: 10.1186/s13071-019-3502-z

Fuller, B. B., Harris, V., Parker, C., Martinez, A., Toubali, E., Ebene, B. C., et al. (2023). Contextual determinants of mass drug administration performance: modelling fourteen years of lymphatic filariasis treatments in West Africa. *PLoS Negl. Trop. Dis.* 17:e0011146. doi: 10.1371/journal.pntd.0011146

Geary, T. G., Mackenzie, C. D., and Silber, S. A. (2019). Flubendazole as a macrofilaricide: history and background. *PLoS Negl. Trop. Dis.* 13:e0006436. doi: 10.1371/journal.pntd.0006436

Gonzalez, A. E., Codd, E. E., Horton, J., Garcia, H. H., and Gilman, R. H. (2019). Oxfendazole: a promising agent for the treatment and control of helminth infections in humans. *Expert Rev. Anti Infect. Ther.* 17, 51–56. doi: 10.1080/14787210.2018.1555241

Hawryluk, N. A. (2020). Macrofilaricides: an unmet medical need for filarial diseases. *ACS Infect. Dis.* 6, 662–671. doi: 10.1021/acsinfecdis.9b00469

Hrckova, G., and Velebny, S. (2001). Treatment of *Toxocara canis* infections in mice with liposome-incorporated benzimidazole carbamates and immunomodulator glucan. *J. Helminthol.* 75, 141–146. doi: 10.1079/JOH2001081

Hübner, M. P., Ehrens, A., Koschel, M., Dubben, B., Lenz, F., Frohberger, S. J., et al. (2019). Macrofilaricidal efficacy of single and repeated oral and subcutaneous doses of flubendazole in *Litomosoides sigmodontis* infected jirds. *PLoS Negl. Trop. Dis.* 13:e0006320. doi: 10.1371/journal.pntd.0006320

Hübner, M. P., Martin, C., Specht, S., Koschel, M., Dubben, B., Frohberger, S. J., et al. (2020). Oxfendazole mediates macrofilaricidal efficacy against the filarial nematode *Litomosoides sigmodontis in vivo* and inhibits *Onchocerca* spec. Motility *in vitro*. *PLoS Negl. Trop. Dis.* 14:e0008427. doi: 10.1371/journal.pntd.0008427

Hübner, M. P., Torrero, M. N., Mccall, J. W., and Mitre, E. (2009). *Litomosoides sigmodontis*: a simple method to infect mice with L3 larvae obtained from the pleural space of recently infected jirds (*Meriones unguiculatus*). *Exp. Parasitol.* 123, 95–98. doi: 10.1016/j.exppara.2009.05.009

Irvine, M. A., Stolk, W. A., Smith, M. E., Subramanian, S., Singh, B. K., Weil, G. J., et al. (2017). Effectiveness of a triple-drug regimen for global elimination of lymphatic filariasis: a modelling study. *Lancet Infect. Dis.* 17, 451–458. doi: 10.1016/S1473-3099(16)30467-4

Jackson-Jones, L. H., Ruckerl, D., Svedberg, F., Duncan, S., Maizels, R. M., Sutherland, T. E., et al. (2016). IL-33 delivery induces serous cavity macrophage proliferation independent of interleukin-4 receptor alpha. *Eur. J. Immunol.* 46, 2311–2321. doi: 10.1002/eji.201646442

James, S. L., Abate, D., Abate, K. H., Abay, S. M., Abbafati, C., Abbasi, N., et al. (2018). Global, regional, and national incidence, prevalence, and years lived with disability for 354 diseases and injuries for 195 countries and territories, 1990–2017: a systematic analysis for the global burden of disease study 2017. *Lancet* 392, 1789–1858. doi: 10.1016/S0140-6736(18)32279-7

Johansson, K., Malmhall, C., Ramos-Ramirez, P., and Radinger, M. (2018). Bone marrow type 2 innate lymphoid cells: a local source of interleukin-5 in interleukin-33-driven eosinophilia. *Immunology* 153, 268–278. doi: 10.1111/imm.12842

King, C. L., Suamani, J., Sanuku, N., Cheng, Y. C., Satofan, S., Mancuso, B., et al. (2018). A trial of a triple-drug treatment for lymphatic filariasis. *N. Engl. J. Med.* 379, 1801–1810. doi: 10.1056/NEJMoa1706854

Lacey, E. (1990). Mode of action of benzimidazoles. *Parasitol. Today* 6, 112–115. doi: 10.1016/0169-4758(90)90227-u

Lachau-Durand, S., Lammens, L., Van Der Leede, B. J., Van Gompel, J., Bailey, G., Engelen, M., et al. (2019). Preclinical toxicity and pharmacokinetics of a new orally bioavailable flubendazole formulation and the impact for clinical trials and risk/benefit to patients. *PLoS Negl. Trop. Dis.* 13:e0007026. doi: 10.1371/journal.pntd.0007026

Mahashur, A., Thomas, P. K., Mehta, P., Nivangune, K., Muchhala, S., and Jain, R. (2019). Pidotimod: in-depth review of current evidence. *Lung India* 36, 422–433. doi: 10.4103/lungindia.lungindia_39_19

Martin, C., Saeftel, M., Vuong, P. N., Babayan, S., Fischer, K., Bain, O., et al. (2001). B-cell deficiency suppresses vaccine-induced protection against murine filariasis but does not increase the recovery rate for primary infection. *Infect. Immun.* 69, 7067–7073. doi: 10.1128/IAI.69.11.7067-7073.2001

Mclure, A., Graves, P. M., Lau, C., Shaw, C., and Glass, K. (2022). Modelling lymphatic filariasis elimination in American Samoa: GEOFIL predicts need for new targets and six rounds of mass drug administration. *Epidemics* 40:100591. doi: 10.1016/j.epidem.2022.100591

Miserocchi, G. (1997). Physiology and pathophysiology of pleural fluid turnover. *Eur. Respir. J.* 10, 219–225. doi: 10.1183/09031936.97.10010219

Murthy, P. K., Tyagi, K., and Chatterjee, R. K. (1992). Brugia malayi in *Mastomys natalensis*: efficacy of mebendazole in combination with Freund's complete adjuvant. *Folia Parasitol.* 39, 51–59.

Owais, M., Misra-Bhattacharya, S., Haq, W., and Gupta, C. M. (2003). Immunomodulator tuftsin augments antifilarial activity of diethylcarbamazine against experimental brugian filariasis. *J. Drug Target.* 11, 247–251. doi: 10.1080/10611860310001620707

Petit, G., Diagne, M., Marechal, P., Owen, D., Taylor, D., and Bain, O. (1992). Maturation of the filaria *Litomosoides sigmodontis* in BALB/c mice; comparative susceptibility of nine other inbred strains. *Ann. Parasitol. Hum. Comp.* 67, 144–150. doi: 10.1051/parasite/1992675144

Rahdar, M., Rafiei, A., and Valipour-Nouroozi, R. (2020). The combination of cytokines and albendazole therapy for prophylaxis and treatment of experimental/hydatid cyst. *Acta Trop.* 201:105206. doi: 10.1016/j.actatropica.2019.105206

Reichwald, J. J., Risch, F., Neumann, A. L., Frohberger, S. J., Scheunemann, J. F., Lenz, B., et al. (2022). ILC2s control Microfilaremia during *Litomosoides sigmodontis* infection in Rag2(−/−) mice. *Front. Immunol.* 13:863663. doi: 10.3389/fimmu.2022.863663

Risch, F., Ritter, M., Hoerauf, A., and Hubner, M. P. (2021). Human filariasis-contributions of the *Litomosoides sigmodontis* and Acanthocheilonema viteae animal model. *Parasitol. Res.* 120, 4125–4143. doi: 10.1007/s00436-020-07026-2

Silva, J. C. S., Bernardes, M., Melo, F. L., Sa, M., and Carvalho, B. M. (2020). Praziquantel versus praziquantel associated with immunomodulators in mice infected with schistosoma mansoni: a systematic review and meta-analysis. *Acta Trop.* 204:105359. doi: 10.1016/j.actatropica.2020.105359

Sjoberg, H. T., Pionnier, N., Aljayyoussi, G., Metuge, H. M., Njouendou, A. J., Chunda, V. C., et al. (2019). Short-course, oral flubendazole does not mediate significant efficacy against *Onchocerca* adult male worms or Brugia microfilariae in murine infection models. *PLoS Negl. Trop. Dis.* 13:e0006356. doi: 10.1371/journal.pntd.0006356

Specht, S., and Keiser, J. (2022). Helminth infections: enabling the World Health Organization road map. *Int. J. Parasitol.* 53, 411–414. doi: 10.1016/j.ijpara.2022.10.006

Surin, J., and Denham, D. A. (1990). Comparative susceptibility to anthelmintics of *Brugia pahangi* in jirds infected by different methods. *J. Helminthol.* 64, 232–238. doi: 10.1017/s0022149x00012219

Taylor, M. J., Hoerauf, A., and Bockarie, M. (2010). Lymphatic filariasis and onchocerciasis. *Lancet* 376, 1175–1185. doi: 10.1016/S0140-6736(10)60586-7

Wanji, S., Chounna Ndongmo, W. P., Fombad, F. F., Kengne-Ouafo, J. A., Njouendou, A. J., Longang Tchounkeu, Y. F., et al. (2018). Impact of repeated annual community directed treatment with ivermectin on loiasis parasitological indicators in Cameroon: implications for onchocerciasis and lymphatic filariasis elimination in areas co-endemic with Loa loa in Africa. *PLoS Negl. Trop. Dis.* 12:e0006750. doi: 10.1371/journal.pntd.0006750

WHO (2020). *Ending the neglect to attain the sustainable development goals: A road map for neglected tropical diseases 2021–2030*. Geneva: World Health Organization.

Zhang, S., Zhou, Y., Su, L., Zhang, X., Wang, H., and Liu, B. (2017). *In vivo* evaluation of the efficacy of combined albedazole-IFN-alpha treatment for cystic echinococcosis in mice. *Parasitol. Res.* 116, 735–742. doi: 10.1007/s00436-016-5339-0

Ziewer, S., Hubner, M. P., Dubben, B., Hoffmann, W. H., Bain, O., Martin, C., et al. (2012). Immunization with *L. sigmodontis* microfilariae reduces peripheral microfilaraemia after challenge infection by inhibition of filarial embryogenesis. *PLoS Negl. Trop. Dis.* 6:e1558. doi: 10.1371/journal.pntd.0001558

Frontiers in
Microbiology

Explores the habitable world and the potential of microbial life

The largest and most cited microbiology journal which advances our understanding of the role microbes play in addressing global challenges such as healthcare, food security, and climate change.

Discover the latest Research Topics

See more →

Frontiers

Avenue du Tribunal-Fédéral 34
1005 Lausanne, Switzerland
frontiersin.org

Contact us

+41 (0)21 510 17 00
frontiersin.org/about/contact

frontiers | Frontiers in Microbiology